Influence of Interface and Type of Strain Hardening Cementitious Composite (SHCC) on Crack Control in SHCC-Concrete Hybrid Beams

Shantanu Singh

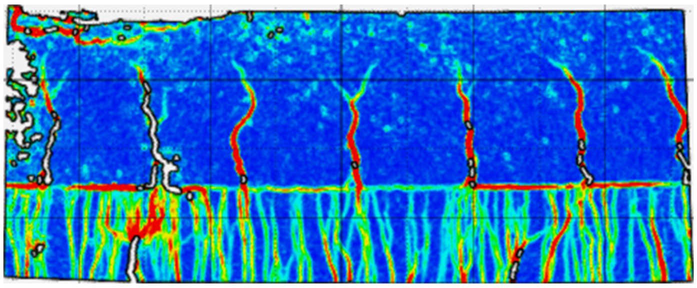

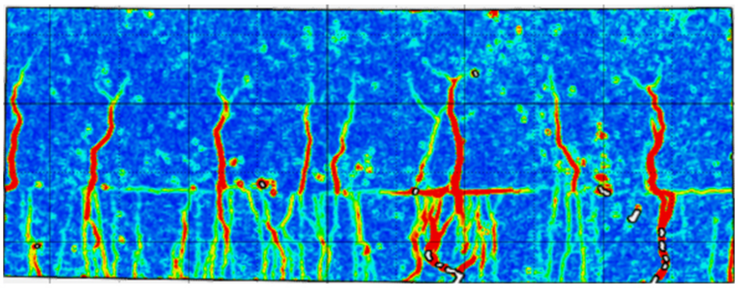

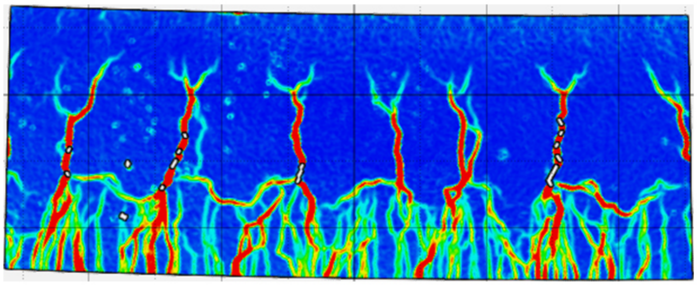

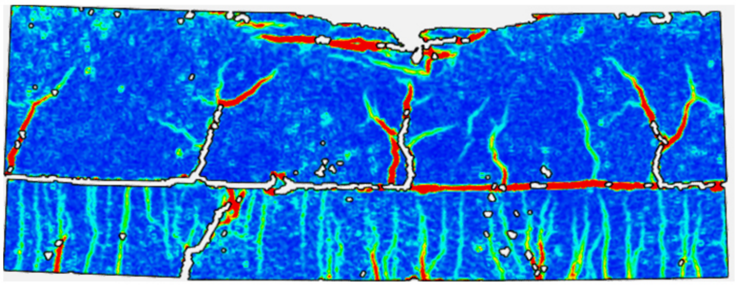

DELFT UNIVERSITY OF TECHNOLOGY

MASTER THESIS

Influence of Interface and Type of Strain Hardening Cementitious Composite (SHCC) on Crack Control in SHCC-Concrete Hybrid Beams

---

submitted in partial fulfillment of the
requirements for the degree of

MASTER OF SCIENCE
in
STRUCTURAL ENGINEERING

Author: SHANTANU SINGH
Student number: 4712102

September 17, 2019

Thesis Committee

Chair and Daily Supervisor	:	Dr. MLADENA LUKOVIC – Concrete Structures, TU Delft.
Member	:	Prof.dr.ir. ERIK SCHLANGEN - Materials and Environment, TU Delft.
Member	:	Dr. BRANKO SAVIJA - Materials and Environment, TU Delft.

Acknowledgement

It feels like a dream to be writing this but here I am. I can confidently say that the people I met during my master's degree contributed to my interesting journey in many ways.

Firstly, I would like to thank Delft University of Technology for accepting me into the master's program of my choice. The experience of working with professors of such par excellence has been life-changing and I appreciate it.

My chair and daily supervisor Mladena Lukovic, is someone I started looking up to in the months of knowing her. Her knowledge pool, dedication and work-ethic inspires and awes me everyday. I hope working with her these past months has helped me capture, at least a few among many of her talents. My heartfelt thanks to her for making a research topic for me when I said that I want to do something related to interface for my master thesis research. I will forever be grateful to her for her valuable inputs and discussions during the course of my research.

I would like to thank Erik Schlangen and Branko Savija for their timely feedback in the progress meetings. This most definitely helped me in keeping my research on track and focused on aspects that contributed to my research.

My parents are my everything and this simply would not have been possible without their unconditional love and support. My siblings Neha and Nikhil, thank you for guiding, listening and supporting me at all times.

If something is bothering you, share it with your friends because they care about you. This is the most valuable lesson I have learnt from my friends I made in Delft. Thank you Shozab, Akshay, Sushmitha and Anna for everything.

Last but not the least, my special one Samyuktha, thank you for the incessant support you have shown during my journey. Your advice has always made an impact on me and I respect them.

Influence of Interface and Type of Strain Hardening Cementitious Composite (SHCC) on Crack Control in SHCC-Concrete Hybrid Beams

---

Abstract

A combination of conventional concrete members with innovative material such as Strain Hardening Cementitious Composite (SHCC) in the tensile zone, can exhibit better crack-width control. This is attributed to the bridging effect by the Polyvinyl Alcohol (PVA) fibers used in SHCC in combination with the special material composition containing fine particles. This hybrid combination is able to satisfy the Serviceability Limit State (SLS) criteria for crack-width control by eliminating the requirement of additional reinforcement. Optimisation of micro-cracking of SHCC requires an investigation to study the influence of the interface in SHCC-Concrete hybrid beam and the type of fiber used in SHCC. This master thesis research is a continuation of the previous Msc. thesis study performed by Zhekang Huang [1] on the experimental flexural behaviour of reinforced concrete beams with a layer of SHCC in the tension zone. Variation in the bond interface property such as smooth interface profile, partially debonded, completely debonded and grooved interface profile are investigated to study their influence on the bearing capacity and crack-width control. To assess the impact of the type of fibers on crack-width control, commonly used PVA fibers are replaced with High Modulus Polyethylene Fibers (HMPE) based on pre-study. All hybrid beams are tested experimentally in a four-point bending set-up to generate cracks within the constant moment region and Digital Image Correlation (DIC) is performed to evaluate the crack patterns and the crack-widths. Numerical analyses of the beams are performed using Finite Element Analysis software Diana {version 10.3} with the modelling of similar interfaces and material properties used in the experiments.

From the obtained results, it is observed that for all the beam specimens tested, varying the interface property did not have a significant impact on their bearing capacity as the interface within the constant moment region is only varied and the surface outside this region is bonded. For beam specimens with partial and completely debonded interface in the constant moment region, it is observed that the initial stiffness is reduced but the overall bearing capacity remains the same.

Within the constant moment region, varying the interface property resulted in different crack patterns. The profiled and smooth interfaces, despite exhibiting different crack patterns, reached the maximum allowable crack-width of 0.3 mm at similar load steps of 69 KN and 71 KN respectively. This is because a sufficient bond at the interface is developed and as a result, due to local adhesion, the surface roughness plays a minor role. The beam specimens with completely and partially debonded interfaces localised at a much earlier load step of 45 KN and 50 KN respectively. This is because the stress generated in the SHCC layer is higher due to the severely cracked concrete layer on top. The beam specimens with smooth interface and HMPE fibers in SHCC perform similar to the beams with smooth interface and PVA fibers in SHCC. This is because of the additional constraint created due to the conventional concrete layer at the top in the SHCC-concrete hybrid beam. Despite the higher flexural capacity of the SHCC layer containing HMPE fibers, the concrete layer crushes much before the SHCC layer fails, thus, compromising the performance of the hybrid beam.

By reducing the interface stiffness properties, an effort is made to reproduce the behaviour of specimen beams in four-point bending test through numerical modelling on Diana FEA. However, the prediction of the number of cracks formed and the crack-widths is inaccurate for all the beam specimens modelled. This is because the material models and interface properties available on Diana FEA to the authors knowledge, are insufficient in replicating the experimental cracking behaviour.

Keywords: hybrid concrete beams, serviceability, interface, localisation

Contents

List of Figures ix

List of Tables xv

1 Background and Motivation 1
- 1.1 Introduction . . . 1
- 1.2 Scope . . . 2
- 1.3 Research Hypothesis . . . 2
- 1.4 Research Questions, Objectives and Set-goals . . . 2
- 1.5 Outline of the Thesis . . . 3

2 Literature Review 5
- 2.1 Strain Hardening Cementitious Composite . . . 5
  - 2.1.1 Introduction . . . 5
  - 2.1.2 Properties of SHCC . . . 5
- 2.2 Hybrid SHCC/Concrete Systems . . . 8
  - 2.2.1 Influence of Interface . . . 8
  - 2.2.2 Influence of Fiber . . . 21
- 2.3 Digital Image Correlation (DIC) . . . 24
- 2.4 General: SHCC-Concrete Systems . . . 25
  - 2.4.1 Reinforced SHCC-Concrete Hybrid beams . . . 25
  - 2.4.2 Repair with SHCC (Structural and Non-Structural) . . . 26

3 Experimental Study 29
- 3.1 Pre-Study . . . 29
  - 3.1.1 Fiber Material . . . 29
  - 3.1.2 Interface Debond Material . . . 31
- 3.2 Design . . . 31
- 3.3 Casting . . . 36
  - 3.3.1 SHCC layer . . . 36
  - 3.3.2 Interface Preparation and Treatment . . . 38
  - 3.3.3 Concrete layer . . . 38
- 3.4 Testing . . . 40
  - 3.4.1 Linear Variable Data Transformer (LVDT) . . . 41
  - 3.4.2 Digital Image Correlation (DIC) . . . 41
- 3.5 Post-Processing . . . 42
  - 3.5.1 Correlation using GOM correlate . . . 42
  - 3.5.2 Validation of GOM results . . . 45
- 3.6 Results and Discussion . . . 49
  - 3.6.1 Results: Bearing Capacity and Crack-width Control . . . 49
  - 3.6.2 Conventional Concrete Beam (CC) . . . 49
  - 3.6.3 Hybrid Beam with Smooth Interface (S-PVA) . . . 57

3.6.4 Hybrid Beam with Partially Delaminated Interface (PD-PVA) 70
3.6.5 Hybrid Beam with Completely Delaminated Interface (CD-PVA) 82
3.6.6 Hybrid Beam with Profiled Interface (P-PVA) 96
3.6.7 Hybrid Beam with Smooth Interface and HMPE Fibers (S-HMPE) 107
3.6.8 Comparison of Experimental Results 119
3.6.9 Dicussion 123

4 Numerical Analyses **131**
4.1 Geometry 131
4.2 Material Properties 132
4.2.1 Concrete 132
4.2.2 SHCC 133
4.2.3 Reinforcement Steel 134
4.2.4 Steel plate 136
4.3 Interface Properties 137
4.4 Loading and Support Conditions 137
4.5 Meshing 138
4.6 Analysis Procedure 138
4.7 Results and Discussion 138
4.7.1 Hybrid Beam with Smooth Interface (S-PVA) 138
4.7.2 Hybrid Beam with Completely Delaminated Interface (CD-PVA) 141

5 Conclusions and Recommendations **143**

Bibliography **147**

List of Figures

1.1 Outline of Thesis Research . . . 3

2.1 Permeability vs crack width [2] . . . 6
2.2 Effective diffusion vs deformation [3] . . . 6
2.3 Tensile force vs deformation for different types of loads [3] . . . 7
2.4 Experiemental fire heating set-up [3] . . . 7
2.5 Temperature response of specimens [3] . . . 8
2.6 Types of bonding at the interface [4] . . . 8
2.7 Two layered old-to-new concrete model [5] . . . 9
2.8 (a) Artificial interface roughness (b) Morphology of concrete interface [6] . . . 9
2.9 Flexural, tensile and bonding strength vs fractal dimensions of artificial roughness [6] . . . 9
2.10 Cross-section of UHTCC specimen [7] . . . 10
2.11 Crack opening in UHTCC25 specimen [7] . . . 10
2.12 Location of first crack in UHTCC25 [7] . . . 11
2.13 Crack opening in UHTCC50 specimen [7] . . . 11
2.14 Crack opening in UHTCC15 specimen [7] . . . 11
2.15 Concrete surface preparation (a) left-as-cast (b) steel reinforcement (c) roughened by wire brush [8] . . . 12
2.16 Push-off test [8] . . . 12
2.17 Interface shear strength vs normal stress; clamping stress (a) left-as-cast; roughened (b) steel reinforcement [8] . . . 12
2.18 Crack pattern at smooth and profiled interface [9] . . . 13
2.19 Tensile behaviour of UHP-SHCC [10] . . . 13
2.20 Uniaxial test set-up [10] . . . 14
2.21 Cracking in uniaxial test set-up with different fiber content [10] . . . 14
2.22 Zero span test set-up [10] . . . 15
2.23 Cracking in Zero-span test set-up with different fiber content [10] . . . 15
2.24 Flexural test set-up [10] . . . 16
2.25 Cracking in flexural test set-up with different fiber content [10] . . . 16
2.26 Strengthening of RCC beams [11] . . . 17
2.27 Four-point bending test set-up [11] . . . 17
2.28 Load vs Deformation plot [11] . . . 17
2.29 Test specimen with load and debonding locations [12] . . . 18
2.30 Load displacement curves of the sandwich beams with and without inital interface debonding in the middle of the beams, beam length: 280 mm, U: core-upper skin debonding, D: core-lower skin debonding [12] . . . 18
2.31 The initial debonding progression in the sandwich beams, experiment (a) CD45-U (b) BD45-U [12] . . . 19
2.32 Load displacement curves of the sandwich beams with and without inital interface debonding in the middle of the beams, beam length: 180 mm, U: core-upper skin debonding, D: core-lower skin debonding[12] . . . 19

2.33 Growth in the core and core-skin interface for BDN45-U specimen with initial core-upper skin interfacial debonding in the shear span [12] 20
2.34 Load displacement curves of the sandwich beams with and without inital interface debonding in the middle of the beams, beam length: 100 mm, U: core-upper skin debonding, D: core-lower skin debonding [12] 20
2.35 Failure mechanism in the sandwich beam with initial interfacial debonding (a) core-upper skin (ADN45-U), (b) core-lower skin (ADN45-D) [12] 21
2.36 Characteristics of different kinds of fibers [3] 21
2.37 Stress vs Strain for SHCC-PVA and SHCC-PE under quasi static and dynamic load [13] 22
2.38 Schematic drawing of relative location of sub-images of deformed images and sub images on surface [14] 24
2.39 Schematic drawing of sub-images (grids) on surface [14] 24
2.40 Hybrid beam with SHCC layer in the tension zone [1] 26
2.41 Specimens tested under four-point bending [1] 26
2.42 Patch repairs [3] 27
2.43 Repair of retaining wall [3] 27
2.44 Maximum crack-width development over time for SHCC and concrete patch [3] 28

3.1 Specimen preparation and Test Set-up 30
3.2 Testing of fibers 30
3.3 Comparison between PVA and HMPE fibers sample 30
3.4 Application of debond at the interface and casting concrete top layer 31
3.5 Demoulding samples and Testing 31
3.6 Geometry of the beam (mm) 32
3.7 Cross-section of the beam (mm) 32
3.8 Casting and Placing SHCC spacers 33
3.9 Cross-section of concrete beam of grade C30/37 33
3.10 Cross-section of SHCC-Concrete Hybrid beam 33
3.11 Conventional concrete beam; No Interface 34
3.12 Hybrid beam; Smooth Interface 34
3.13 Hybrid beam; Partially Delaminated Interface 34
3.14 Hybrid beam; Completely Delaminated Interface 35
3.15 Hybrid beam; Profiled Interface 35
3.16 Hybrid beam; Smooth Interface; HMPE fibers 35
3.17 Mould for casting along with steel reinforcement 36
3.18 Casting 37
3.19 Covering to retain moisture 37
3.20 Interface preparation 38
3.21 Casting of concrete top layer 39
3.22 Levelling of the top surface of concrete 40
3.23 Four-point bending set-up 40
3.24 LVDTs placed on the side face of the beam 41
3.25 LVDTs on the bottom face of the beam 41
3.26 LVDTs located on the face side and bottom side of the beam 41
3.27 Surface component selected using GOM correlate 42
3.28 von Mises strain generated over the constant moment region 43
3.29 Section 1, 2 and 3 indicating strain and displacement in X direction at load step 0 of CD-PVA 43
3.30 Section 1, 2 and 3 indicating strain and displacement in X direction at load step 30 of CD-PVA 44
3.31 Cracking pattern in SHCC and CC layer of Hybrid beams 44
3.32 Location of LVDT on the side face of the beam 46

3.33 Points corresponding to the end locations of LVDT's . . . 46
3.34 Comparison of deformation from GOM with LVDT's . . . 46
3.35 Image of cracks on the bottom-side of CC beam (Load step 60 kN) . . . 47
3.36 Image of the crack-width measured using Image J on the bottom side of CC beam (Load step 60 kN) . . . 47
3.37 Measurement of cracks using crack-width scale . . . 48
3.38 Load (P) vs Deformation (D) vs Maximum crack-width (Max CW) . . . 50
3.39 Cracking in CC specimen . . . 50
3.40 1-LVDT side, 2-Bottom side and 3-DIC side of CC beam specimen . . . 51
3.41 Development of cracks at load step 15 KN . . . 52
3.42 Development of cracks at load step 20 KN . . . 52
3.43 Development of cracks at load step 25 KN . . . 52
3.44 Development of cracks at load step 30 KN . . . 53
3.45 Development of cracks at load step 35 KN . . . 53
3.46 Development of cracks at load step 40 KN . . . 53
3.47 Development of cracks at load step 45 KN . . . 54
3.48 Development of cracks at load step 50 KN . . . 54
3.49 Development of cracks at load step 55 KN . . . 54
3.50 Development of cracks at load step 60 KN . . . 55
3.51 Development of cracks at load step 62 KN . . . 55
3.52 Development of cracks at load step 60 KN . . . 55
3.53 Comparison of maximum crack-widths measured using GOM, Image J and Visual Inspection . . . 56
3.54 Calibration plots of GOM deformation with LVDT deformation . . . 56
3.55 Load (P) vs Deformation (D) vs Maximum Crack-Width (Max CW) . . . 57
3.56 Cracking in S-PVA specimen . . . 58
3.57 1-LVDT side, 2-Bottom side and 3-DIC side of S-PVA beam specimen . . . 59
3.58 Development of cracks at load step 15 KN . . . 60
3.59 Development of cracks at load step 20 KN . . . 60
3.60 Development of cracks at load step 25 KN . . . 61
3.61 Development of cracks at load step 30 KN . . . 61
3.62 Development of cracks at load step 35 KN . . . 62
3.63 Development of cracks at load step 40 KN . . . 62
3.64 Development of cracks at load step 45 KN . . . 63
3.65 Development of cracks at load step 50 KN . . . 63
3.66 Development of cracks at load step 55 KN . . . 64
3.67 Development of cracks at load step 60 KN . . . 64
3.68 Development of cracks at load step 65 KN . . . 65
3.69 Development of cracks at load step 70 KN . . . 65
3.70 Development of cracks at load step 73 KN . . . 66
3.71 Development of cracks at load step 75 KN . . . 66
3.72 Development of cracks at load step 77 KN . . . 67
3.73 Development of large cracks at the last load step (77 KN) . . . 67
3.74 Comparison of maximum crack-widths measured using GOM, Image J and Visual Inspection . . . 68
3.75 Calibration plots of GOM deformation with LVDT deformation . . . 69
3.76 Load (P) vs Deformation (D) vs Maximum Crack-Width (Max CW) . . . 70
3.77 Cracking in PD-PVA specimen . . . 71
3.78 1-LVDT side, 2-Bottom side and 3-DIC side of PD-PVA beam specimen . . . 72
3.79 Development of cracks at load step 15 KN . . . 73
3.80 Development of cracks at load step 20 KN . . . 73

3.81 Development of cracks at load step 25 KN 74
3.82 Development of cracks at load step 30 KN 74
3.83 Development of cracks at load step 35 KN 75
3.84 Development of cracks at load step 40 KN 75
3.85 Development of cracks at load step 45 KN 76
3.86 Development of cracks at load step 50 KN 76
3.87 Development of cracks at load step 55 KN 77
3.88 Development of cracks at load step 60 KN 77
3.89 Development of cracks at load step 65 KN 78
3.90 Development of cracks at load step 70 KN 78
3.91 Development of cracks at load step 73 KN 79
3.92 Development of large cracks at load step 70 KN 79
3.93 Development of large cracks at final load step 73 KN 80
3.94 Comparison of maximum crack-widths measured using GOM, Image J and Visual Inspection 80
3.95 Calibration plots of GOM deformation with LVDT deformation 81
3.96 Load (P) vs Deformation (D) vs Maximum Crack-Width (Max CW) 82
3.97 1-LVDT side, 2-Bottom side and 3-DIC side of CD-PVA beam specimen 83
3.98 Cracking in CD-PVA specimen 84
3.99 Development of cracks at load step 15 KN 84
3.100 Development of cracks at load step 20 KN 85
3.101 Development of cracks at load step 25 KN 85
3.102 Development of cracks at load step 30 KN 86
3.103 Development of cracks at load step 35 KN 86
3.104 Development of cracks at load step 40 KN 87
3.105 Development of cracks at load step 45 KN 87
3.106 Development of cracks at load step 50 KN 88
3.107 Development of cracks at load step 55 KN 88
3.108 Development of cracks at load step 60 KN 89
3.109 Development of cracks at load step 65 KN 89
3.110 Development of cracks at load step 70 KN 90
3.111 Development of cracks at load step 75 KN 90
3.112 Development of cracks at load step 60 KN 91
3.113 Development of large cracks at load step 65 KN 92
3.114 Development of large cracks at final load step 70 KN 92
3.115 Development of large cracks at final load step 75 KN 93
3.116 Development of large cracks at final load step 60 KN 93
3.117 Comparison of maximum crack-widths measured using GOM, Image J and Visual Inspection 94
3.118 Calibration plots of GOM deformation with LVDT deformation 95
3.119 Load (P) vs Deformation (D) vs Maximum Crack-Width (Max CW) 96
3.120 1-LVDT side, 2-Bottom side and 3-DIC side of P-PVA beam specimen 97
3.121 Cracking in P-PVA specimen 98
3.122 Development of cracks at load step 20 KN 98
3.123 Development of cracks at load step 25 KN 99
3.124 Development of cracks at load step 30 KN 99
3.125 Development of cracks at load step 35 KN 100
3.126 Development of cracks at load step 40 KN 100
3.127 Development of cracks at load step 45 KN 101
3.128 Development of cracks at load step 50 KN 101
3.129 Development of cracks at load step 55 KN 102

3.130 Development of cracks at load step 60 KN . . . 102
3.131 Development of cracks at load step 65 KN . . . 103
3.132 Development of cracks at load step 70 KN . . . 103
3.133 Development of cracks at load step 75 KN . . . 104
3.134 Development of cracks at load step 77 KN . . . 104
3.135 Development of cracks at load step 78 KN . . . 105
3.136 Comparison of maximum crack-widths measured using GOM, Image J and Visual Inspection . . . 105
3.137 Calibration plots of GOM deformation with LVDT deformation . . . 106
3.138 Load (P) vs Deformation (D) vs Maximum Crack-Width (Max CW) . . . 107
3.139 1-LVDT side, 2-Bottom side and 3-DIC side of S-HMPE beam specimen . . . 108
3.140 Cracking in S-HMPE specimen . . . 109
3.141 Development of cracks at load step 15 KN . . . 109
3.142 Development of cracks at load step 20 KN . . . 110
3.143 Development of cracks at load step 25 KN . . . 110
3.144 Development of cracks at load step 30 KN . . . 111
3.145 Development of cracks at load step 35 KN . . . 111
3.146 Development of cracks at load step 40 KN . . . 112
3.147 Development of cracks at load step 45 KN . . . 112
3.148 Development of cracks at load step 50 KN . . . 113
3.149 Development of cracks at load step 55 KN . . . 113
3.150 Development of cracks at load step 60 KN . . . 114
3.151 Development of cracks at load step 65 KN . . . 114
3.152 Development of cracks at load step 70 KN . . . 115
3.153 Development of cracks at load step 75 KN . . . 115
3.154 Development of cracks at load step 77 KN . . . 116
3.155 Development of large cracks at load step 75 KN . . . 116
3.156 Development of large cracks at final load step 77 KN . . . 117
3.157 Comparison of maximum crack-widths measured using GOM, Image J and Visual Inspection . . . 117
3.158 Calibration plots of GOM deformation with LVDT deformation . . . 118
3.159 Comparison between S-PVA and CC indicating the load at which maximum allowable crack-width at SLS is exceeded . . . 119
3.160 Comparison between S-PVA and CC indicating the load at which maximum allowable crack-width at SLS is exceeded . . . 120
3.161 Comparison between S-PVA and PD-PVA indicating the load at which maximum allowable crack-width at SLS is exceeded . . . 120
3.162 Comparison between S-PVA and CD-PVA indicating the load at which maximum allowable crack-width at SLS is exceeded . . . 121
3.163 Comparison between S-PVA and P-PVA indicating the load at which maximum allowable crack-width at SLS is exceeded . . . 122
3.164 Comparison between S-PVA and S-HMPE indicating the load at which maximum allowable crack-width at SLS is exceeded . . . 122
3.165 Comparison between S-PVA and CC indicating the load at which maximum allowable crack-width at SLS is exceeded . . . 123
3.166 Strain in y direction at load step 30 KN . . . 126
3.167 Strain in y direction at load step 35 KN . . . 126
3.168 Strain in y direction at load step 40 KN . . . 126
3.169 Strain in y direction at load step 45 KN . . . 127
3.170 Strain in y direction; S-PVA; Load Step 0 . . . 127
3.171 Strain in y direction; PD-PVA; Load Step 0 . . . 127

3.172 Strain in y direction; S-PVA; Load Step 10 127
3.173 Strain in y direction; PD-PVA; Load Step 10 128
3.174 Strain in y direction; S-PVA; Load Step 20 128
3.175 Strain in y direction; PD-PVA; Load Step 20 128
3.176 Strain in y direction; S-PVA; Load Step 30 128
3.177 Strain in y direction; PD-PVA; Load Step 30 128
3.178 Strain in y direction; S-PVA; Load Step 40 129
3.179 Strain in y direction; PD-PVA; Load Step 40 129
3.180 Strain in y direction; S-PVA; Load Step 50 129
3.181 Strain in y direction; PD-PVA; Load Step 50 129

4.1 Geometry of the beam 131
4.2 Hybrid beam; Smooth Interface; PVA fiber 132
4.3 Hybrid beam; Partially delaminated interface; PVA fiber 132
4.4 Hybrid beam; Completely delaminated Interface; PVA fiber 132
4.5 Hybrid beam; Profiled Interface; PVA fiber 132
4.6 Hybrid beam; Smooth Interface; HMPE fibers 132
4.7 Material properties of modelled concrete 133
4.8 Tensile behaviour of SHCC 134
4.9 Compressive behaviour of SHCC 134
4.10 Properties of reinforcing steel 136
4.11 Elements used in the beam models 138
4.12 Comparison between numerical (Num) and the experimental (Exp) results of S-PVA specimen 139
4.13 Comparison between numerical (Num) and the experimental (Exp) results of S-PVA specimen with reduced stiffness at the interface 140
4.14 Crack comparison in S-PVA specimen 140
4.15 Comparison between numerical (Num) and the experimental (Exp) results of CD-PVA specimen 141
4.16 Comparison between numerical (Num) and the experimental (Exp) results of CD-PVA specimen with reduced stiffness at the interface 142
4.17 Crack comparison in CD-PVA specimen 142

5.1 Code to calculate maximum crack-width on Matlab 145

List of Tables

2.1 Summary . . . 23

3.1 Material ingredients of SHCC with PVA fibers . . . 37
3.2 Material ingredients of SHCC with HMPE fibers . . . 37
3.3 Properites of fibers used in SHCC . . . 38
3.4 Interface Preparation . . . 38
3.5 Material ingredients of concrete grade C30/37 . . . 39
3.6 Properties of CC beam specimen in constant moment region after testing . . . 50
3.7 Properties of S-PVA beam specimen in constant moment region after testing . . . 57
3.8 Properties of PD-PVA beam specimen in constant moment region after testing . . . 70
3.9 Properties of CD-PVA beam specimen in constant moment region after testing . . . 82
3.10 Properties of P-PVA beam specimen in constant moment region after testing . . . 96
3.11 Properties of S-HMPE beam specimen in constant moment region after testing . . . 107
3.12 Properties of Concrete layer . . . 123
3.13 Properties of SHCC layer . . . 123
3.14 Stresses in completely bonded composite beam . . . 125
3.15 Stresses in completely unbonded composite beam . . . 125
3.16 Reduced Young's Modulus of concrete layer . . . 125
3.17 Stresses in completely bonded composite beam . . . 126
3.18 Stresses in completely unbonded composite beam . . . 126

4.1 Material properties of concrete grade C30/37 . . . 133
4.2 Material properties of SHCC . . . 134
4.3 Material properties of Reinforcing steel . . . 135
4.4 Normal and Shear stiffness for bond-slip in concrete layer . . . 135
4.5 Normal and Shear stiffness for bond-slip in SHCC layer . . . 135
4.6 Properties of interface between steel plate and beam . . . 137
4.7 Material properties of Interface . . . 137
4.8 Normal and Shear stiffness of the bonded part of the interface . . . 137
4.9 Normal and Shear stiffness of the delaminated part of the interface . . . 137
4.10 Normal and Shear stiffness of the bonded part of the interface . . . 139

Chapter 1

Background and Motivation

1.1 Introduction

Reinforced Concrete (RC) has been the most commonly used construction material until now. The steel reinforcement is capable of withstanding tensile forces while concrete is competent in handling compression. From a structural design perspective, Limit State Design (LSD) requires structures to satisfy two principal criteria namely, the Serviceability Limit State (SLS) and the Ultimate Limit State (ULS). To satisfy the ULS, a structure designed for its peak load must not collapse. This is possible if the factored bending, shear, tensile and compressive stresses are below the factored resistance calculated. To satisfy the SLS, the structure must remain functional for its intended use. The functional aspects include deflection, vibration and crack-width, out of which, crack-width criterion is given sufficient importance in Eurocode [15]. It is stated in Eurocode [15] that the maximum allowable crack-width in SLS is 0.3 mm under quasi-permanent load for all exposure classes except X0 and XC1 beyond which, additional reinforcement needs to be added for crack width control. However, this addition can create an excessive capacity in ULS than required, making the provision uneconomical.

The concept of composite beams is found to improve the capacity of conventional concrete beams by incorporating an innovative material such as Strain Hardening Cementitious Composite (SHCC) [3]. The micro-cracking behaviour of SHCC improves the ductility of the beam and provides better crack-width control [3]. The fibers used in SHCC smears a single large crack into many small distributed cracks by bridging effect [3]. Thus, the SLS criteria requirement can be met without providing additional reinforcement for crack-width control.

The master thesis project by Zhekang Huang (2017) [1] experimentally validates that an optimal design can be achieved by using a combination of conventional concrete and SHCC containing Poly(Vinyl) Alcohol (PVA) fibers. From his experimental results, it can be concluded that maximum crack width control can be achieved in test beams using a 70 mm layer SHCC in the tension zone of a beam having a height of 200 mm.

Huang (2017) [1] in his master thesis project titled "Flexural behaviour of reinforced concrete beams with a layer of SHCC in the tension zone: Experimental study" maintained a smooth interface for all his test beams. However, the surface texture at the interface can contribute to a higher cohesion and friction providing a better bond [8]. The study conducted by Lukovic (2016) [9] investigated the influence of interface and SHCC properties on the performance of concrete repairs by maintaining a smooth interface. It is concluded that providing a smooth interface generated a sufficient debonding length for the cracks to smear but may reduce the overall bearing capacity due to limited bond strength. Thus, a further investigation to understand the influence of interface on bearing capacity and crack-width control becomes relevant.

This master thesis project will focus on studying and explaining the influence of interface on crack-width control hybrid SHCC/Concrete beams by varying it locally (within the constant moment region) and the impact of fibers in SHCC. At end of this report, the influence of interface and the impact of the type of fiber in the optimisation of micro-cracking in the hybrid beam is elucidated.

1.2 Scope

In order to study the influence of interface, variation between smooth, profiled, partial delamination and complete delamination interface profiles are studied. For the influence of fiber in controlling the crack-width, the PVA fibers are replaced with High-Modulus Polyethylene fibers (HMPE). In order to investigate the crack pattern and the crack-widths, Digital Image Correlation (DIC) along with image analysis is applied. Further, a numerical analysis for all beams with varying interface is also modelled using Diana FEA software in order to validate if a similar trend as observed in the experimental results can be obtained. The results of the numerical analyses are to be validated using the obtained experimental results.

1.3 Research Hypothesis

The results of Huang (2017) [1] are specific to one type of interface (smooth) and one kind of fiber (PVA) for all the hybrid beam specimens. However, from literature it is apparent that varying the interface property and the type of fiber can play a vital role in optimising the cracking behaviour. Therefore, in this thesis a hypothesis is formulated as, "Varying the interface property and the type of fiber used in SHCC can vary the micro-cracking behaviour of SHCC".

1.4 Research Questions, Objectives and Set-goals

The main objective of this research is to utilize the micro-cracking behaviour of SHCC to the fullest. The effect of interface between the two layers of concrete and the type of fibers used in SHCC has to be investigated. Therefore, from the literature study and the hypothesis stated above, the research questions to be answered in this thesis are formulated and stated below:

1. What is the impact of varying the interface locally on the crack-width and bearing capacity in concrete-SHCC hybrid beams?

   a. In what ways will varying the interface property by smoothing, profiling and partial and complete delamination, impact the crack-width control and bearing capacity?

2. What is the impact of varying the fiber type used in SHCC on crack-width and bearing capacity in concrete-SHCC hybrid beams?

   a. In what way will replacing PVA fibers by HMPE fibers in SHCC benefit in crack-width control and bearing capacity?

A choice has been made to vary the interface property between smooth, profiled and partial or complete delamination based on the concept of debond length suggested by Lukovic (2016) [9] discussed in the chapter 2 of this report. The choice to use HMPE fibers instead of PVA fibers is based on the pre-study conducted and discussed in chapter 2 as well.

At the end of this research project, with the help of results obtained from the four-point bending experimental testing, a coherence on the influence of interface and type of fiber on crack-width control can be obtained. An educated choice can then be made in selecting the interface property and the type of fiber which will provide the best crack-width control without compromising the bearing capacity of the beam.

1.5 Outline of the Thesis

The outline of this research project is shown in Figure 1.1.

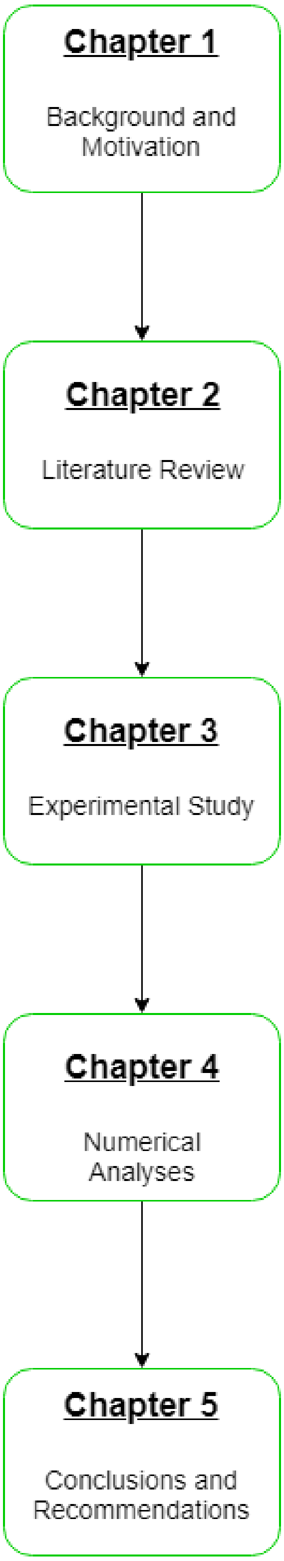

Figure 1.1: Outline of Thesis Research

The first chapter 1 gives a theoretical background along with the motivation for the research. The scope, research objective and research questions to be answered are also discussed in this chapter.

The second chapter 2 discusses in detail researches related to Strain Hardening Cementitious Composites (SHCC), impact of interface in hybrid beams and influence of fibers in SHCC. Principle of Digital Image Correlation (DIC) along with practical application of SHCC is also discussed briefly in this chapter.

The third chapter 3 covers the experimental study conducted to answer the research questions. First, a pre-study is conducted to choose the right interface debond material and fiber material. This is followed by the design stage where the parameters such as geometry of the beam specimen, location of reinforcement and spacers and type of interface variations are laid out clearly. After finalising the design stage, the casting is carried out in two steps as the beam specimens contain SHCC and conventional concrete layers. Finally, testing is carried out in a four-point bending set-up. The image data obtained from the tests are digitally correlated using GOM correlate {v2.0.1} and validated by visual inspection and microscopic images.

The fourth chapter 4 deals with the numerical analyses of the the beam specimens tested experimentally. Aspects used in the modelling such as geometry, material properties, interface properties, support and loading conditions, meshing and analysis procedure are defined. Based on the numerical inputs, the results obtained are compared to the experimental results for validation.

The fifth chapter 5 summarises all the conclusions obtained from the experimental study and the numerical analyses performed. Also, the research questions and the hypothesis stated at the beginning of this master thesis are answered and recommendations are made.

Chapter 2

Literature Review

The State-of-the-art is sub-divided into the following sections. The first section is an introduction to Strain Hardening Cementitious Composite (SHCC) and properties specific to durability and crack-width. The second section is a discussion about the research on SHCC-Concrete structural applications. The third section explains the theory of Digital Image Correlation (DIC) and its relevance to this master thesis research. The final section is a general discussion on the practical applications of SHCC in crack-width control and repairs.

2.1 Strain Hardening Cementitious Composite

2.1.1 Introduction

SHCC, also known as Engineered Cementitious Composite (ECC), is a bendable mortar-based composite with polymer fibers giving it a ductile, metal like, property leading to a wide range of applications. When SHCC is loaded past its elastic limit, the stretching or the straining strengthens the material. This strain-hardening behaviour of SHCC is because of multiple microscopic cracks following fiber bridging behaviour.

With a very small volume of fibers (around 2%) in the matrix, micro cracks can be controlled to very specific widths. This micro cracking behaviour also improves durability as it does not allow aggressive substances to penetrate and attack the steel reinforcement preventing corrosion.

2.1.2 Properties of SHCC

The master thesis research deals mainly with the durability and crack-width control aspects of SHCC and so the properties of SHCC discussed here are within the scope of the specified domain only.

Durability

In the serviceability limit state, crack width control is an important criterion for structural durability as the ingress of damaging salts and gases can occur. The crack bridging behaviour of fibers in SHCC can help in limiting the crack width. This is in contrast to the tension-softening behaviour of normal/conventional concrete where fracture localisation occurs once a crack is formed, so the crack-width is not contained and the load bearing capacity decreases.

The superior mechanical property of SHCC leads to micro cracking in SLS. According to Wang et al. (1997) [16], there is a decrease in water permeability in several orders of magnitude as the crack width decreased from 550 μm to 100 μm. The plot of total permeability by the number of cracks in the specimen vs the crack width (Figure 2.1) for SHCC and reinforced mortar by Lepech & Li (2005) [2] shows that flow rate was found to be lower in SHCC than reinforced mortar.

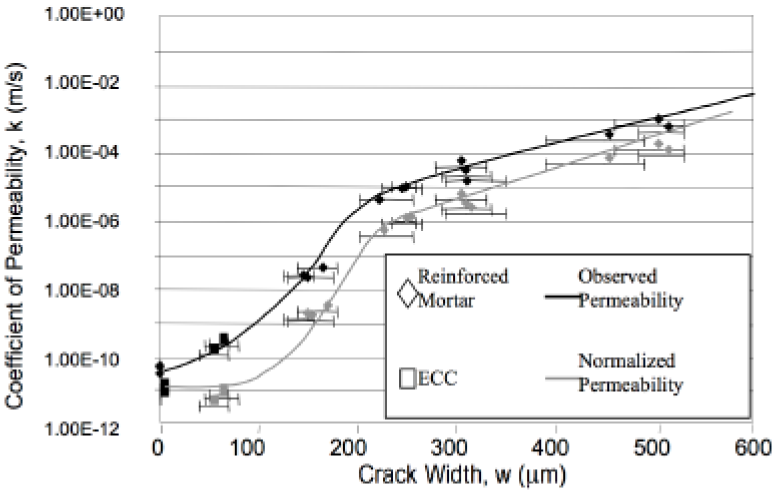

Figure 2.1: Permeability vs crack width [2]

Chloride Permeability

Increase in crack width can result in increased rate of penetration the chloride ions in cement composites. According to Sahmaran et al. (2007) [17], the results of immersion tests show that the chloride penetration depth is found to be lower in uncracked SHCC specimens as compared to uncracked mortar. Based on the ponding tests of pre-cracked specimens, the effective chloride diffusion coefficient of SHCC is linearly proportional to the number of cracks and the effective diffusion coefficient of reinforced mortar is proportional to the square of the crack width as shown in Figure 2.2. It is conclusive that SHCC is effective in reducing the diffusion of chloride ions under combined mechanical and environmental loading.

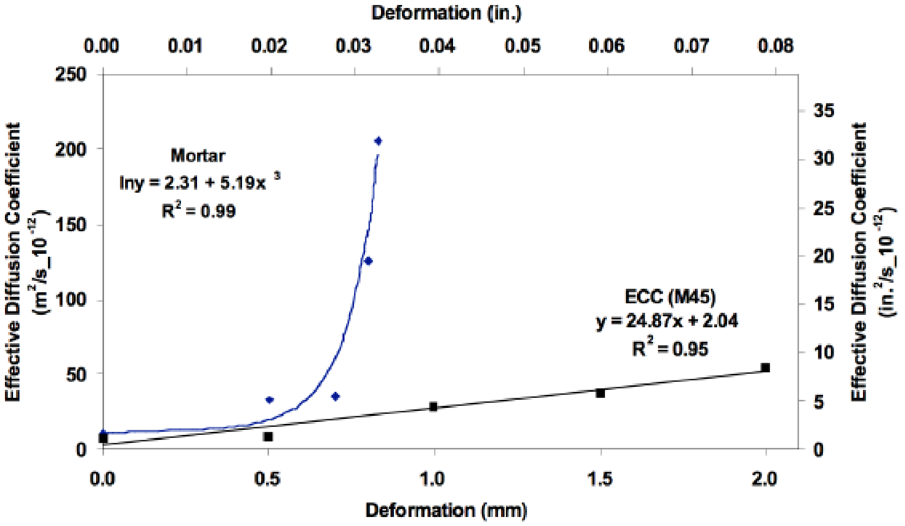

Figure 2.2: Effective diffusion vs deformation [3]

Sustained and Cyclic Load

For structures exposed to cyclic loads, or relatively high permanent/sustained loads, it is essential to control the cracks in service condition to prevent the ingress of moisture, gas and chloride. Figure 2.3 shows the results of Jun & Mechtcherine (2007) [18], which indicate that at the same level of deformation there exists a limited sensitivity of various loading conditions on the total number of cracks.

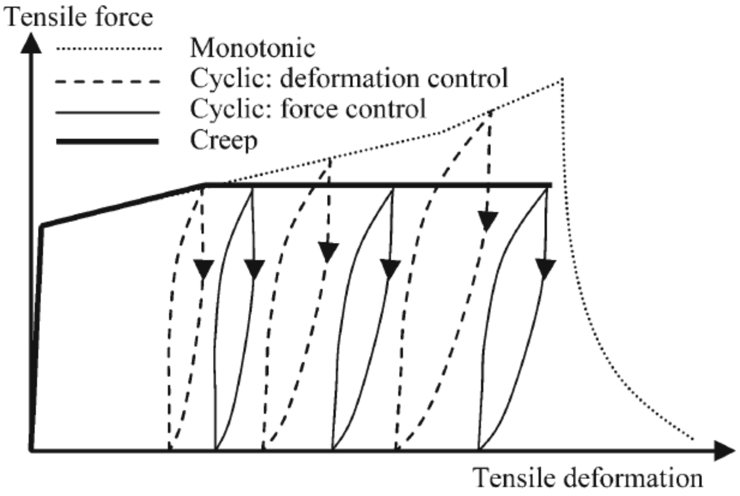

Figure 2.3: Tensile force vs deformation for different types of loads [3]

Response to Thermal Loads

According to Nishida and Yamazaki (1995) [19], a significant amount of chemical and micro-structural changes can be seen in concrete heated above 105° Celsius . This includes a loss of stiffness and strength due to dehydration, and rapid heating may also lead to spalling of concrete. SHCC on the other hand consists of fibers which can reduce the effect of thermal loading by melting at a temperature lower than the spalling temperature and relieving the vapours from the cement mass. Yoshitake et al (2006) [20] compared the response of specimens made out of plain concrete (PLC), steel (SFRC), polypropylene (PPFRC) and Poly(vinyl) Alcohol (PVA-FRC) to fire as shown in Figure 2.5. From the results of the experimental testing shown in Figure 2.4, it was observed that the surface temperatures instantly escalates as soon as it is exposed to heating but the heating was seen to be delayed with increasing depths. It was observed that an extreme condition is reached at which the thermal decomposition of the fibre materials begins to occur at significant depths in the structural elements.

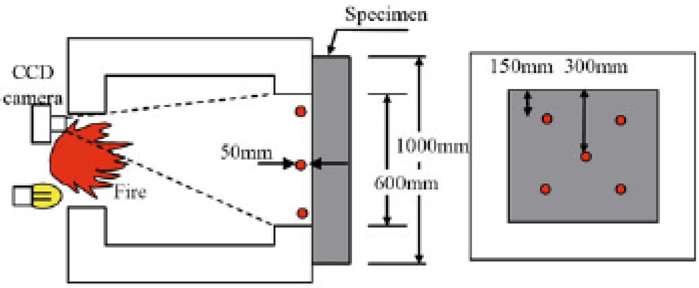

Figure 2.4: Experiemental fire heating set-up [3]

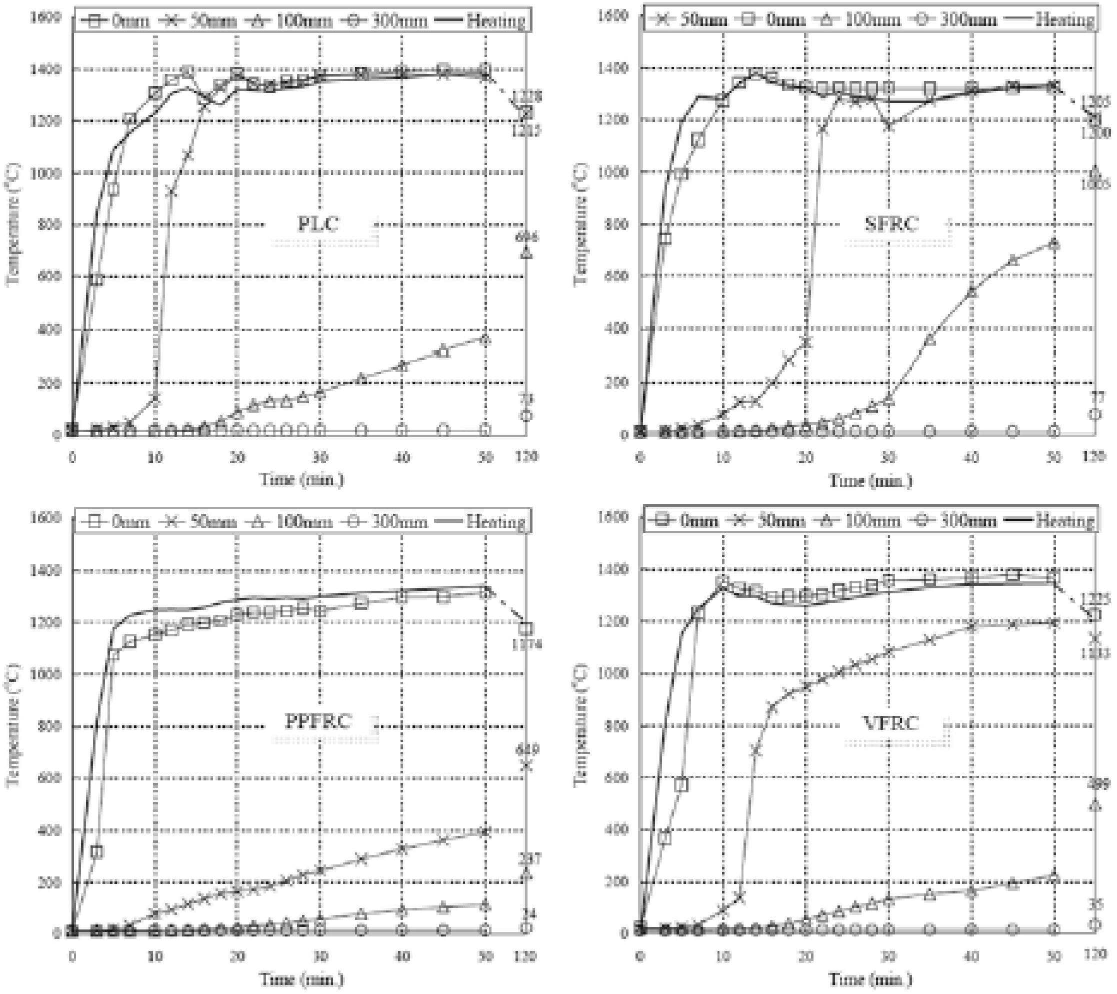

Figure 2.5: Temperature response of specimens [3]

2.2 Hybrid SHCC/Concrete Systems

2.2.1 Influence of Interface

In hybrid beams, a good bond between the different layers of concrete plays a key role to produce a monolithic action. Bond is classified into the following groups as shown in Figure 2.6

(1) complete bond (2) uncertain bond (3) poor bond or debonding.

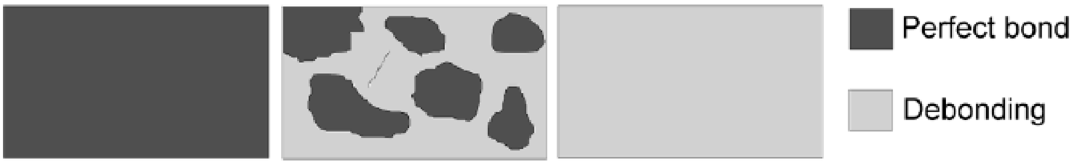

Figure 2.6: Types of bonding at the interface [4]

A complete bond ensures a monolithic action whereas an uncertain bond is the unpredictable one. This is because the overlay is bonded to the substrate in certain areas and can generate higher restraint causing wider cracks perpendicular to and between two areas of bonding. In case of complete debond, the overlay may be considered as a slab on a stiff grade.

Pigeon and Saucier (1992) [21] state that the interface between two layers of concrete is very similar to the bond between the aggregates and cement matrix. According to this research, a wall effect dominates the transition zone which weakens the interface. This theory was later confirmed by Beushausen (2005) [5], who studied the failure in shear bond tests at the interface, proving the occurrence of failure very close to the interface and confirming that an interfacial transition zone exists as shown in Figure 2.7. Yan He et al. (2017) [6] created an artificial roughness as shown in Figure 2.8 (a) on their 180-day concrete with iron-combs of different-shaped saw-teeth and studied the influence. The morphology of the concrete interface was captured using laser triangulation ranging and processed in three dimensions using Matlab as shown in Figure 2.8 (b). The two layered model of new-to-old concrete bonding was classified into three zones as shown in Figure 2.7. The interfacial transition zone was observed to be the governing aspect in terms of obtained mechanical strength, flexural strength and bonding strength. From the results of the experimental research shown in Figure 2.9, it can be concluded that higher the interfacial roughness, greater the mechanical strength.

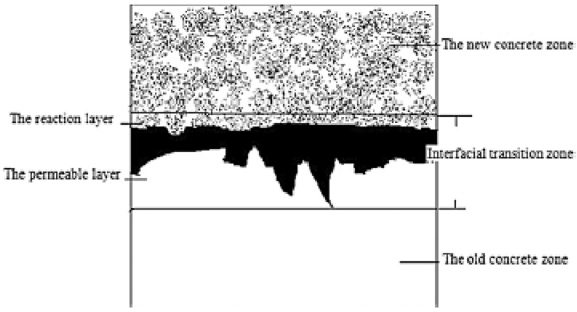

Figure 2.7: Two layered old-to-new concrete model [5]

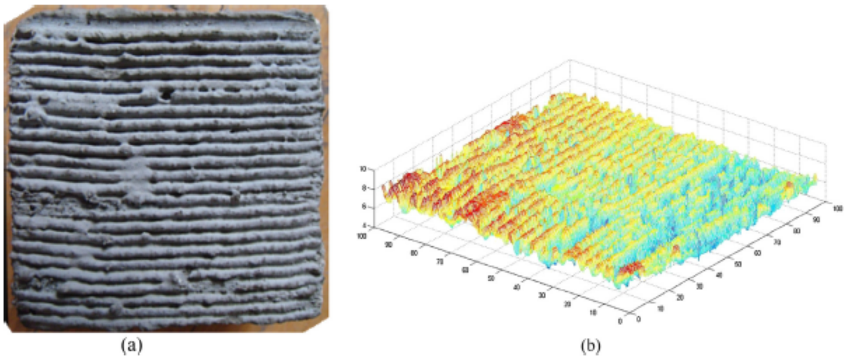
(a)
(b)

Figure 2.8: (a) Artificial interface roughness (b) Morphology of concrete interface [6]

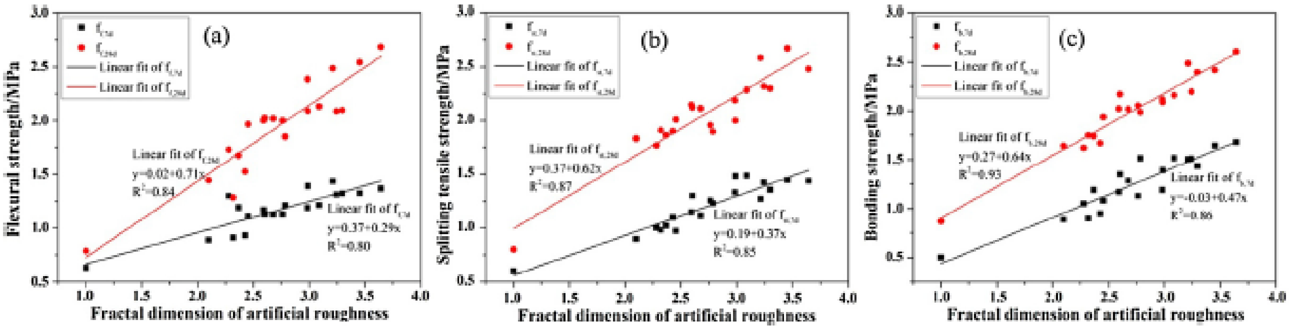

Figure 2.9: Flexural, tensile and bonding strength vs fractal dimensions of artificial roughness [6]

Li et al.(2009) [7] experimentally investigated the flexural performance of a functionally graded concrete namely, Ultra High Toughness Cementitious Composties (UHTCC) also known as (UHTCC-FGC), by substituting a part of the concrete around the main longitudinal reinforcement in reinforced concrete member. Long beams of 120 mm x 80 mm rectangular cross-section were designed to ensure flexural failure and the thickness of the UHTCC-FGC layer was varied as 15 mm, 25 mm, 35 mm and 50 mm respectively as shown in Figure 2.10. From Figure 2.11, it can be seen that, the sample with 25 mm thickness of UHTCC showed severe bond failure at the interface of the two layers. This is because the interface coincided exactly with the centroid of the steel reinforcement. However, comparing samples with 50 mm and 35 mm thickness of UHTCC layers, the latter showed higher ultimate moment and higher deformation capacity with material usage of 30 % less than the former. Hence, it was concluded that UHTCC layer overlay just above the centroid of steel reinforcement was more appropriate. Even a sample with 15 mm thick UHTCC layer showed a higher yield load and ductility when compared to plain RC beams.

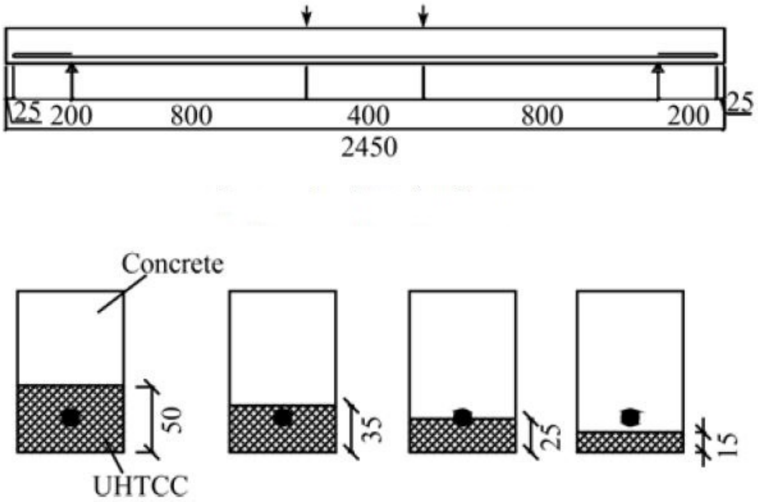

Figure 2.10: Cross-section of UHTCC specimen [7]

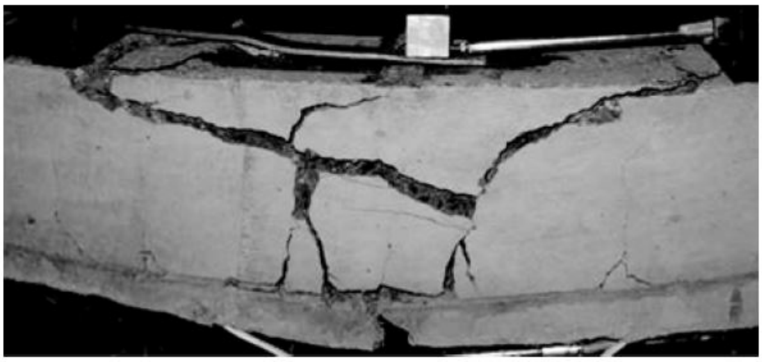

Figure 2.11: Crack opening in UHTCC25 specimen [7]

To determine the occurrence and the location of the first-crack, strain gauges at the bottom and side of the beams are placed during testing. There was a jump in the tensile strain as soon as the crack appeared in the range of the strain gauge and when the cracks appeared outside this range, the tensile strain reduced instantaneously. It was also observed from the experiment that if a thick layer of UHTCC was designed, cracks first appeared in the UHTCC layer rather than concrete layer. From Figure 2.12, it is seen that the tensile strain of concrete layer keeps increasing till there is a sudden drop of the tension strain at the bottom of the UHTCC layer. Also, in Figure 2.12, HB represents the strain gauges placed to gauge the drop or jump in strains.

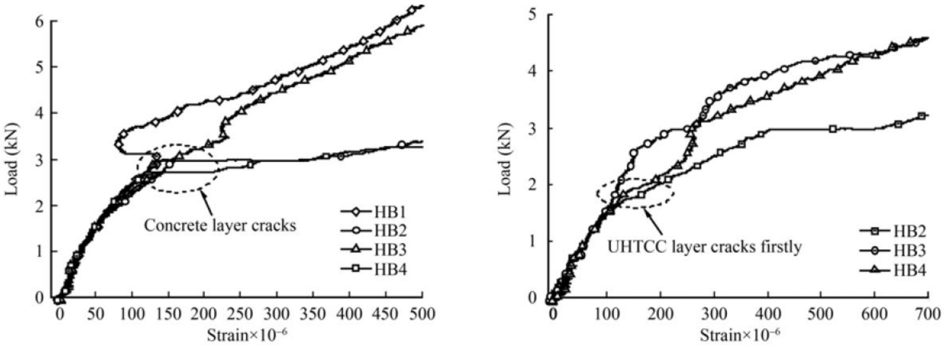

Figure 2.12: Location of first crack in UHTCC25 [7]

The development of the crack opening in the 50 mm UHTCC layered sample was seen to be small and more evenly distributed than compared to the reinforced concrete sample as shown in Figure 2.13. It was also observed that few wide cracks developed in the concrete layer of UHTCC sandwich beams diffused into many fine cracks at the interface. Delamination was observed between concrete and UHTCC layer of 25 mm (Figure 2.12). The sample with 15mm layer of UHTCC (Figure 2.14) acts as a protective cover for the steel reinforcement embedded in concrete. Large number of distributed cracks with far lower crack-widths were also observed in this specimen contrary to the reinforced concrete specimen.

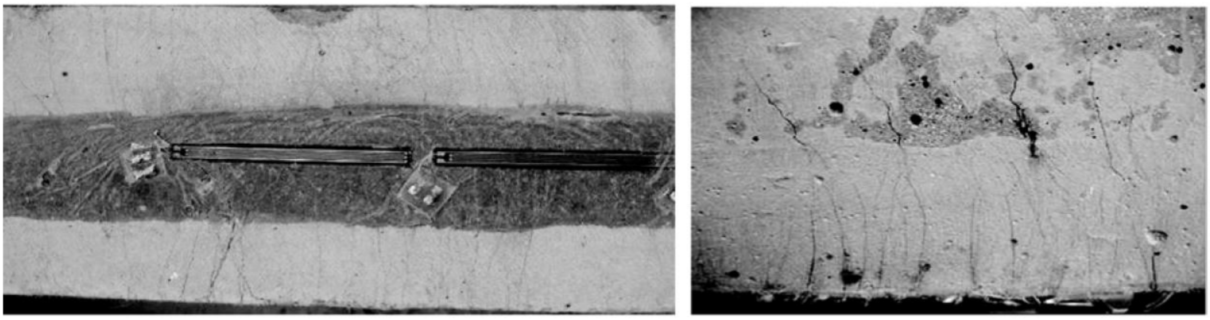

(a) Bottom (b) One side

Figure 2.13: Crack opening in UHTCC50 specimen [7]

Figure 2.14: Crack opening in UHTCC15 specimen [7]

Mohamad et al. (2015) [8] conducted a total of 36 push-off tests as shown in Figure 2.16 to study the influence of surface texture and steel reinforcement crossing the interface. The concrete surface of the samples was prepared in three ways; smooth or left-as-cast, roughened by wire brush in transverse direction and steel reinforcement sticking out at the interface as seen in Figure 2.15. It was observed from his experimental results that the transverse roughened surface produced the highest interface shear strength of $6.42 N/mm^2$ as compared to others as also seen in Figure 2.17. It can be concluded that with an increase in degree of roughness at the interface, a higher degree of concrete cohesion and friction can be achieved. In case of steel reinforcement projecting out of the interface, the failure was not as sudden as expected in the other cases. This was because of the clamping stress or the normal stress from dowel action.

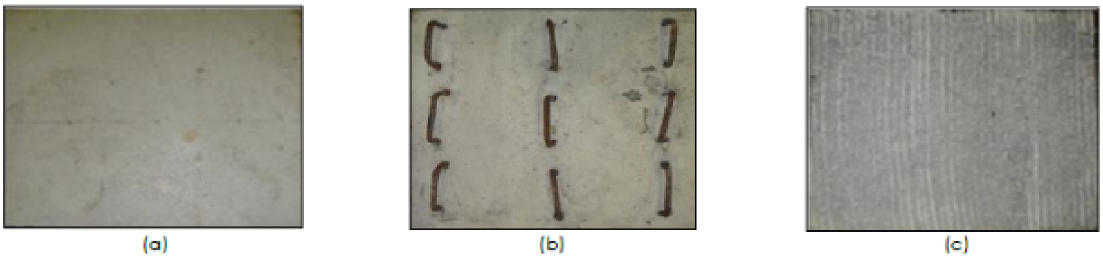
(a) (b) (c)

Figure 2.15: Concrete surface preparation (a) left-as-cast (b) steel reinforcement (c) roughened by wire brush [8]

(b)

Figure 2.16: Push-off test [8]

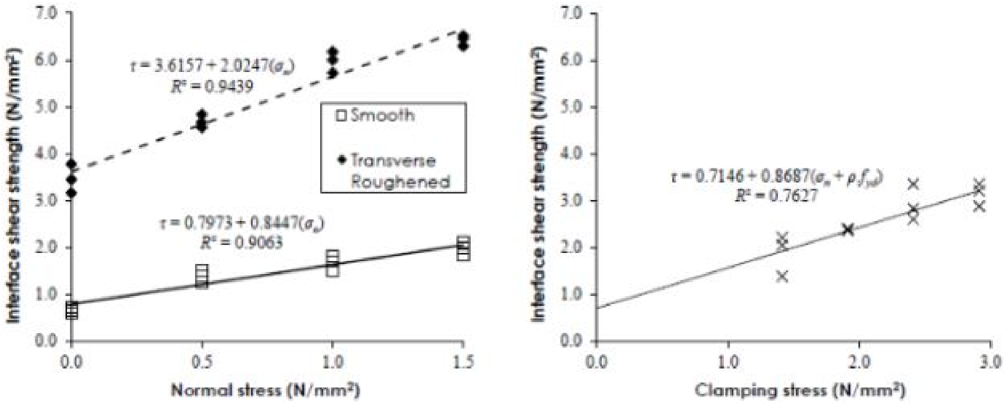

Figure 2.17: Interface shear strength vs normal stress; clamping stress (a) left-as-cast; roughened (b) steel reinforcement [8]

Lukovic (2016) [9] made a comparison in the crack patterns when SHCC was applied as a repair material on a smooth surface and grooved surface of old concrete as shown in Figure 2.18. It was observed that the smooth interface has a larger debonding length due to low bond strength. Thus, the strain can be distributed over a larger debonding length giving rise to uniformly distributed cracks. Whereas, for the grooved interface, because of better bond strength the debonding length was small, there was an intense accumulation of the cracks which is less favourable. From this, it still cannot be concluded that a smooth interface is more favourable as the structural integrity may be impaired if the delamination occurs too early.

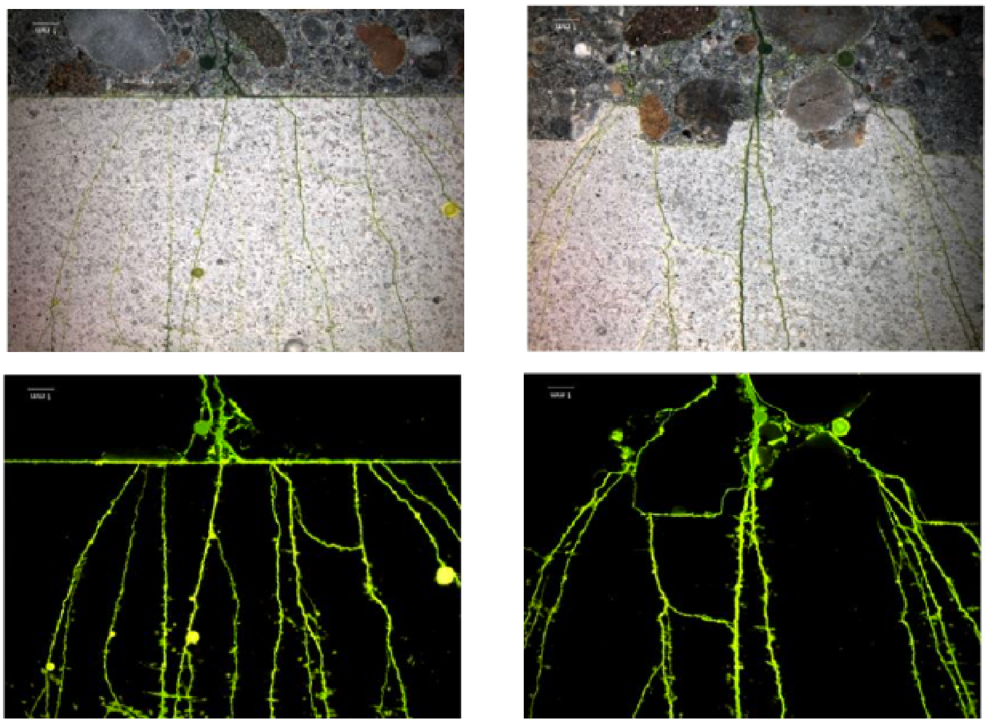

Figure 2.18: Crack pattern at smooth and profiled interface [9]

Kamal et al. (2008) [10] studied the crack distribution in SHCC as a repair material adjacent to an existing crack in the substrate using three tests; uniaxial tensile test, zero-span tensile test and flexural tests on RC beams. A ultra high performance strain hardening cementitious concrete (UHP-SHCC) with different fiber content of 0.5%, 1% and 1.5% was used as a repair material. The tensile strength vs tensile strain plot of UHP-SHCC is shown in Figure 2.19.

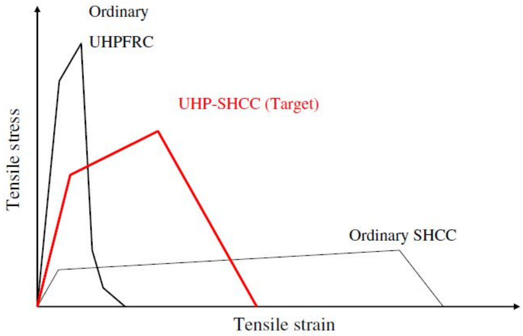

Figure 2.19: Tensile behaviour of UHP-SHCC [10]

Five dumbbell-shaped specimens made with UHP-SHCC containing different volumes of fiber were tested after 14 days of casting in a fixed boundary set-up using uniaxial tests as shown in Figure 2.20. It can be seen from the stress-strain relationship that all the samples exhibited strain hardening behaviour and the number of cracks formed depended on the fiber content in the specimen as seen in the Figure 2.21.

Figure 2.20: Uniaxial test set-up [10]

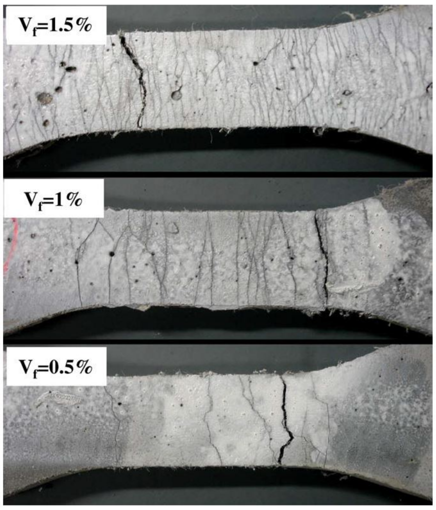

Figure 2.21: Cracking in uniaxial test set-up with different fiber content [10]

Zero-span tensile test is proposed as shown in Figure 2.22. Here, a 3mm thick steel plate was glued on to one side of the substrate with an epoxy adhesive and an artificial crack is created to replicate the crack in the substrate. Insufficient bond properties between the steel plate and the substrate can cause delamination and influence the crack opening performance. To avoid this scenario proper bond was ensured between the two layers using epoxy adhesive. Four specimens with different percentage of fibers is again tested in the arrangement as shown in Figure 2.22 after 14 days of curing. It was observed that most of the cracks were adjacent to the artificial crack and the number of cracks formed depend on the fiber content as seen in Figure 2.23.

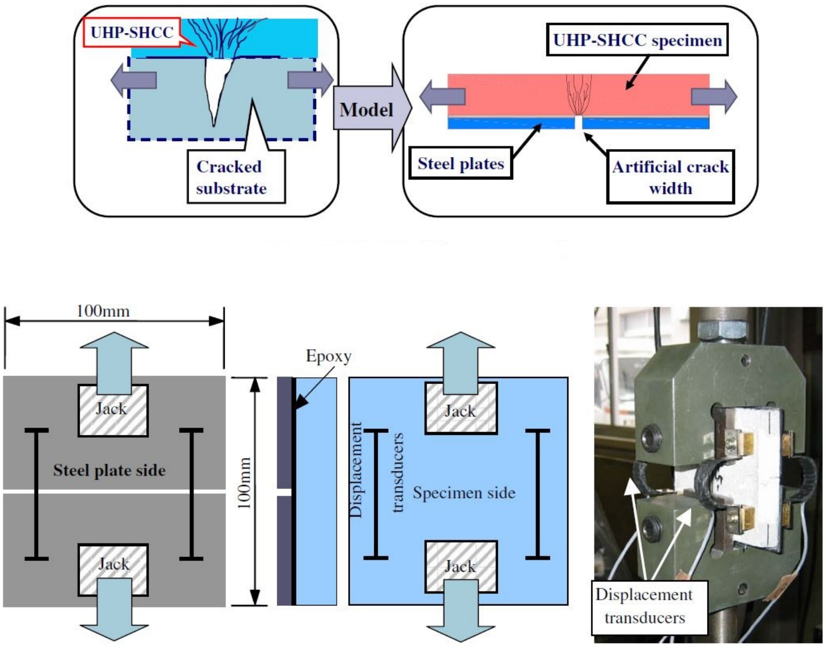

Figure 2.22: Zero span test set-up [10]

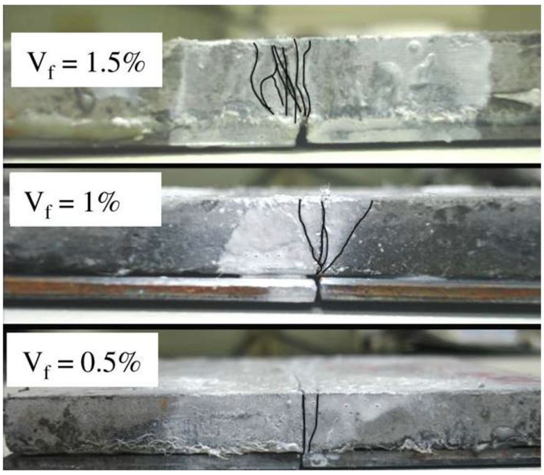

Figure 2.23: Cracking in Zero-span test set-up with different fiber content [10]

For the flexure test of RC beams repaired with UHP-SHCC, six specimens with a length of 1800 mm and cross-section of 100 mm x 200 mm were casted as shown in Figure 2.24. After 2 days the specimens were demoulded and the bottom surface was washed with a retarder to obtain perfect bond with the repair material. The specimens were initially loaded till the crack-width of the specimen ranged from 0.05 to 0.15 mm. Later, a 10 mm thick repair layer of UHP-SHCC was applied to the bottom side of the specimen and cured for 14 days. The specimens were later investigated using a four-point bending load set-up and very similar crack-widths, as obtained using the zero-span test, were obtained as shown in Figure 2.25.

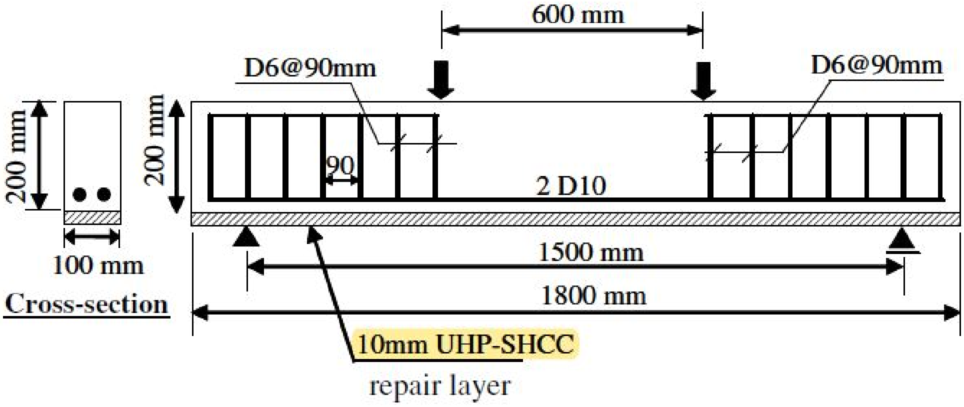

Figure 2.24: Flexural test set-up [10]

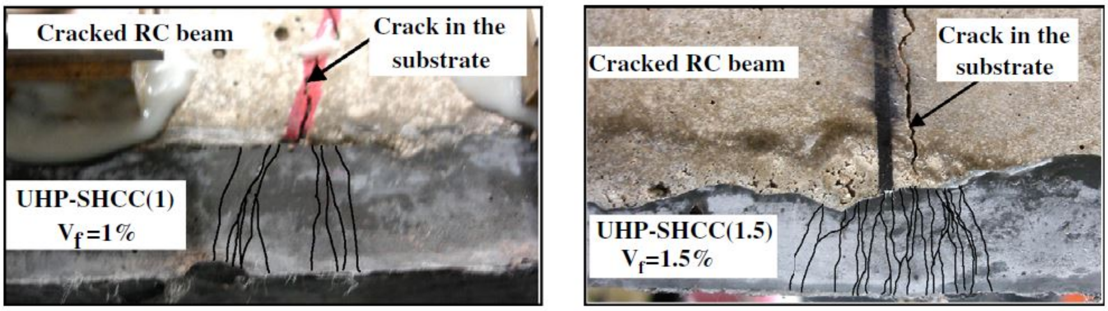

Figure 2.25: Cracking in flexural test set-up with different fiber content [10]

It was concluded from their research that the width of the cracks obtained from the direct tensile tests were more widely distributed along the specimen length and in the zero-span test and the flexural test, the cracks were distributed mainly around the artificial crack region. Hence, it was seen that there is a dependency of the crack width not only on the material properties of the tested specimens but also on the boundary conditions.

Esmaeeli et al. [11] evaluated the enhancement in the flexural strength of reinforced concrete beams using a Hybrid Composite Plate (HCP) composed of Strain Hardening Cementitious Composite (SHCC) and Carbon Fiber Reinforced Polymer (CFRP). Test specimens were strengthened using H plate on the tension side as shown in the Figure 2.26. A reference sample(FB_R), without any HCP plate, was also casted for comparison. Six other beams were strengthened by either a SHCC plate or a HCP plate. Only FB0-G was strengthened by an adhesively bonded SHCC plate and all the others were strengthened using HCP plate. HCP plated beams were further classified on the basis of having two laminates (FB2_B, FB2_G and FB2_BG or four CFRP laminates (FB4_BG_phi8 and FB4_BG_phi10). The bond quality was enhanced at the interface by sand blasting and using chemical anchors as seen in Figure 2.26 and tested under four-point bending set-up as shown in Figure 2.27. From their research, it was concluded that by attaching HCP plate to the beam soffit, the flexural capacity significantly increased as seen in Figure 2.28. However, the deflection ductility of all the HCP plate strengthened beams was lower as compared to the reference beams due to delamination. It was also observed that a fracture involving the disintegration of concrete was observed in CFRP strengthened RC beams but the beams strengthened with SHCC did not show this type of failure. This was attributed to the fiber reinforced mechanisms of arresting micro-cracks in SHCC.

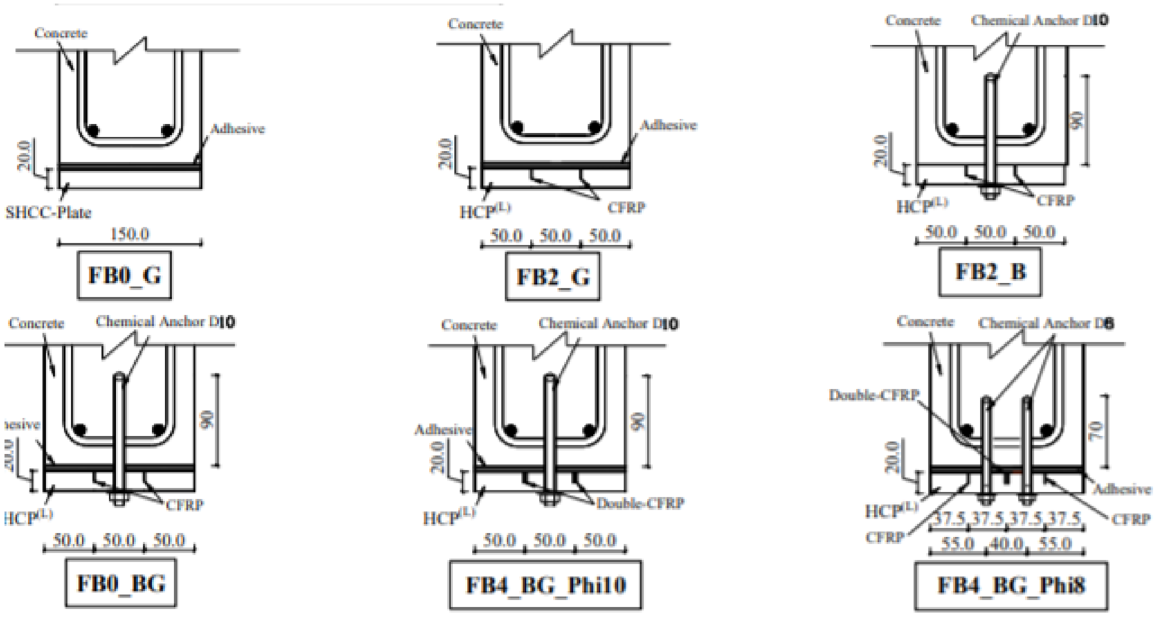

Figure 2.26: Strengthening of RCC beams [11]

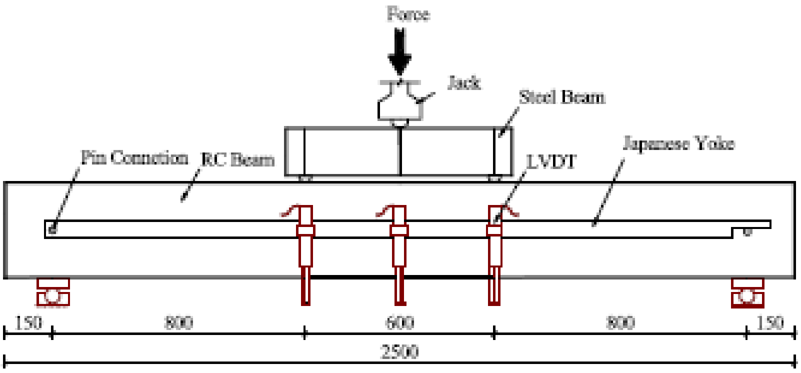

Figure 2.27: Four-point bending test set-up [11]

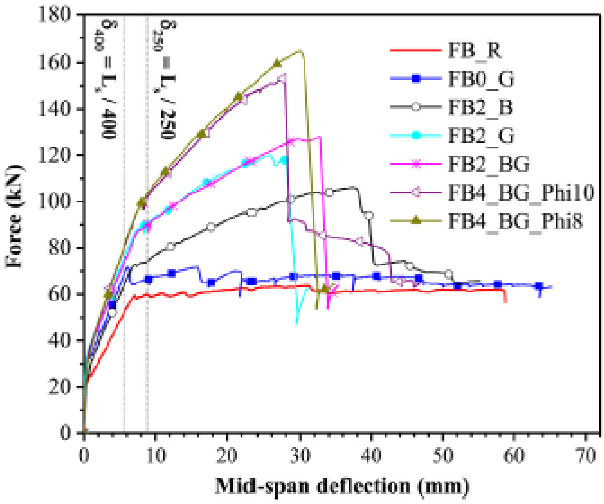

Figure 2.28: Load vs Deformation plot [11]

Mansourinik et al. (2018) [12] studied the behaviour of sandwich beams of various lengths with and without initial core-skin debonding under flexural loads as shown in Figure 2.29. The core material of all sandwich beams was closed cell PVC foam with density of 70 kg/m^3. Composite skin was made of two layers of Twill-woven E-glass fabric. Initial artificial debonding was created between the core and face sheets by using Teflon strips placed at locations labelled as numbers 1-4 in Figure 2.29. It was observed from the experiments that in medium sized specimens (Figure 2.33) and short sized specimens (Figure 2.35), the face sheets had no effect on failure initiation but in long-sized beams, the face sheets changed the load-displacement response of the beams as seen in Figure 2.30 and 2.31. Also, it was observed that the sandwich beams with initial debonding on the tension side had negligible effect on the load carrying capacity of the beams, while the beams with debonding on the compression side had a remarkable effect i.e. the ultimate load carrying capacity of the long-sized beams decreased by 56%. In medium sized beam, there was a decrease in capacity by 20%. Figure 2.32 shows the load carrying capacity of the beams with initial core-skin debond. It was also an important observation that from Figure 2.33, the crack began to grow from the corner of the initial core-upper skin debonding area to the lower skin with an angle of 45 degrees to the initial debonding direction and propagated through the lower skin interface. Because of this the concentrated load acted on a localised zone leading to a reduction in the load bearing capacity by 10 %.

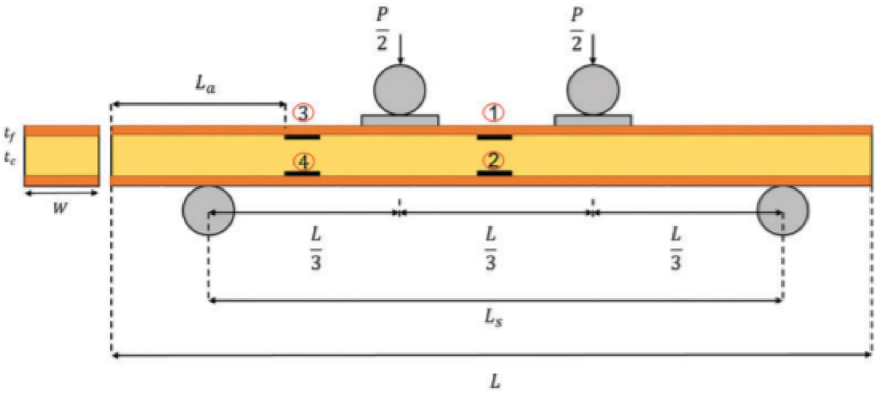

Figure 2.29: Test specimen with load and debonding locations [12]

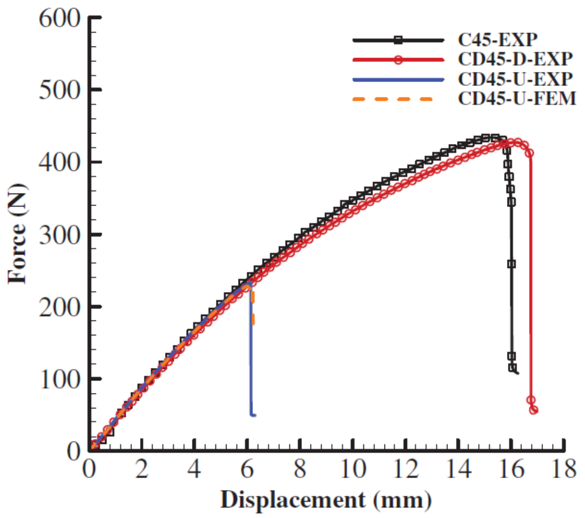

Figure 2.30: Load displacement curves of the sandwich beams with and without inital interface debonding in the middle of the beams, beam length: 280 mm, U: core-upper skin debonding, D: core-lower skin debonding [12]

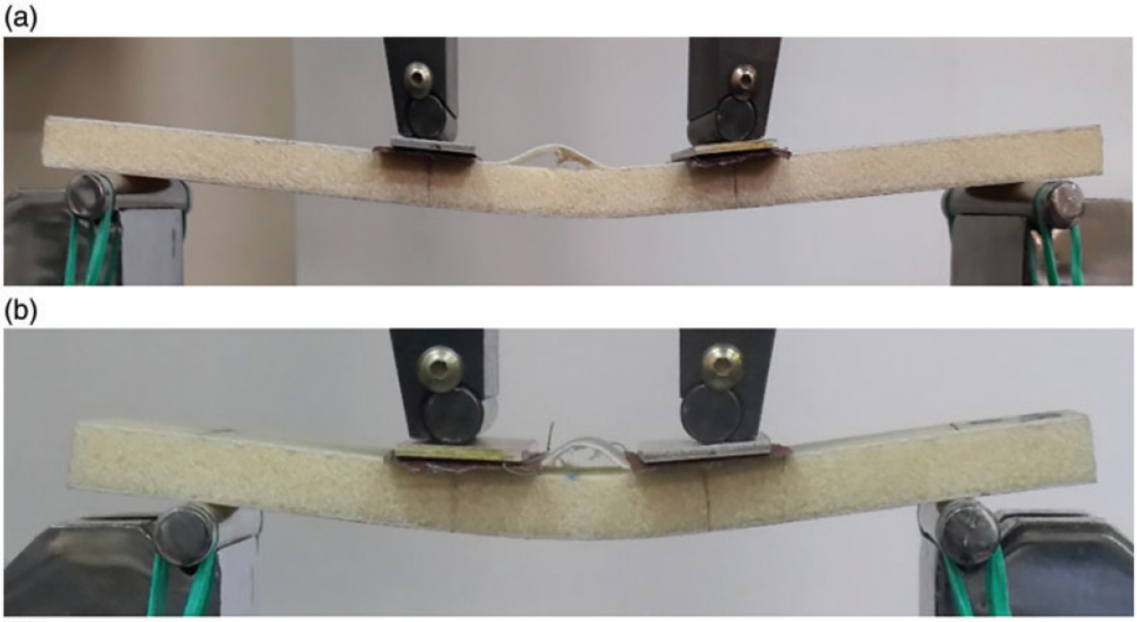

Figure 2.31: The initial debonding progression in the sandwich beams, experiment (a) CD45-U (b) BD45-U [12]

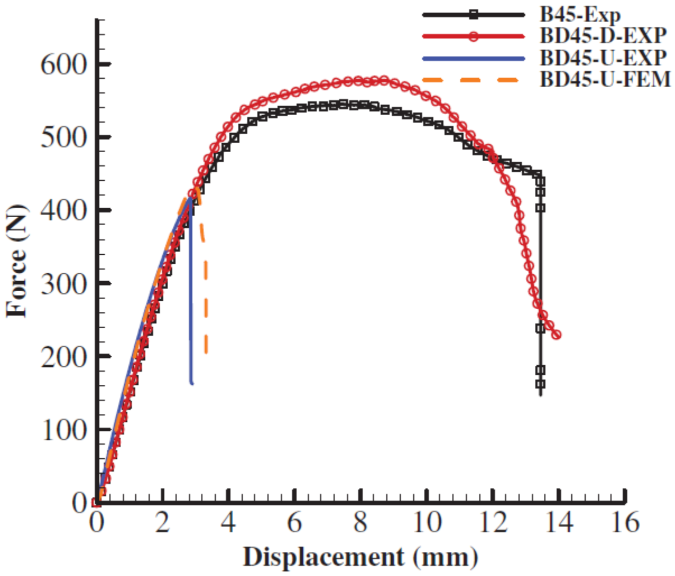

Figure 2.32: Load displacement curves of the sandwich beams with and without inital interface debonding in the middle of the beams, beam length: 180 mm, U: core-upper skin debonding, D: core-lower skin debonding[12]

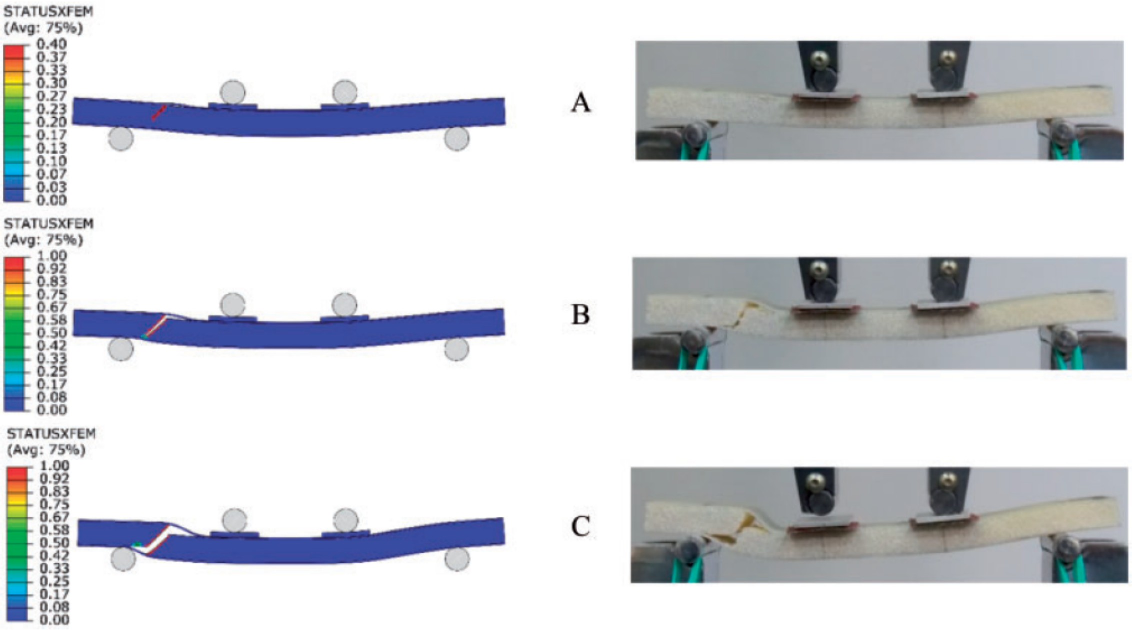

Figure 2.33: Growth in the core and core-skin interface for BDN45-U specimen with initial core-upper skin interfacial debonding in the shear span [12]

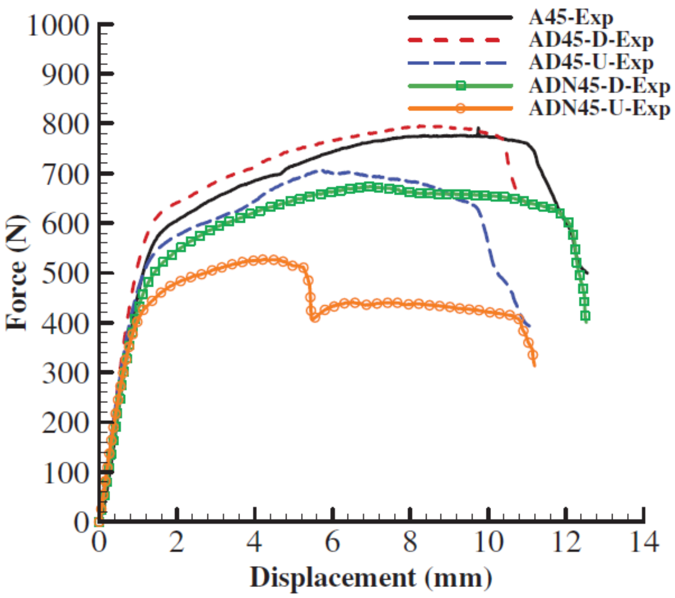

Figure 2.34: Load displacement curves of the sandwich beams with and without inital interface debonding in the middle of the beams, beam length: 100 mm, U: core-upper skin debonding, D: core-lower skin debonding [12]

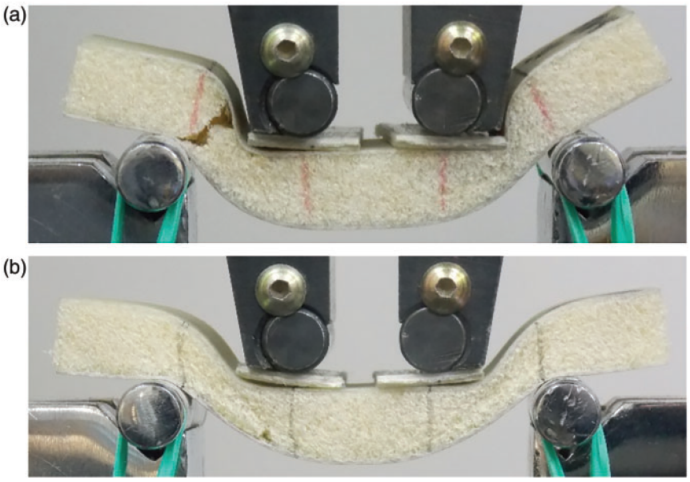

Figure 2.35: Failure mechanism in the sandwich beam with initial interfacial debonding (a) core-upper skin (ADN45-U), (b) core-lower skin (ADN45-D) [12]

Yan He et al. (2017) [6] also studied the effect of interface adhesion agents on old to new concrete interface. The mechanical strength was remarkably increased because of the bonding agents used and different bonding agents have different effectiveness leading to a different mechanical strength. Using bonding agents such as Portland cement grout, latex modified Portland cement grout and epoxy resins can actually improve the bond [22]. However, if the surface preparation is improper, it can act as a bond breaker (Pigeon et al (1992) [21], Schrader et al (1992) [23]). B. Bissonnette [4] suggests that the bonding agents should be avoided as they create two possible planes of weaknesses instead of one.

2.2.2 Influence of Fiber

The bridging effect of SHCC is because of the fibers in the mix. There are several types of fibers that have been used to enhance the tensile property of concrete namely steel, glass and PVA etc. Out of these, PVA fibers have a Young's Modulus relatively higher or similar to that of a normal concrete, thus holding a potential of crack bridging in cement-based construction materials. PVA fibers are strongly hydrophilic, which results in a good chemical bond with the cementitious matrix. However, an excessively strong bond may lead to premature fiber rupture during cracking. This may cause a brittle fracture of the composite. Polyethylene fibers (PE), on the other hand, have superior mechanical properties and hydrophobic nature which makes them suitable for high-strength SHCC. They have a denser cementitious matrix but a weaker frictional bond between the fibers and the cement matrix [24]. The characteristics of different types of fibers is shown in 2.36

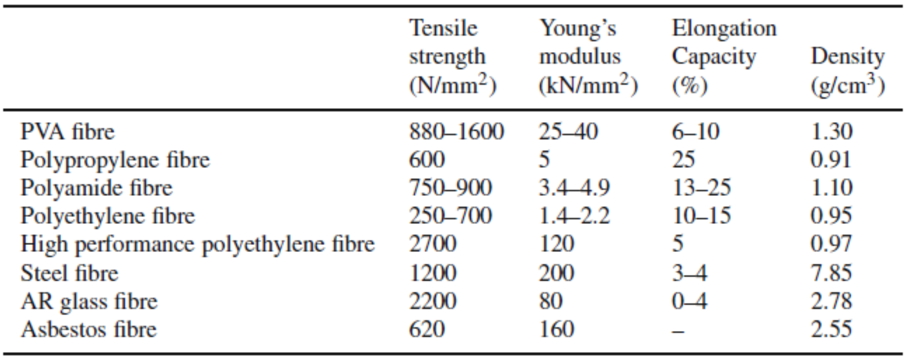

	Tensile strength (N/mm^2)	Young's modulus (kN/mm^2)	Elongation Capacity (%)	Density (g/cm^3)
PVA fibre	880–1600	25–40	6–10	1.30
Polypropylene fibre	600	5	25	0.91
Polyamide fibre	750–900	3.4–4.9	13–25	1.10
Polyethylene fibre	250–700	1.4–2.2	10–15	0.95
High performance polyethylene fibre	2700	120	5	0.97
Steel fibre	1200	200	3–4	7.85
AR glass fibre	2200	80	0–4	2.78
Asbestos fibre	620	160	–	2.55

Figure 2.36: Characteristics of different kinds of fibers [3]

Curosu et al. (2016) [13] highlighted the influence of matrix composition and type of fiber on the tensile behaviour of SHCC under impact loading. From the experiments, it was concluded that performance of SHCC-PVA was much better under quasi-static loading but SHCC-PE was much superior under dynamic loading. It was summarised that the strain-rate sensitivity depends strongly on the fiber type. Under high strain rates, the strong bond between the PVA and cement matrix undergoes a peculiar alteration causing a reduced dynamic composite cracking strength. Whereas, the very weak frictional bond between the PE fibers and cement matrix showed better results under high strain rates in comparison to the behaviour under quasi-static loading as seen in Figure 2.37.

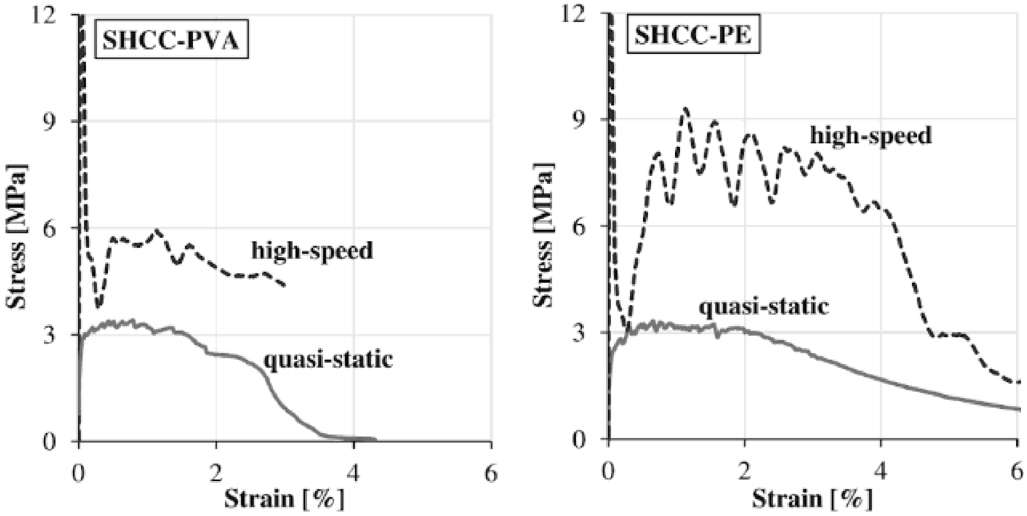

Figure 2.37: Stress vs Strain for SHCC-PVA and SHCC-PE under quasi static and dynamic load [13]

Summary

The main findings of the various authors discussed in detail in literature review are summarised in Table 2.1. The conclusions from their research motivates to investigate the influence of interface variations and the impact of the type of fiber used in SHCC-Concrete Hybrid beams.

Table 2.1: Summary

Author	**Conclusion**
Beushausen (2005) [5]	Experimentally proved the existence of interfacial transition zone at the interface.
Yan He et al (2017) [6]	Experimentally proved that higher the interfacial roughness, greater the mechanical strength.
Li et al. (2009) [7]	Experimentally proved that UHTCC layer overlay just above the centroid of steel reinforcement is more appropriate.
Mohamad et al. (2015) [8]	Experimentally proved that increasing the degree of roughness increased the concrete cohesion and friction at the interface and using steel reinforcement at the interface prevented sudden failure.
Lukovic (2016) [9]	Experimentally proved that providing a smooth interface between SHCC and concrete substrate showed large debonding length for the cracks to distribute due to low bond strength and grooved interface showed a great bond strength but also showed accumulation of cracks which is not favourable.
Kamal et al.(2008) [10]	Experimentally proved the dependency of crack-widths not only on material properties but also on boundary conditions.
Esmaeeli et al.(2008) [11]	Experimentally proved that concrete beams strengthened with SHCC did not show failure involving the disintegration of concrete.
Mansourinik et al.(2018) [12]	Experimentally and numerically proved that introducing artificial debonding on the compression side of the specimen drastically reduced the bearing capacity.
Curosu et al. (2016) [13]	Experimentally proved that the performance of SHCC-PVA was much better under quasi-static load but SHCC-PE was much superior under dynamic load.

2.3 Digital Image Correlation (DIC)

DIC is an image identification technique where the term "Digital" indicates the use of computer, "Image" indicates the images captured by camera and "Correlation" indicates the comparison of images at different stages of deformation [25]. It is an optical non-contact technique used for displacement and strain measurements. It works on the principle of comparing the local correlation between two images. The relationship between deformed and un-deformed images is identified as shown in Figure 2.38 where the central point prior to deformation is point P and it changed to P* after deformation. The functional relationship is established as

$$x* = x + u(x, y) \tag{2.1}$$

$$y* = y + v(x, y) \tag{2.2}$$

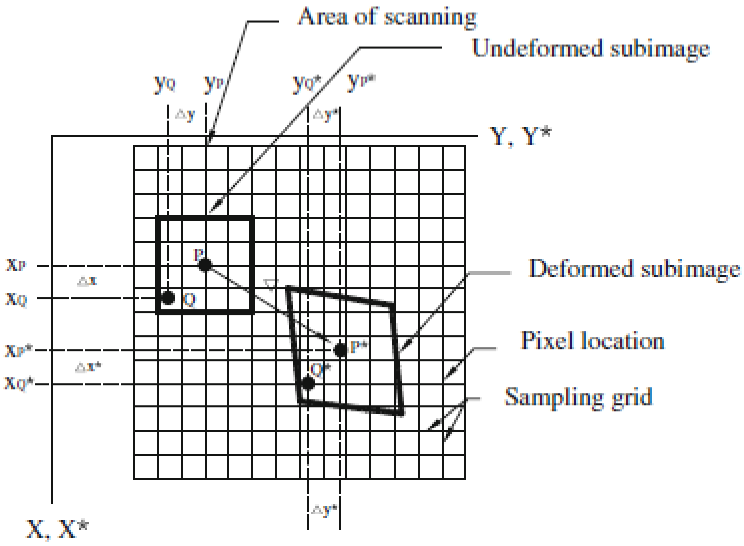

Figure 2.38: Schematic drawing of relative location of sub-images of deformed images and sub images on surface [14]

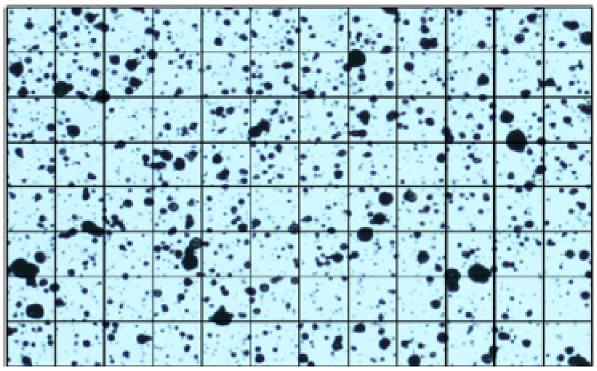

Figure 2.39: Schematic drawing of sub-images (grids) on surface [14]

Finite element method is used to divide the image into several sub images as seen in Figure 2.39. If A is an un-deformed sub image and B is a deformed sub image, then a correlation coefficient is used to determine the relationship as shown in equation 2.3 between sub-images A and B. When sub image B is same as sub-image A then the correlation coefficient is 1.

$$COF = \frac{\Sigma g_{ij}\tilde{g}_{\bar{i}\bar{j}}}{\sqrt{\Sigma g_{ij}^2 \cdot \Sigma \tilde{g}_{\bar{i}\bar{j}}^2}} \tag{2.3}$$

Here, g_{ij} and $\tilde{g_{ij}}$ are grey scale of image A on coordinate (i,j) and image B on coordinate ($\bar{i}$,$\bar{j}$).

Calculation of Strain field:
Green-Lagrange's tensor E is defined as shown in equation 2.4

$$E = \frac{1}{2}[F^T \otimes F - I] \tag{2.4}$$

where, F is gradient tensor of displacement field, and I is the unit matrix.

Tensor E can be rewritten into the function of displacement field as shown in equation 2.5,

$$E_{ij} = \frac{1}{2}(u_{i,j} + u_{j,i}) + \frac{1}{2}u_{k,i}u_{k,j} \tag{2.5}$$

where, i, j, k belong to (x,y) and $u_{i,j} = \frac{\partial u_i}{\partial j}$. Strain is computed using the equations 2.6 to 2.9

$$\varepsilon_{xx} = \frac{\partial u_x}{\partial x} + \frac{1}{2}\left[\left(\frac{\partial u_x}{\partial x}\right)^2 + \left(\frac{\partial u_y}{\partial x}\right)^2\right] \tag{2.6}$$

$$\varepsilon_{yy} = \frac{\partial u_y}{\partial y} + \frac{1}{2}\left[\left(\frac{\partial u_x}{\partial y}\right)^2 + \left(\frac{\partial u_y}{\partial y}\right)^2\right] \tag{2.7}$$

$$\varepsilon_{xy} = \frac{1}{2}\left(\frac{\partial u_x}{\partial y} + \frac{\partial u_y}{\partial x}\right) + \frac{1}{2}\left[\frac{\partial u_x}{\partial x}\frac{\partial u_x}{\partial y} + \frac{\partial u_y}{\partial x}\frac{\partial u_y}{\partial y}\right] \tag{2.8}$$

$$\varepsilon_{vM} = \frac{\sqrt{2((\varepsilon_1 - \varepsilon_3)^2 + \varepsilon_1^2 + \varepsilon_3^2)}}{3} \tag{2.9}$$

Here, ε_{vM} is the von-Mises strain and ε_1 and ε_3 are the major and minor principal strains.

Ming-Hsiang Shih et al. (2013) [14] in their research concluded that cracks developed in reinforced concrete beams can be observed with better precision using the von Mises strain field. Since this master thesis also focuses on studying the influence of interface on cracking pattern and crack-widths, von-Mises strain is used to generate the exact crack pattern and measure the precise crack-widths for all the specimens in the region of interest (i.e. the constant moment region) .

2.4 General: SHCC-Concrete Systems

2.4.1 Reinforced SHCC-Concrete Hybrid beams

In order to utilise the ductility and the crack controlling behaviour of Strain Hardening Cementitious Concrete, Huang (2017) [1] in his master thesis project performed an experimental study to investigate the cracking behaviour of reinforced concrete beams by applying SHCC in the tension zone of the hybrid beams as shown in Figure 2.40. He casted specimens with variable heights of SHCC and reinforcement having different cover in the tension zone as shown in Figure 2.41. For all the beam specimens, PVA fibers were used and the interface between overlay and substrate was kept smooth. Control specimen beams of the conventional concrete were also casted for comparison. A four-point bending test was performed on all samples and the crack width was studied using Digital Image correlation and Image Analysis technique.

It was concluded from the experiments that hybrid beams showed better results than control beams in terms of crack-width control and bending moment capacity. Beams with 70 mm layer of

SHCC showed better crack-width control. The study also indicated that using SHCC can help achieve optimal design.

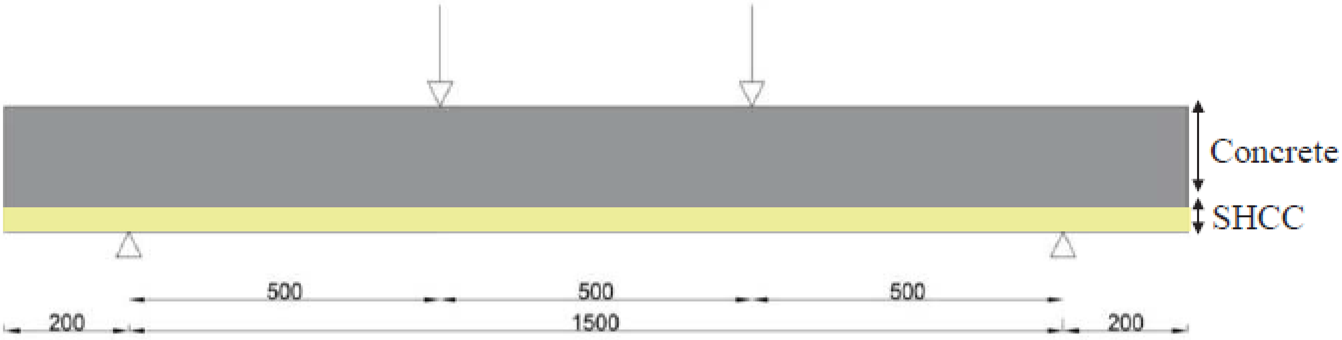

Figure 2.40: Hybrid beam with SHCC layer in the tension zone [1]

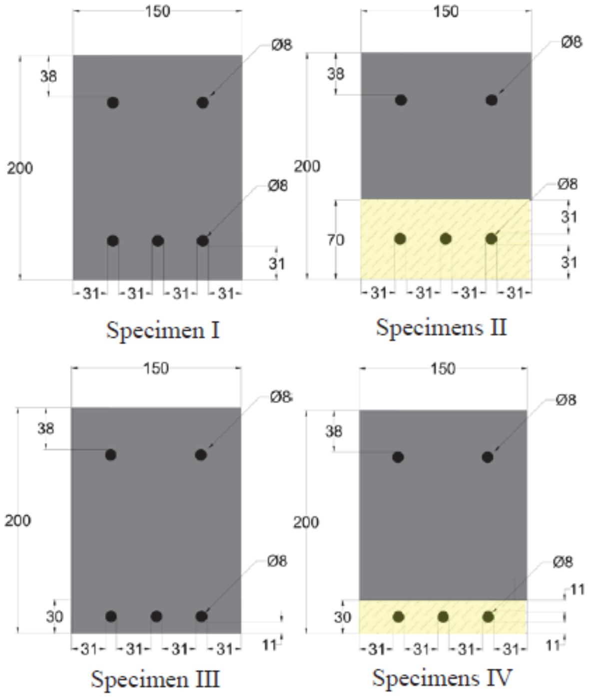

Figure 2.41: Specimens tested under four-point bending [1]

2.4.2 Repair with SHCC (Structural and Non-Structural)

Patch Repairs (U.S.A & Germany)

SHCC can be utilised as a repair material because of its durability. To verify this, a deteriorated bridge deck in Michigan, U.S.A was repaired with SHCC and other ordinary repair products as shown in Figure 2.42a. After five harsh winter cycles, it was observed that no significant abrasion was observed in the SHCC patch as seen in Figure 2.42b. The maximum observed crack-width value was close to 50 μm. However, the crack-width in the ordinary repair material widened up to 2 mm after two years and was replaced partially after three years. In Altenburg, Germany, a concrete slab of a petrol pump was patched with SHCC. The slab was exposed to freeze-thaw cycles along with live loads from heavy and chained traffic. The observed cracks were much smaller than the PCC-mortar as a reference material, without any significant abrasion after one and half years.

(a) Concrete and SHCC patch applied for repairs **(b)** Concrete and SHCC patches after 1.5 years

Figure 2.42: Patch repairs [3]

Surface Repair of Retaining Wall (Japan)

To restore the visual appearance of a gravity concrete retaining wall in Gifu Prefecture, Japan, SHCC was sprayed as shown in Figure 2.43a. The wall initially exhibited cracking due to alkali-silica reaction (ASR). To assess the performance of SHCC, different mixtures of SHCC along with normal repair mortar of varying thickness were applied onto the wall divided into several panels as shown in Figure 2.43b. After two years, a fine mesh of cracks developed at the surface with cracks growing from 50 μm at 10 months to up to 120 μm after two years. Whereas, in the ordinary repair mortars, the cracks grew much faster (300 μm) after two years as seen in Figure 2.44 .

(a) SHCC spray on retaining wall **(b)** Concrete patch repair

Figure 2.43: Repair of retaining wall [3]

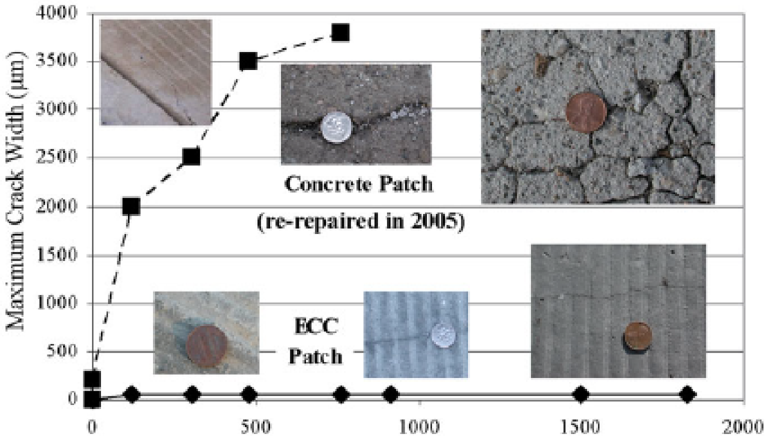

Figure 2.44: Maximum crack-width development over time for SHCC and concrete patch [3]

Chapter 3

Experimental Study

To investigate the influence of interface and the type of fiber used in SHCC, an experimental study is conducted. This chapter gives a detailed description of the pre-study conducted along with the procedures followed during the design, casting, testing and post-processing of the beam specimens. The processed data is discussed and compared in the results and discussion section of this chapter and finally, conclusions are summarised and recommendations are made.

3.1 Pre-Study

Before starting experimental testing of the hybrid beams, a pre-study is performed to determine whether HMPE fibers will be a suitable replacement for PVA fibers. Additionally, the choice of the material to be used for creating debond at the interface is also important. Therefore, a pre-study is conducted to determine these choices before the start of the casting process for the experimental testing.

3.1.1 Fiber Material

The hypothesis postulated at the beginning of this master thesis suggests that by varying the type of fibers in SHCC, the bearing capacity and crack-width control can be improved. The research conducted by Huang (2017) [1] showed considerable amount of crack-width control with SHCC containing Polyvinyl Alcohol fibers (PVA) of 8 mm length. However, High Modulus Polyethylene Fibers (HMPE) of 6mm seemed to be a promising replacement because of their very high Young's Modulus, superior mechanical properties and hydrophobic nature as shown in Figure 2.36. To affirm the behaviour, specimens containing sample PVA and HMPE fibers each, are casted as shown in Figure 3.1a and tested after 14 days in a four-point bending set-up as shown in Figure 3.1b.

A displacement controlled load of 0.01 mm/sec is applied on to the four specimens of each fiber type of standard cross-section 30mm x 8mm as shown in Figure 3.2a. Based on the results obtained from testing, it can be observed that samples containing HMPE fibers showed a much higher deformation capacity than samples containing PVA fibers as seen in Figure 3.2b. In terms of crack-width control, specimens containing HMPE fibers show a more distributed crack pattern as compared to PVA fibers. This is a very important result/observation in terms of crack-width criterion to be satisfied at SLS. From Figure 3.3, it can be concluded that using HMPE fibers in SHCC can enhance the bearing capacity as well as provide better crack-width control as seen in Figure 3.3b compared to PVA fibers as seen in Figure 3.3a.

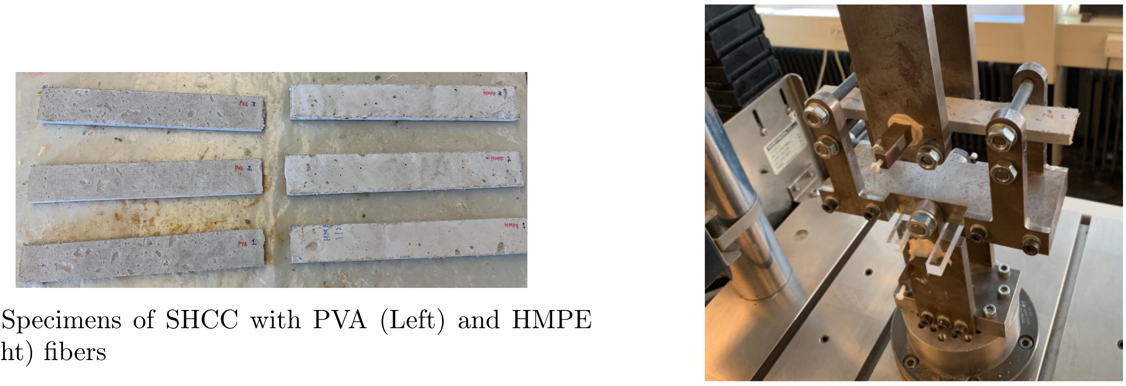

(a) Specimens of SHCC with PVA (Left) and HMPE (Right) fibers

(b) Four-point bending test before loading

Figure 3.1: Specimen preparation and Test Set-up

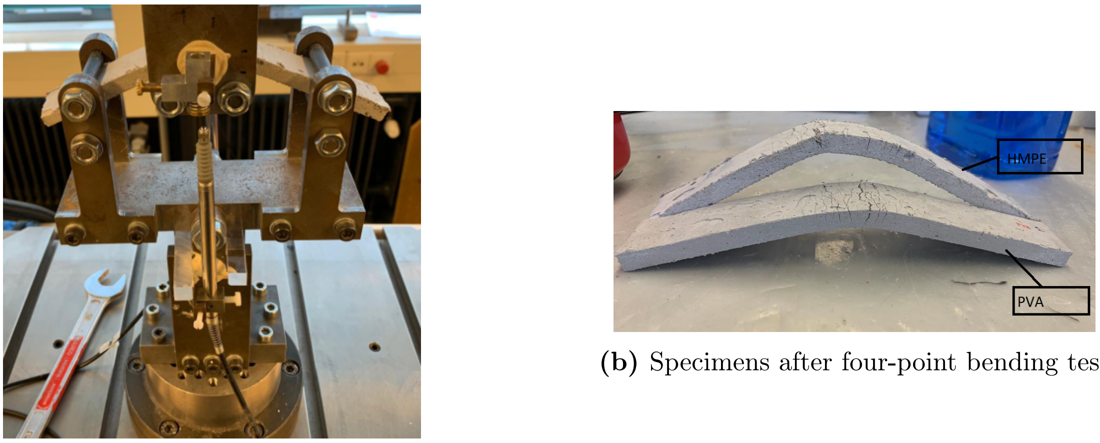

(a) Four-point bending test after loading

(b) Specimens after four-point bending test

Figure 3.2: Testing of fibers

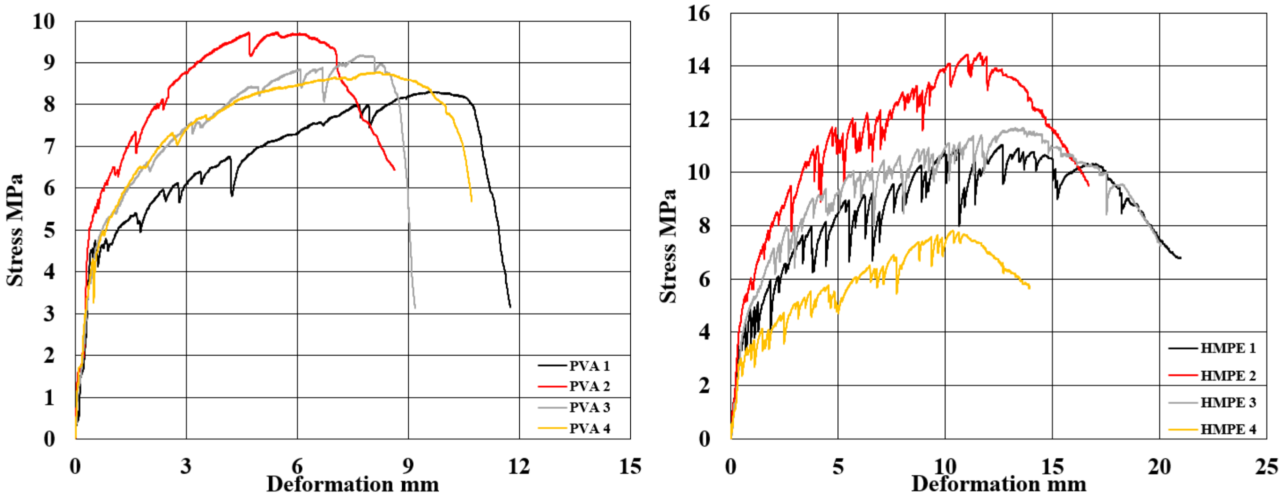

(a) Stress vs Deformation plot for PVA fiber samples **(b)** Stess vs Deformation plot for HMPE fiber samples

Figure 3.3: Comparison between PVA and HMPE fibers sample

3.1.2 Interface Debond Material

To create an artificial debonding between the two layers of concrete in beam sample in Figures 3.13 and3.14, two options of either using tape or Vaseline strips are considered. To check these, two small specimens of SHCC are casted and debond is applied at the interface of one of the specimens by using tape at intervals and for the other using Vaseline strips at same intervals as shown in Figure 3.4a. Later, a layer of normal concrete is poured on to the interfaces as seen in Figure 3.4b and covered with plastic to prevent the escape of moisture. The specimens are kept in the mould for 2 days and then demoulded as shown in Figure 3.5a.

(a) Application of Vaseline strips (left) and tape (right) **(b)** Pouring normal concrete layer on both specimens

Figure 3.4: Application of debond at the interface and casting concrete top layer

It can be seen from Figure 3.5b that, upon opening the interface of the hardened specimens using chisel and hammer, the specimen with Vaseline strips at the interface show some material adhered to it indicating bond as seen in Figure 3.5b (A). Whereas, the specimen with tape show a proper debond as seen in Figure 3.5b (B). Based on this observation, a choice to use tape instead of Vaseline strips is made.

(a) Samples A and B demoulded after 2 days **(b)** Breaking open at the interface of sample A and B

Figure 3.5: Demoulding samples and Testing

3.2 Design

This master thesis is an optimisation study on the research done by Huang (2017) [1] and so a cross-section with 70 mm layer of SHCC is selected. In the experiments conducted by Huang (2017)

[1], better crack-width control is achieved in specimens with the above-specified height of SHCC. The length of the beams is 1900 mm with a cross-section of 150 mm x 200 mm as shown in Figures 3.6 and 3.7, respectively.

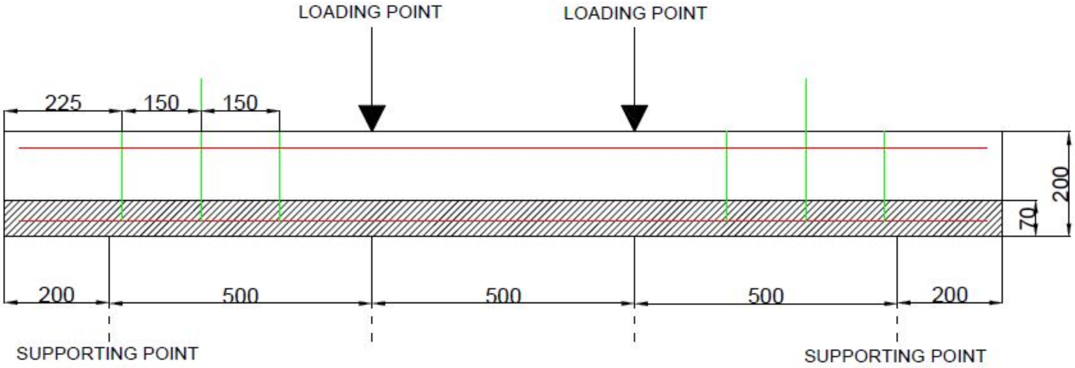

Figure 3.6: Geometry of the beam (mm)

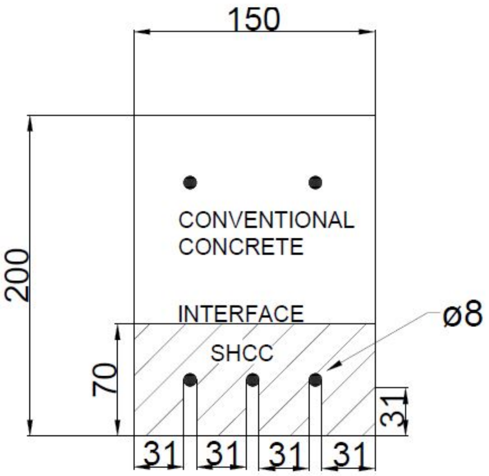

Figure 3.7: Cross-section of the beam (mm)

To allow large flexural cracks in the constant moment region, the percentage of reinforcement is kept near to minimum. Three tensile reinforcement bars of 8 mm diameter are used (0.54 %) as shown in Figure 3.6. To avoid shear failure, six 2-legged stirrups with 3 stirrups on each side of the constant moment region are provided, located at specific distances as shown in Figure 3.7. The middle stirrup in Figure 3.9a and 3.10a is made larger for lifting purposes. Uniform cover is maintained by placing spacers of 31 mm height casted and placed as shown in Figure 3.8a and 3.8b.

(a) Casting of SHCC spacers

(b) Placement of SHCC spacers

Figure 3.8: Casting and Placing SHCC spacers

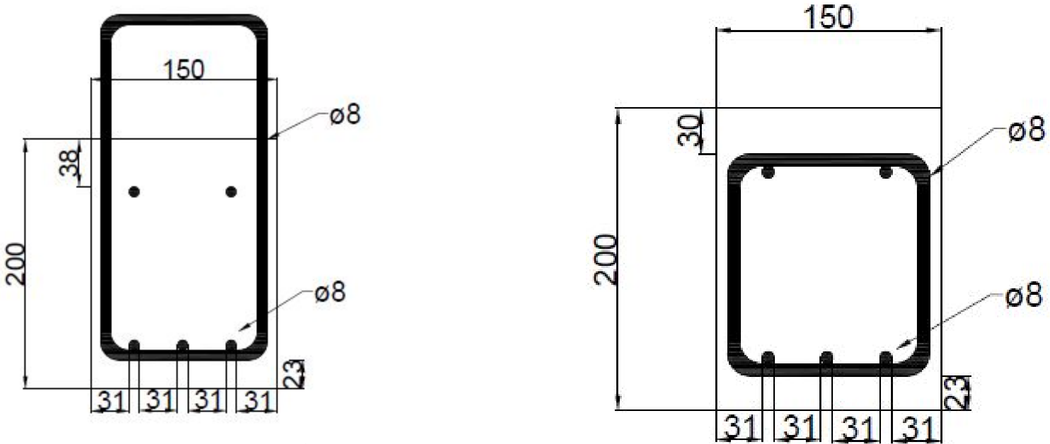

(a) Extended stirrup in C30/37 beam

(b) Stirrup in C30/37 beam

Figure 3.9: Cross-section of concrete beam of grade C30/37

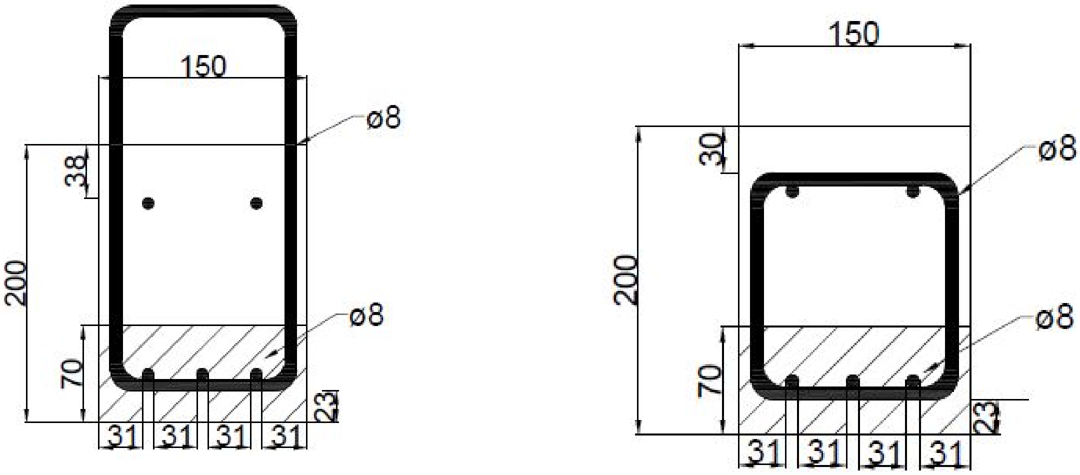

(a) Extended stirrup in hybrid beam

(b) Stirrup in hybrid beam

Figure 3.10: Cross-section of SHCC-Concrete Hybrid beam

A total of six beam specimens are designed to study the influence of interface and type fiber used. Out of these, one beam specimen is designed with conventional concrete (CC) as shown in Figure 3.11 of grade C30/37. Another beam with smooth interface and PVA fibers (S-PVA) as seen in Figure 3.12 is designed as a reference specimen for all the other beams with varied interfaces tested during the research.

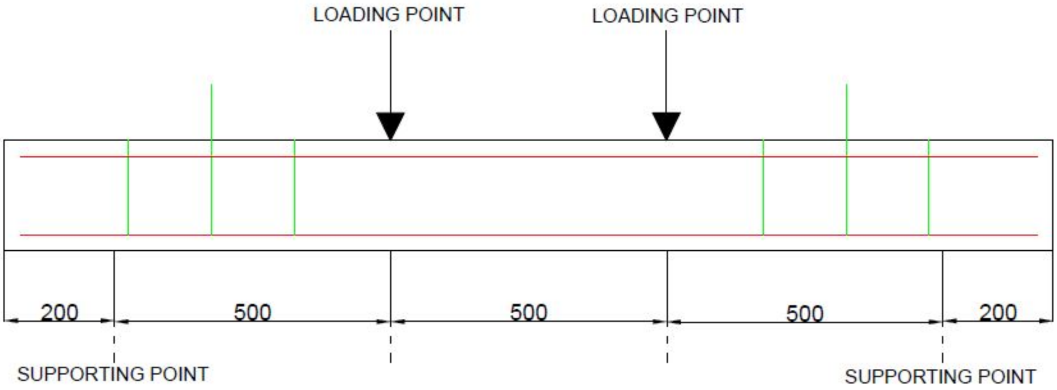

Figure 3.11: Conventional concrete beam; No Interface

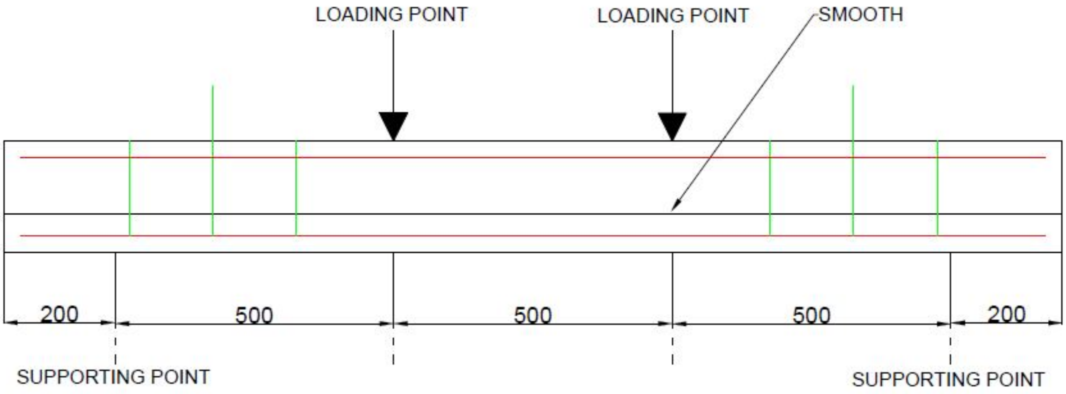

Figure 3.12: Hybrid beam; Smooth Interface

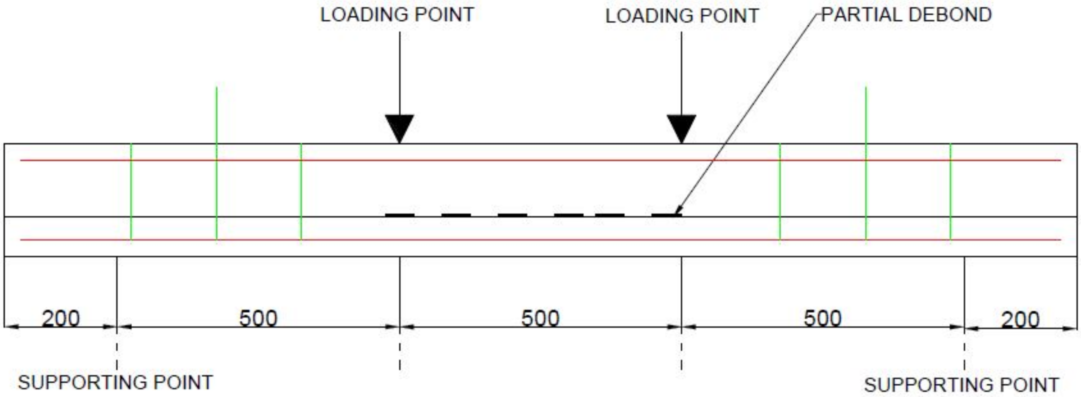

Figure 3.13: Hybrid beam; Partially Delaminated Interface

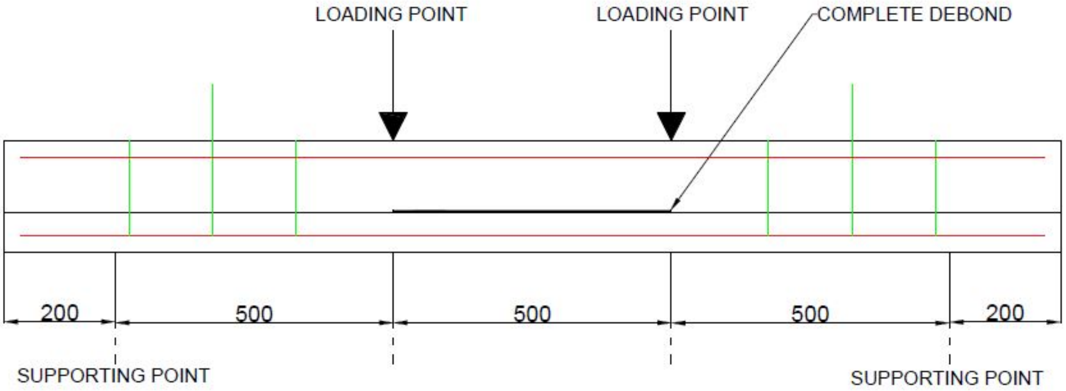

Figure 3.14: Hybrid beam; Completely Delaminated Interface

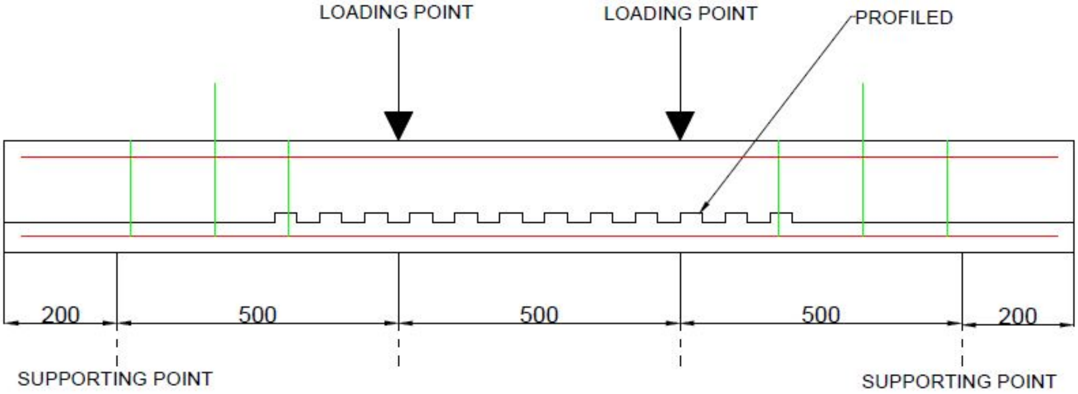

Figure 3.15: Hybrid beam; Profiled Interface

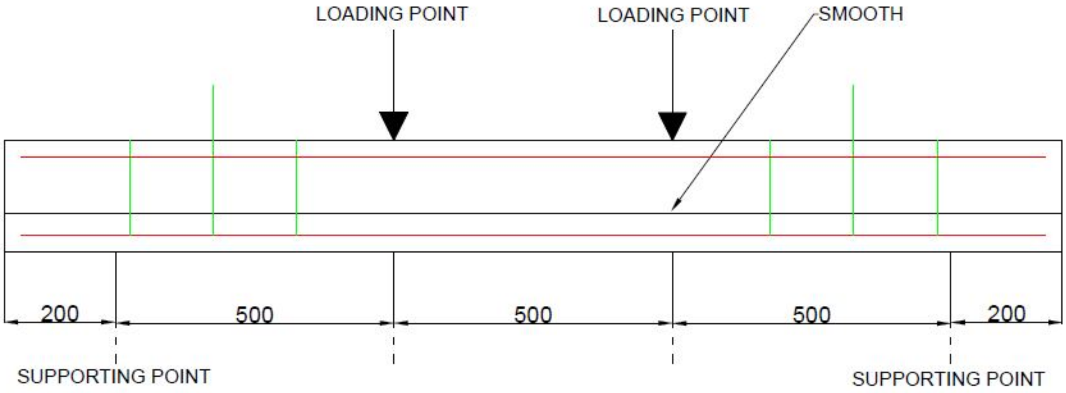

Figure 3.16: Hybrid beam; Smooth Interface; HMPE fibers

Furthermore, two beam specimens with partially (PD-PVA) and completely delaminated (CD-PVA) interface within the constant moment region with PVA fibers in SHCC are designed to study the influence of interface on crack-width control as shown in Figures 3.13 and 3.14. Finally, a profiled interface specimen (P-PVA) as shown in Figure 3.15 is also designed to study the same influence.

To understand the impact of fibers on crack-width control, the final specimen with HMPE fibers instead of PVA fibers is designed with a smooth interface (S-HMPE) as seen in Figure 3.16.

3.3 Casting

To cast the beams, first the moulds of standard size 1900 mm x 150 mm x 200 m is prepared out of plywood sheets bolted together. The steel reinforcement is tied together and placed in the moulds. Spacers are placed to maintain a uniform cover and to keep the reinforcement intact during vibrating and pouring operations as seen in Figure 3.17.

Figure 3.17: Mould for casting along with steel reinforcement

The hybrid beam is casted in two layers. A detailed description on the casting procedure along with the material quantity is discussed in the following sub-sections.

3.3.1 SHCC layer

The mix composition of SHCC constitutes of ingredients such as limestone powder, cement (CEM IIIB), super plasticizer, water, PVA and HMPE fibers. A detailed description of these constituents is discussed in Tables 3.1, 3.2 and 3.3. A step by step mixing regime is followed. First, all the solid materials along with the fibers are mixed for a duration of 2.5 minutes at a low speed. Then, water and super plasticizer is added to this dry mix and mixed for 1 minute at a low speed. Finally, after considerable uniformity is seen, the mixture is mixed at a high speed for a time duration of 4 minutes.

The height of SHCC layer casted (70 mm) is not sufficient for needle vibration so it is preferred to vibrate the mix by placing the moulds containing SHCC directly on the vibrating table as shown in Figure 3.18a. The top layer of SHCC is levelled using a levelling apparatus. For beam specimen with profiled interface (P-PVA), the plastic mould containing the toothed grain of 150 mm x 40 mm as shown in Figure 3.18b is placed on the wet SHCC mix and pressed with a wooden log to imprint the toothed profile after drying. Finally, all the moulds containing SHCC are covered with plastic sheets to retain the moisture and left at the room temperature for 14 days as seen in Figure 3.19.


(a) Casting of SHCC layer **(b)** Profiling at the interface of SHCC layer

Figure 3.18: Casting

Figure 3.19: Covering to retain moisture

Table 3.1: Material ingredients of SHCC with PVA fibers

Ingredients	**Dry Weight** (kg/m^3)
CEM III B	790
Limestone Powder	790
PVA Fiber	26
Water	411
Superplasticizer	2.13

Table 3.2: Material ingredients of SHCC with HMPE fibers

Ingredients	**Dry Weight** (kg/m^3)
CEM III B	790
Limestone Powder	790
HMPE Fiber	19.4
Water	411
Superplasticizer	2.13

Table 3.3: Properites of fibers used in SHCC

Type of fiber	**Density** (g/cm^3)	**Length** (mm)	**ft** (MPa)	**E** (GPa)
PVA	1.3	8	1600	40
HMPE	0.97	6	2700	120

3.3.2 Interface Preparation and Treatment

After the curing period of 14 days, the plastic sheets are removed and the interface surface of all the specimens are first cleaned with a vacuum cleaner to remove any dust. The interfaces of all beams to be tested are prepared and listed in the Table 3.4.

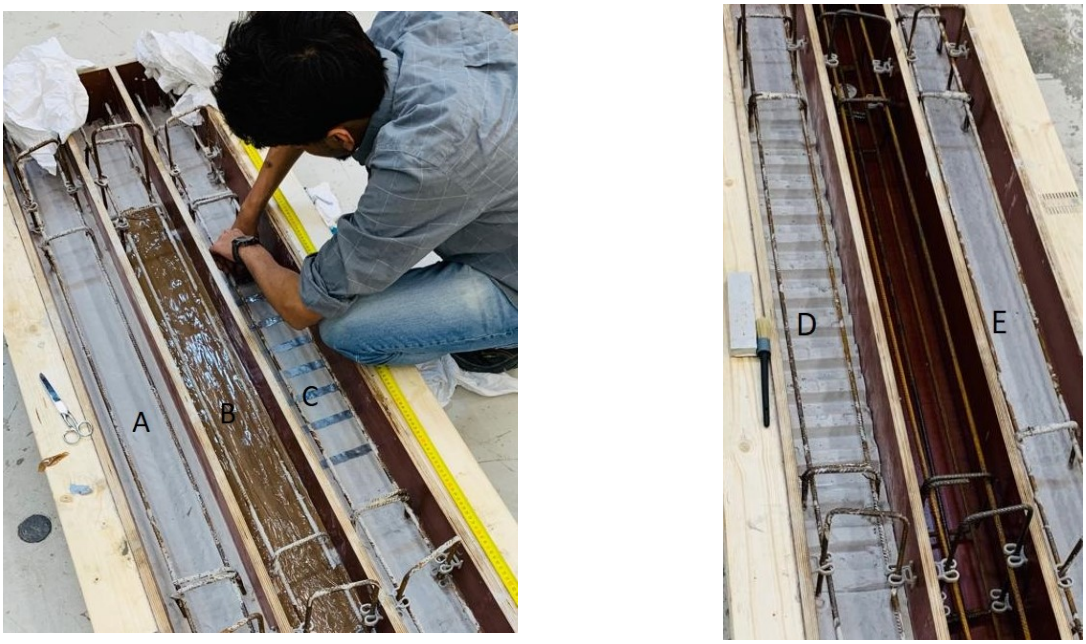

(a) A-Smooth; B-Complete debond; C-Partial debond

(b) D-Profiled; E-Smooth-HMPE fibers

Figure 3.20: Interface preparation

Table 3.4: Interface Preparation

Beam Specimen	**Reference**	**Interface preparation**
CC		No preparation
S-PVA	A	Roughened with a steel brush to increase bond
CD-PVA	B	The constant moment region is covered with tape completely
PD-PVA	C	20 mm wide strips of tape are placed at 50 mm intervals.
P-PVA	D	The plastic toothed mould placed during casting is removed
S-HMPE	E	Roughened with an abrasive steel brush to increase bond

Once all the interface surfaces are prepared, the surface is re-vacuumed and wiped with ethanol using a clean clothing material.

3.3.3 Concrete layer

After the interface surface is prepared for all the six beam specimens, the second layer of the hybrid beam comprising of normal concrete is directly poured into the mould as shown in Figure 3.21a. The constituents of the normal concrete layer are listed in the table 3.5

Table 3.5: Material ingredients of concrete grade C30/37

Ingredients	**Dry Weight** (kg/m^3)
CEM IB 52.5R	260
Sand 0.125-0.25 mm	78.83
Sand 0.25-0.5	256.199
Sand 0.5-1mm	256.199
Sand 1-2 mm	157.661
Sand 2-4 mm	98.538
Sand 4-8 mm	394.152
Gravel 8-16 mm	729.181
Water	156
Super plasticizer	0.26

Due to the availability of sufficient depth for vibration, poker stick vibration is applied to expel the excess air entrapped in the concrete layer as seen in Figure 3.21b. Finally, the top surface is levelled as shown in Figure 3.22 and specimens are covered with plastic sheets to retain moisture. The beams are left at room temperature and demoulded 38 days after the casting of the top layer of concrete.

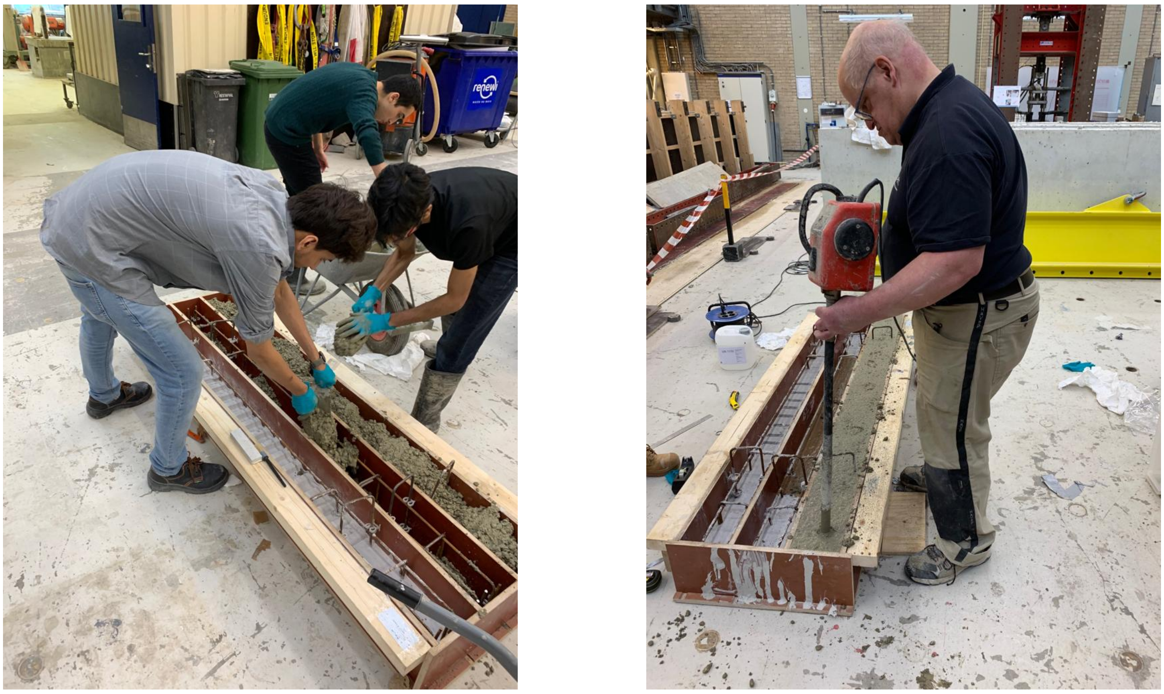

(a) Filling the mould with concrete

(b) Vibration to remove excess air

Figure 3.21: Casting of concrete top layer

Figure 3.22: Levelling of the top surface of concrete

3.4 Testing

To determine the bearing capacity and crack propagation due to variation of the interface and the type of fiber in SHCC, a four-point bending test set-up as shown in Figure 3.23. The four-point bend test is performed with a displacement-controlled jack loading the beams at a rate of 0.01 mm/sec, maintaining the boundary condition of the beams as simply supported. The LVDT positioning and the surface preparation for digital image correlation (DIC) are shown in Figure 3.23a and 3.23b respectively. A detailed description on the procedure followed to determine the above-mentioned parameters is discussed.

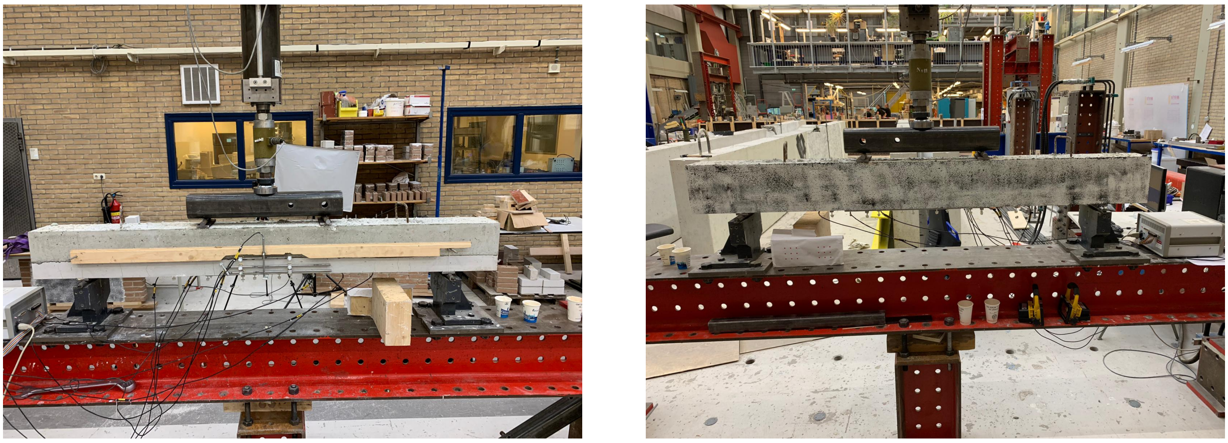

(a) LVDT arrangement to measure deformation

(b) DIC surface preparation

Figure 3.23: Four-point bending set-up

3.4.1 Linear Variable Data Transformer (LVDT)

To measure the deformation of the beam specimen in the horizontal and vertical directions, a number of Linear Variable Data Transformers (LVDTs) are used. In total, ten LVDTs are used for every beam out of which, one is used to measure the vertical deformation (LVDT 5), three to measure the horizontal deformation placed on the face side of the beam (LVDT 2, LVDT 3, LVDT 4) and six are placed at the bottom face of the beam (LVDT 1, LVDT 6, LVDT 7, LVDT 8, LVDT 9 & LVDT 10) to measure the horizontal displacement. The location of all the LVDT's is shown in the Figure 3.24 and Figure 3.25. Only LVDT 10 has a measuring range of 500 mm and the rest of them have a measuring range of 200 mm.

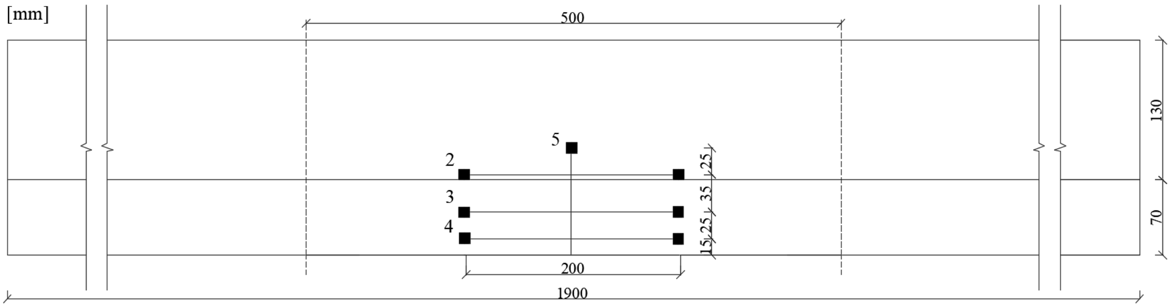

Figure 3.24: LVDTs placed on the side face of the beam

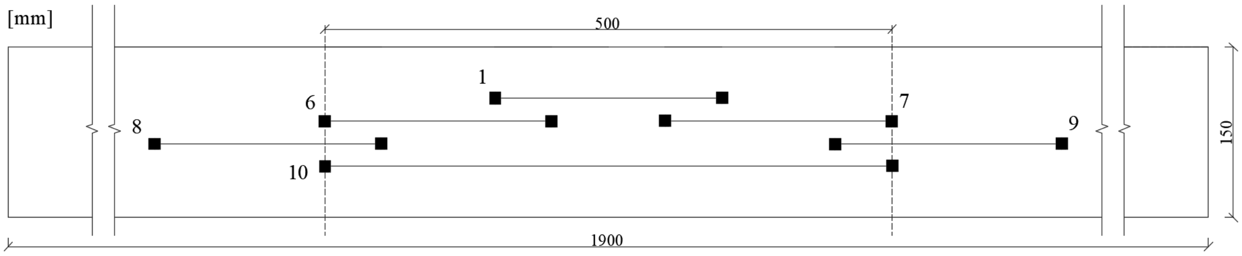

Figure 3.25: LVDTs on the bottom face of the beam

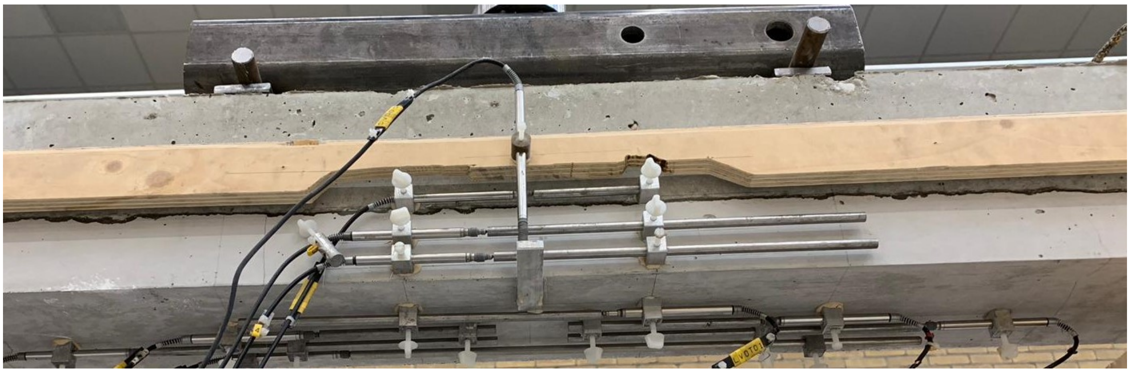

Figure 3.26: LVDTs located on the face side and bottom side of the beam

3.4.2 Digital Image Correlation (DIC)

The DIC is used to study the crack pattern and maximum crack-width of the beams. With LVDTs positioned on bottom and one of the side faces of the beams, the other side face is painted white and covered with a number of black spots/patches as seen in Figure 3.23b. Once the load is applied on the beam, for every 5 KN of the applied load, three images of the painted side of the beam are captured. The images are later on post-processed using the GOM correlate software.

3.5 Post-Processing

After testing the beam specimens in a four-point bending set-up, the crack pattern and the crack-widths in the constant moment region can be studied by correlating the images in DIC using GOM correlate software analysis tool. Also, the feasibility of using this method in determining the cracking behaviour is verified to confirm the reliability of results. For this, Image J tool, visual inspection during loading and comparison with LVDT deformations is carried out to validate the obtained results.

This section is sub-divided as follows,

3.5.1 Correlation using GOM correlate

A step by step procedure carried out to correlate the images from the experiment to determine the crack pattern and crack-widths at a certain section using GOM correlate software tool is discussed.

Introduction

GOM Correlate software is based on the parametric concept that ensures all the process stages are traceable. In this software, parameters such as measurement series, calibration parameters and surface components are initialised by the user as seen in Figure 3.27. The software then automatically finds square-shaped facets in the zone specified (surface component). For identification, the GOM correlate software uses the stochastic pattern quality structure where point distance between the center point of the adjacent square facets is measured at all stages. This impacts the measurement point density within the surface component. A better resolution can be obtained by having facets closer to each other [26].

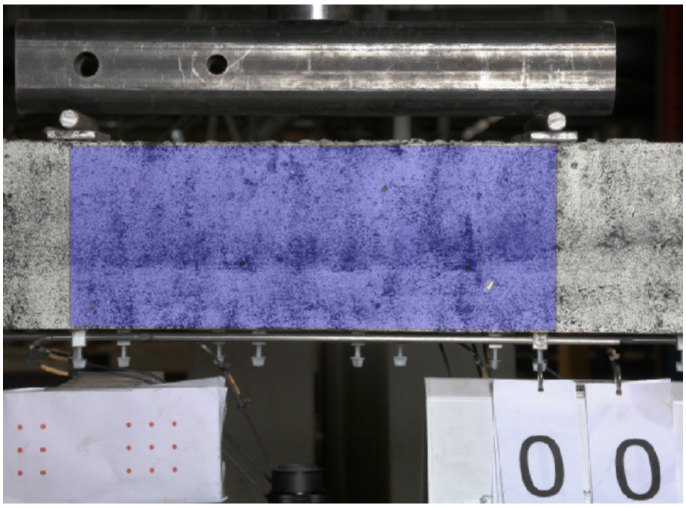

Figure 3.27: Surface component selected using GOM correlate

Correlation Procedure

As mentioned in the chapter 2 of this report, the precision in crack study is very high when von Mises strain is used [14]. GOM correlate provides an option to generate the von Mises strain over a selected surface area thus, making the crack-width study accurate.

Specific to this research, the constant moment region is chosen as the surface component under study and the von Mises strain is generated for all the beam specimens tested. As an example, the constant moment region of beam specimen CD-PVA is shown in Figure 3.28. Following this, three inspection sections are created at a distance of 1 mm, 69 mm and 71 mm from the bottom edge of the beam indicated as section 1,2 and 3 in Figure 3.29. The reason behind choosing such sections is to inspect the crack-widths close to the bottom of the beam and at the interface of SHCC and normal concrete layer and report the maximum value.

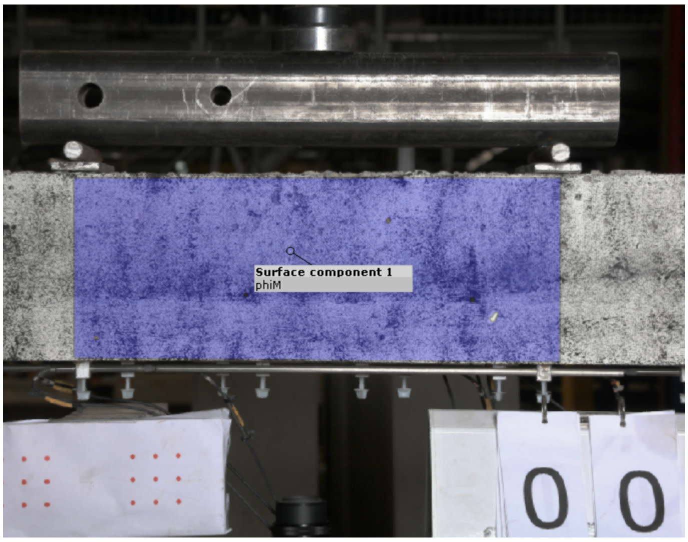

Figure 3.28: von Mises strain generated over the constant moment region

To determine the crack-widths of the various cracks at these sections, the strain in the x-direction (ε_x) and the corresponding displacement in the X-direction (dx) is generated as shown in Figure 3.29. Once the load is applied and as soon as the cracking strain (ε_{cr}) of either SHCC or conventional concrete is exceeded, cracks will occur.

The location of the cracks can be identified from the plot of ε_x in X direction and magnitude of the cracks is indicated from the corresponding plot of dx in the X direction for a specific load step. As seen in the Figure 3.30, the jump in ε_x indicates the location of cracks along the length and the jump in dx plot gives the magnitude of the crack-width of the various cracks along the length.

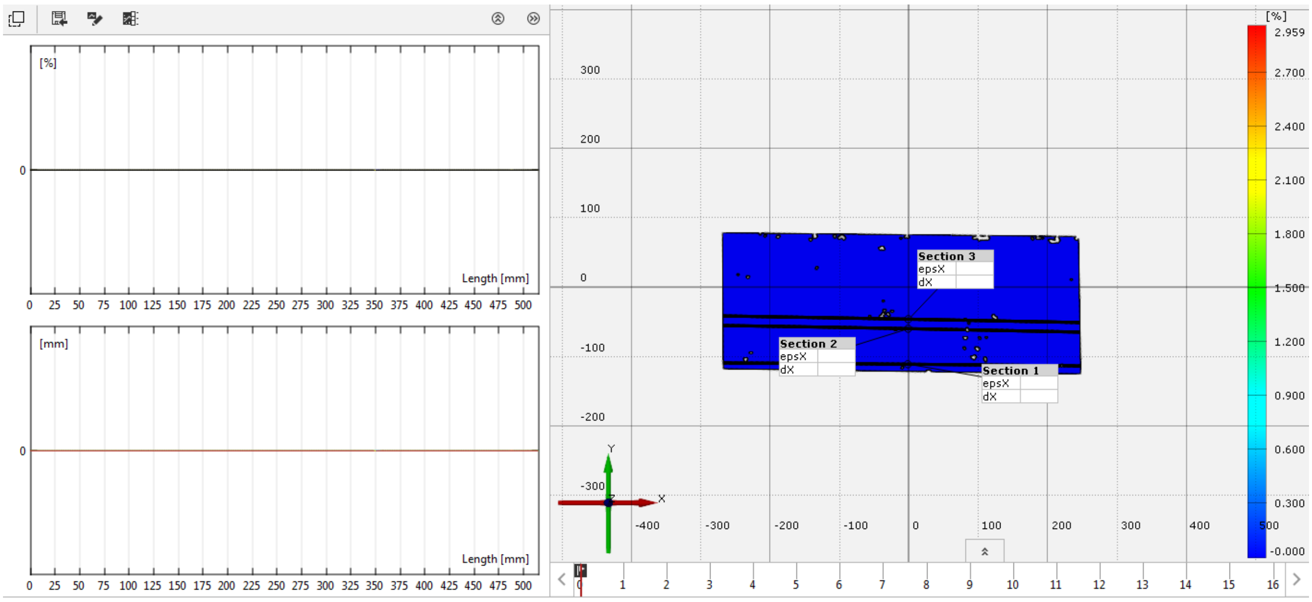

Figure 3.29: Section 1, 2 and 3 indicating strain and displacement in X direction at load step 0 of CD-PVA

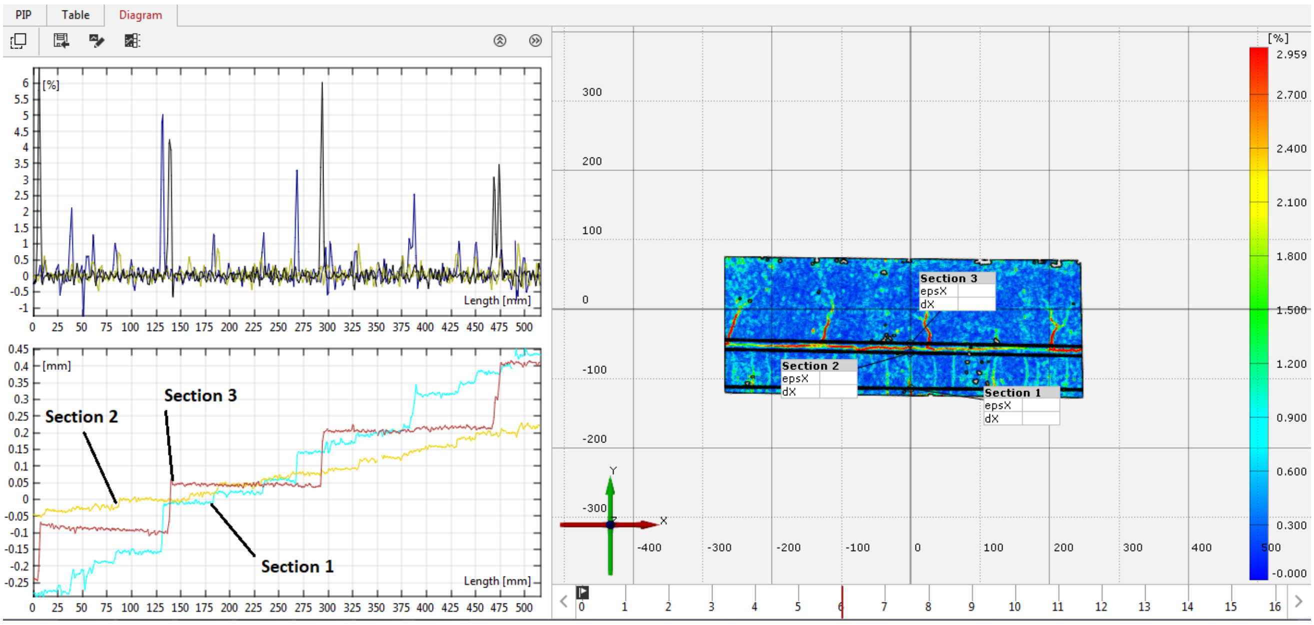

Figure 3.30: Section 1, 2 and 3 indicating strain and displacement in X direction at load step 30 of CD-PVA

This correlation tool also provides an option to export the strain and displacement values for all loads steps in various formats. Analytical calculation is done to determine the precise crack-widths at all load steps by exporting the strain and the displacement plots to Excel. For precision, first the cracking strain (ε_{cr}) for concrete and SHCC is calculated to be 0.0089 % and 0.0167 % respectively. A filter is then applied to all load steps by comparing the strains generated across the length to the cracking strain, which is calculated for locating the crack positions. Later, a Matlab code shown in the appendix is developed to measure the sum of all the differences in displacements (dx) corresponding to the strain (ε_x) exceeding the cracking strain (ε_{cr}).

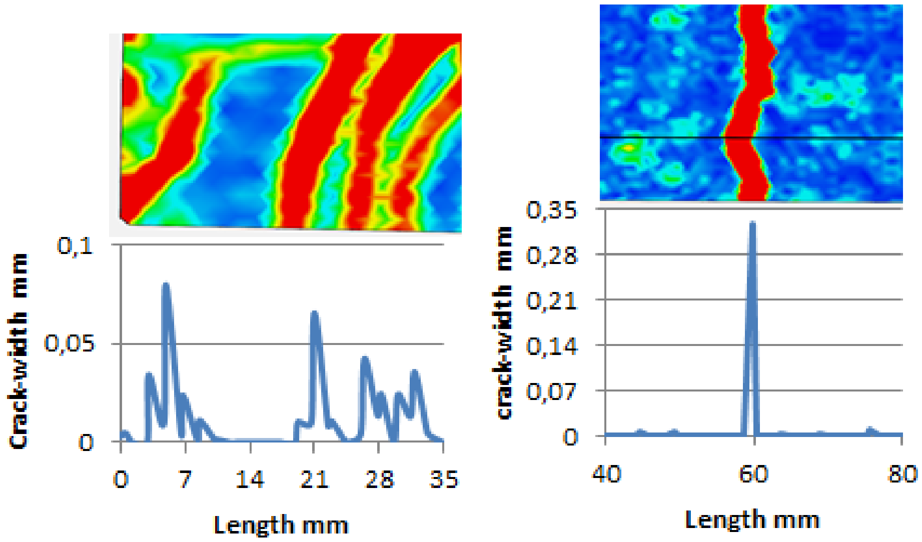

(a) Distributed Cracks in the SHCC layer **(b)** Localised Crack in CC layer

Figure 3.31: Cracking pattern in SHCC and CC layer of Hybrid beams

It is important to note that both SHCC and conventional concrete (CC) have different crack patterns as shown in Figure 3.31. When ε_{cr} of 0.0167 % is used as a filtering strain value for the SHCC layer, it is noticed that a number of small cracks are being summed together as one single crack and maybe over estimating the crack-widths. For example, in the beam specimen with a profiled interface with ε_{cr}= 0.0167 %, all the cracks shown in Figure 3.31a are presented as a single crack of width of 0.46 mm although it is evident that there are four such cracks of different widths. To investigate the chance of over estimation, the ε_{cr} is increased up to 0.2 % for SHCC and the crack-width is measured for the four individual cracks. To also verify if this increase in ε_{cr} underestimates the actual crack-width, a comparison is drawn between the crack-width measured (0.46 mm) at a ε_{cr} of 0.0167 % and the sum of individual cracks measured (0.45 mm) at a cracking strain of 0.2 %. Since the calculated crack-widths of 0.46 mm and 0.45 mm are comparable, it is decided to use ε_{cr} of 0.2 % for SHCC layer for a more realistic representation of the cracks and their corresponding crack-widths. Whereas, in the case of concrete layer the same trend is not observed. When the ε_{cr} is increased to 0.2 % from 0.0089 %, a reduction in the measured crack-width is observed. This is because unlike SHCC, conventional concrete develops triangular-shaped cracks as shown in Figure 3.31b upon loading. Thus, when the ε_{cr} is increased, the measured crack-width is smaller and not comparable to the actual crack-width indicated by GOM correlate. A possible reason could be the steep profile of the crack which underestimates the crack-width at a higher stain range. So it is decided to measure the crack-width at a cracking strain (ε_{cr}) higher than 0.0089 % to generate realistic crack-widths.

3.5.2 Validation of GOM results

To validate the correlation results obtained from GOM correlate software tool, the validation procedures carried out are discussed in this sub-section.

Comparison with LVDT Deformation

To measure the possible deformations of the beam specimens during the four-point bending test, a set of ten LVDT's are being used to record the horizontal and vertical deformations. The availability of this data can be used to validate the results from GOM in the following manner.

There are four LVDTs numbered as LVDT 2, LVDT 3, LVDT 4 and LVDT 5 positioned on the side face at specific distance from the bottom edge of the beam as seen in Figures 3.24 and 3.32. At the exact same locations, points are placed on the mapped image of the constant moment region using GOM correlate software tool representing the two ends of each LVDT as seen in Figure 3.33. With every applied load step, the horizontal movement of six points (dx) and the vertical movement of one point (dy) is recorded. The difference in the horizontal movement between two points for example (point 13 and point 14) gives the horizontal displacement (referred as GOM 2) at every load step as shown in Figure 3.33. This measured value is comparable to the horizontal displacement measured by LVDT 2 positioned at that exact location during the experiment. The vertical movement of point 4 (referred as GOM 5) recorded is directly comparable to the vertical deformations measured using LVDT 5 during the experiment at that same location. Figure 3.34a and 3.34b show the validation plots between the deformation obtained using GOM correlate and LVDT's.

Figure 3.32: Location of LVDT on the side face of the beam

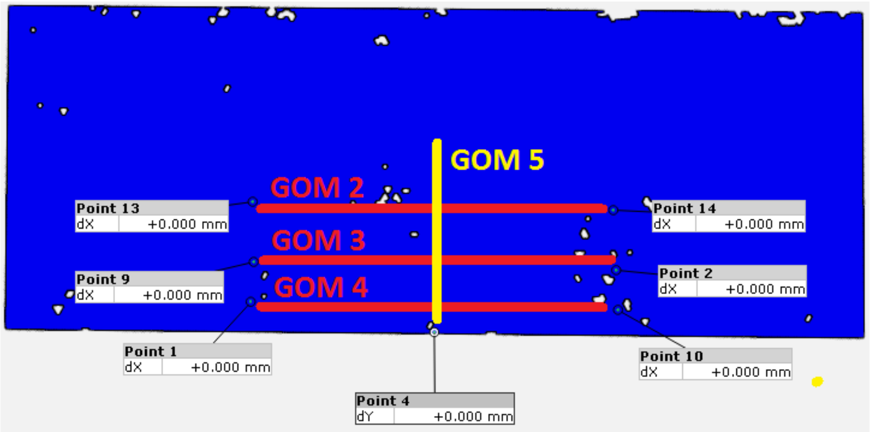

Figure 3.33: Points corresponding to the end locations of LVDT's

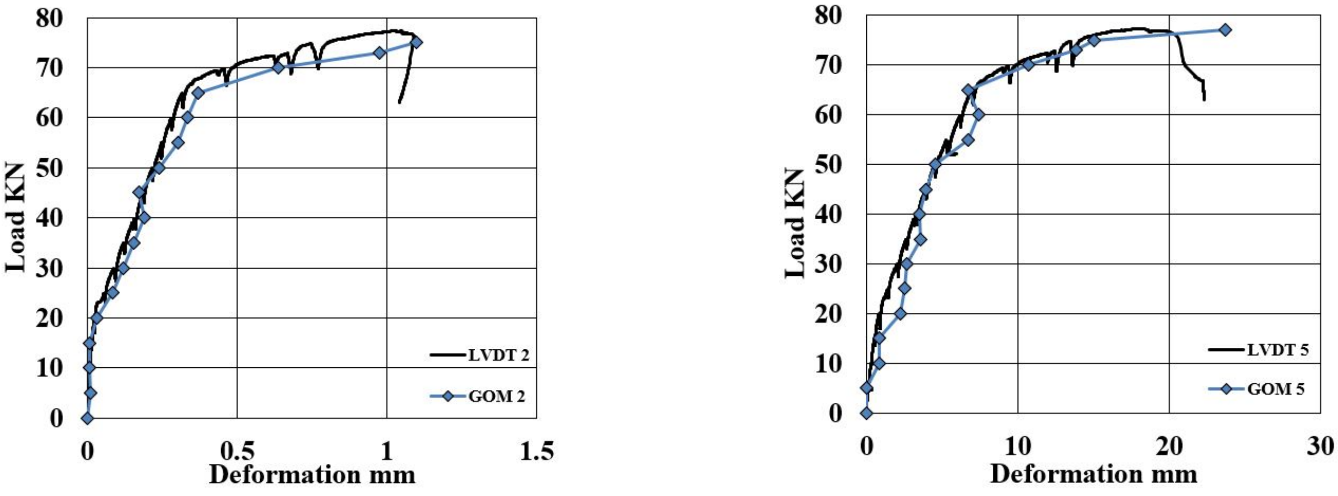

(a) Horizontal calibration

(b) Vertical calibration

Figure 3.34: Comparison of deformation from GOM with LVDT's

Image J

Image J is a java based tool developed by the National Institute of Health and the Laboratory for Optical Health and Computational Instrumentation (Wisconsin,U.S.A). With the help of this software standard image processing functions such as contrast manipulation, sharpening and smoothing of images and geometric transformations such as scaling is possible.

During the process of testing the beam specimens, a camera with a focus to the bottom side of the beam was placed and for every load step of 10 kN, a picture is taken. Later, the images are processed using the Image J tool.

The procedure to determine the crack-width starts with importing the image on to the Graphical User Interface (GUI) of the software as seen in Figure 3.35 and defining the scale using the set-scale option. The images are then zoomed in to get the best possible view of the cracks and a straight line is drawn through the cracks at atleast two to three places to measure the size of the cracks as shown in Figure 3.36.

Figure 3.35: Image of cracks on the bottom-side of CC beam (Load step 60 kN)

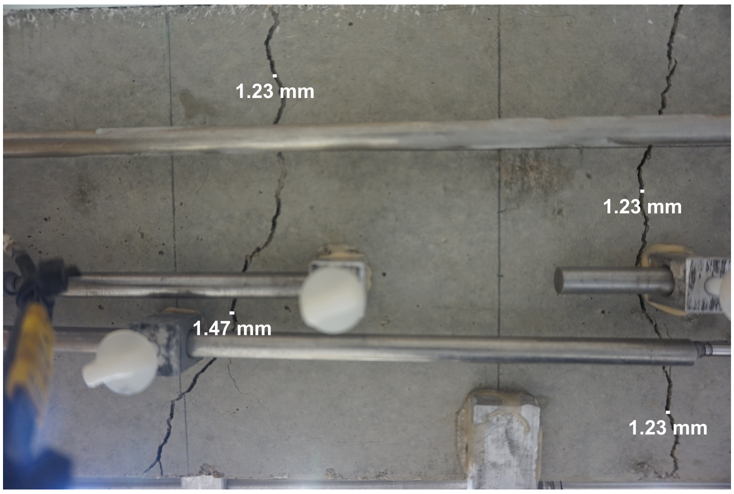

Figure 3.36: Image of the crack-width measured using Image J on the bottom side of CC beam (Load step 60 kN)

Visual Inspection

Visual inspection is also carried out during the testing of the beam specimens. A standard crack-width measurement scale is used for this. For every load step of 5 kN, the cracks visible to eye are measured using the measurement scale as shown in Figure 3.37.

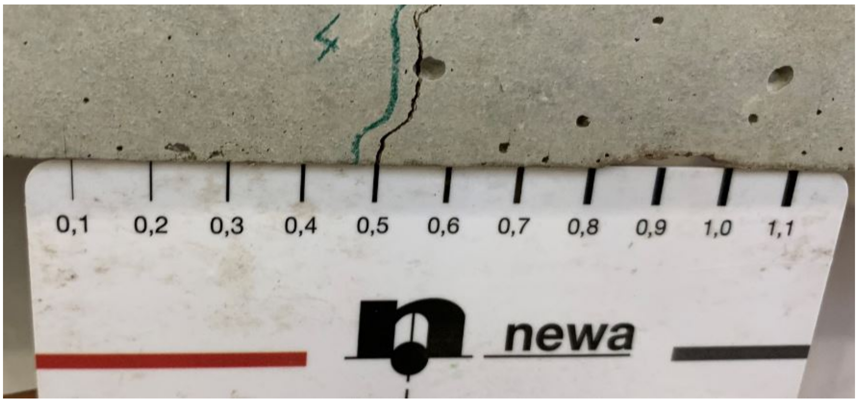

Figure 3.37: Measurement of cracks using crack-width scale

3.6 Results and Discussion

The four-point bending test performed gives the load bearing capacity of the beam specimens with varying interface and the fiber used in SHCC. Using GOM correlate, the images taken during testing are post-processed. The cracking behaviour is studied and the crack-widths are calculated.

The first subsection consists of:

1. Figures indicating the cracking pattern of all the beam specimens on the two side faces (LVDT side & DIC side) and bottom face.

2. Graphical plots of load vs deformation vs maximum crack-width for all the six beam specimens along with the load at which the maximum crack-width at SLS (0.3 mm) is reached.
   In the post-processing section, it is mentioned that the crack-widths are measured at three sections placed at 1 mm, 69 mm and 71 mm from the bottom edge of the beam. However, it was observed that upon calculating crack-widths at these three sections, the maximum value was obtained always at the section 1 mm above the bottom edge of the beam specimens tested. Hence, in the plots of load vs deformation vs maximum crack-width, the values calculated at a section 1 mm above the bottom edge of the beam specimen are only indicated.

3. Tabulated properties of the beam specimen in the constant moment region after cracking.

4. A step-by-step propagation of cracks along with the measured crack-widths in CC and SHCC layers.
   Since this study mainly focuses on crack-width control at SLS (maximum 0.3 mm), the crack-width range in plots indicating the step-by-step propagation of crack-width is limited to 0.5 mm even though crack-widths of size greater than 0.5 mm exist. This is done to check explicitly the exact load steps at which the crack localises i.e the crack-width exceeds 0.3 mm. However, crack-widths above the range of 0.5 mm are shown separately since they are very few and occur at higher load steps.

5. The graphical validation plots obtained by using Image J, visual inspection and comparison with LVDT deformations.

The second subsection is a comparative study of the behaviour in terms of load at which the maximum allowable crack-width at SLS is reached for all the beam specimens with varying interfaces. The final subsection provides a detailed discussion on the behaviour observed in the beam specimens with variable interface and the fiber used in SHCC.

3.6.1 Results: Bearing Capacity and Crack-width Control

3.6.2 Conventional Concrete Beam (CC)

Upon application of the load on the beam specimen of grade C30/37 in a four-point bending set-up, the load vs deformation vs maximum crack-width obtained is plotted as shown in Figure 3.38. The maximum crack-width shown in Figure 3.38 is determined by correlating the images on GOM correlate software tool. Table 3.6 gives information on the various properties of CC beam specimen after testing is complete.

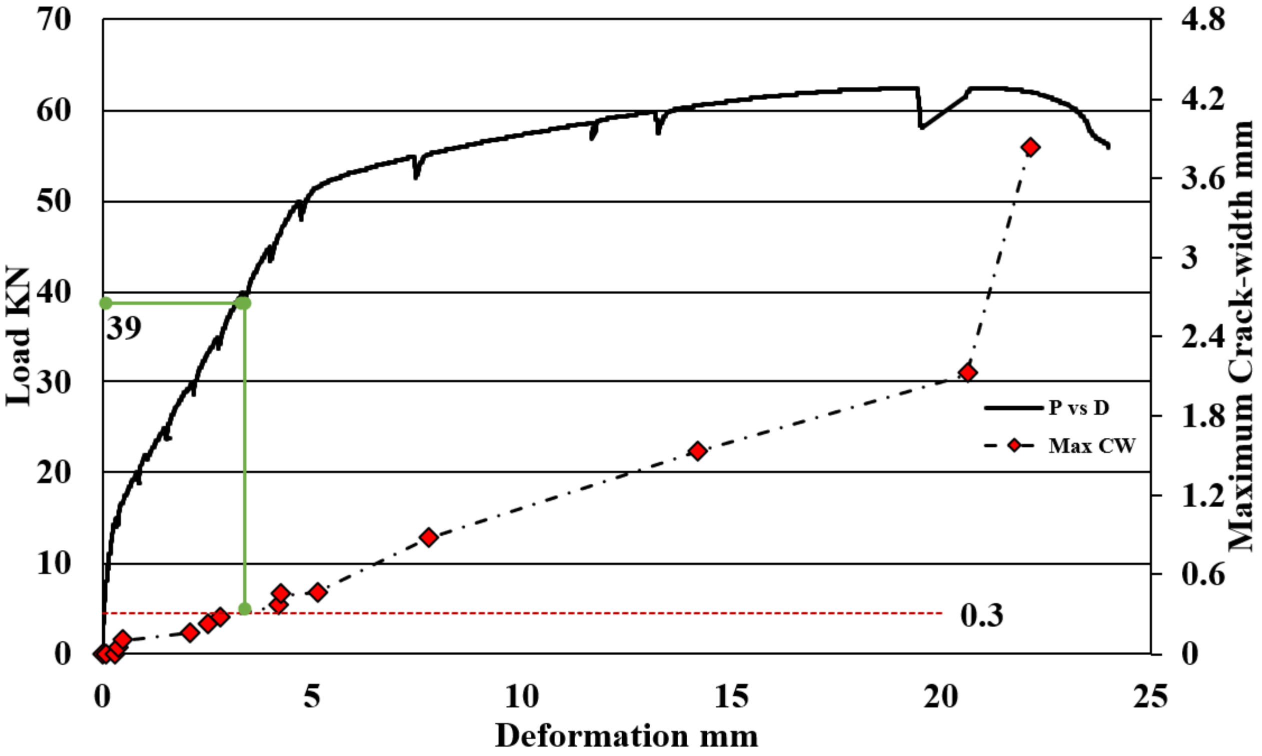

Figure 3.38: Load (P) vs Deformation (D) vs Maximum crack-width (Max CW)

Table 3.6: Properties of CC beam specimen in constant moment region after testing

Property	**Value**
Number of cracks	4
Average spacing between cracks	124.89 mm
Maximum load	62 KN
Maximum deformation	22.12 mm
Maximum crack-width	3.82 mm
Load at crack-width of 0.3 mm	39 KN

The initial cracks appear at a load step of 15 KN indicated within the circle shown in Figure 3.39a. The plot of ε_x at this load step shows a sudden jump in the strain value indicating a crack. At the last load step , four localised cracks are observed reaching an average height of 160 mm in a 200 mm high specimen as shown in Figure 3.39. Figure 3.40 shows the cracking pattern on three sides of the CC beam specimen.

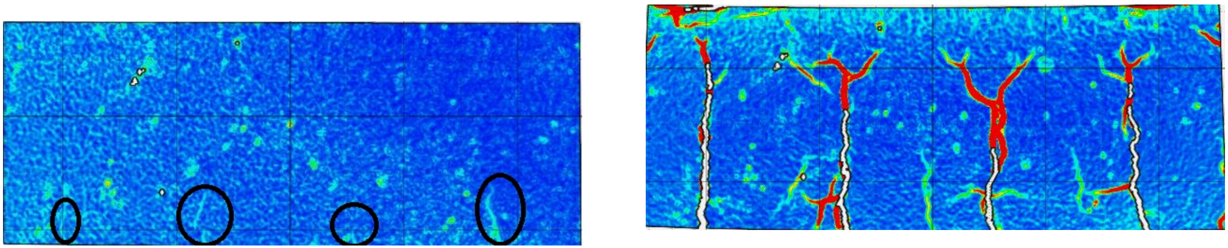

(a) First crack in CC specimen at a load step of 15 KN

(b) Localised cracks in CC specimen at last load step (60 KN)

Figure 3.39: Cracking in CC specimen

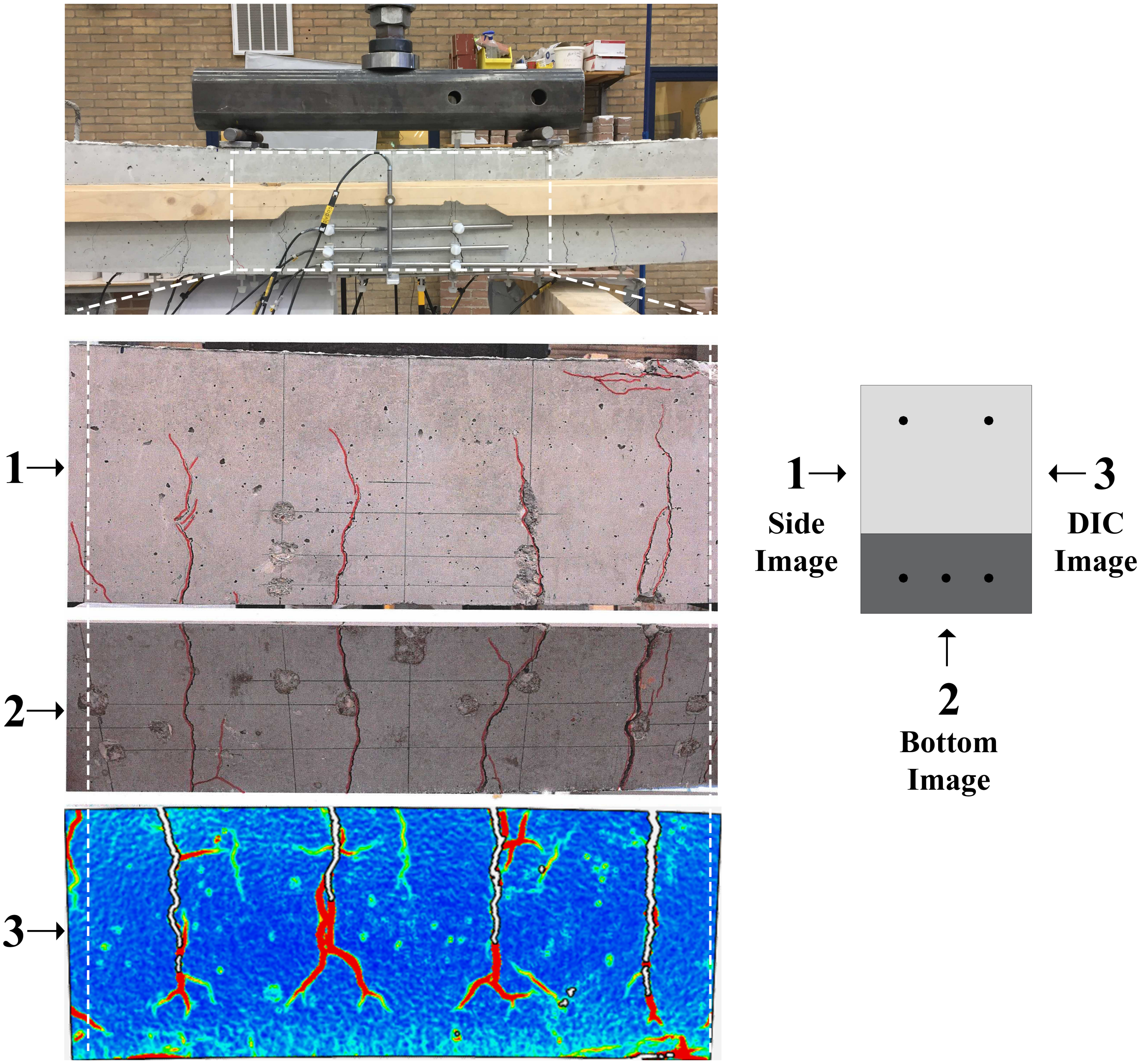

Figure 3.40: 1-LVDT side, 2-Bottom side and 3-DIC side of CC beam specimen

A step-by-step propagation of cracks along with the crack-width for all the load steps applied to the CC beam specimen is shown in Figures 3.41 to 3.52. The crack-widths are measured at the section indicated in Figures 3.41 to 3.52 and labelled next to the cracks. The labelled crack-widths are in millimeters (mm).

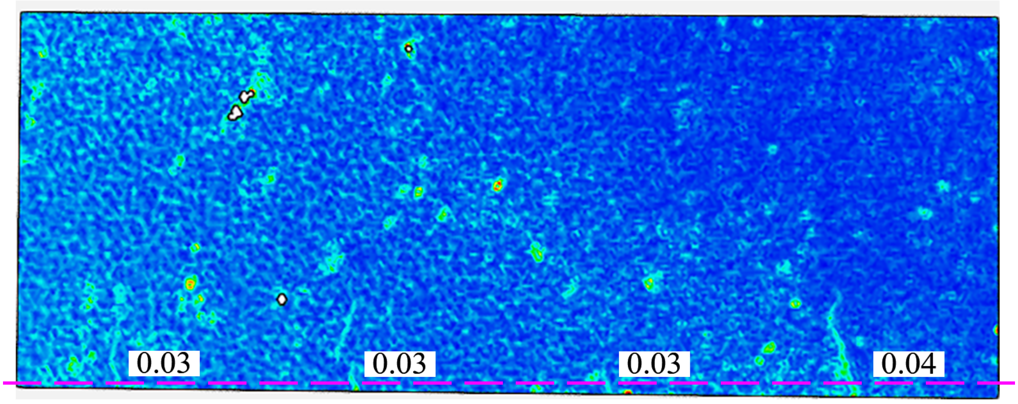

Figure 3.41: Development of cracks at load step 15 KN

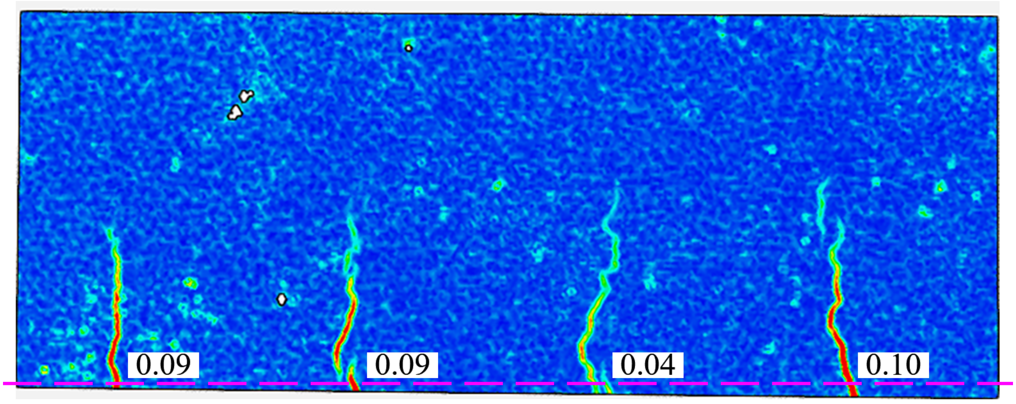

Figure 3.42: Development of cracks at load step 20 KN

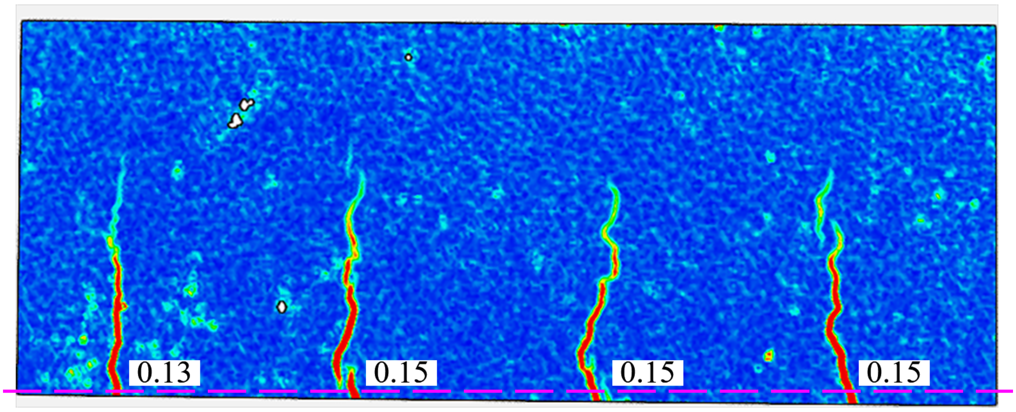

Figure 3.43: Development of cracks at load step 25 KN

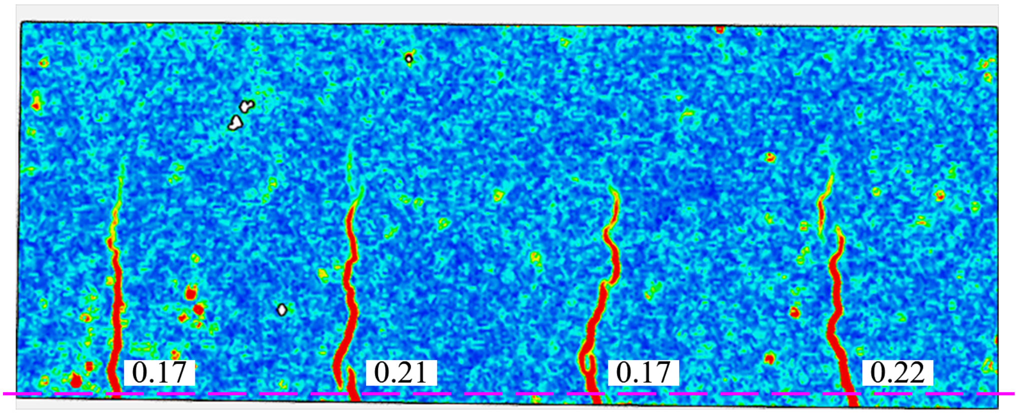

Figure 3.44: Development of cracks at load step 30 KN

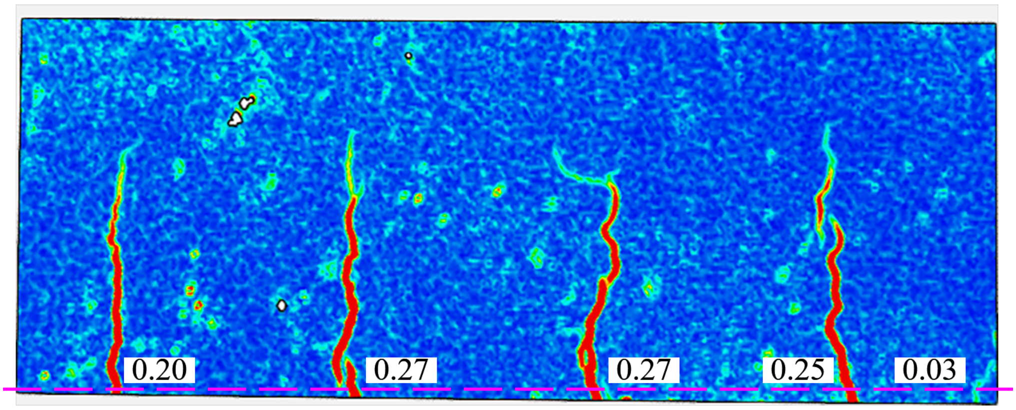

Figure 3.45: Development of cracks at load step 35 KN

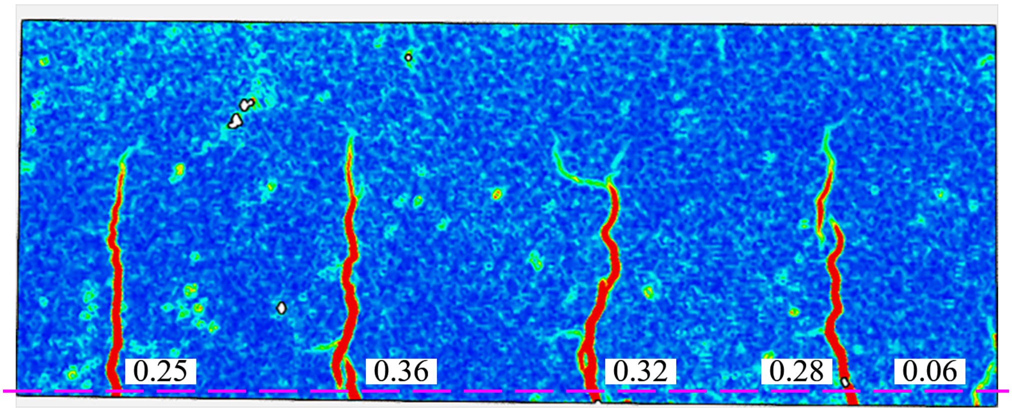

Figure 3.46: Development of cracks at load step 40 KN

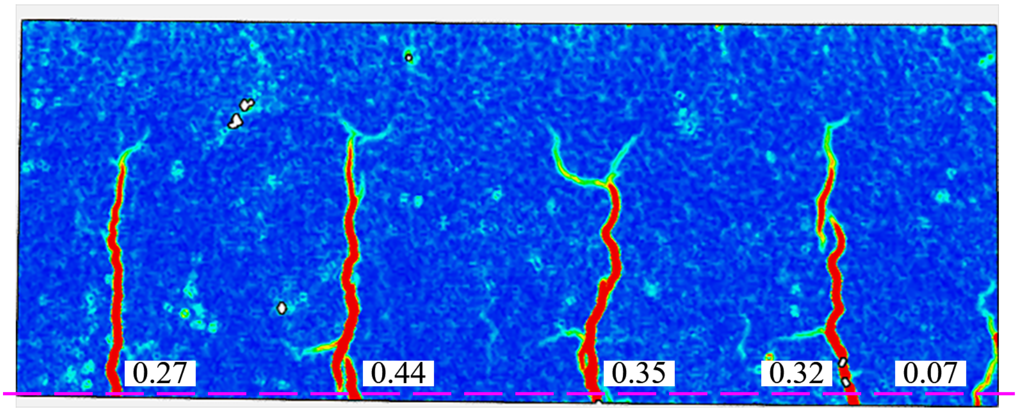

Figure 3.47: Development of cracks at load step 45 KN

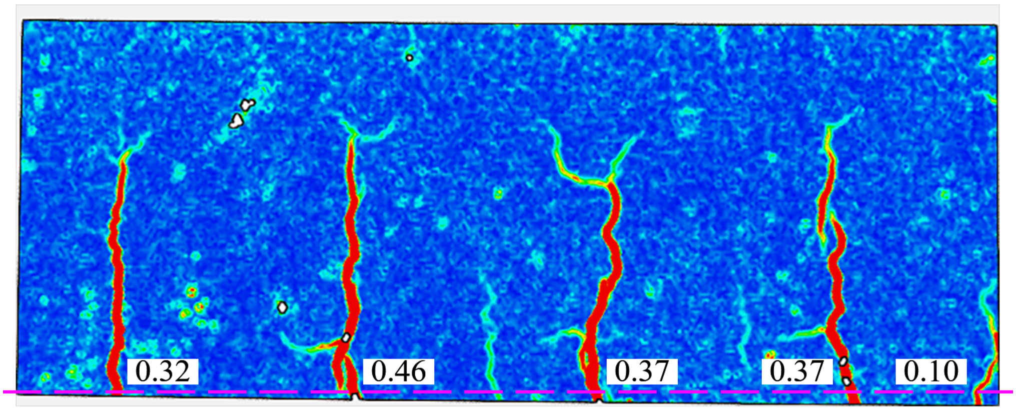

Figure 3.48: Development of cracks at load step 50 KN

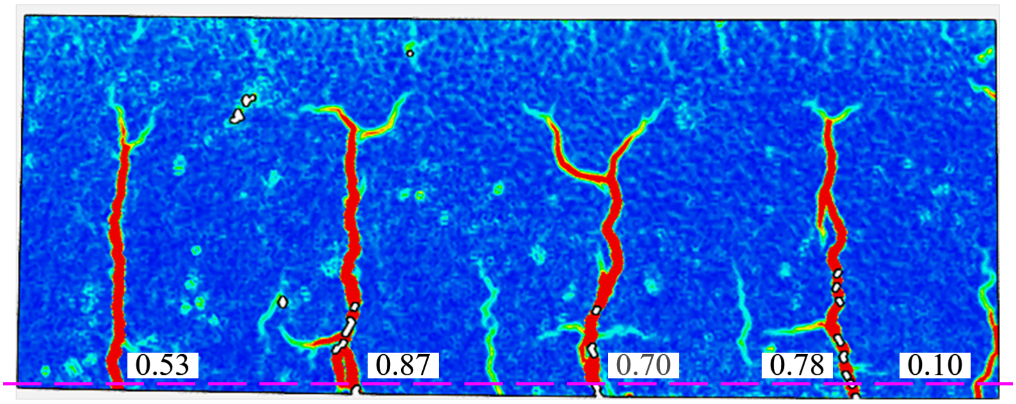

Figure 3.49: Development of cracks at load step 55 KN

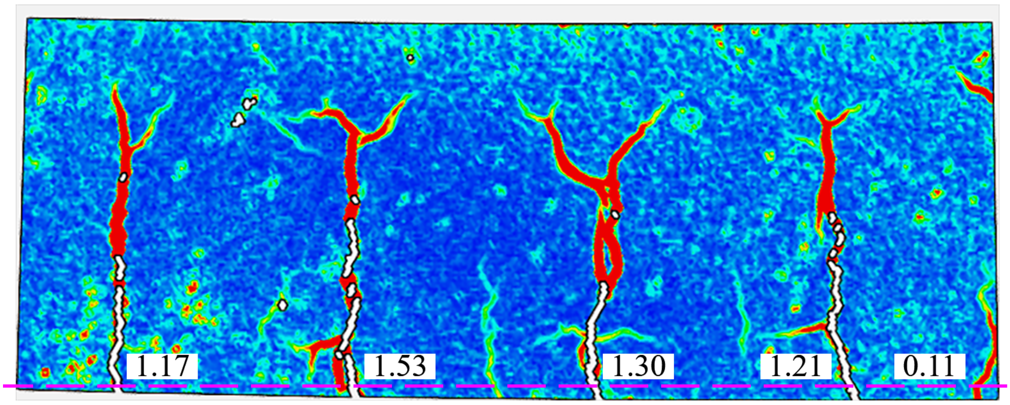

Figure 3.50: Development of cracks at load step 60 KN

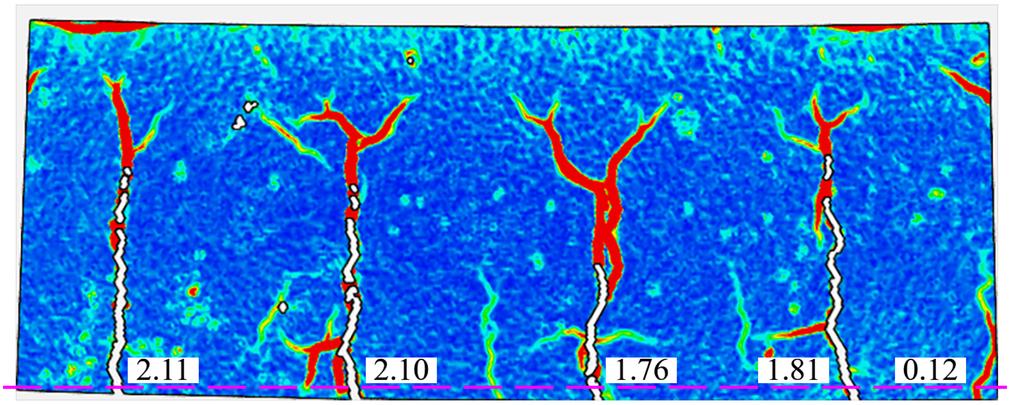

Figure 3.51: Development of cracks at load step 62 KN

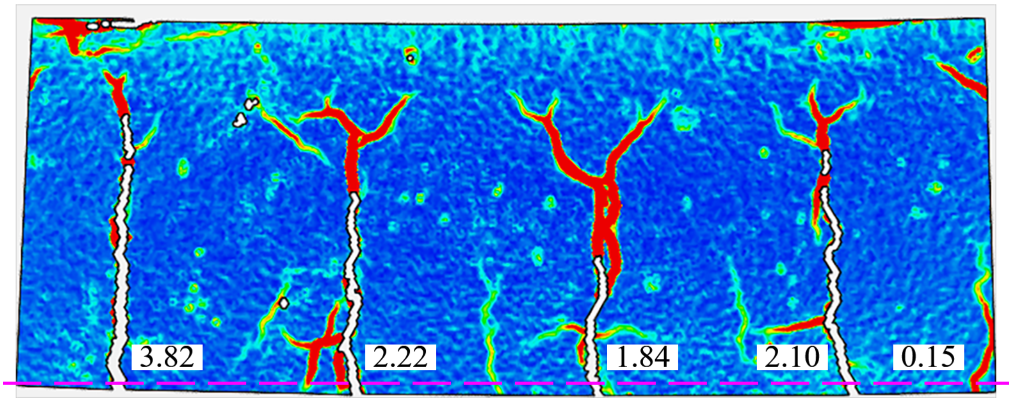

Figure 3.52: Development of cracks at load step 60 KN

To validate the values of maximum crack-width obtained using GOM correlate, a comparison with the maximum crack-width calculated using Image J and visual inspection is shown in Figure 3.53. It can be seen that the maximum crack-width plot of GOM correlate and Image J are over-lapping at few points. Whereas, the results of visual inspection show an underestimation when compared to other results. Determination of crack-width by eye-view using measurement scale is prone to errors as it is based on the individual's observation skill and intuition and also the crack-widths developed on the two faces of the specimen need not be the same. The deformations measured using GOM correlate are calibrated with the deformations measured using LVDTs as shown in Figure 3.54.

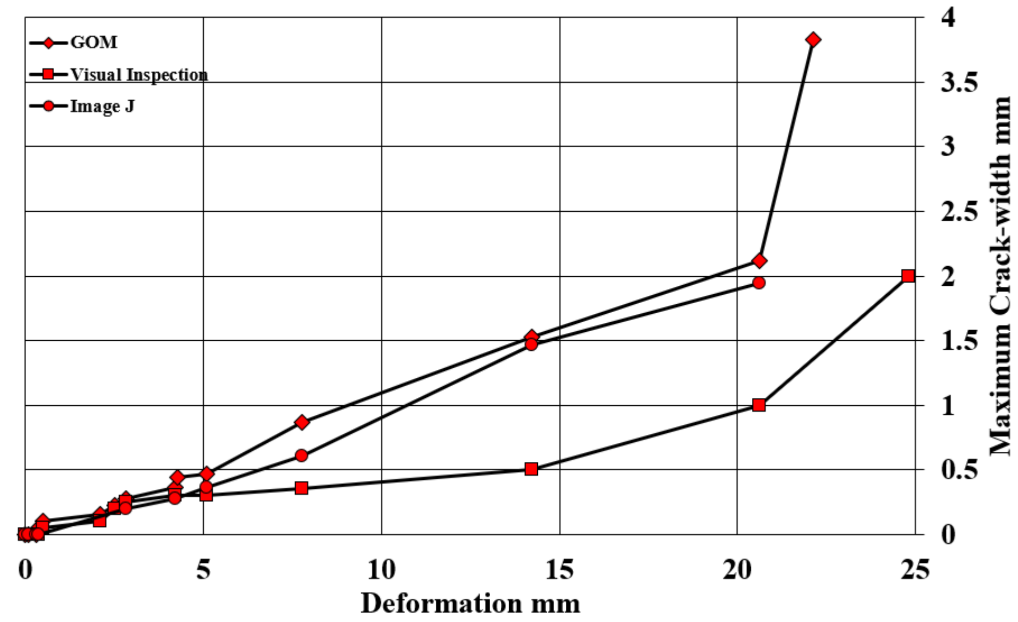

Figure 3.53: Comparison of maximum crack-widths measured using GOM, Image J and Visual Inspection

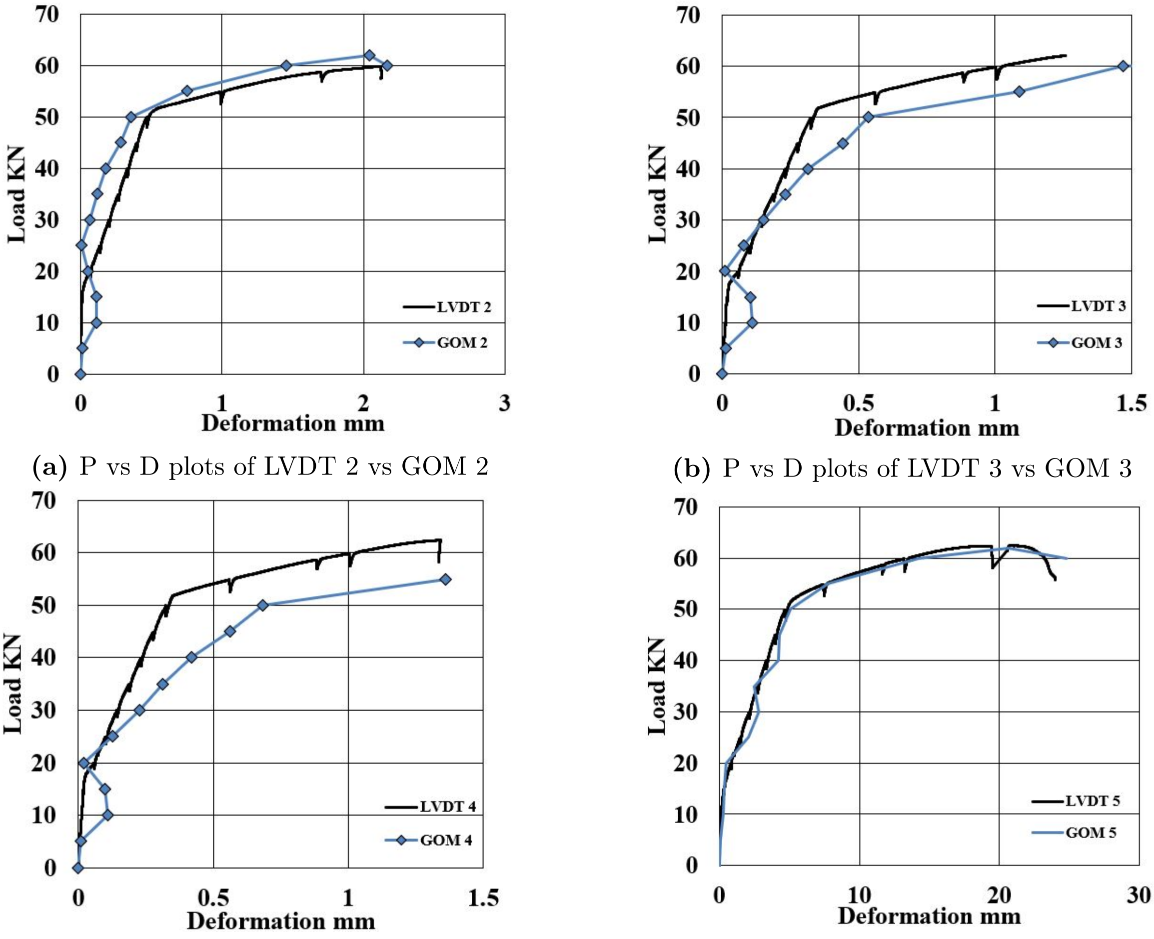

(a) P vs D plots of LVDT 2 vs GOM 2

(b) P vs D plots of LVDT 3 vs GOM 3

(c) P vs D plots of LVDT 4 vs GOM 4

(d) P vs D plots of LVDT 5 vs GOM 5

Figure 3.54: Calibration plots of GOM deformation with LVDT deformation

3.6.3 Hybrid Beam with Smooth Interface (S-PVA)

Unlike the conventional concrete beam, the maximum crack-width is measured at three sections, i.e, 1 mm, 69 mm, 71 mm from the bottom edge of the beam. The load vs deformation vs maximum crack-width plot is shown in Figure 3.55. A tabulation indicating the properties of the beam specimen in the constant moment region after maximum loading is shown in Table 3.7.

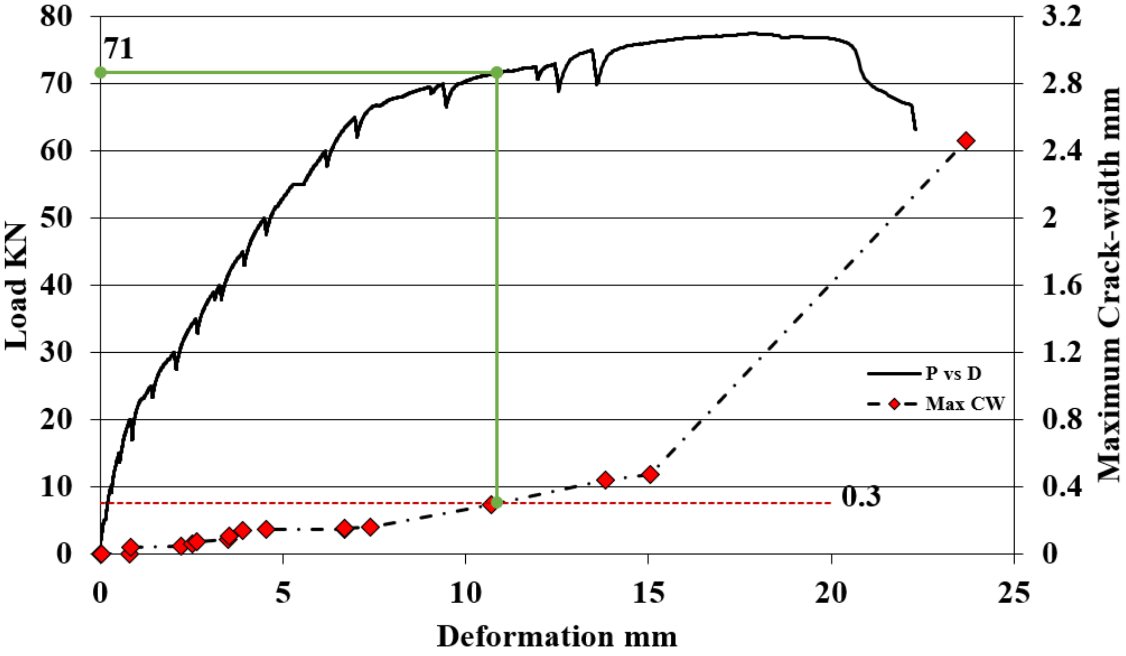

Figure 3.55: Load (P) vs Deformation (D) vs Maximum Crack-Width (Max CW)

Table 3.7: Properties of S-PVA beam specimen in constant moment region after testing

Property	Value
Number of cracks in the concrete layer	7
Average spacing between cracks	79.95 mm
Maximum load	77 KN
Maximum deformation	22.30 mm
Maximum crack-width	2.46 mm
Load at crack-width of 0.3 mm	71 KN

It was observed that the initial cracks appeared at a load step of 10 KN in the SHCC layer as seen in Figure 3.56a. This is validated by observing a jump in strain ε_x measured in section located at 1 mm from the bottom edge of the beam. The initial cracks in the concrete layer are observed at a load step of 15 KN as seen in Figure 3.56b, again validated by the jump in strain ε_x measured at section 3 located at 71 mm from the bottom edge of the beam. Cracking or delamination of the interface is first observed at a load step 55 KN as seen in Figure 3.56c. At the final load step of 77 KN, it can be seen that the cracks are uniformly distributed throughout the length of the specimen in the SHCC layer indicating that sufficient debond length at the interface is available for the cracks to be uniformly distributed as shown in Figure 3.56d. Figure 3.57 shows the cracking pattern in a smooth interface specimen with PVA fibers on the LVDT side, bottom side and DIC side.

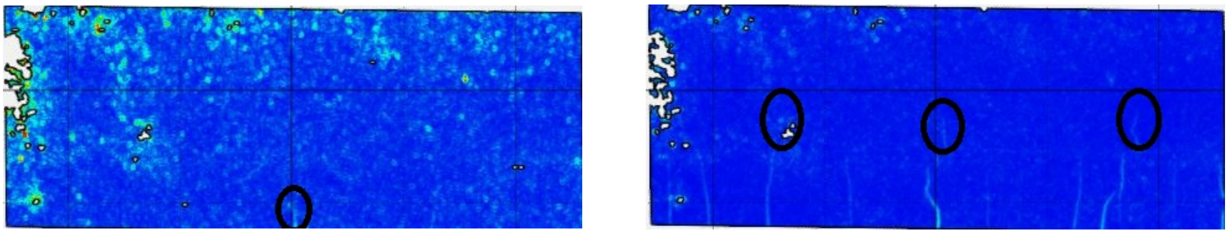

(a) First crack in SHCC layer at a load step of 10 KN **(b)** First crack in CC layer at a load step of 15 KN

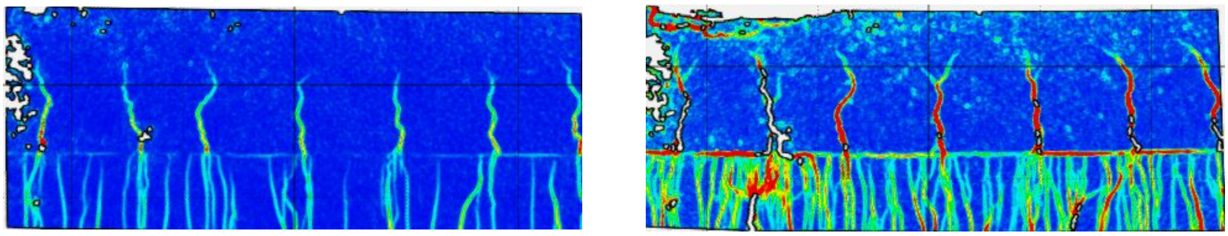

(c) Cracking at the interface first observed at 55KN **(d)** Cracks in SHCC and CC layers at last load step

Figure 3.56: Cracking in S-PVA specimen

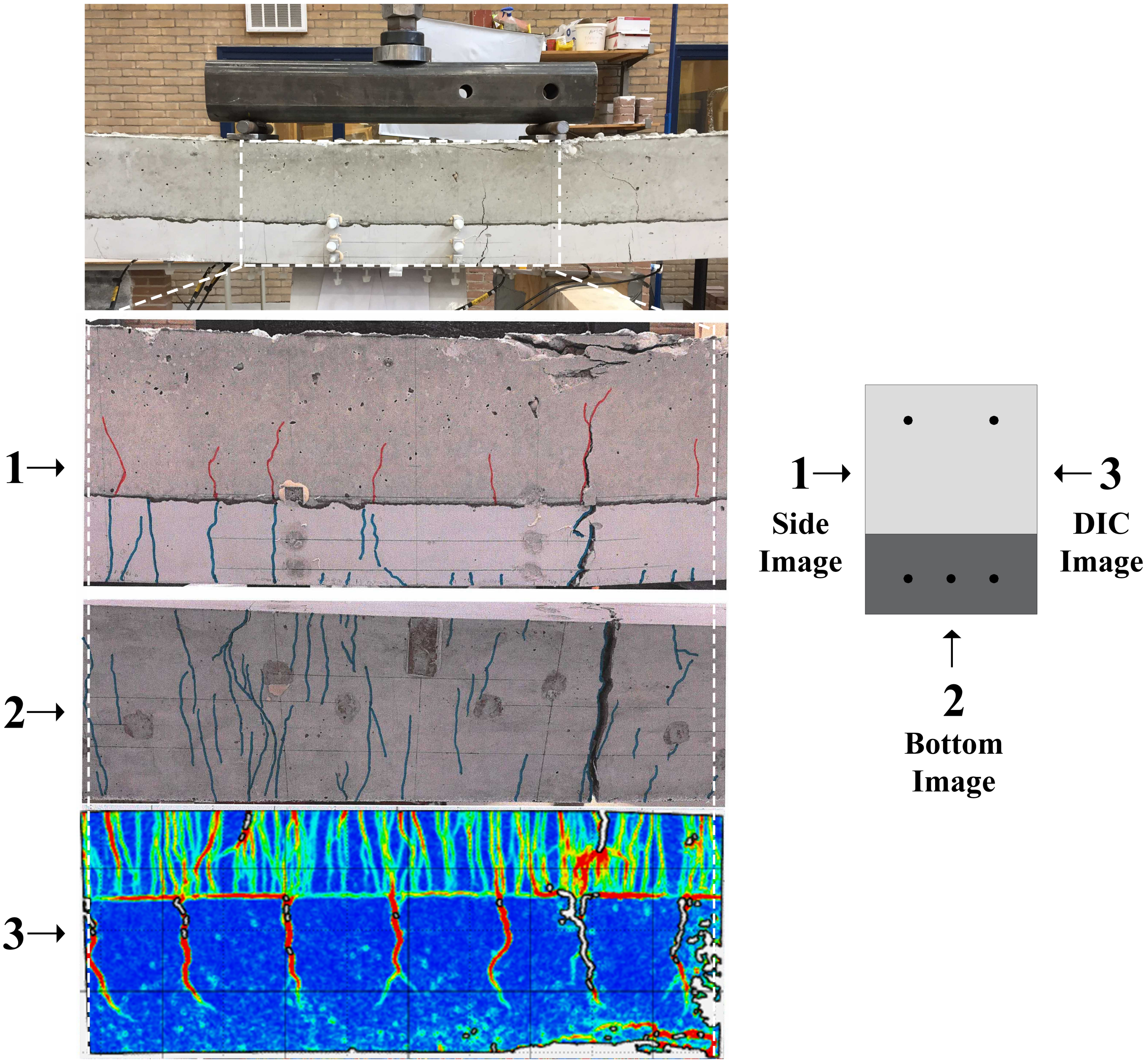

Figure 3.57: 1-LVDT side, 2-Bottom side and 3-DIC side of S-PVA beam specimen

A step-by-step propagation of cracks along with an increase in the crack-width for all the load steps applied to the S-PVA beam specimen is shown in Figures 3.58 to 3.72. The crack-widths are measured in the SHCC layer and concrete layer at the section indicated in all figures from 3.58 to 3.72. Since number of cracks in the concrete layer are less, the crack-width at every load step is labelled next to the cracks itself. However, the number of cracks in the SHCC layer are too many to be individually labelled and so a scatter plot indicating the crack-width of various cracks is shown for every load step. The cracks are measured at the two sections indicated in all the images. The labelled crack-widths are in millimeters (mm).

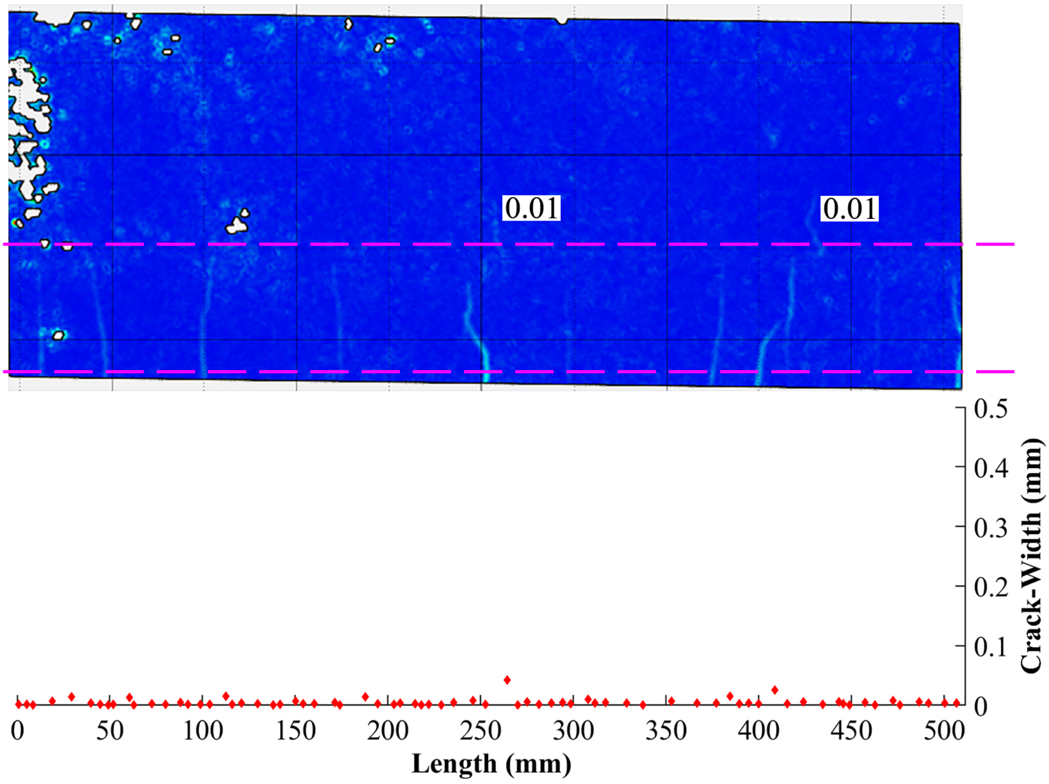

Figure 3.58: Development of cracks at load step 15 KN

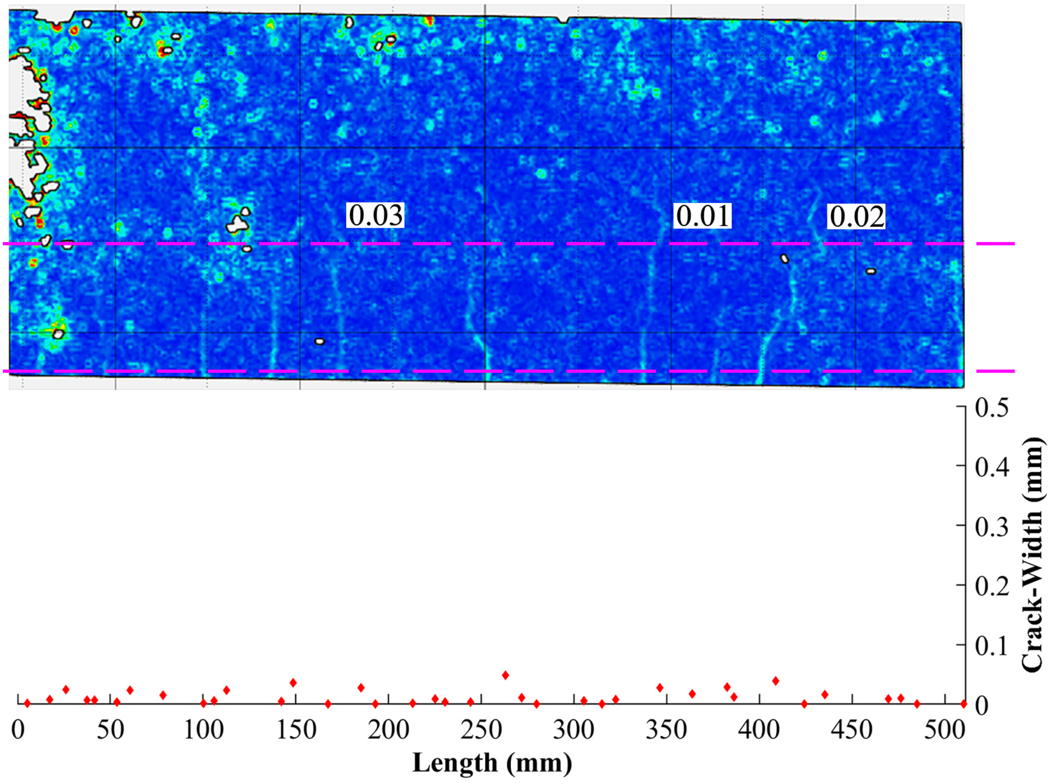

Figure 3.59: Development of cracks at load step 20 KN

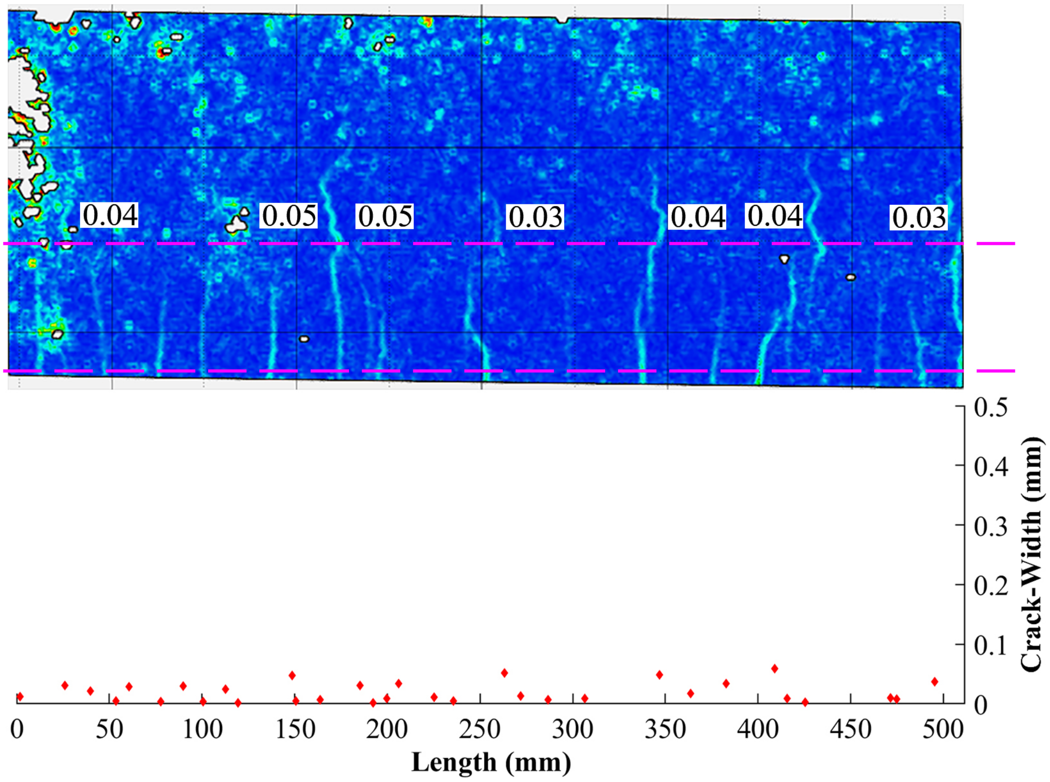

Figure 3.60: Development of cracks at load step 25 KN

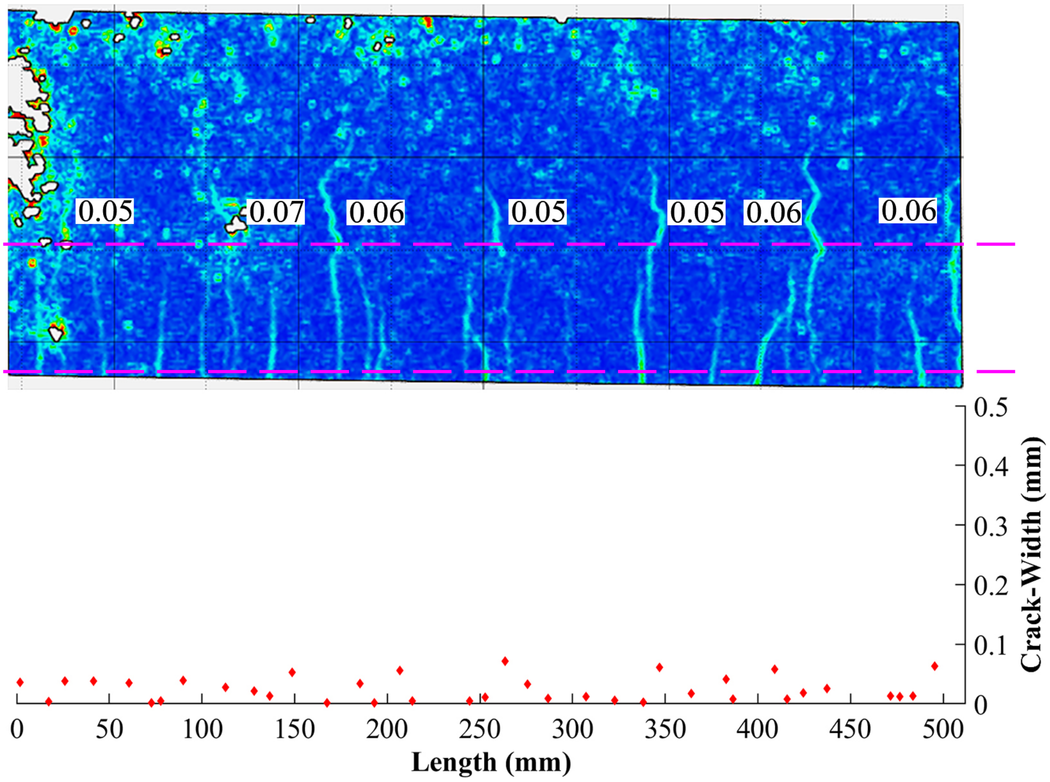

Figure 3.61: Development of cracks at load step 30 KN

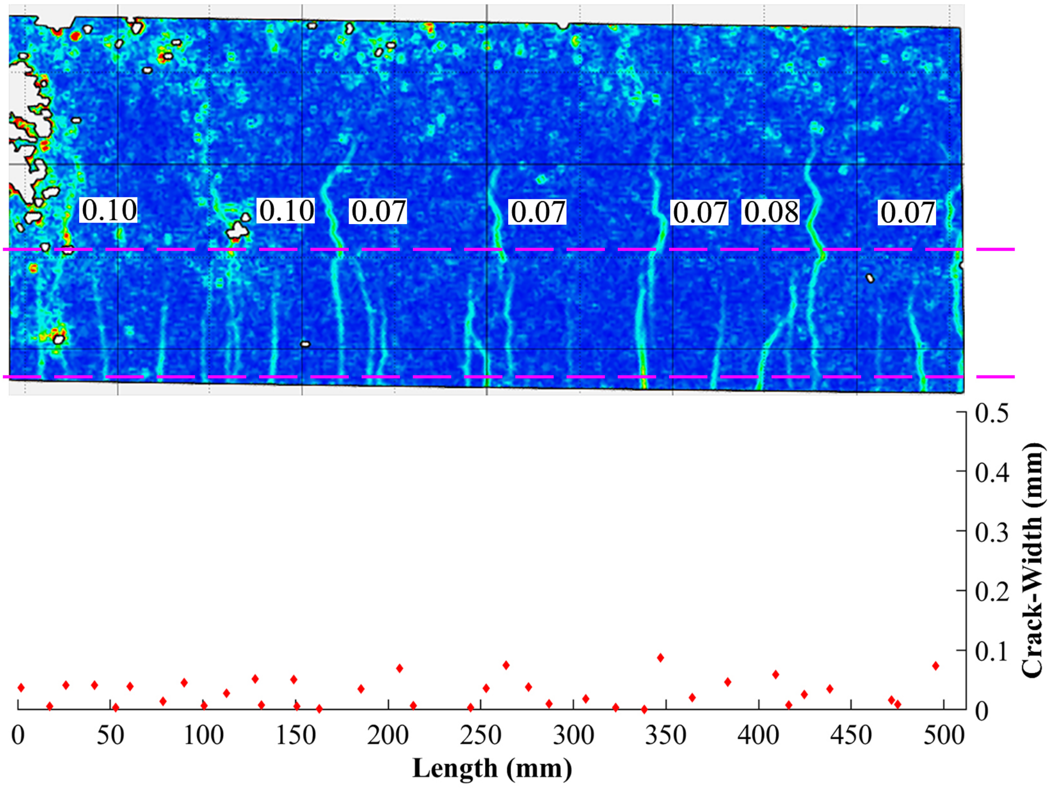

Figure 3.62: Development of cracks at load step 35 KN

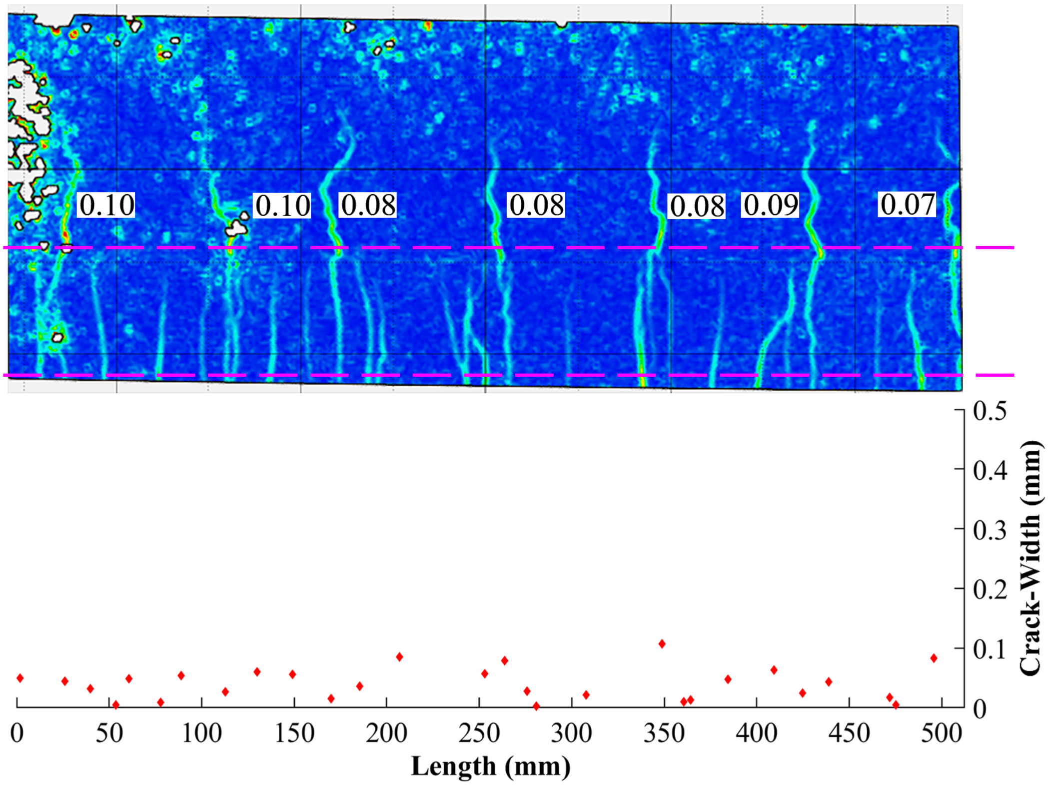

Figure 3.63: Development of cracks at load step 40 KN

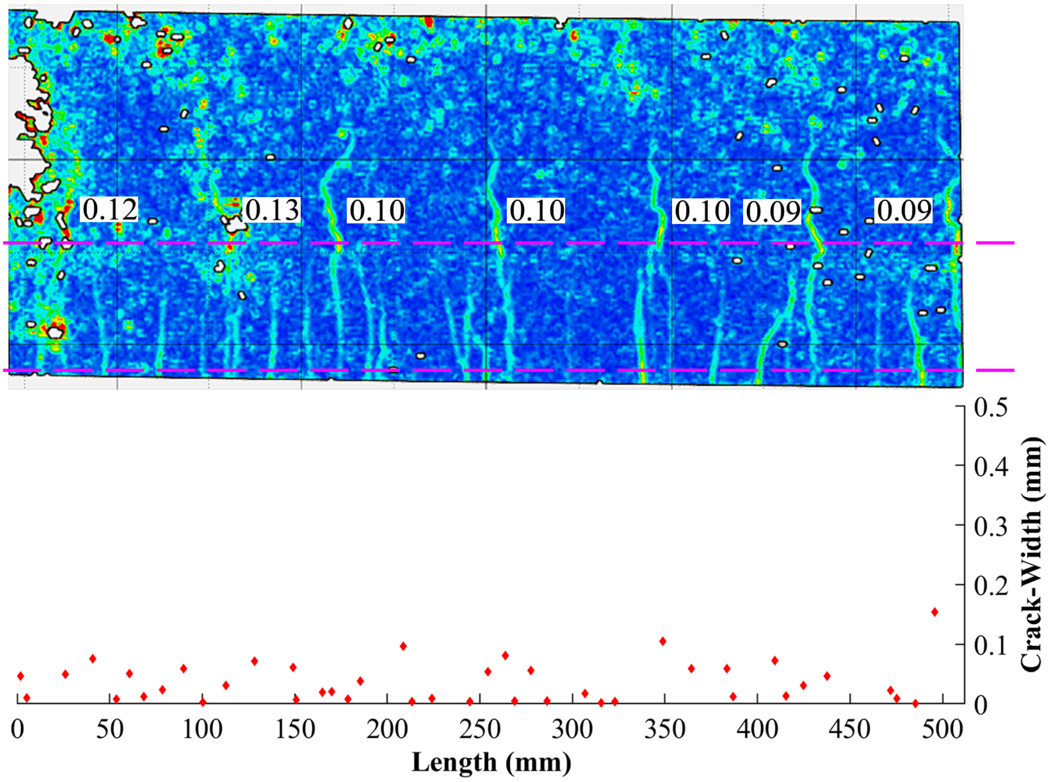

Figure 3.64: Development of cracks at load step 45 KN

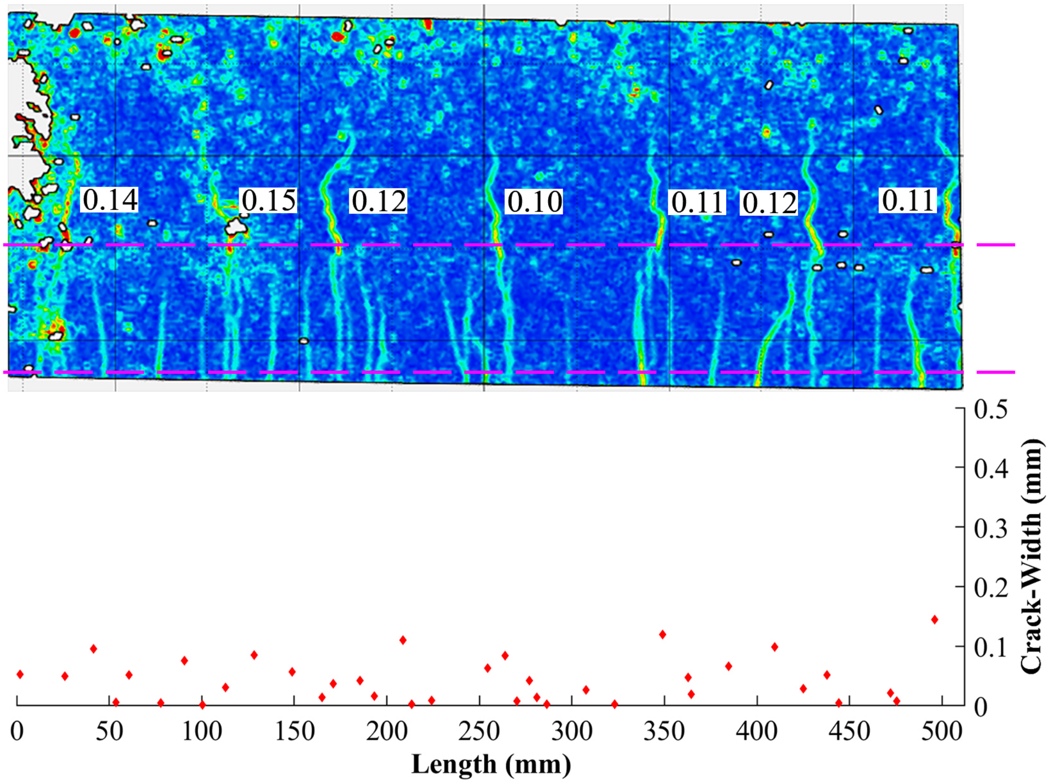

Figure 3.65: Development of cracks at load step 50 KN

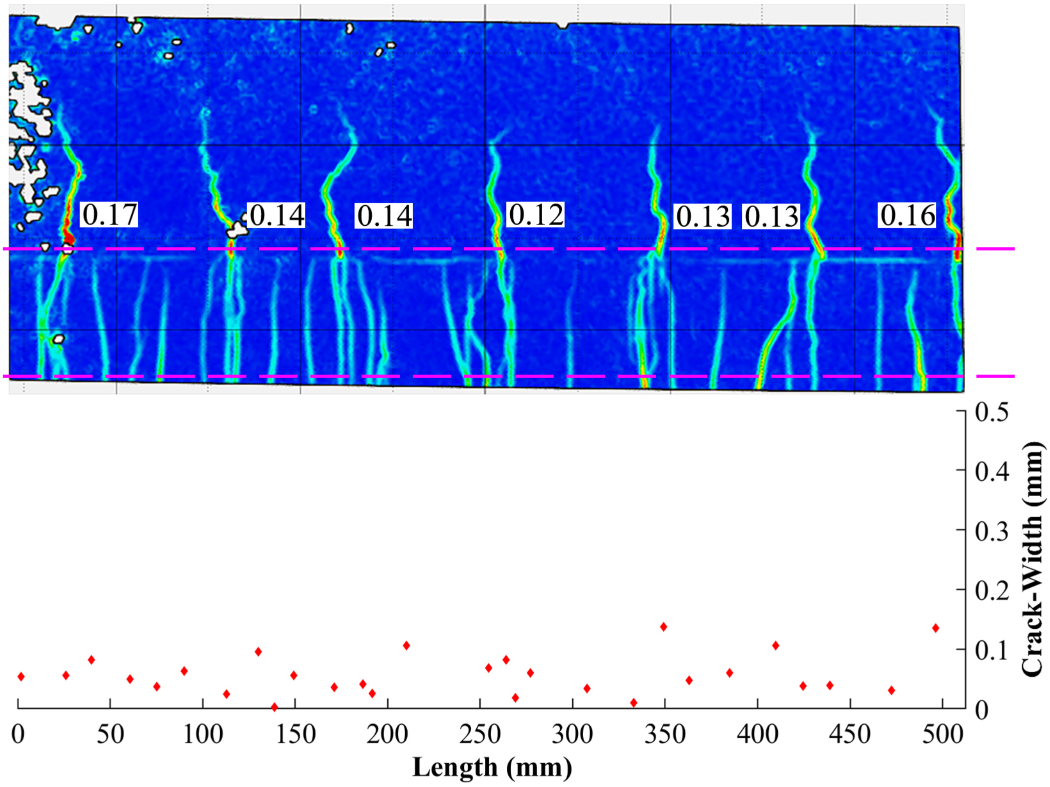

Figure 3.66: Development of cracks at load step 55 KN

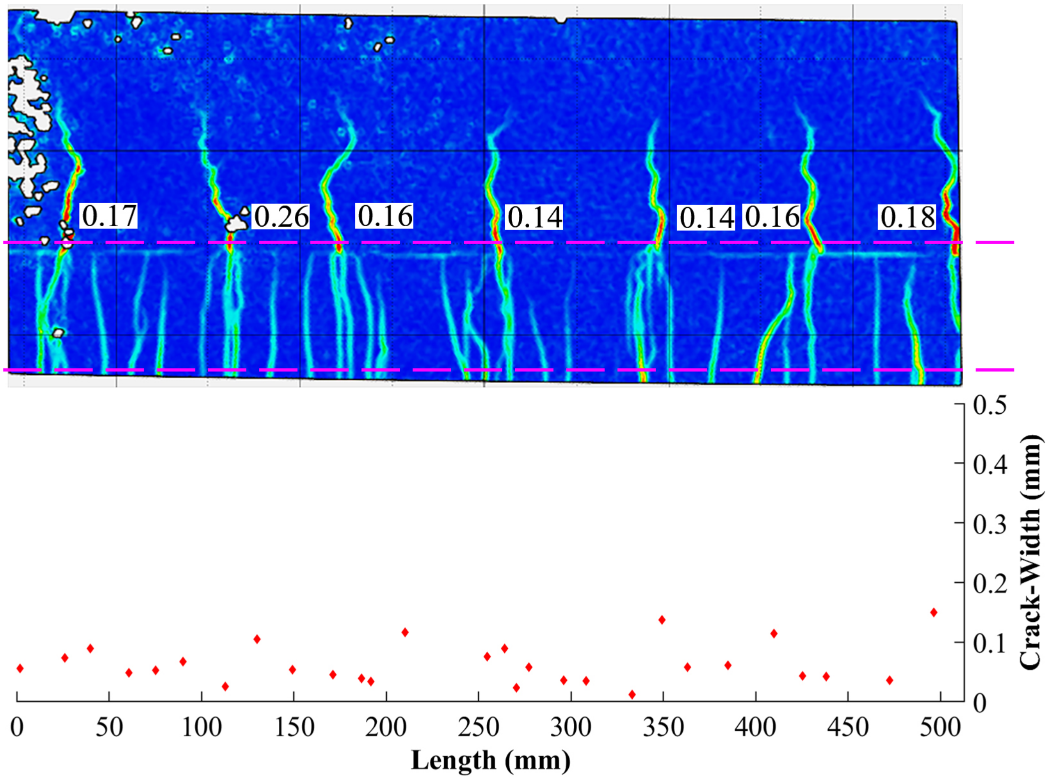

Figure 3.67: Development of cracks at load step 60 KN

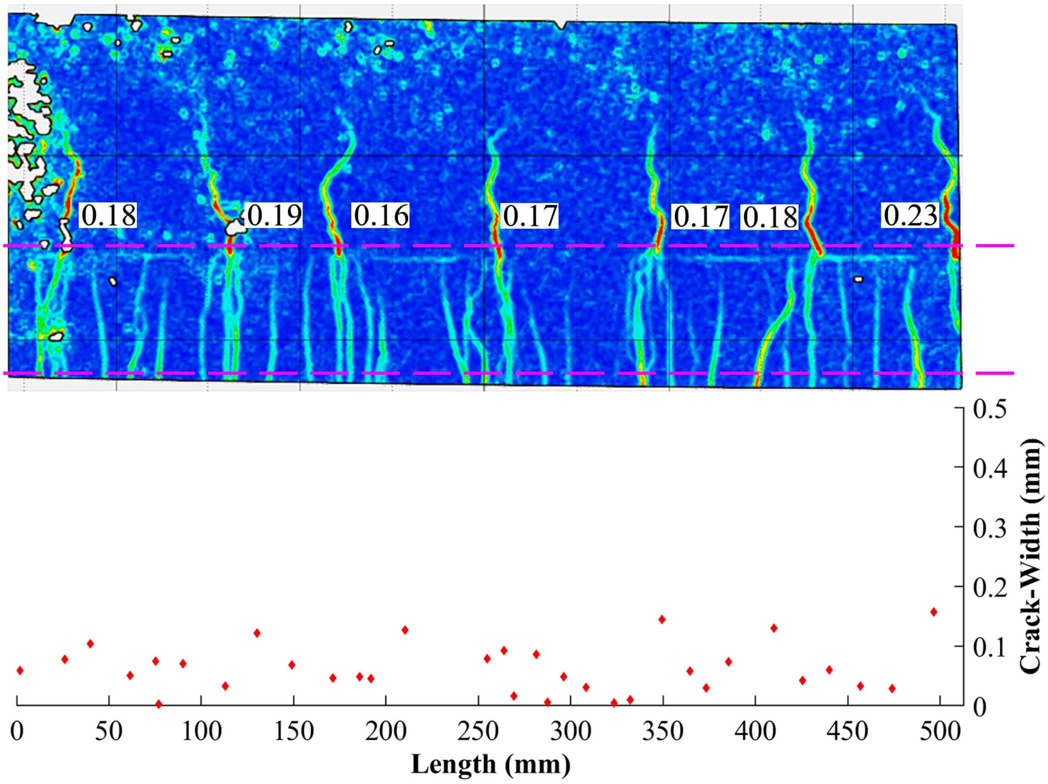

Figure 3.68: Development of cracks at load step 65 KN

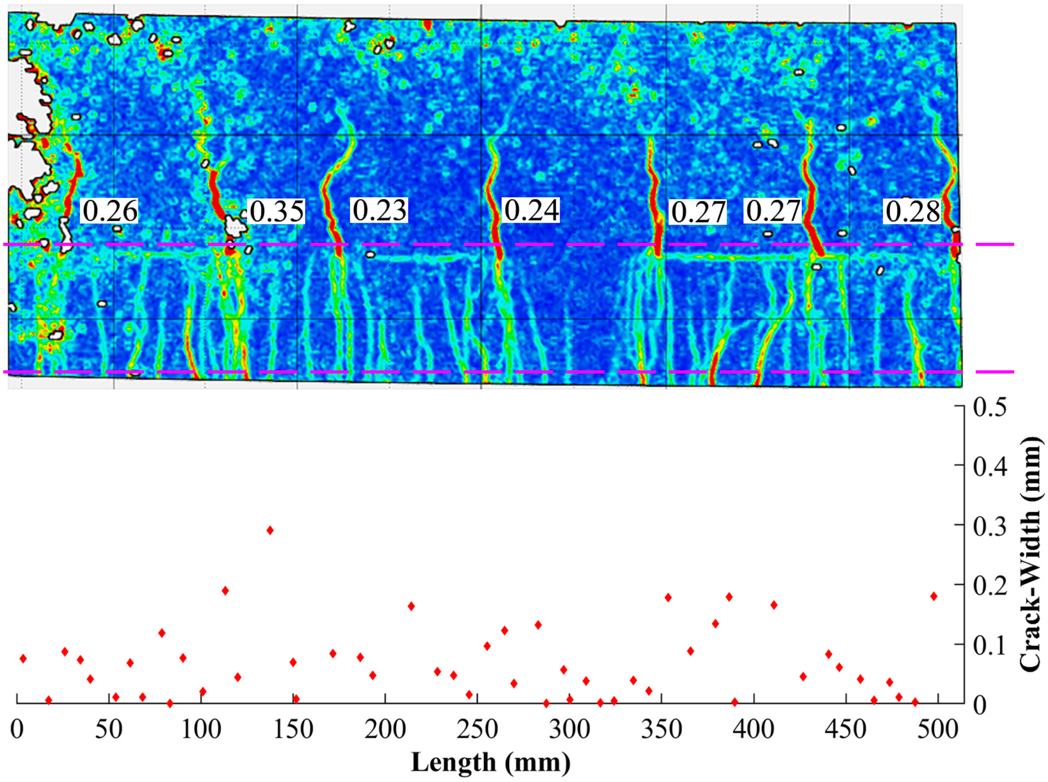

Figure 3.69: Development of cracks at load step 70 KN

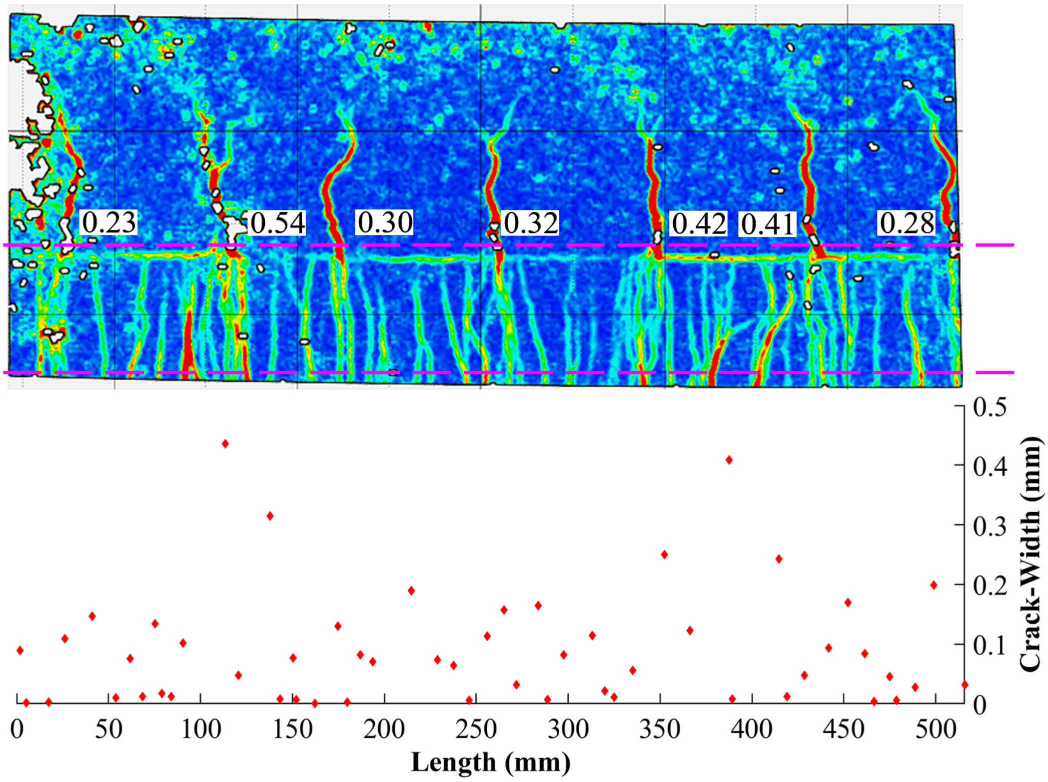

Figure 3.70: Development of cracks at load step 73 KN

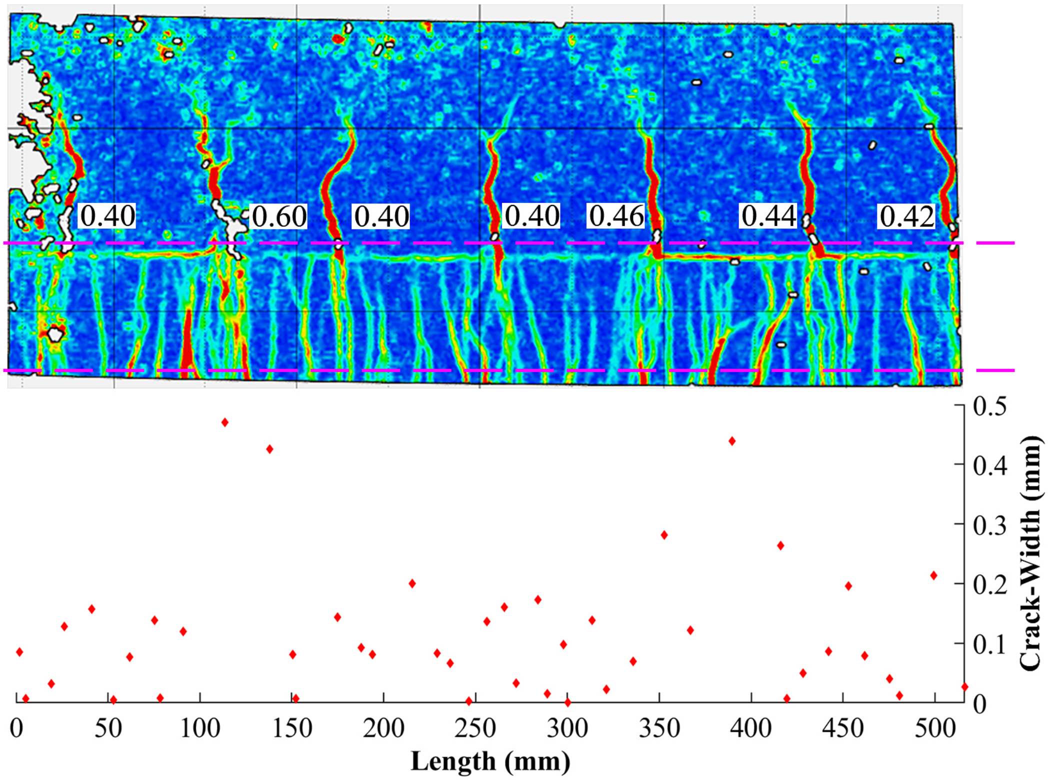

Figure 3.71: Development of cracks at load step 75 KN

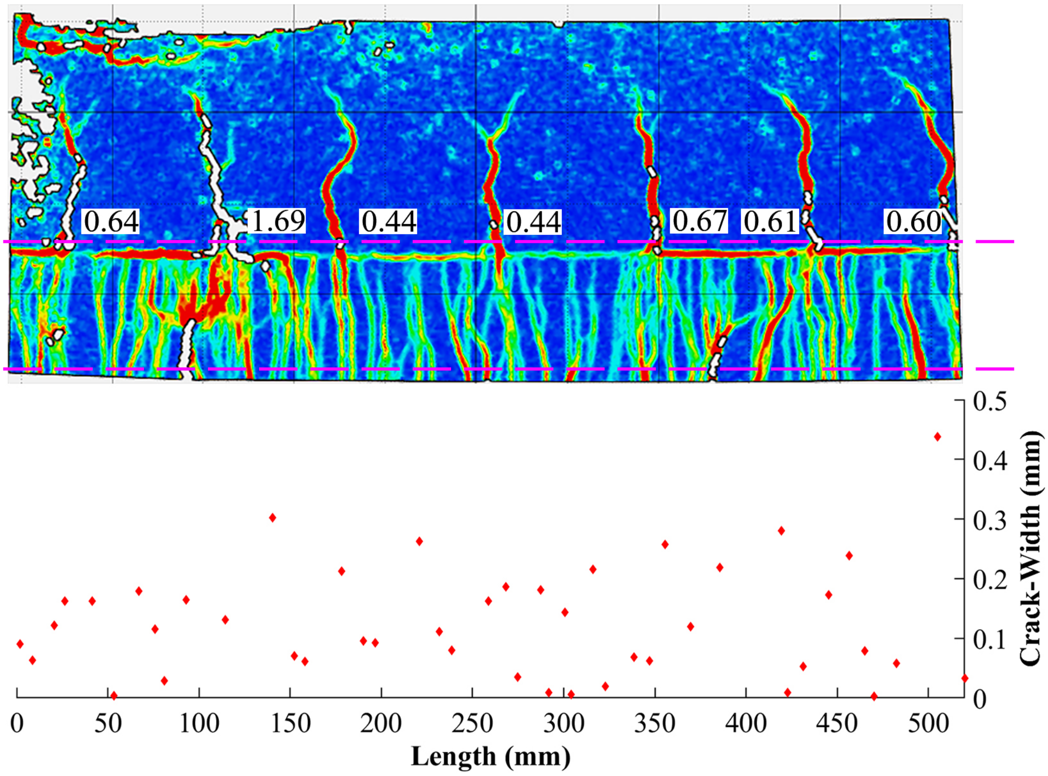

Figure 3.72: Development of cracks at load step 77 KN

At the last load step the measured crack-widths exceed 0.5 mm and are not shown in Figure 3.72 as the limit of the crack-width plots is set to 0.5 mm. Figure 3.73 shows the crack-width of all the cracks in the SHCC layer at the last load step.

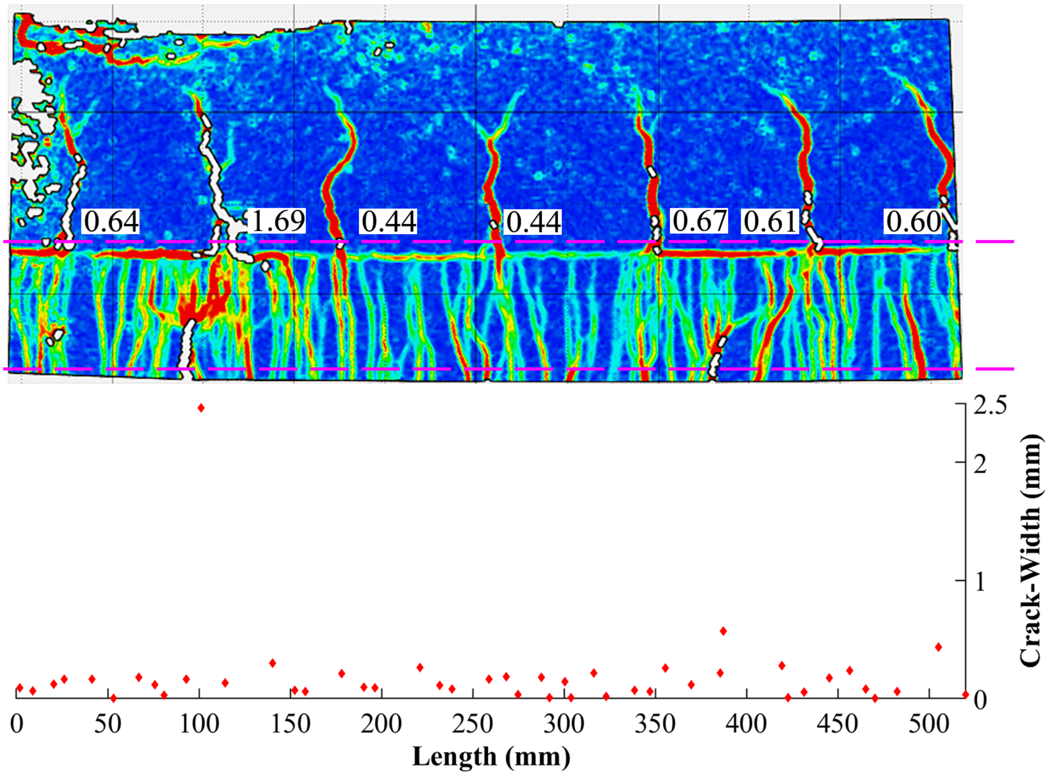

Figure 3.73: Development of large cracks at the last load step (77 KN)

The crack-widths measured in DIC are validated from the results obtained using Image J and visual inspection as shown in figure 3.74. The deformations measured using GOM correlate are calibrated with the deformations measured using LVDTs as shown in Figure 3.75.

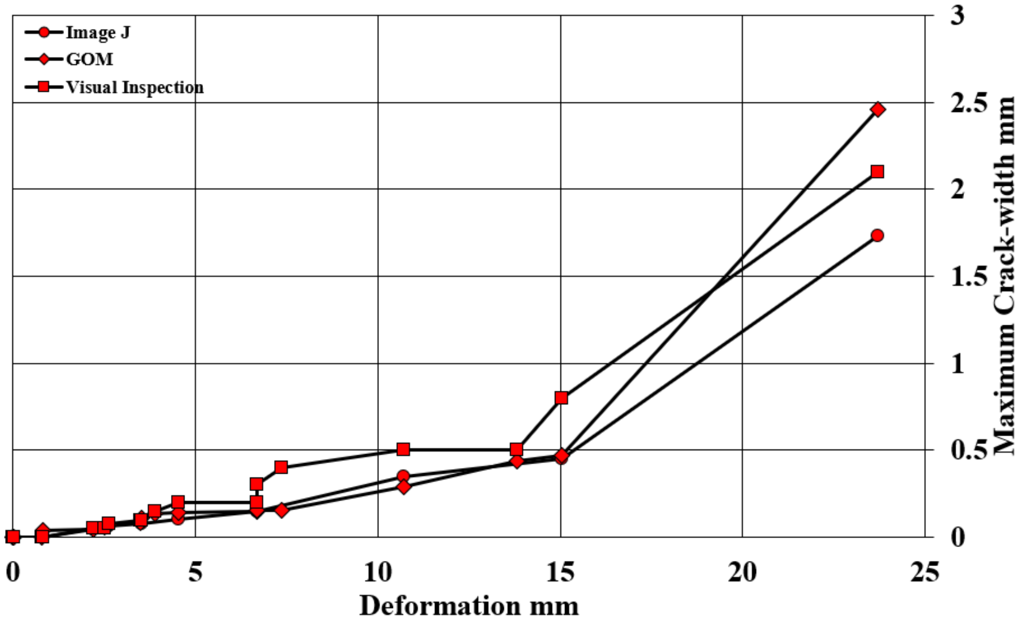

Figure 3.74: Comparison of maximum crack-widths measured using GOM, Image J and Visual Inspection

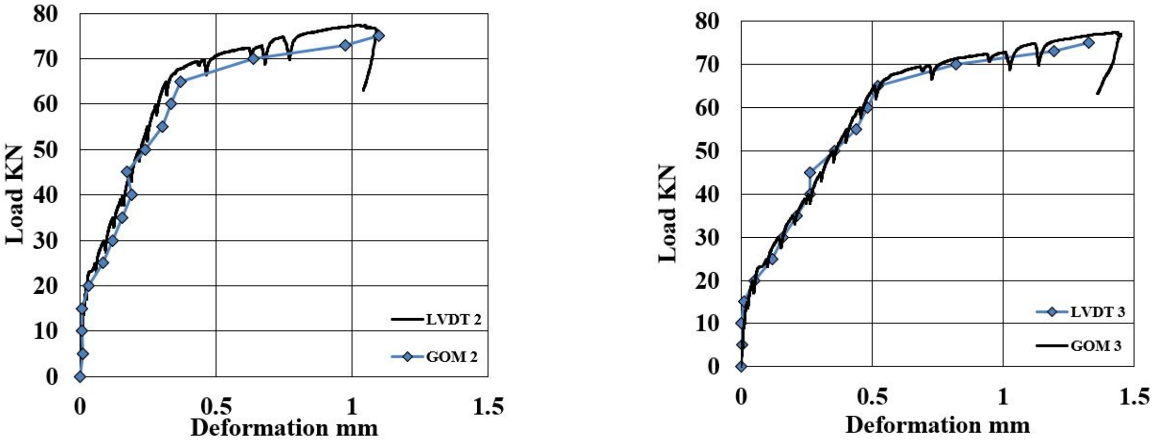

(a) P vs D plots of LVDT 2 vs GOM 2

(b) P vs D plots of LVDT 3 vs GOM 3

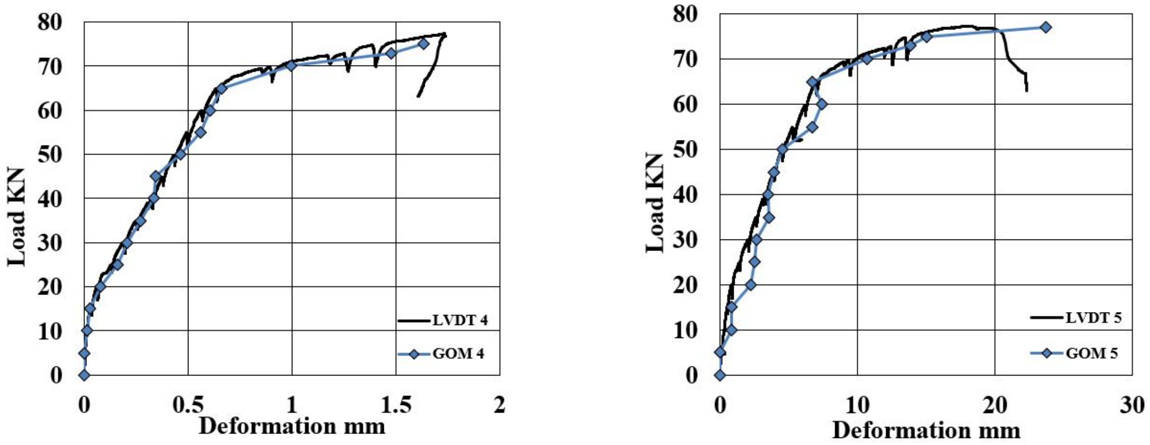

(c) P vs D plots of LVDT 4 vs GOM 4

(d) P vs D plots of LVDT 5 vs GOM 5

Figure 3.75: Calibration plots of GOM deformation with LVDT deformation

3.6.4 Hybrid Beam with Partially Delaminated Interface (PD-PVA)

The beam specimen with delamination strips of 20 mm placed at an intervals of 50 mm at the interface within the constant moment region behaves as shown in Figure 3.76 in terms of load vs deformation vs maximum crack-width when subjected to a four-point bending test. Tabulated properties of the specimen in the constant moment region after testing are shown in Table 3.8.

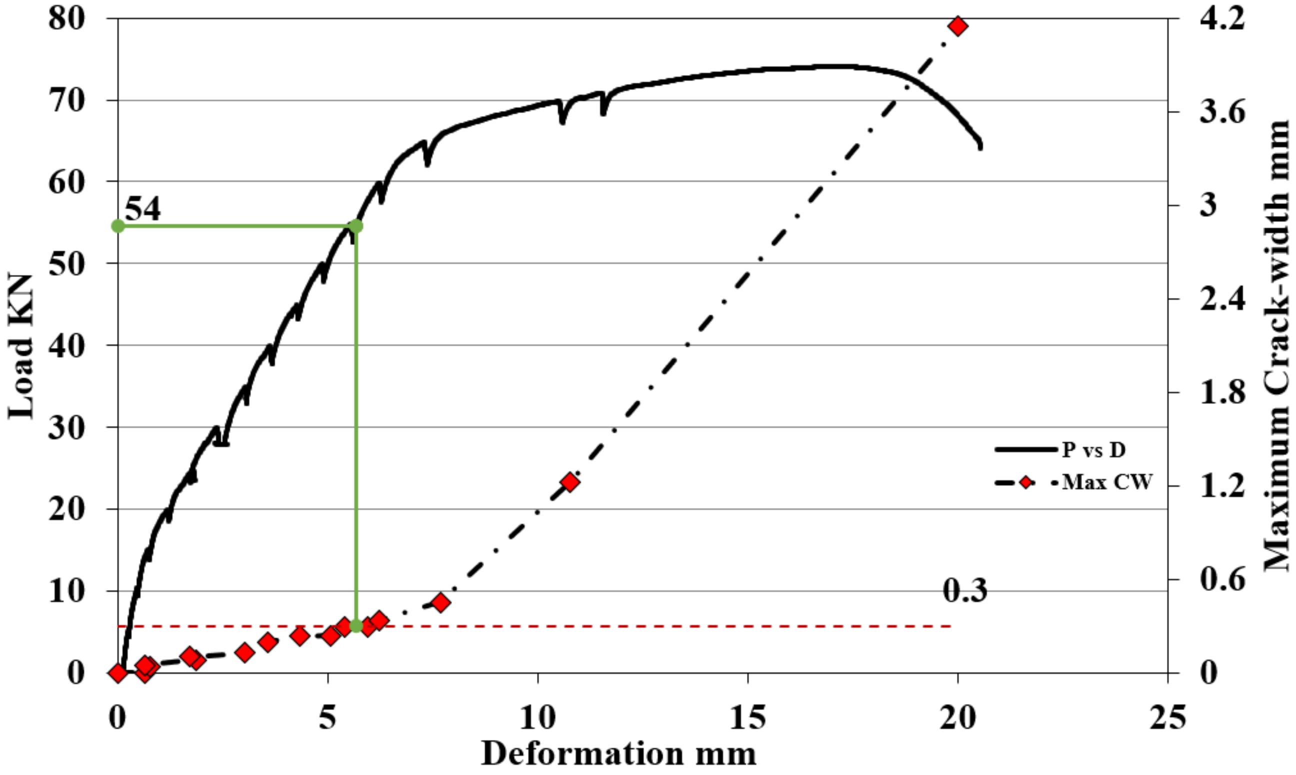

Figure 3.76: Load (P) vs Deformation (D) vs Maximum Crack-Width (Max CW)

Table 3.8: Properties of PD-PVA beam specimen in constant moment region after testing

Property	**Value**
Number of cracks in the concrete layer	8
Average spacing between cracks	62.68 mm
Maximum load	73 KN
Maximum deformation	20.554 mm
Maximum crack-width	4.14 mm
Load at crack-width of 0.3 mm	54 KN

The initial cracks in the SHCC layer appear at a load step of 10 KN (Figure 3.77a) and the initial cracks in the CC layer occur at a load step of 15 KN (Figure 3.77b). The jump in strain ε_x at section 1 and section 3 confirm the occurrence of first cracks in SHCC and CC layers of the hybrid beam. At the locations indicated in Figure 3.77c, delamination is introduced by using tape strips of 20 mm. It is observed that the small cracks in the SHCC layer are not uniformly distributed anymore. All the cracks divert from their expected path and concentrate in the region of small debond created at the interface as seen in Figure 3.78. The cracking pattern on the LVDT side, bottom side and DIC side of PD-PVA is shown in Figure 3.78.

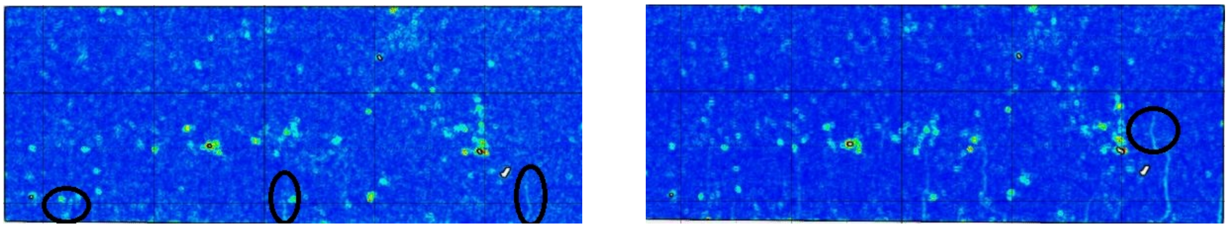

(a) First crack in SHCC layer at a load step of 10 KN **(b)** First crack in CC layer at a load step of 15 KN

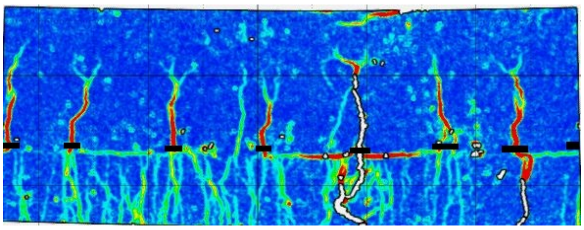

(c) Location of artificially introduced debond

Figure 3.77: Cracking in PD-PVA specimen

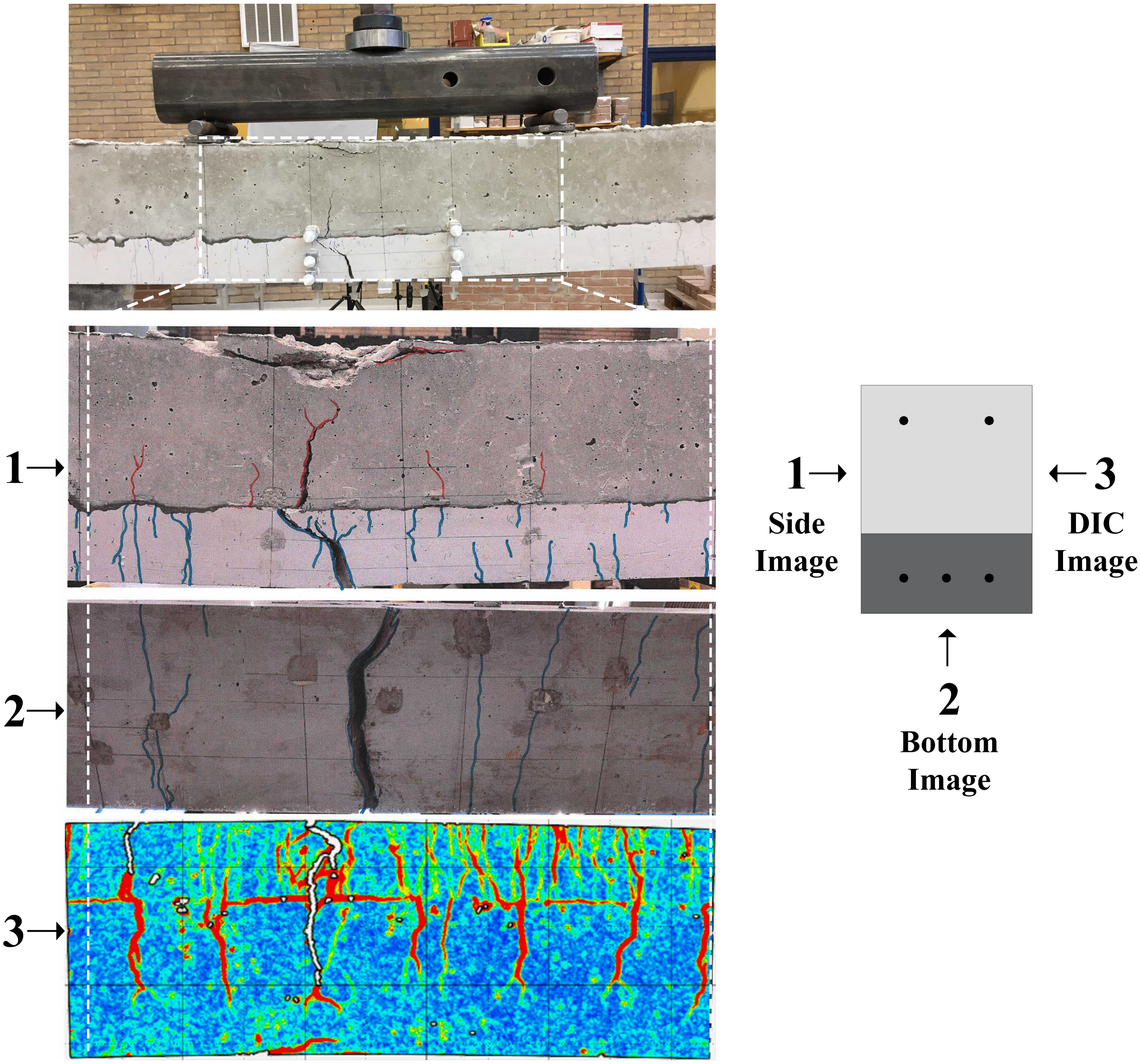

Figure 3.78: 1-LVDT side, 2-Bottom side and 3-DIC side of PD-PVA beam specimen

A step-by-step propagation of cracks along with an increase in the crack-width for all the load steps applied to the PD-PVA beam specimen is shown in Figures 3.79 to 3.91. The crack-widths are measured in the SHCC layer and concrete layer at the section indicated in all Figures 3.79 to 3.91. Since number of cracks in the concrete layer are less, the crack-width at every load step is labelled next to the cracks itself. However, the number of cracks in the SHCC layer are too many to be individually labelled and so a scatter plot indicating the crack-width of various cracks is shown for every load step. The labelled crack-widths are in millimeters (mm).

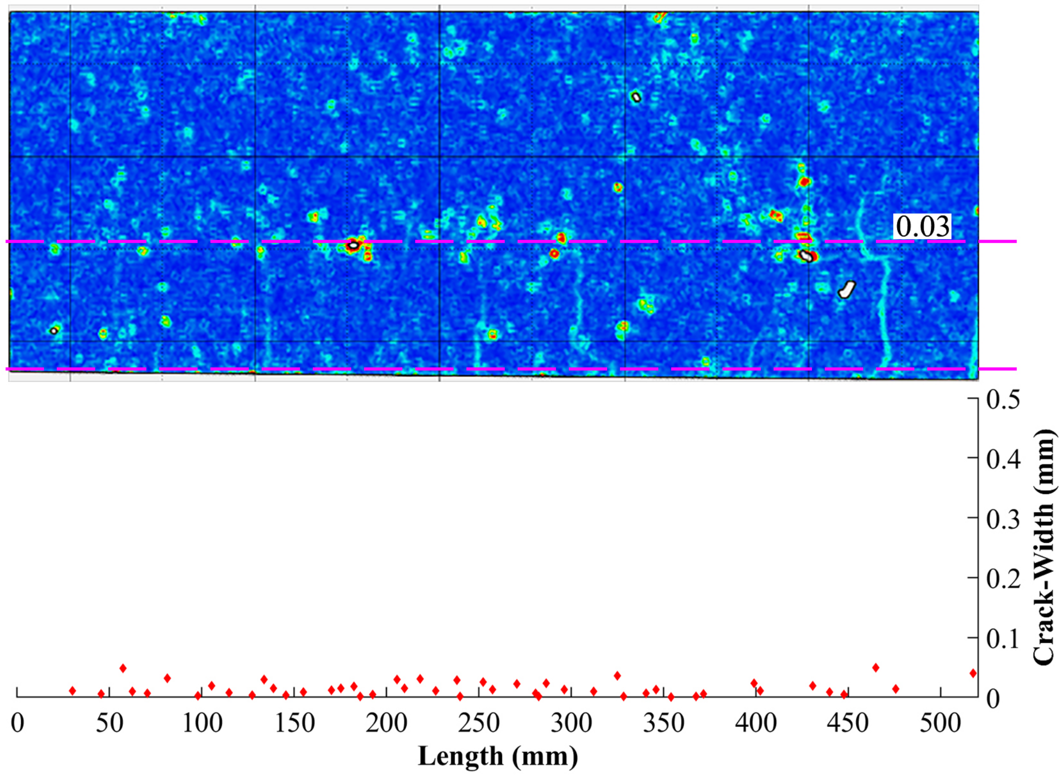

Figure 3.79: Development of cracks at load step 15 KN

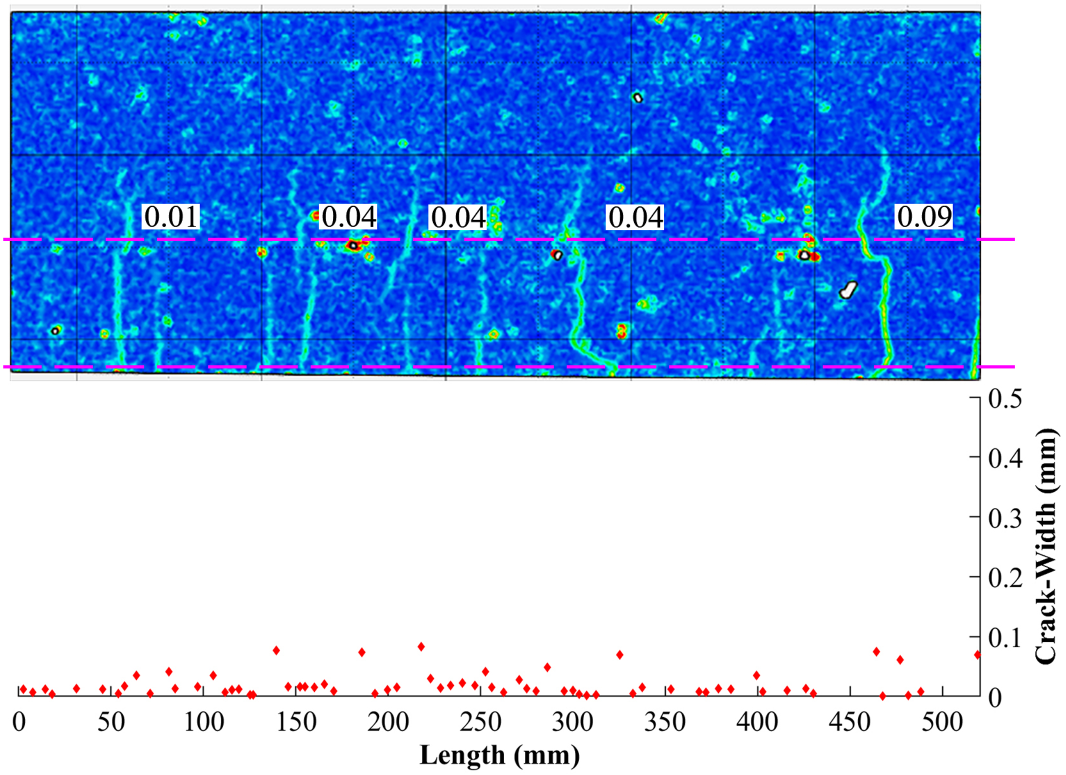

Figure 3.80: Development of cracks at load step 20 KN

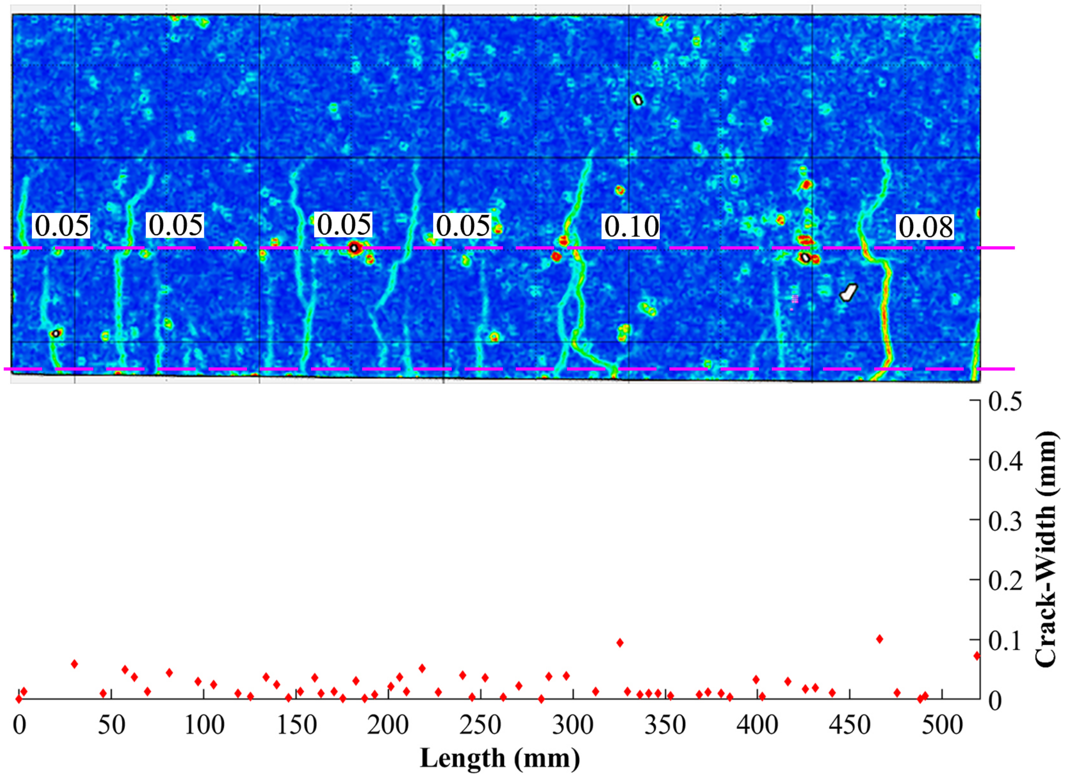

Figure 3.81: Development of cracks at load step 25 KN

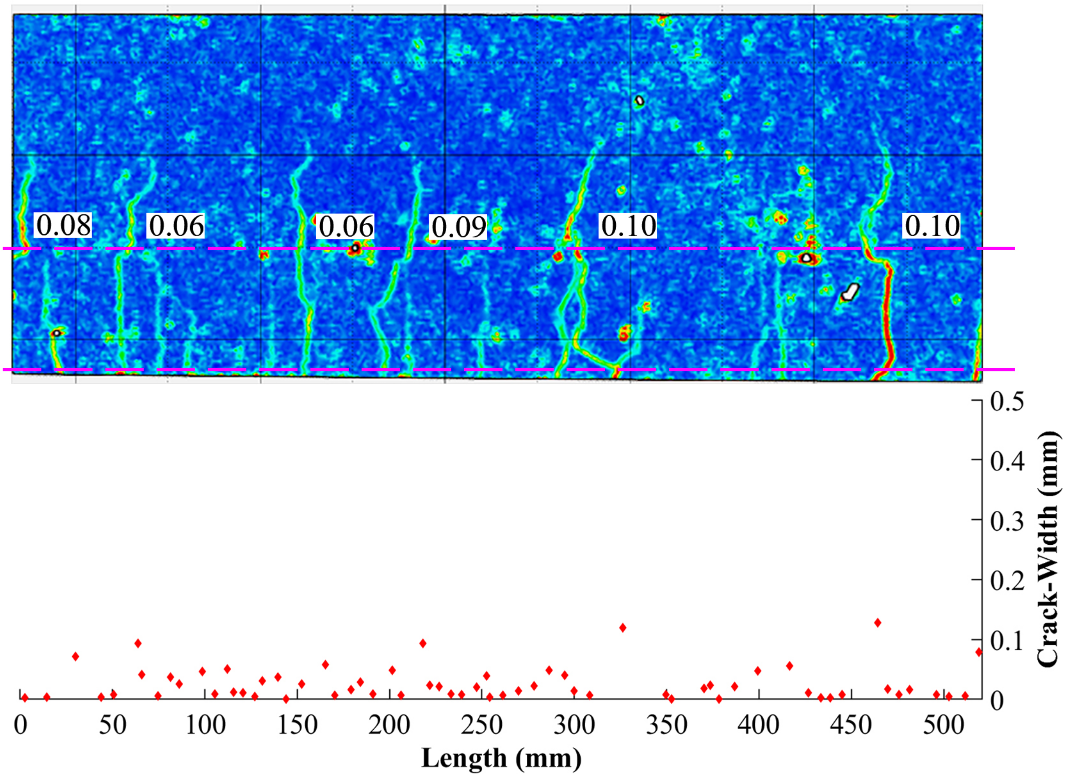

Figure 3.82: Development of cracks at load step 30 KN

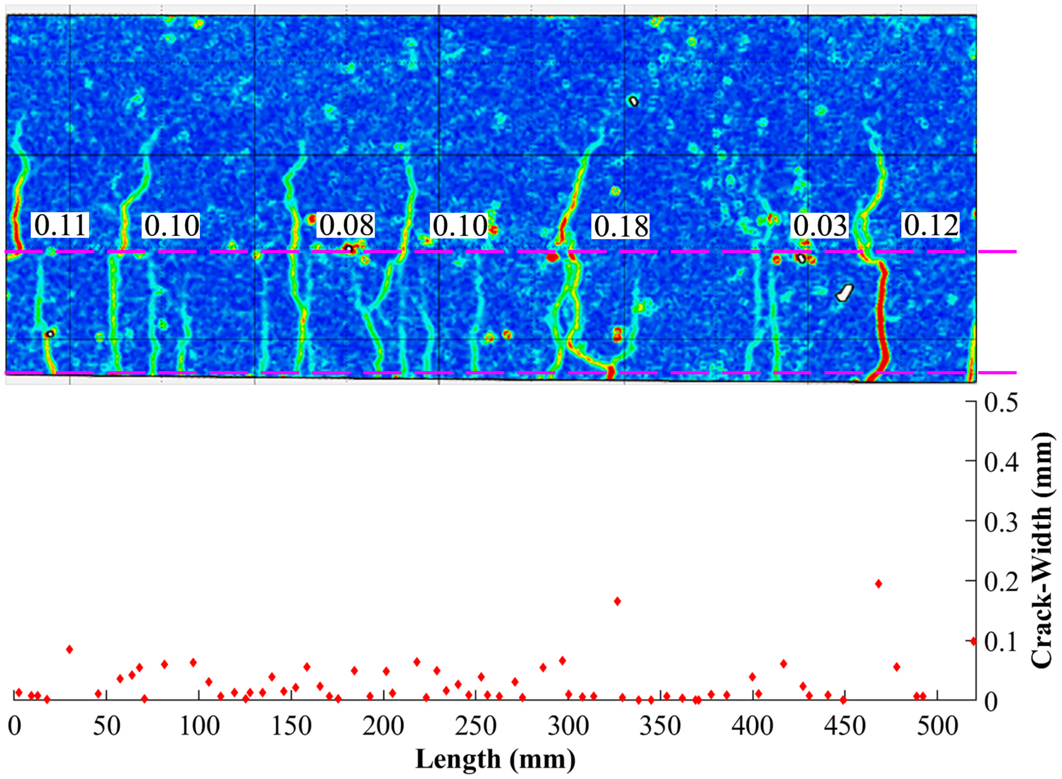

Figure 3.83: Development of cracks at load step 35 KN

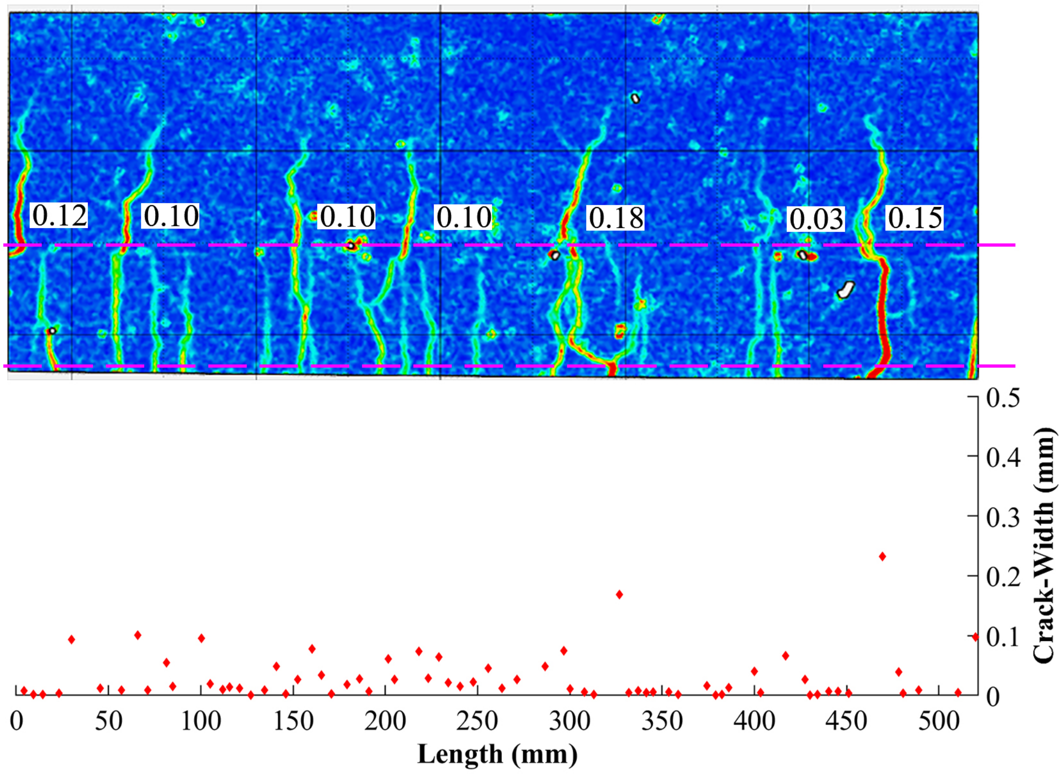

Figure 3.84: Development of cracks at load step 40 KN

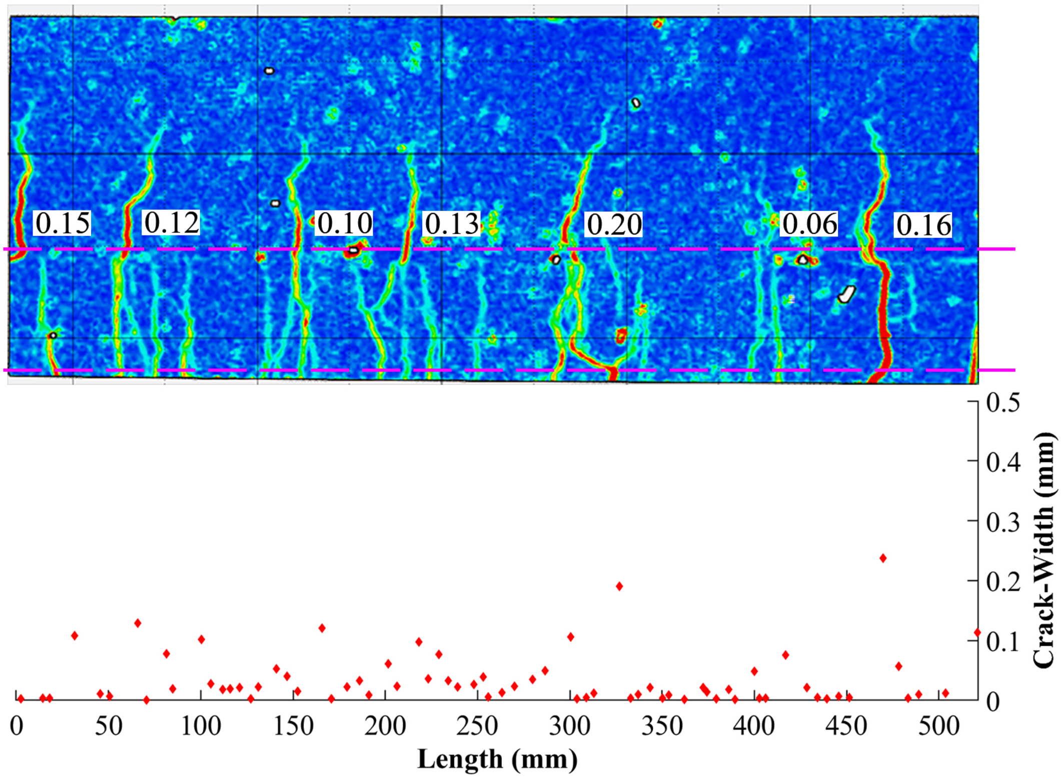

Figure 3.85: Development of cracks at load step 45 KN

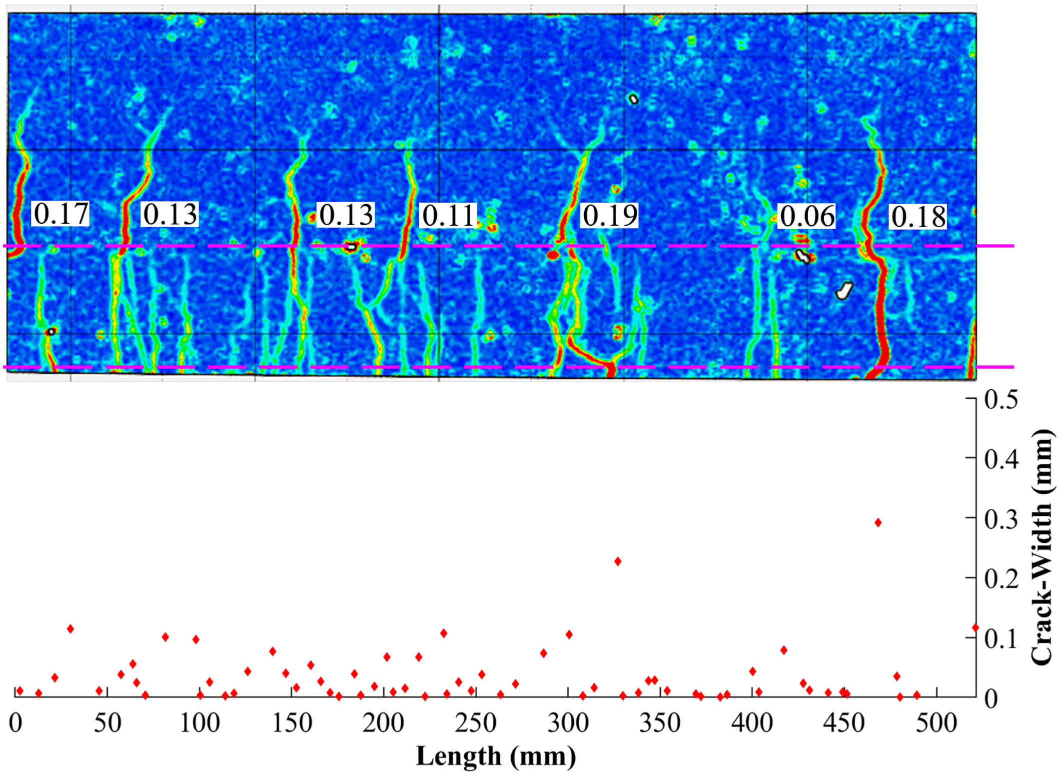

Figure 3.86: Development of cracks at load step 50 KN

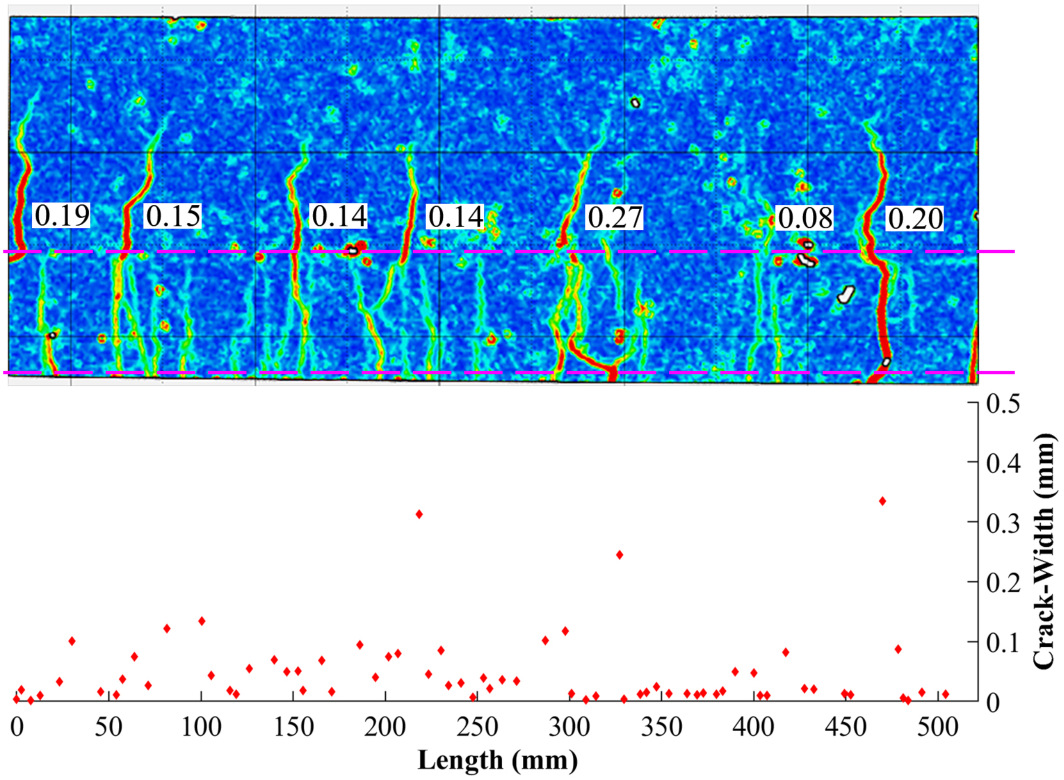

Figure 3.87: Development of cracks at load step 55 KN

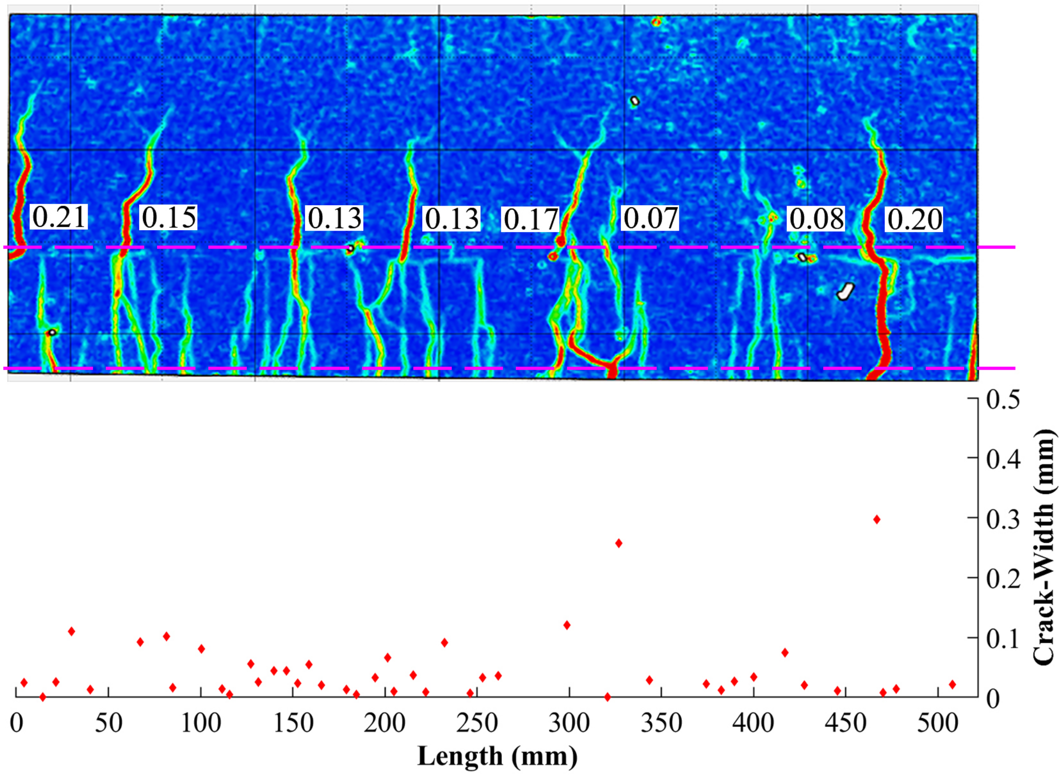

Figure 3.88: Development of cracks at load step 60 KN

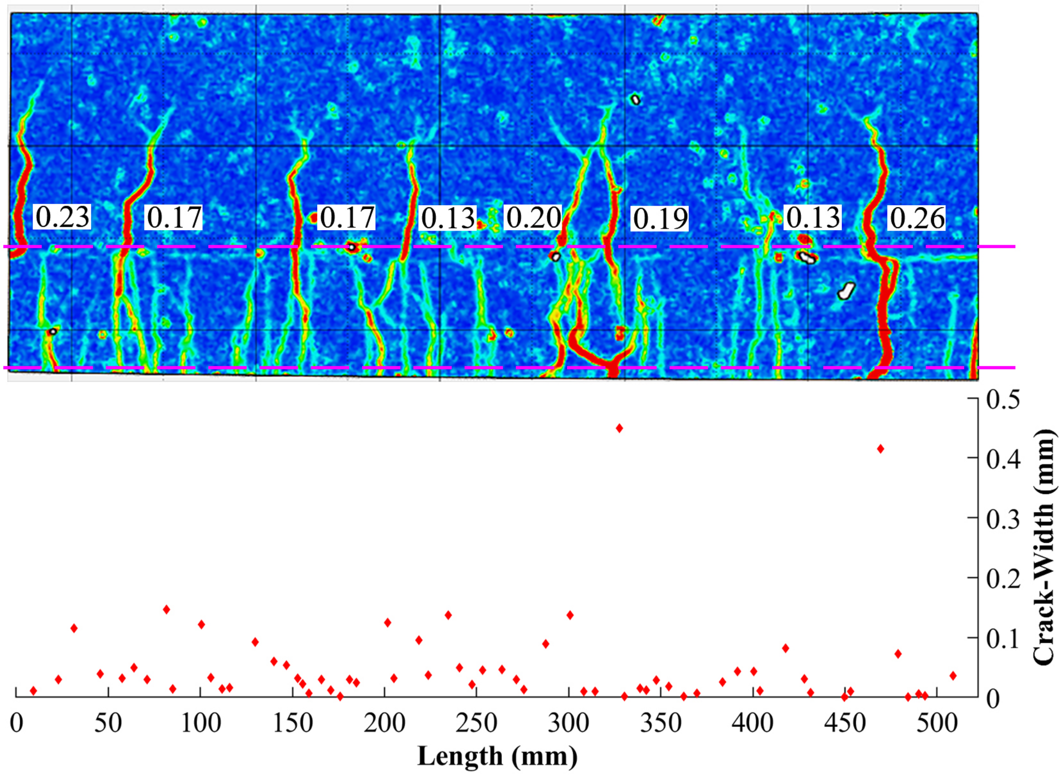

Figure 3.89: Development of cracks at load step 65 KN

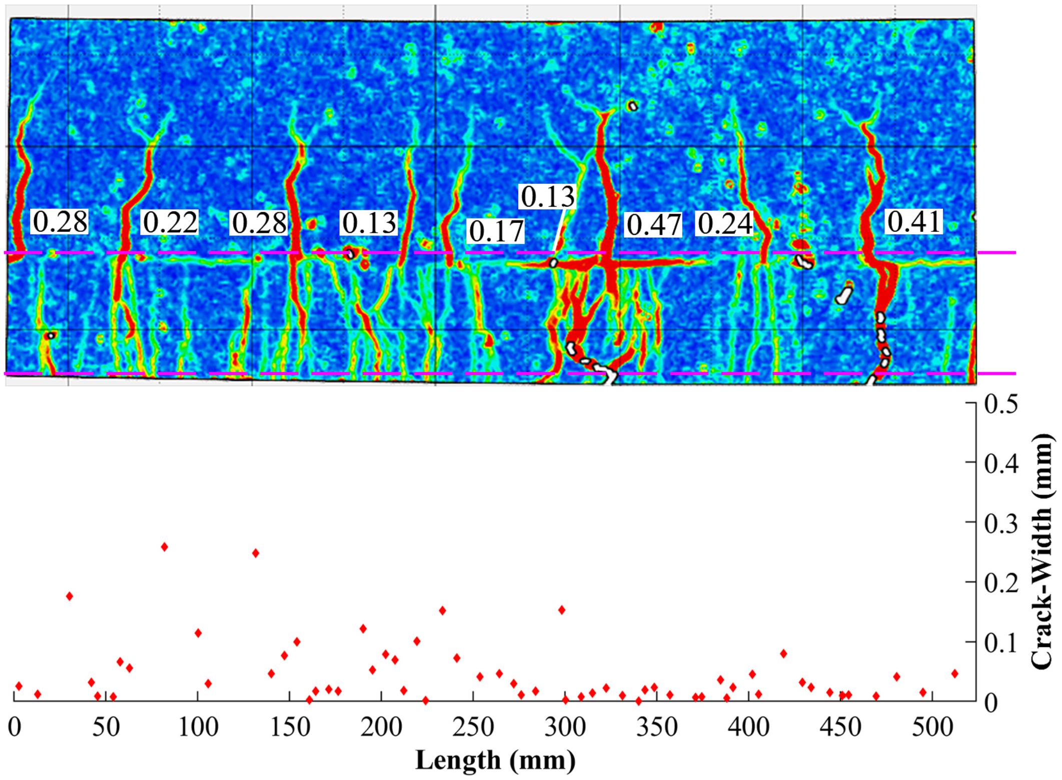

Figure 3.90: Development of cracks at load step 70 KN

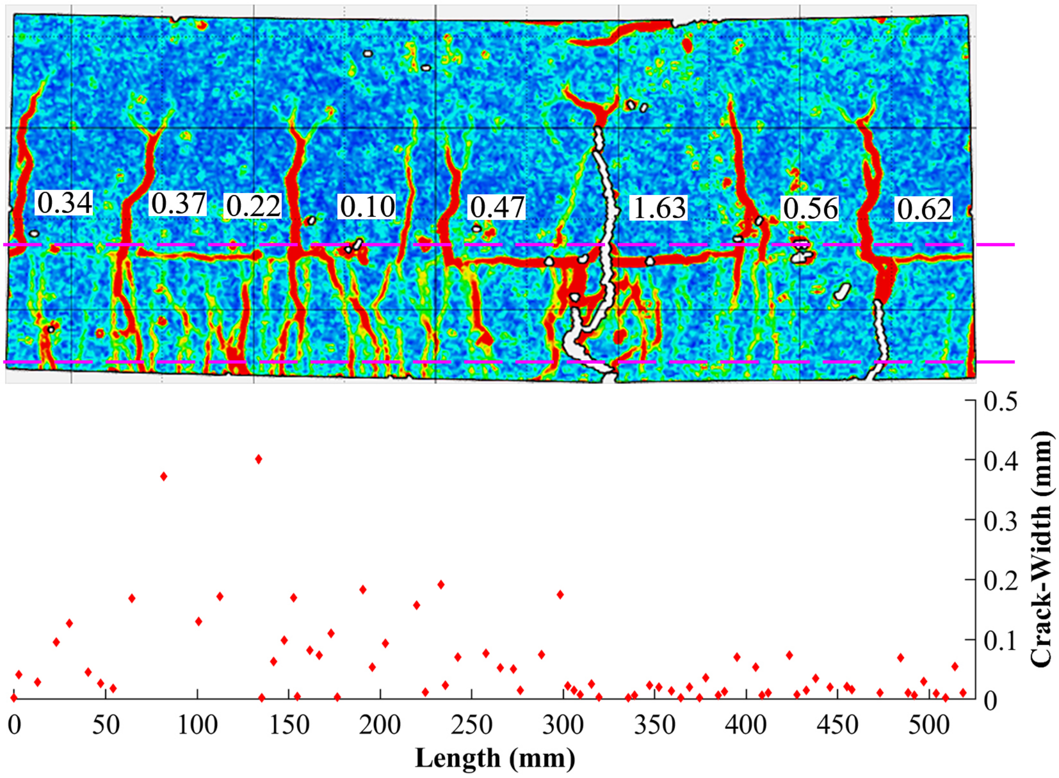

Figure 3.91: Development of cracks at load step 73 KN

At the last two load steps, the measured crack-widths exceed 0.5 mm and are not shown in 3.90 and 3.91 as the limit of the crack-width plots is set to 0.5 mm. Figures 3.92 and 3.93 show the crack-width of all the cracks in the SHCC layer for the last two load step.

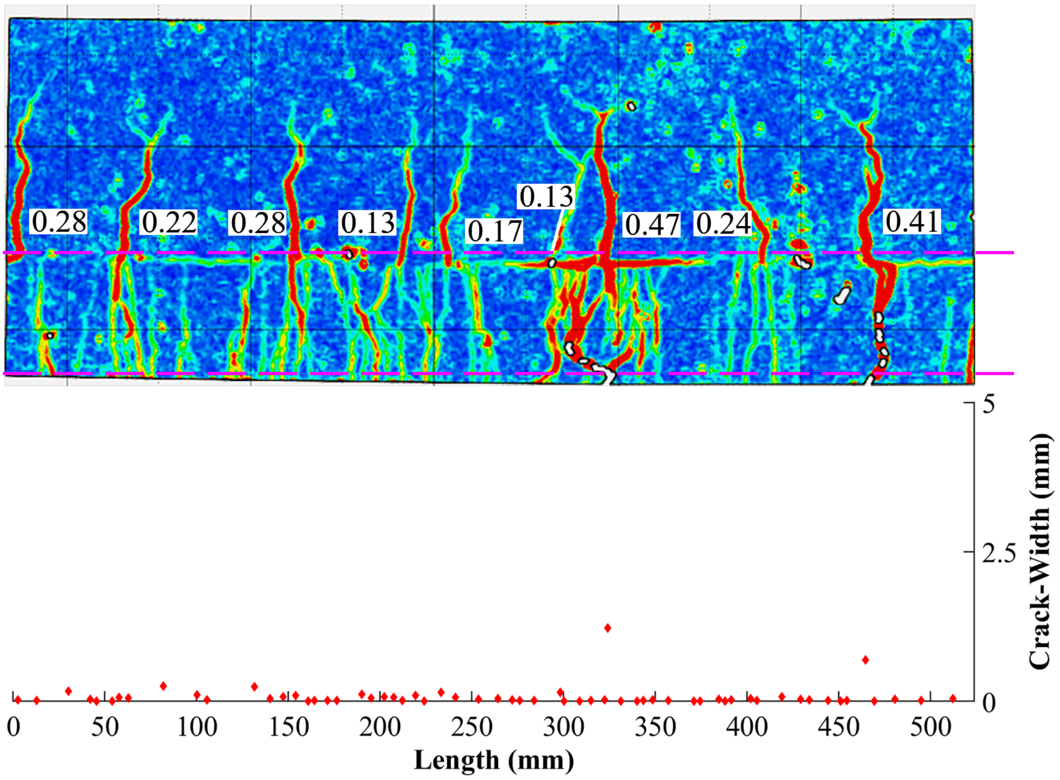

Figure 3.92: Development of large cracks at load step 70 KN

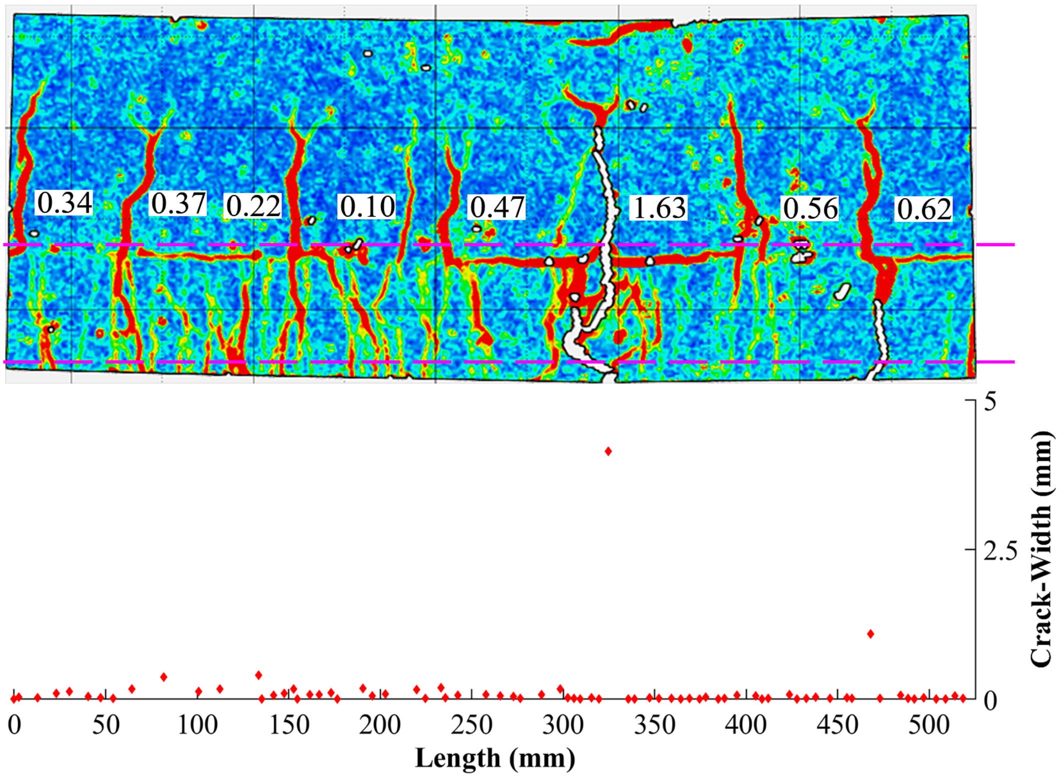

Figure 3.93: Development of large cracks at final load step 73 KN

The accuracy of the cracks measured using DIC is validated by comparing the plots of maximum crack-widths calculated using GOM correlate with crack-widths measure using Image J and visual inspection as shown in Figure 3.94. The deformations measured using GOM correlate are plotted with the deformations measured using LVDTs for comparison as shown in Figure 3.95.

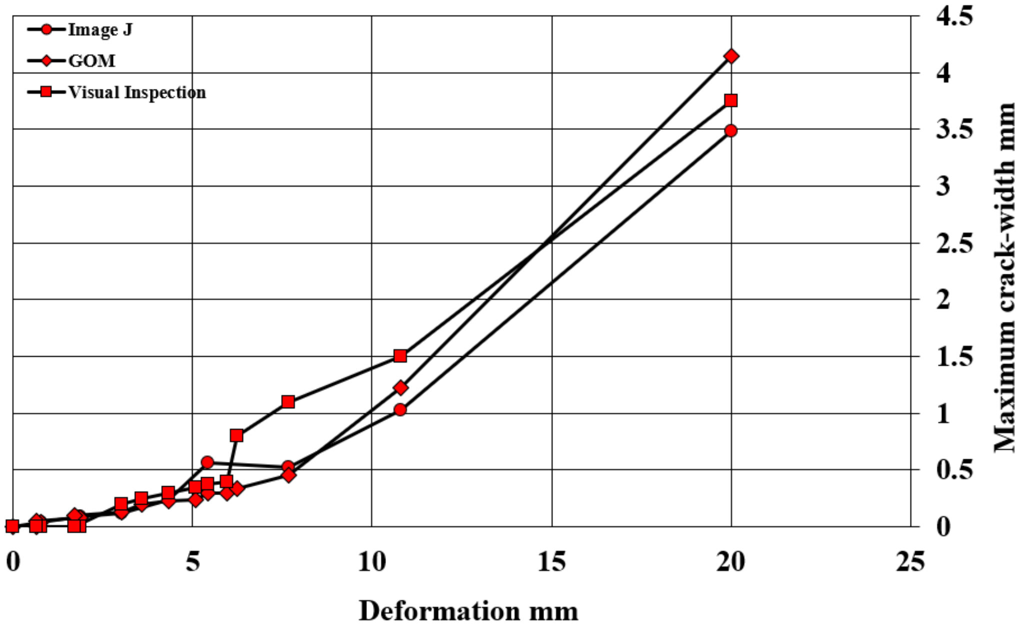

Figure 3.94: Comparison of maximum crack-widths measured using GOM, Image J and Visual Inspection

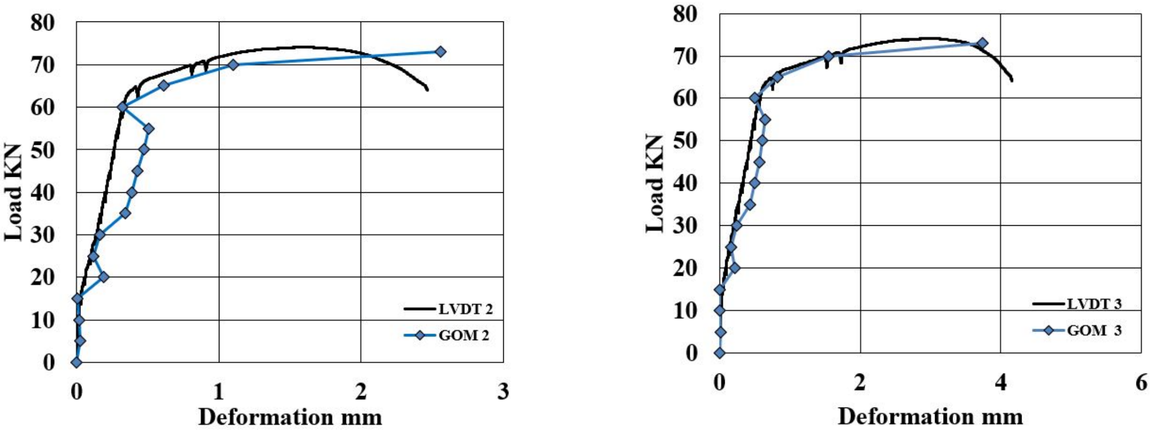

(a) P vs D plots of LVDT 2 vs GOM 2

(b) P vs D plots of LVDT 3 vs GOM 3

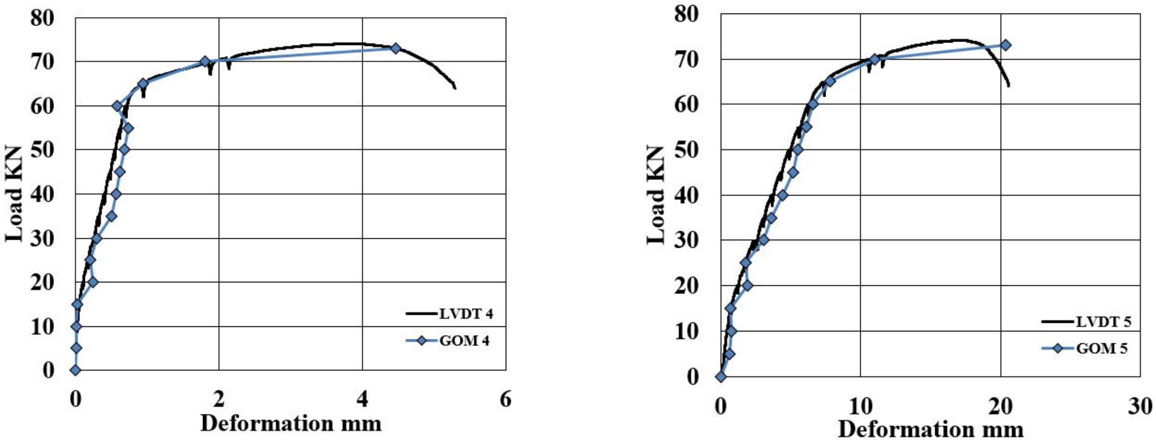

(c) P vs D plots of LVDT 4 vs GOM 4

(d) P vs D plots of LVDT 5 vs GOM 5

Figure 3.95: Calibration plots of GOM deformation with LVDT deformation

3.6.5 Hybrid Beam with Completely Delaminated Interface (CD-PVA)

The behaviour of load vs deformation vs maximum crack-width at a section of 1 mm from the bottom edge of the beam specimen with completely delaminated interface in the constant moment region is shown in Figure 3.96. Effect of delaminated interface when the beam is subjected to four-point loading is discussed in Table 3.9.

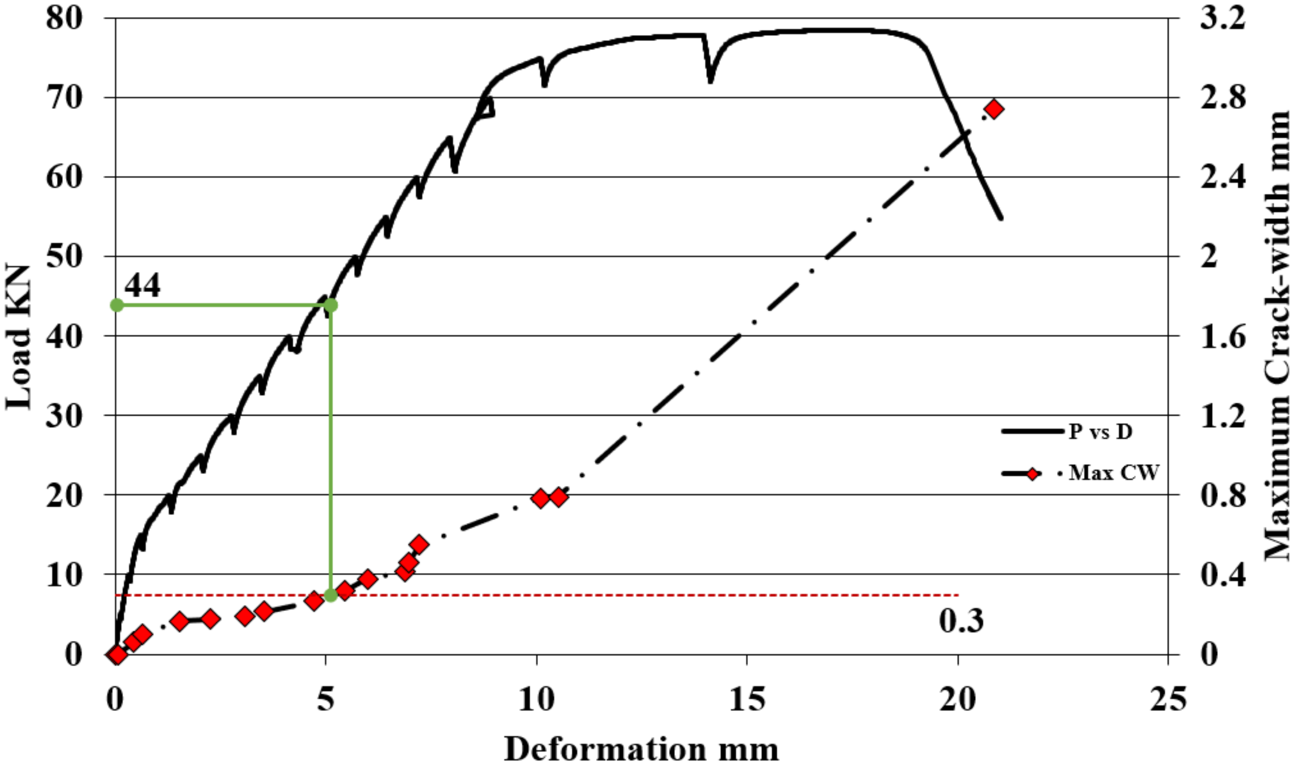

Figure 3.96: Load (P) vs Deformation (D) vs Maximum Crack-Width (Max CW)

Table 3.9: Properties of CD-PVA beam specimen in constant moment region after testing

Property	**Value**
Number of cracks in the concrete layer	7
Average spacing between cracks	78.38 mm
Maximum load	75 KN
Maximum deformation	21.0334 mm
Maximum crack-width	2.74 mm
Load at crack-width of 0.3 mm	44 KN

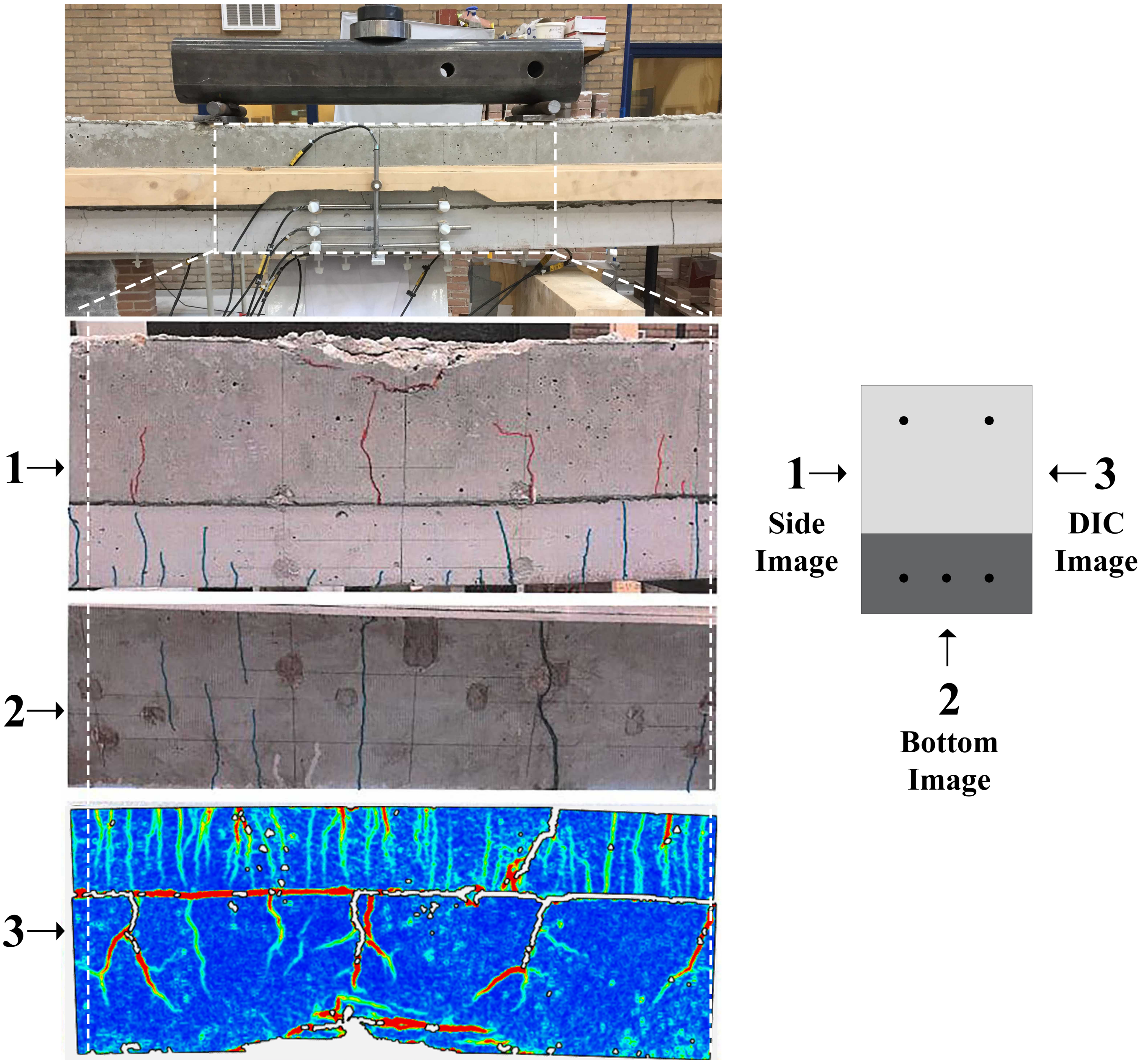

Figure 3.97: 1-LVDT side, 2-Bottom side and 3-DIC side of CD-PVA beam specimen

The cracking pattern of the beam specimen (CD-PVA) in the constant moment region on the LVDT side, bottom side and DIC side is shown in Figure 3.97. The initial cracks in SHCC layer are seen at a load step of 10 KN as shown in Figure 3.98a which is also confirmed by the jump in strain ε_x at section 1. An artificial debond is introduced by applying tape throughout the interface in the constant moment region and at a load step of 10 KN, cracking at the interface is observed as shown in Figure 3.98a. The initial cracks in the CC layer appear at the load step of 15 KN as shown in Figure 3.98b and is re-confirmed by observing the jump in strain ε_x at section 3. It can be observed that the cracks are uniformly distributed in the SHCC layer and also evenly spaced at the region closer to the interface in the SHCC layer as seen in Figure 3.98c. This is because the interface between the CC and SHCC layer is completely debonded, thereby creating the largest debond length available for the cracks to smear. At the last load step, a gap is observed at the interface as shown in Figure 3.98d.

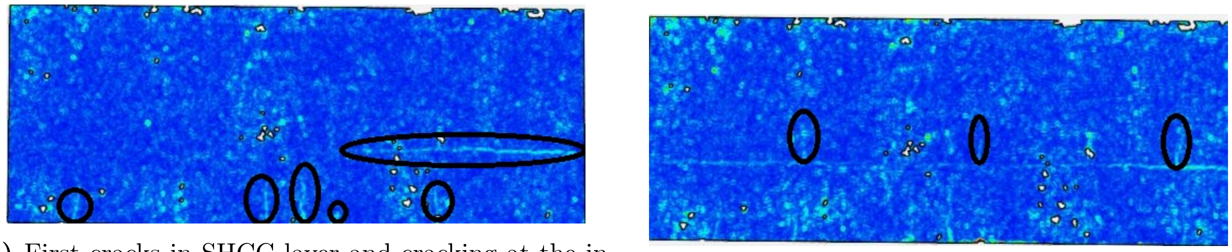

(a) First cracks in SHCC layer and cracking at the interface at load step 10 KN

(b) First cracks in CC layer at load step of 15 KN

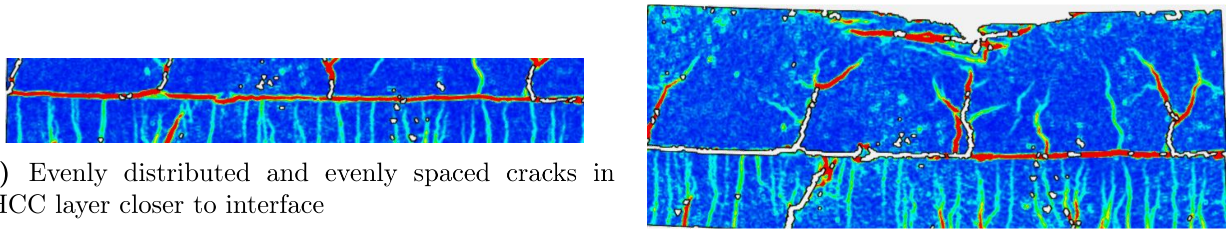

(c) Evenly distributed and evenly spaced cracks in SHCC layer closer to interface

(d) P vs D plots of LVDT 5 vs GOM 5

Figure 3.98: Cracking in CD-PVA specimen

A step-by-step propagation of cracks along with an increase in the crack-widths for all the load steps applied to the CD-PVA beam specimen are shown in Figures 3.99 to 3.112. The crack-widths are measured in the SHCC layer and concrete layer at the section indicated in all Figures 3.99 to 3.112. Since number of cracks in the concrete layer are less, the crack-width at every load step is labelled next to the cracks. However, the number of cracks in the SHCC layer are too many to be individually labelled and so a scatter plot indicating the crack-width of various cracks is shown for every load step. The labelled crack-widths are in millimeters (mm).

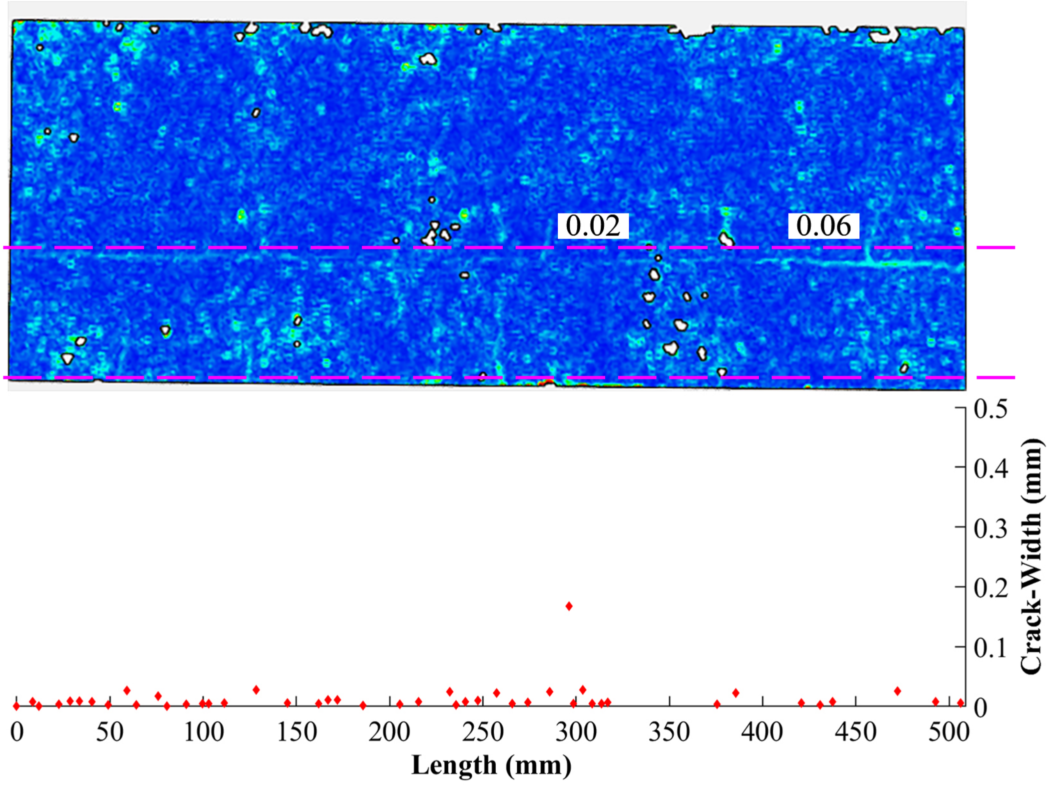

Figure 3.99: Development of cracks at load step 15 KN

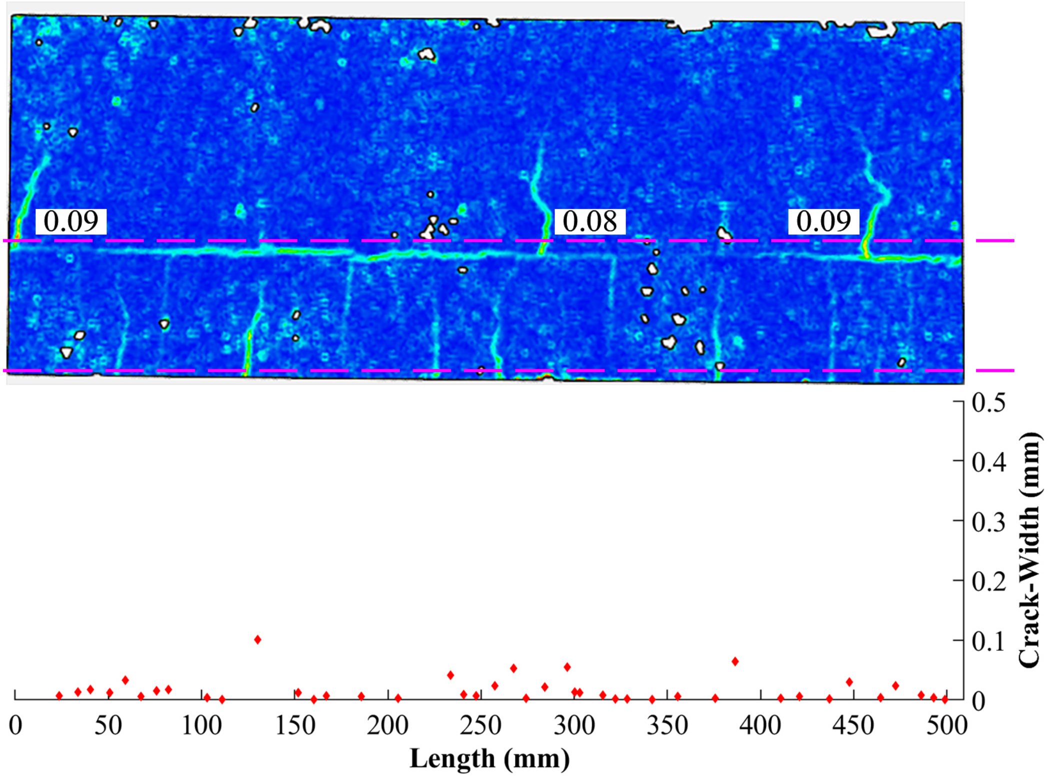

Figure 3.100: Development of cracks at load step 20 KN

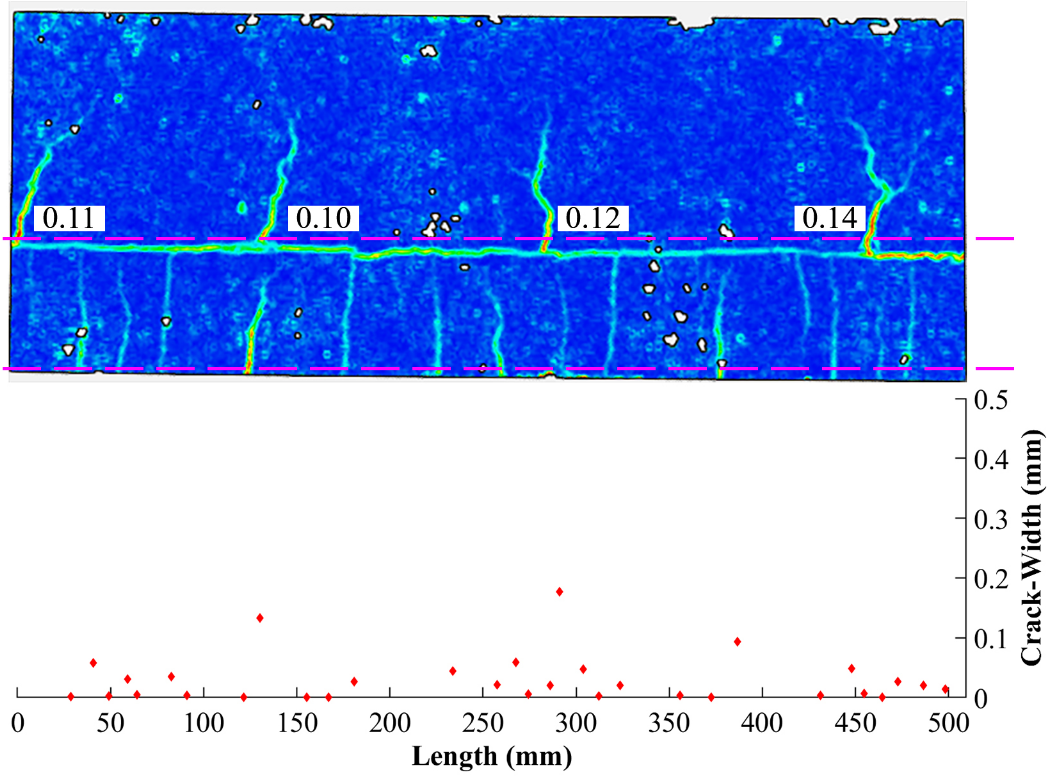

Figure 3.101: Development of cracks at load step 25 KN

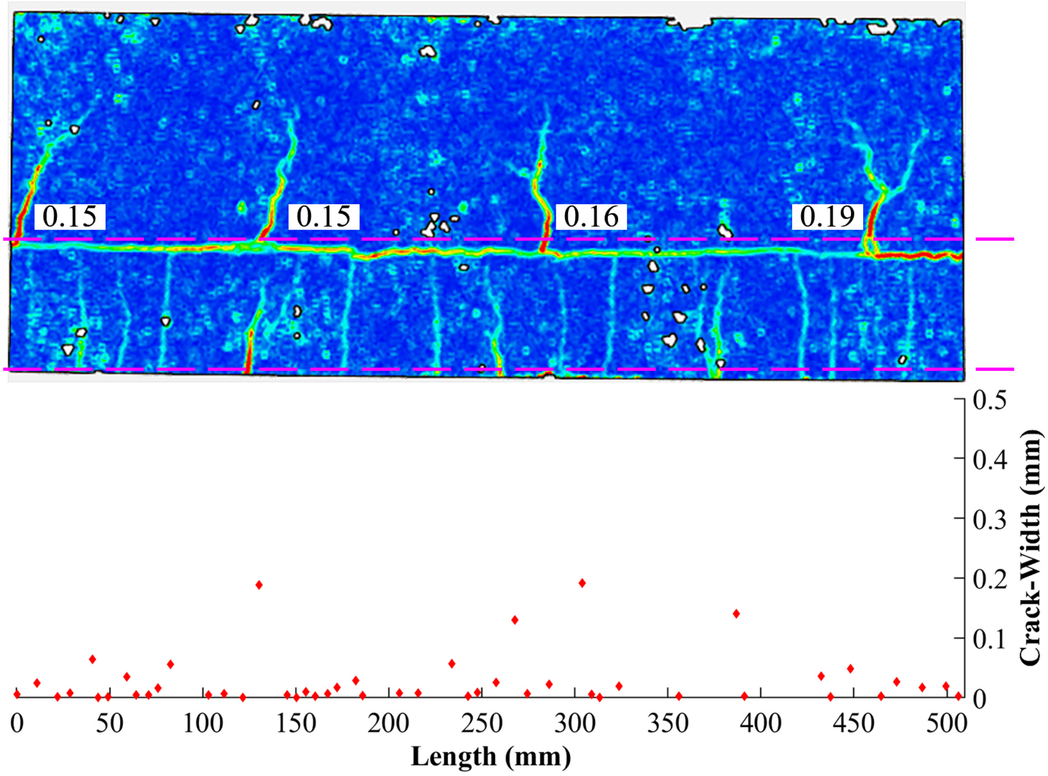

Figure 3.102: Development of cracks at load step 30 KN

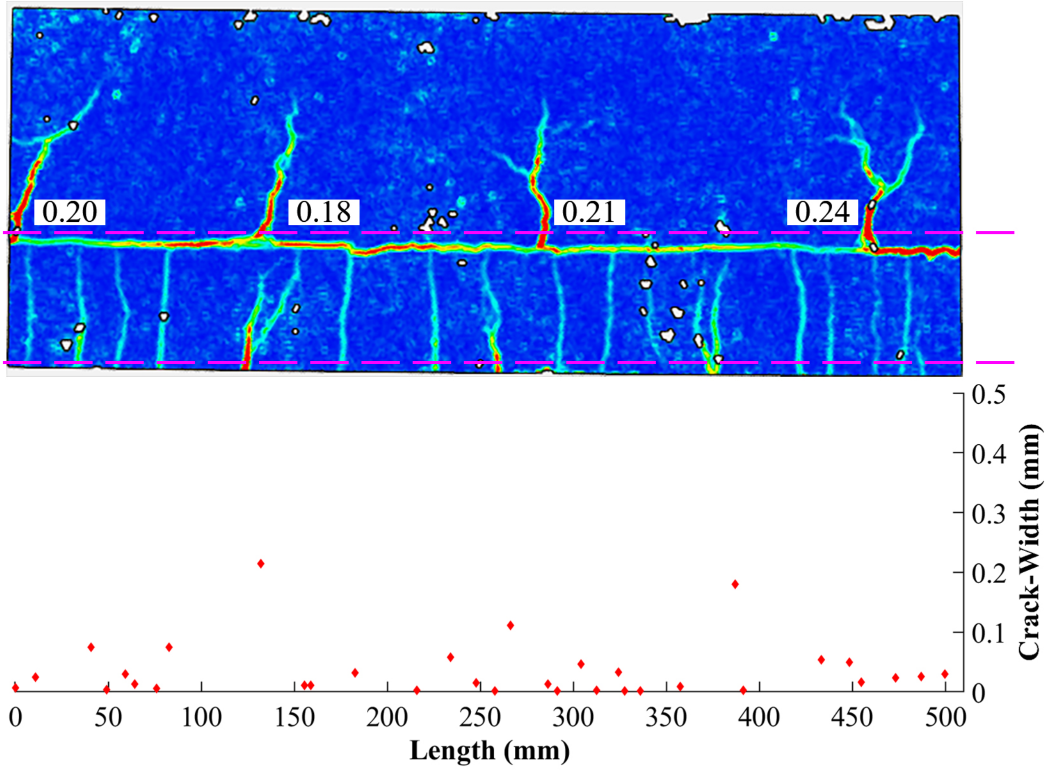

Figure 3.103: Development of cracks at load step 35 KN

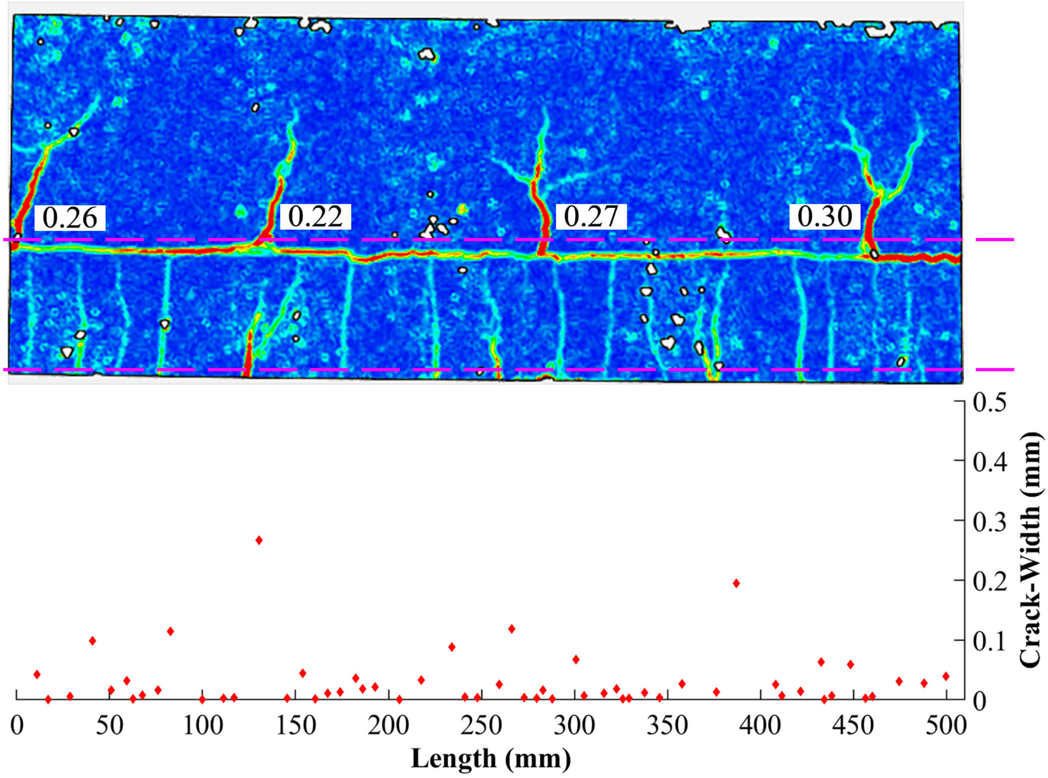

Figure 3.104: Development of cracks at load step 40 KN

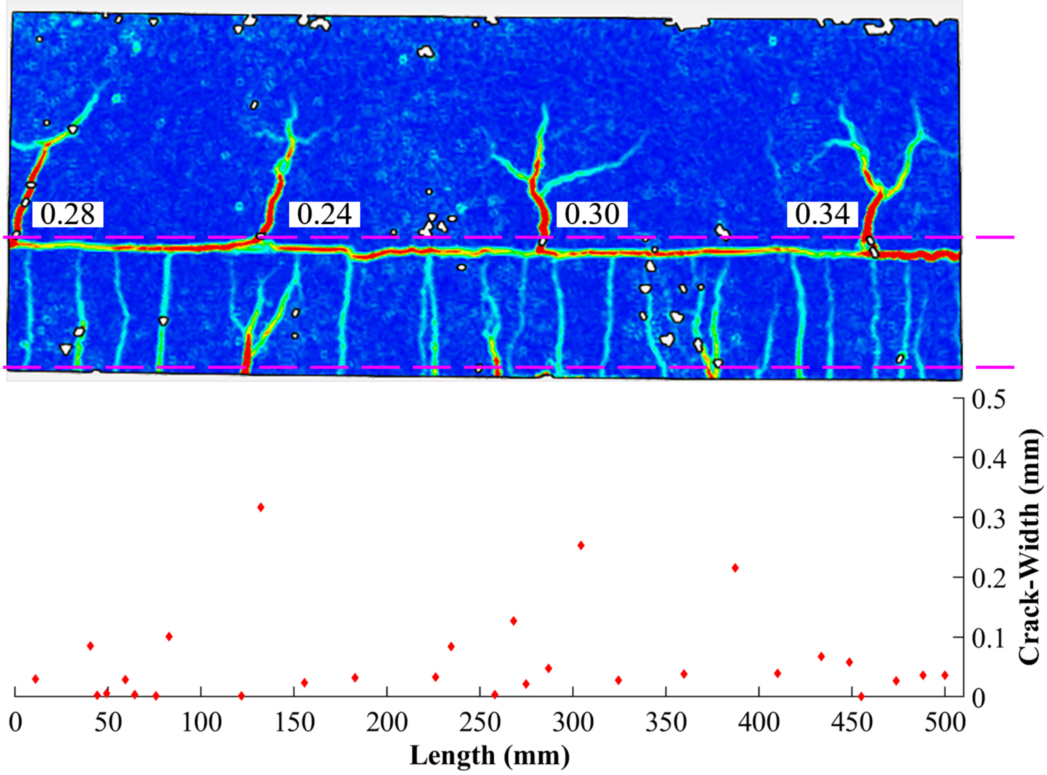

Figure 3.105: Development of cracks at load step 45 KN

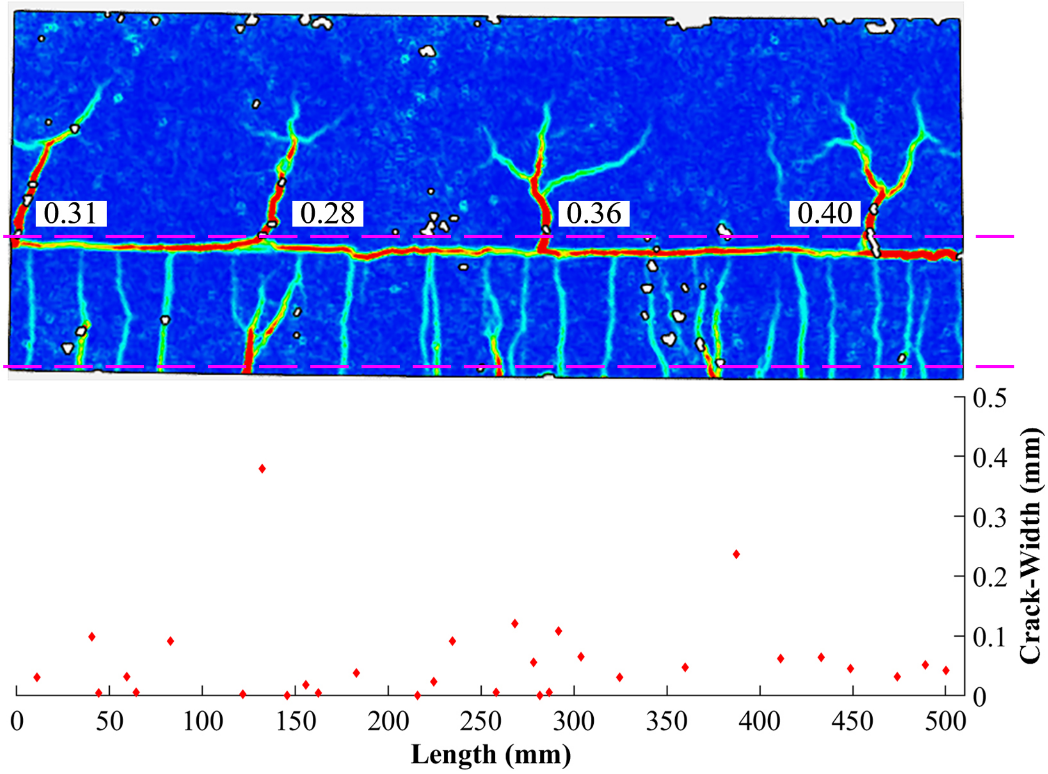

Figure 3.106: Development of cracks at load step 50 KN

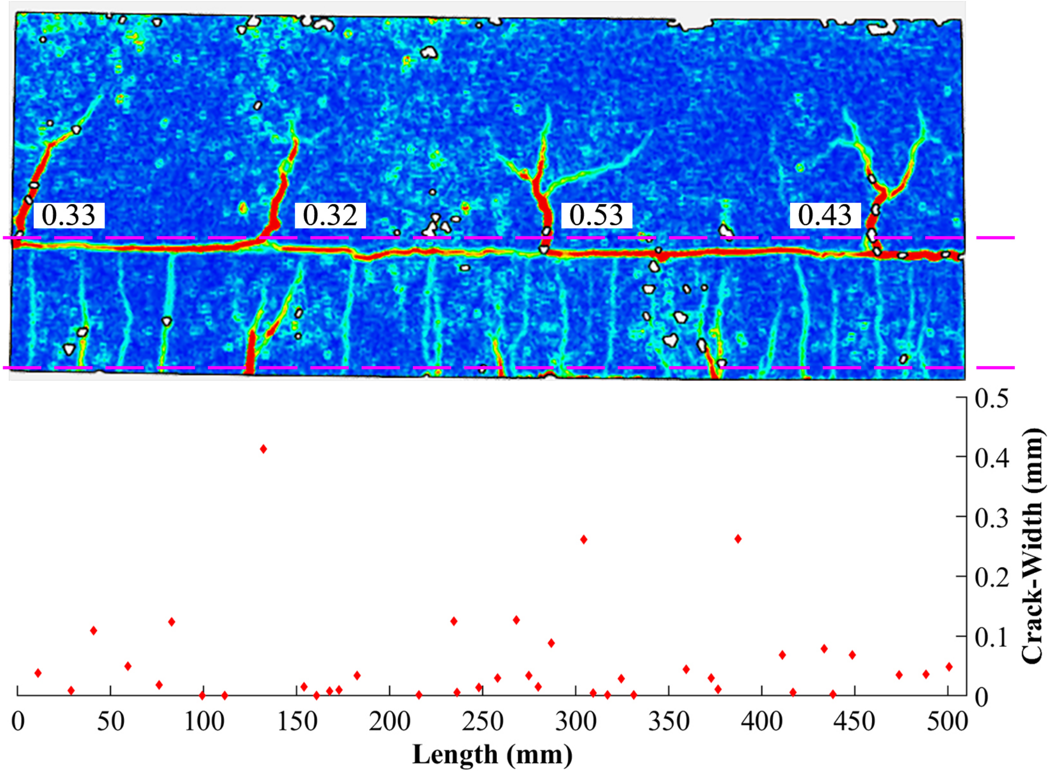

Figure 3.107: Development of cracks at load step 55 KN

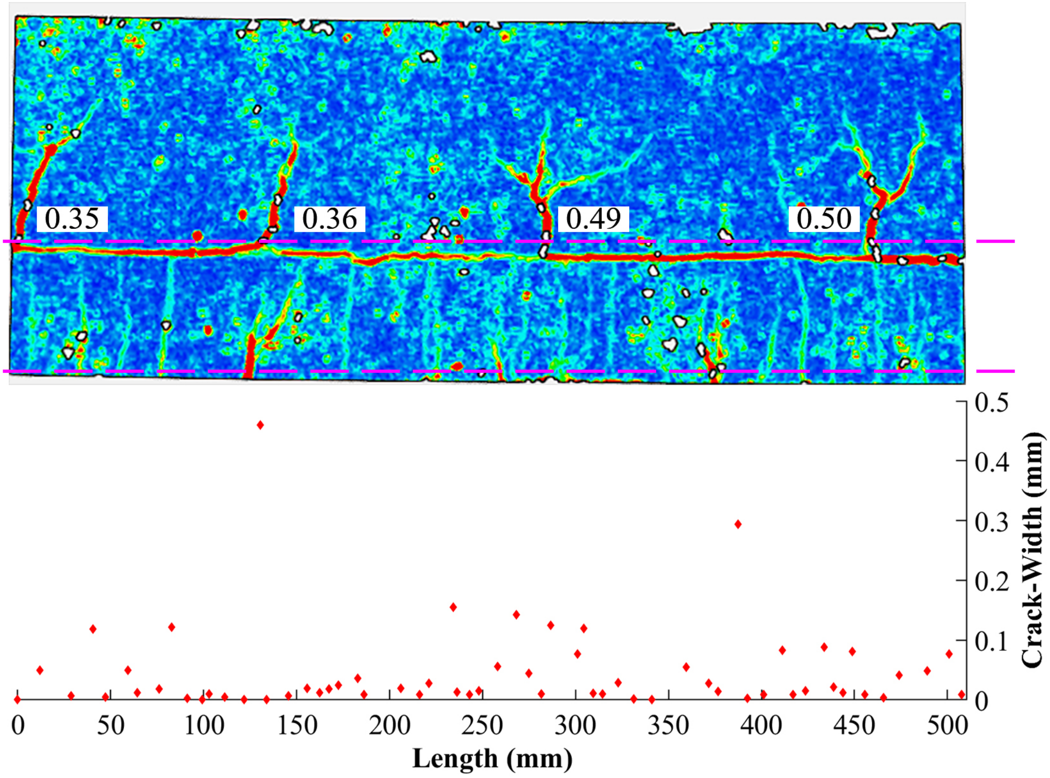

Figure 3.108: Development of cracks at load step 60 KN

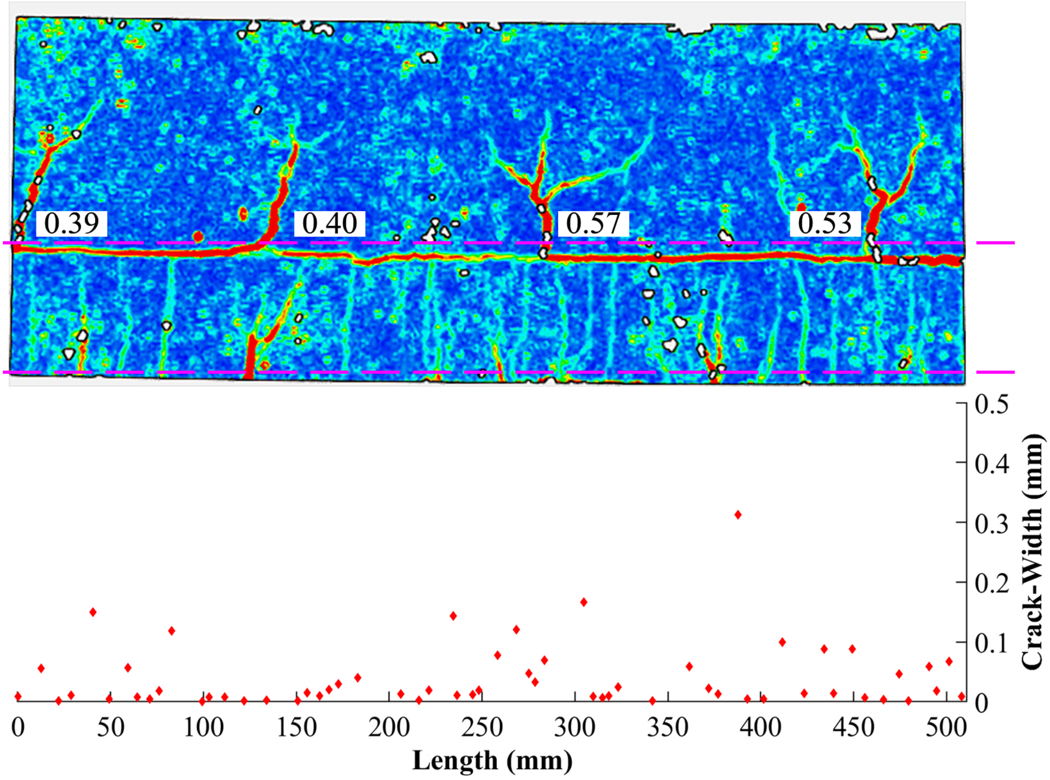

Figure 3.109: Development of cracks at load step 65 KN

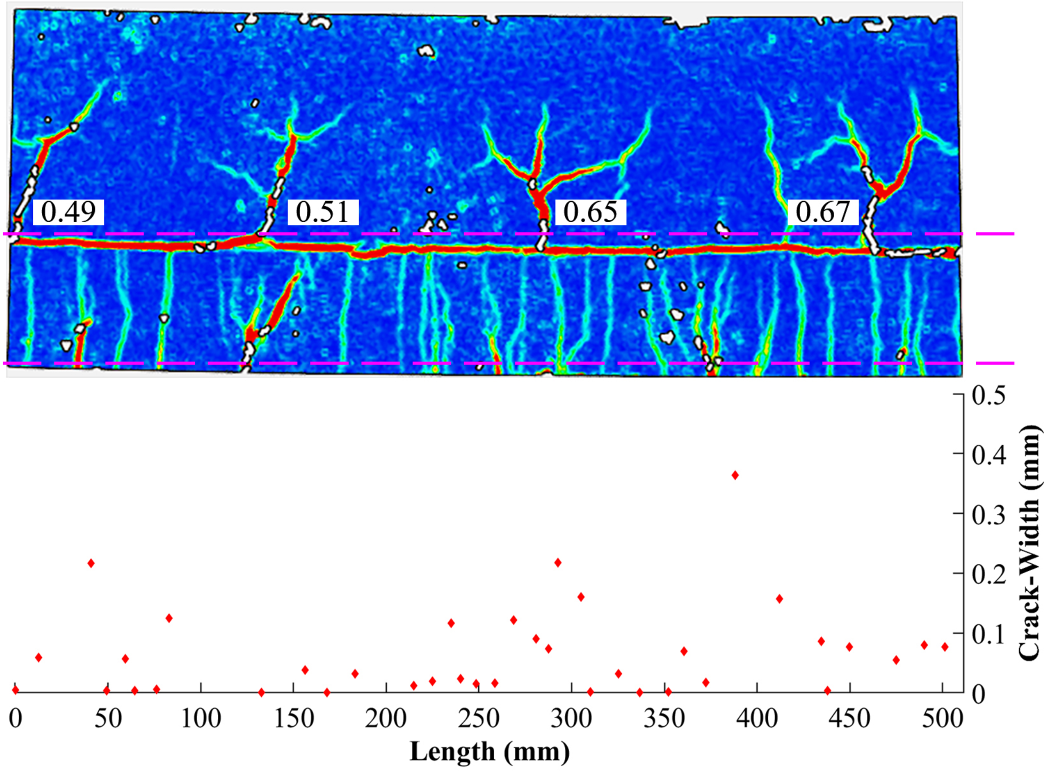

Figure 3.110: Development of cracks at load step 70 KN

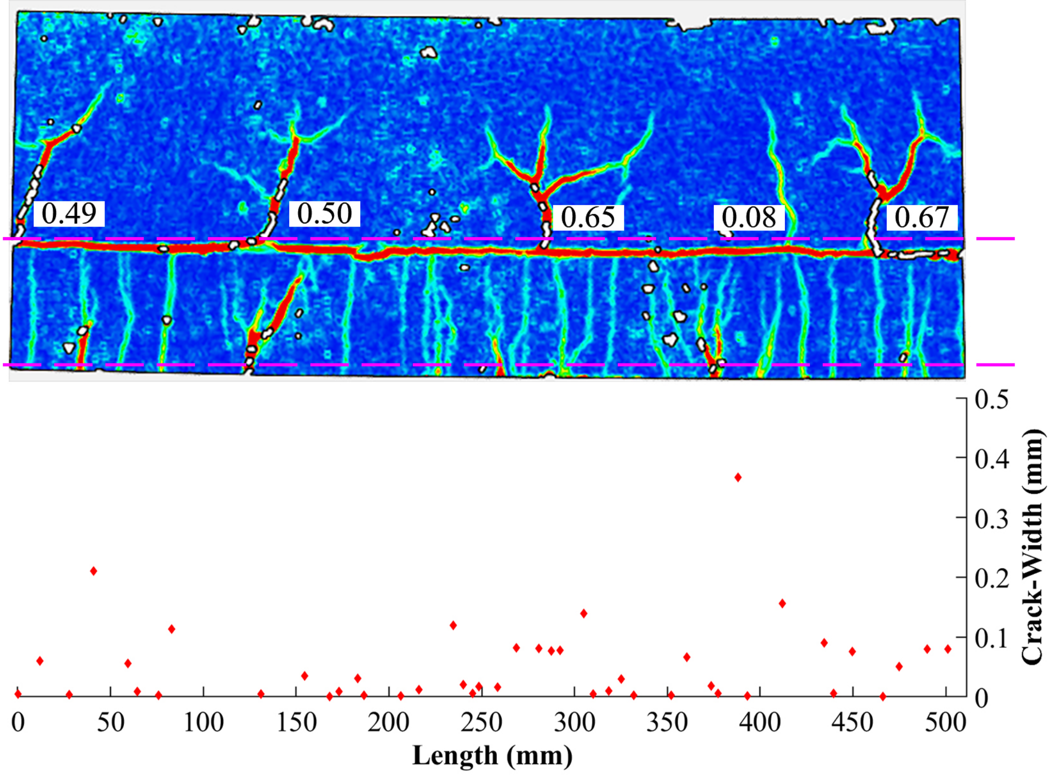

Figure 3.111: Development of cracks at load step 75 KN

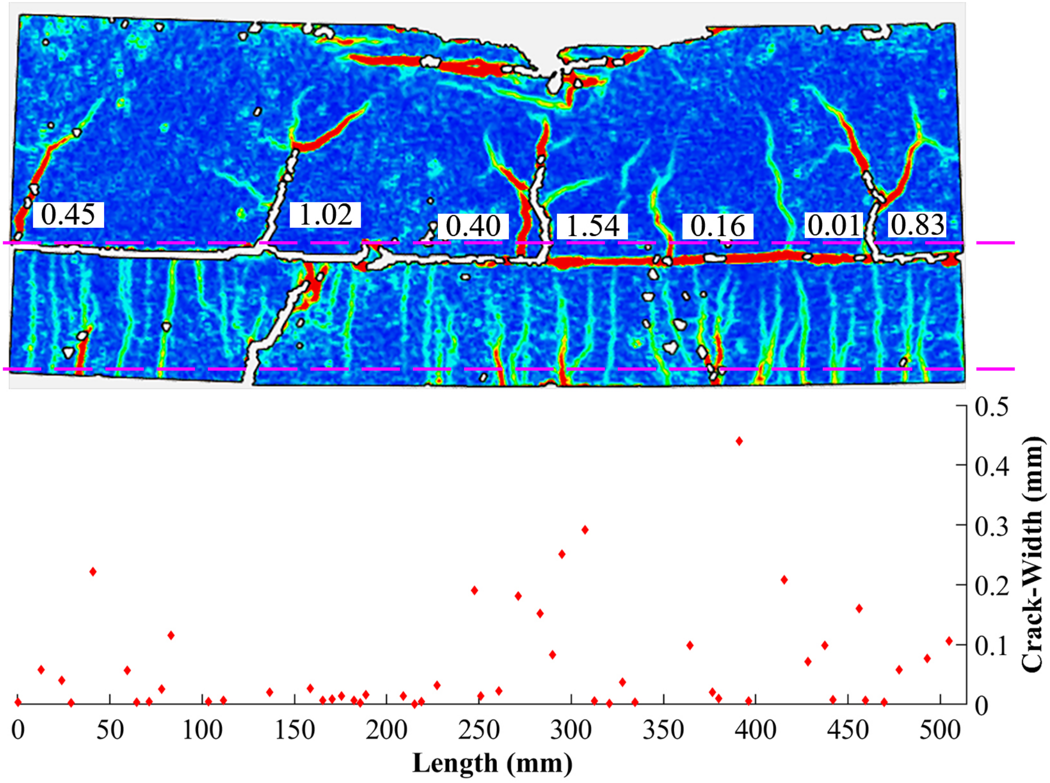

Figure 3.112: Development of cracks at load step 60 KN

At the last four load steps, the measured crack-widths exceeds 0.5 mm and are not shown in 3.109, 3.110, 3.111 and 3.112 as the limit of the crack-width plots is set to 0.5 mm. Figure 3.113 to 3.116 show the crack-widths of all the cracks in the SHCC layer at the last four load steps.

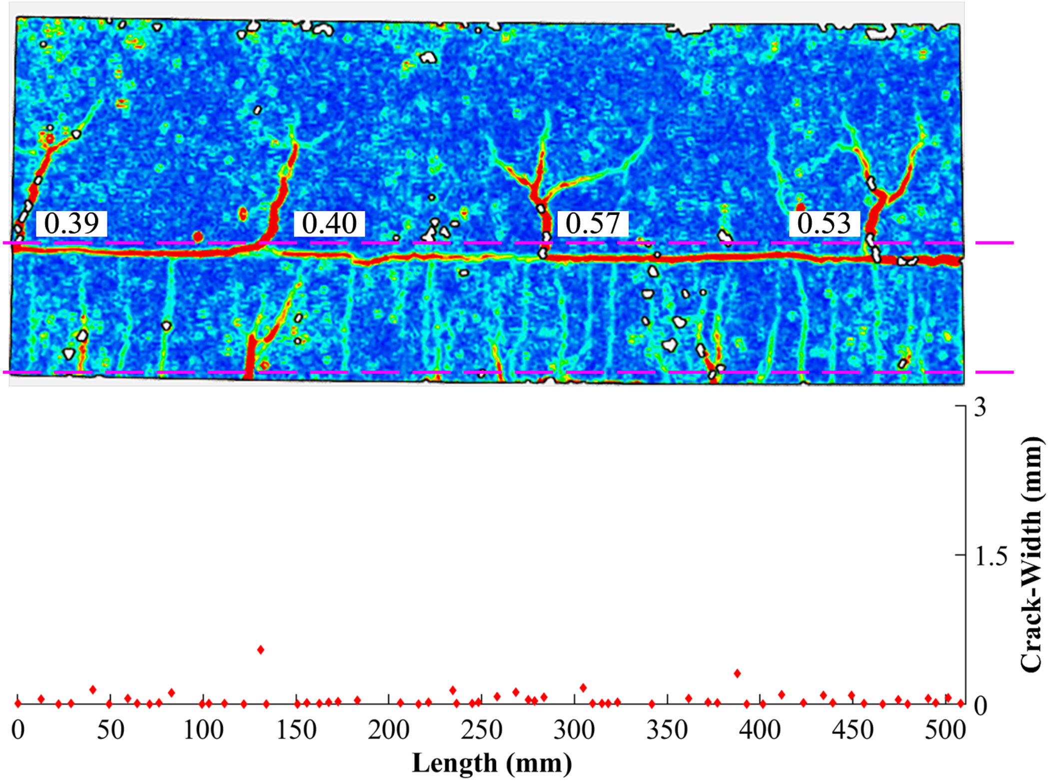

Figure 3.113: Development of large cracks at load step 65 KN

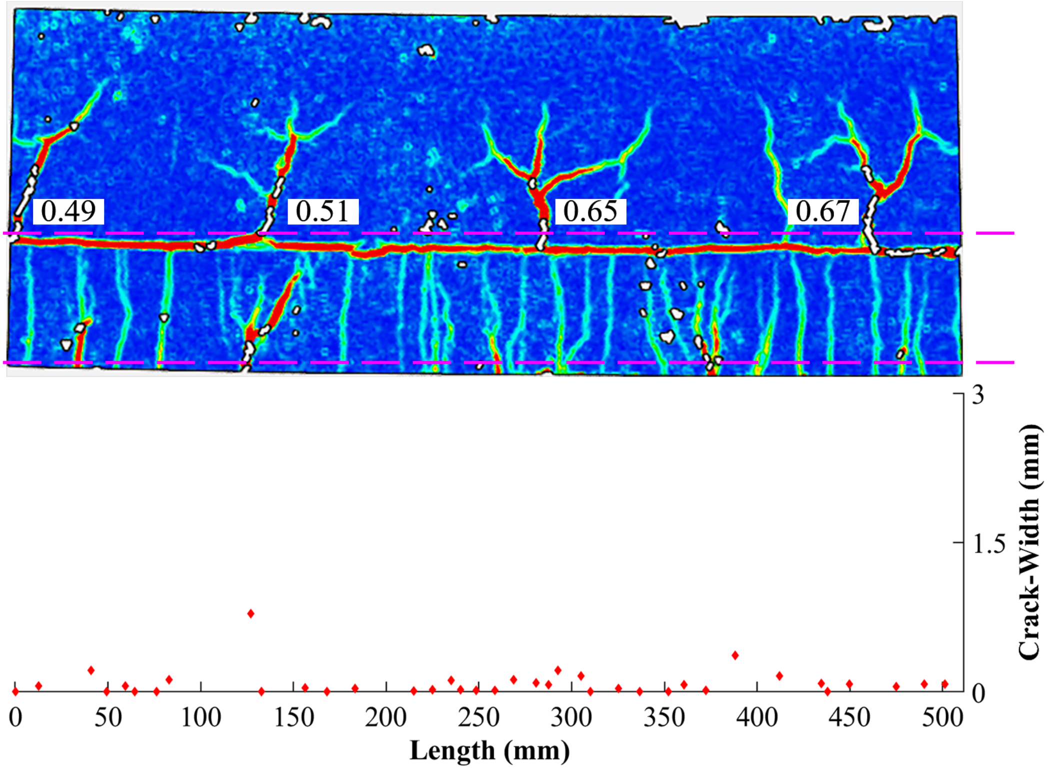

Figure 3.114: Development of large cracks at final load step 70 KN

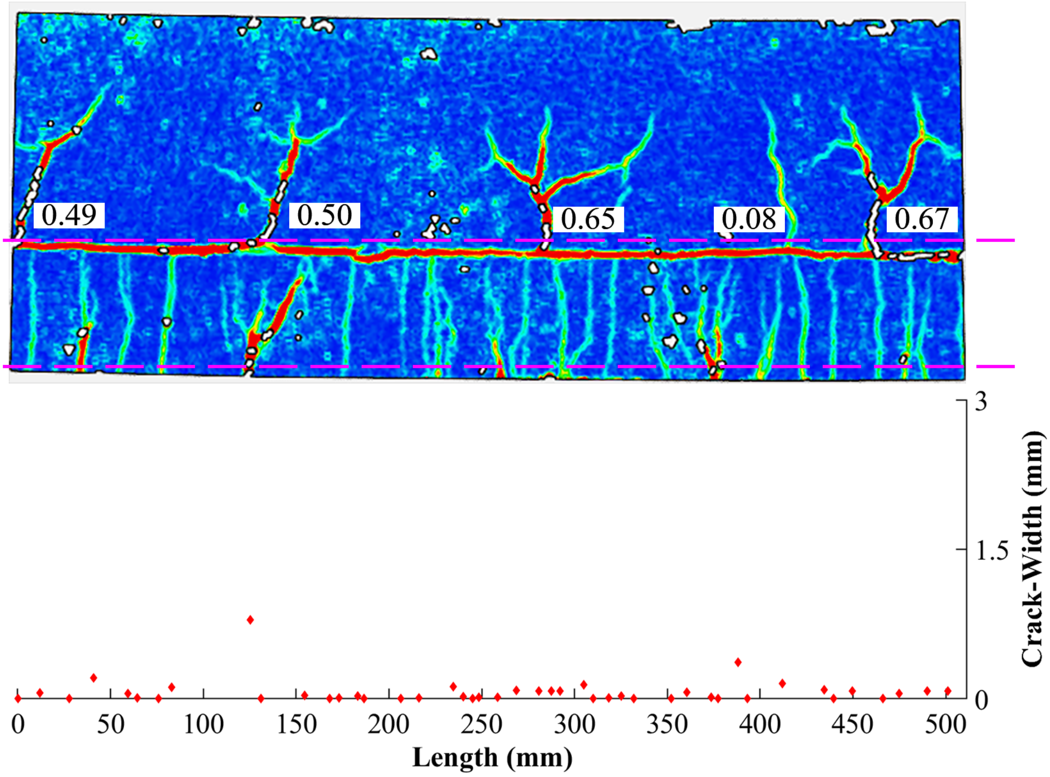

Figure 3.115: Development of large cracks at final load step 75 KN

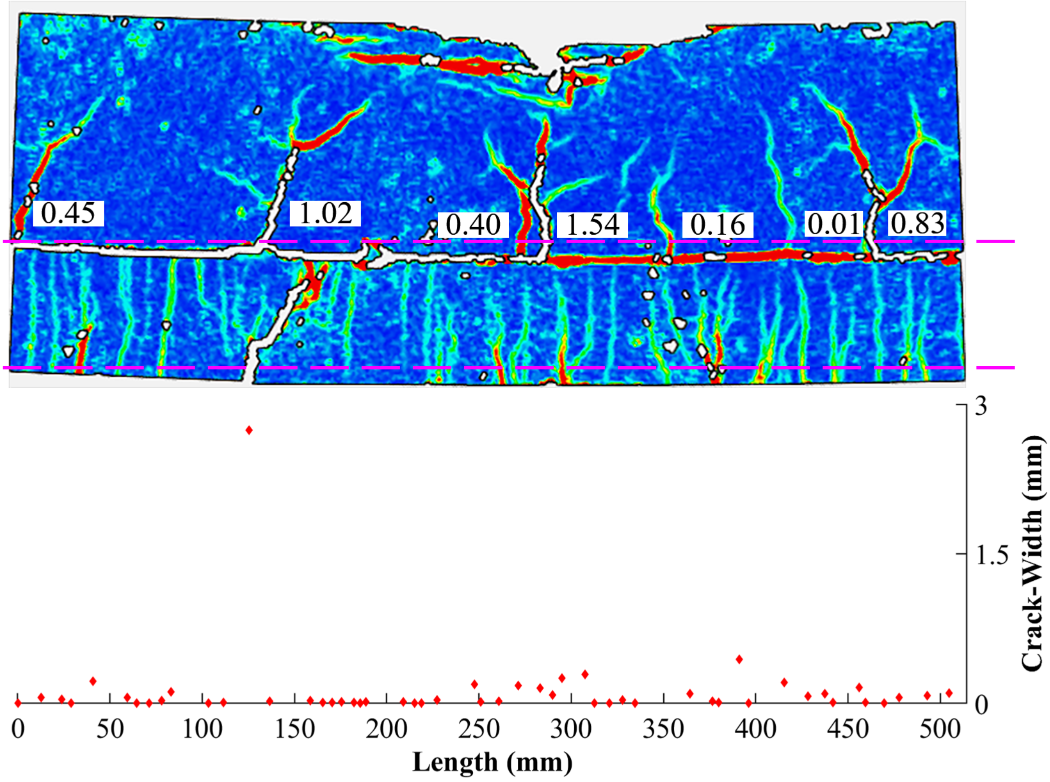

Figure 3.116: Development of large cracks at final load step 60 KN

The crack-widths measured during DIC are validated by comparing the plots of maximum crack-widths calculated using GOM correlate with crack-widths measure using Image J and visual inspection as shown in Figure 3.117. The deformations measured using GOM correlate are plotted with the deformations measured using LVDTs for comparison as shown in Figure 3.118.

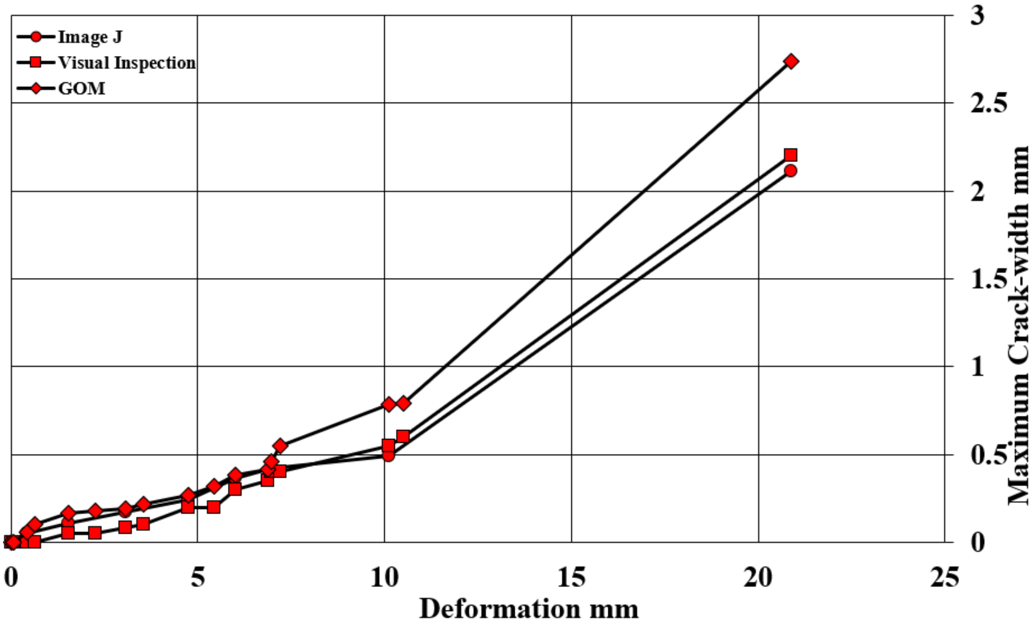

Figure 3.117: Comparison of maximum crack-widths measured using GOM, Image J and Visual Inspection

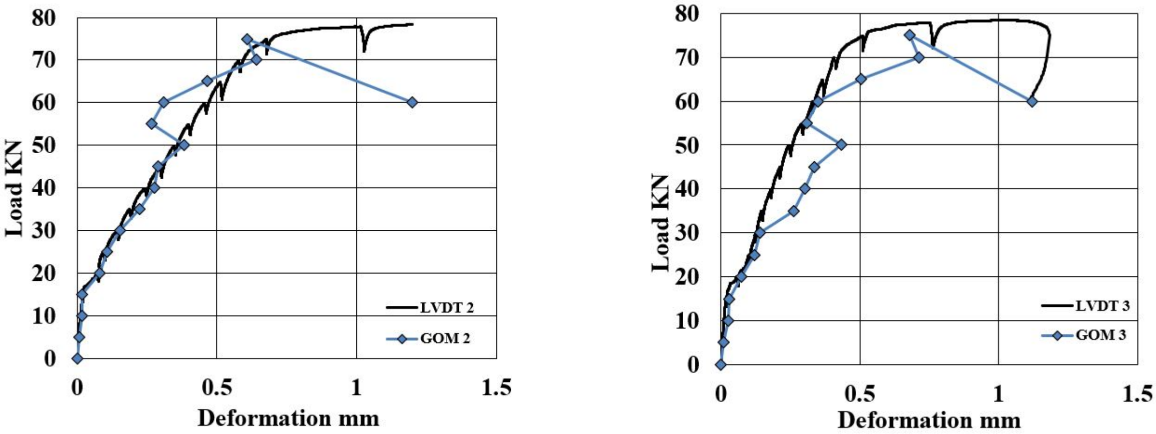

(a) P vs D plots of LVDT 2 vs GOM 2

(b) P vs D plots of LVDT 3 vs GOM 3

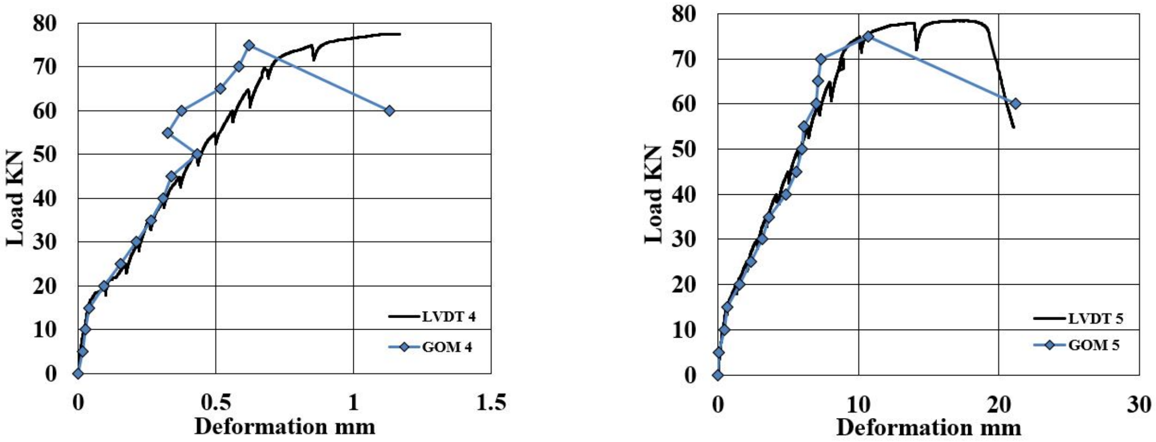

(c) P vs D plots of LVDT 4 vs GOM 4

(d) P vs D plots of LVDT 5 vs GOM 5

Figure 3.118: Calibration plots of GOM deformation with LVDT deformation

3.6.6 Hybrid Beam with Profiled Interface (P-PVA)

For the beam specimen with a profiled interface, the load vs deformation vs maximum crack-width measured at section 1 mm above the bottom edge is plotted as shown in Figure 3.119. A tabulation containing the properties of P-PVA specimen in constant moment region after the testing is discussed in Table 3.10.

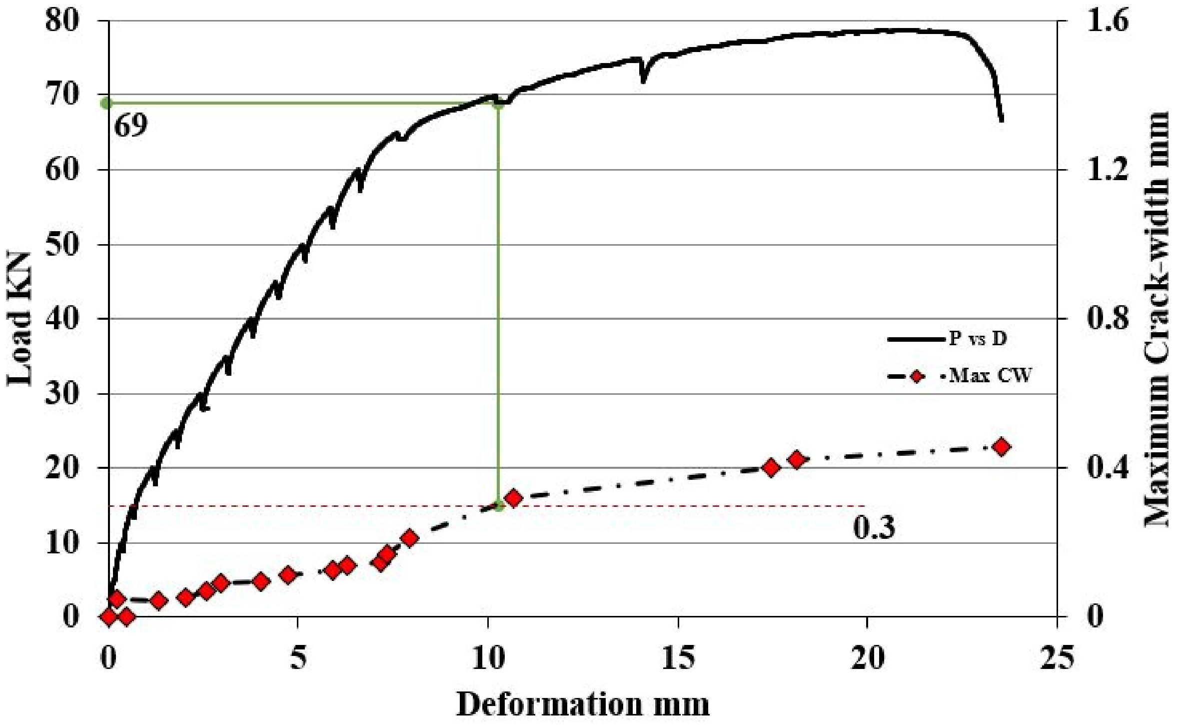

Figure 3.119: Load (P) vs Deformation (D) vs Maximum Crack-Width (Max CW)

Table 3.10: Properties of P-PVA beam specimen in constant moment region after testing

Property	**Value**
Number of cracks in the concrete layer	9
Average spacing between cracks	69.811 mm
Maximum load	78 KN
Maximum deformation	23.53 mm
Maximum crack-width	0.46 mm
Load at crack-width of 0.3 mm	69 KN

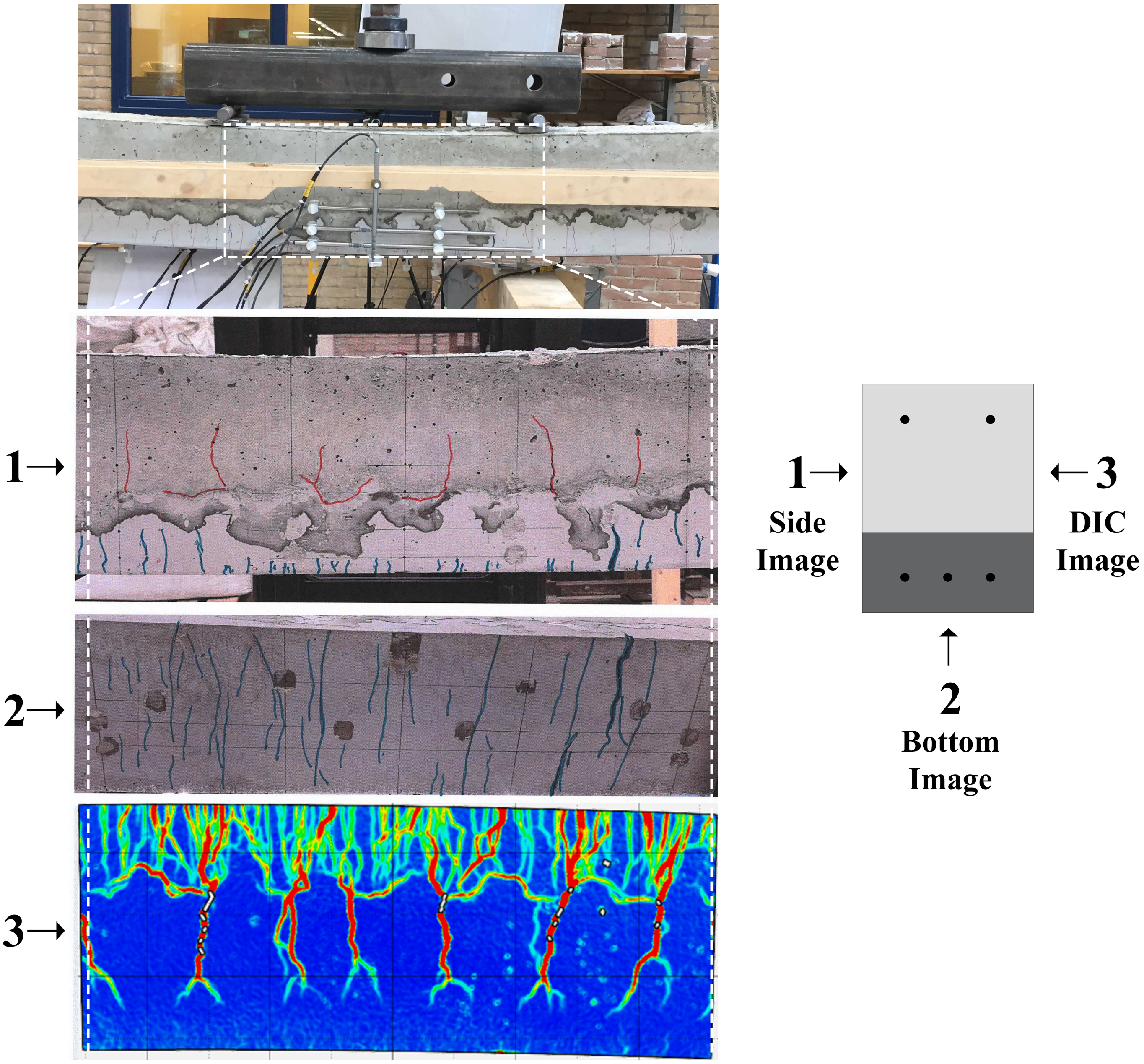

Figure 3.120: 1-LVDT side, 2-Bottom side and 3-DIC side of P-PVA beam specimen

The cracking pattern of the beam specimen (P-PVA) on the LVDT side, bottom side and DIC side is shown in Figure 3.120. The initial cracks appears in the SHCC layer at a load step of 10 KN as shown in Figure 3.121a. This is confirmed by observing a jump in strain ε_x at section 1. The initial cracks in the CC layer occur at a load step of 20 KN as seen in Figure 3.121b. The strain jump in section 3 confirms the presence of cracks in the CC layer. From Figure 3.121c, it can be observed that the cracks in the SHCC layer are not uniformly distributed and are directed towards the small debond lengths created at the interface during loading.

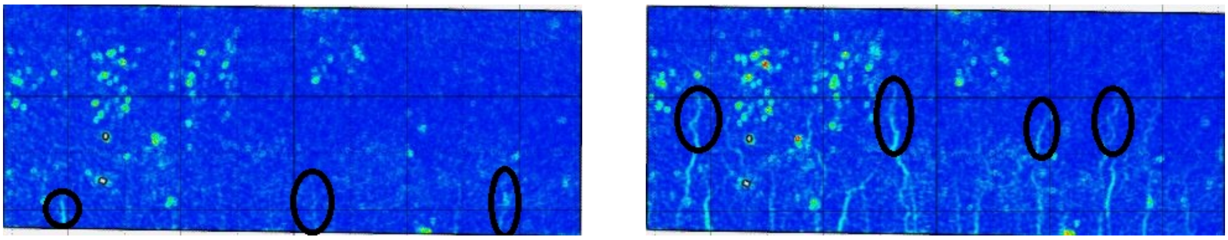

(a) First crack in SHCC layer at a load step of 10 KN **(b)** First crack in CC layer at a load step of 20 KN

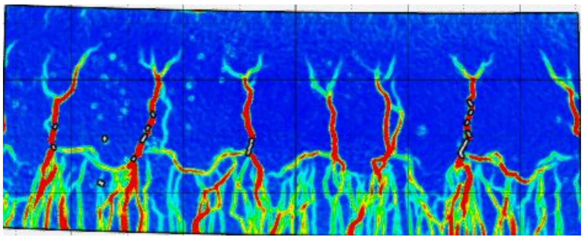

(c) Crack concentrations at very small debond lengths

Figure 3.121: Cracking in P-PVA specimen

A step-by-step propagation of cracks along with an increase in the crack-widths for all the load steps applied to the P-PVA beam specimen are shown in Figures 3.122 to 3.135. The crack-widths are measured in the SHCC layer and concrete layer at the section indicated in Figures 3.122 to 3.135. Since number of cracks in the concrete layer are less, the crack-widths at every load step are labelled next to the cracks. However, the number of cracks in the SHCC layer are too many to be individually labelled and so a scatter plot indicating the crack-width of various cracks is shown for every load step. The labelled crack-widths are in millimeters (mm).

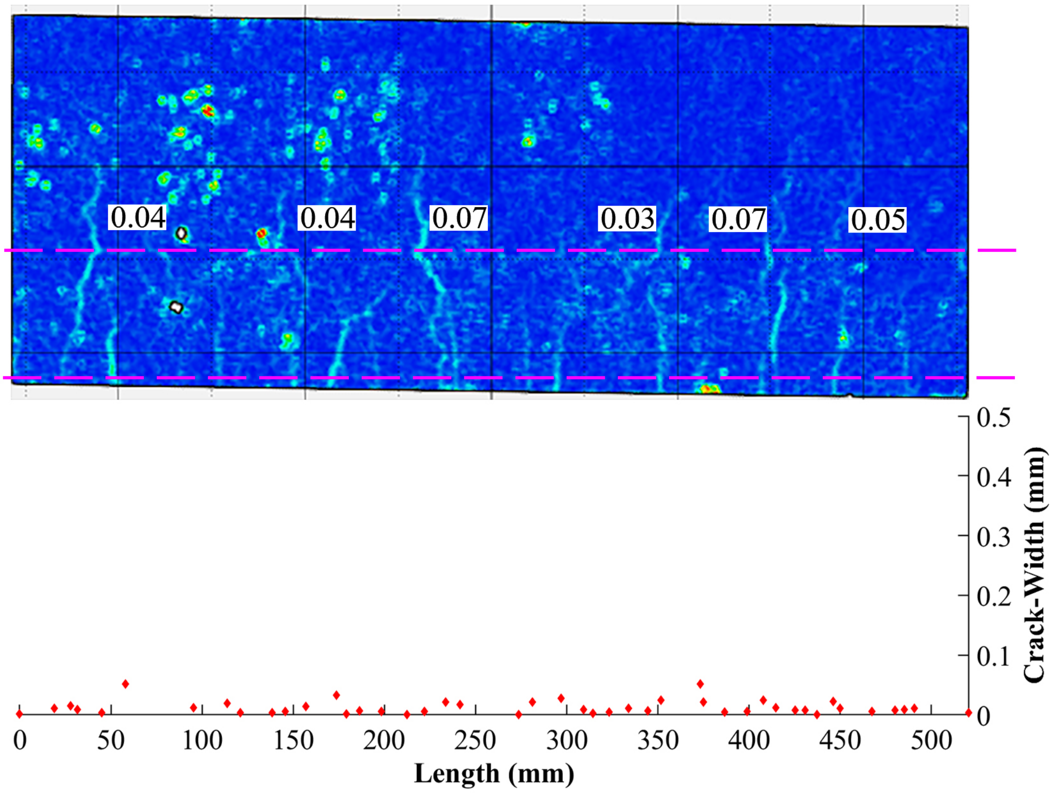

Figure 3.122: Development of cracks at load step 20 KN

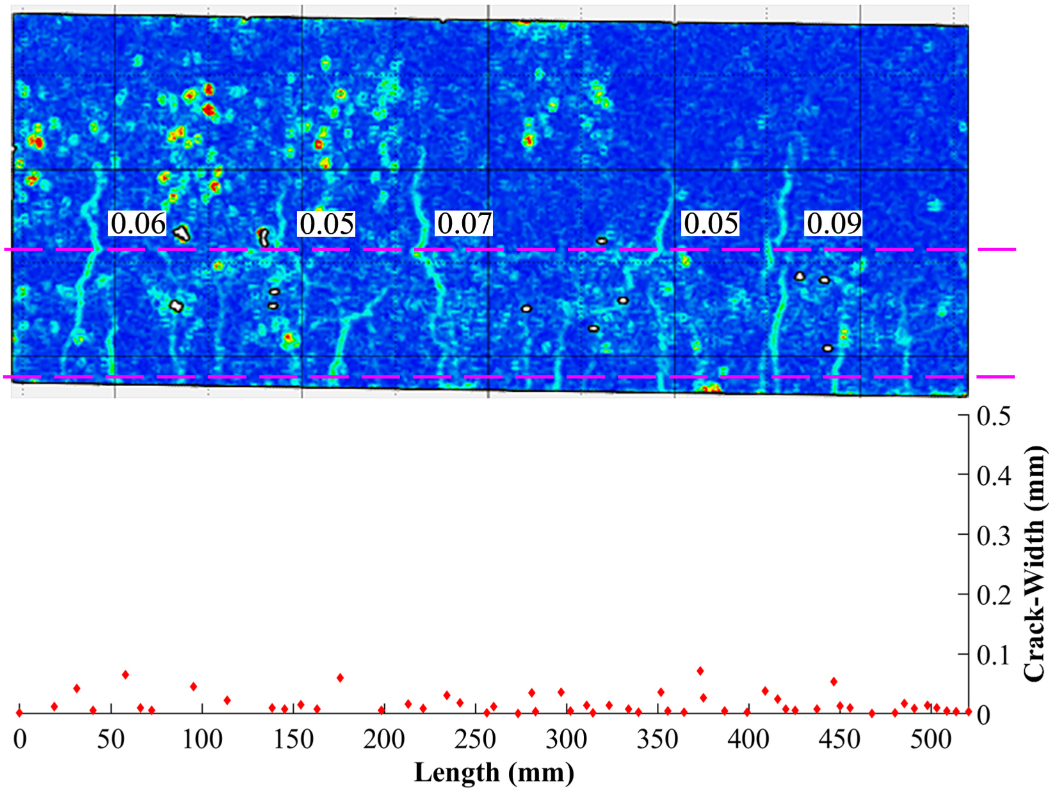

Figure 3.123: Development of cracks at load step 25 KN

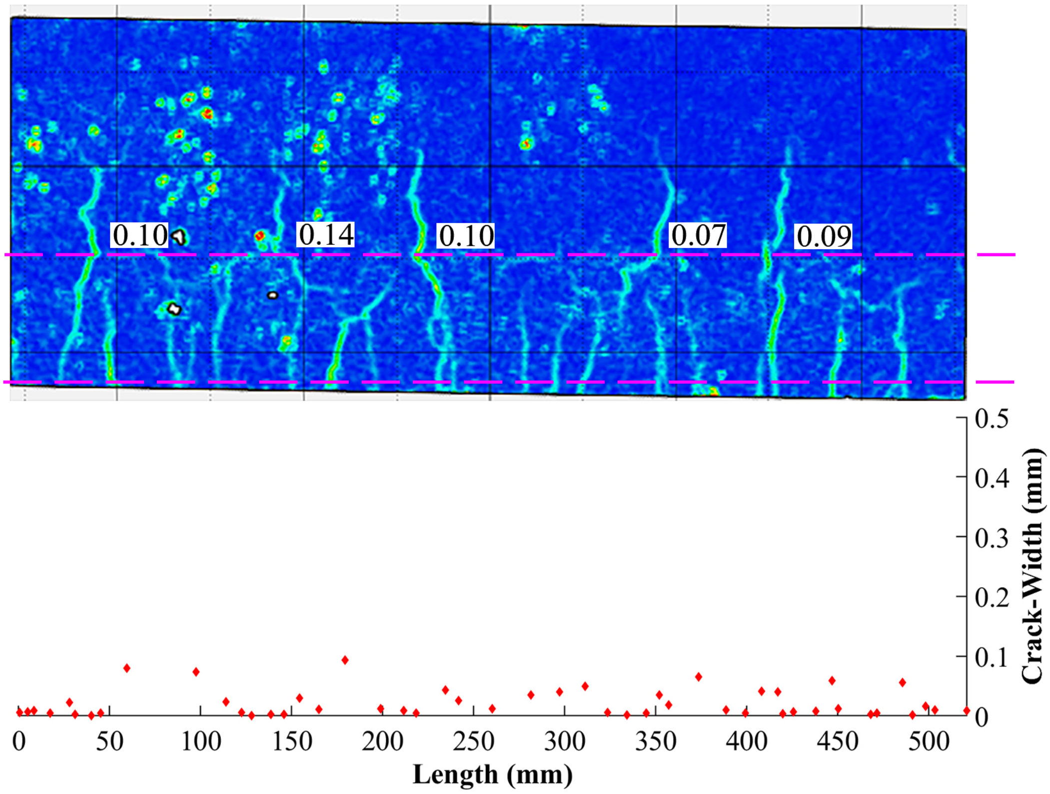

Figure 3.124: Development of cracks at load step 30 KN

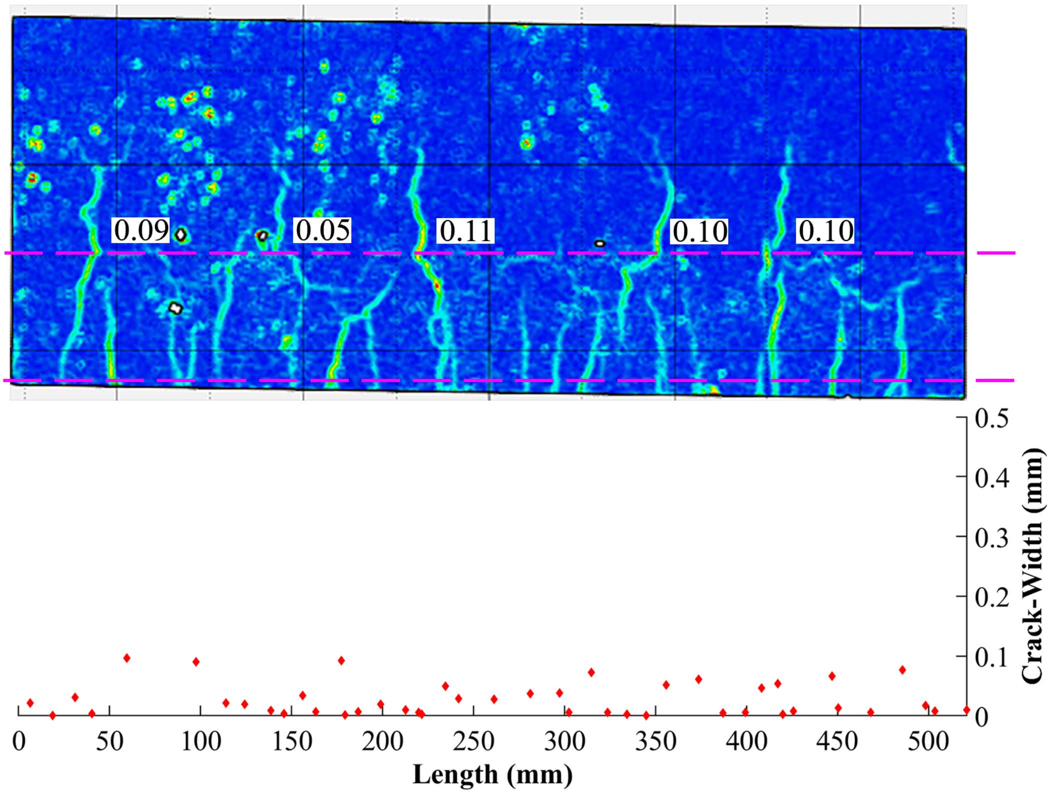

Figure 3.125: Development of cracks at load step 35 KN

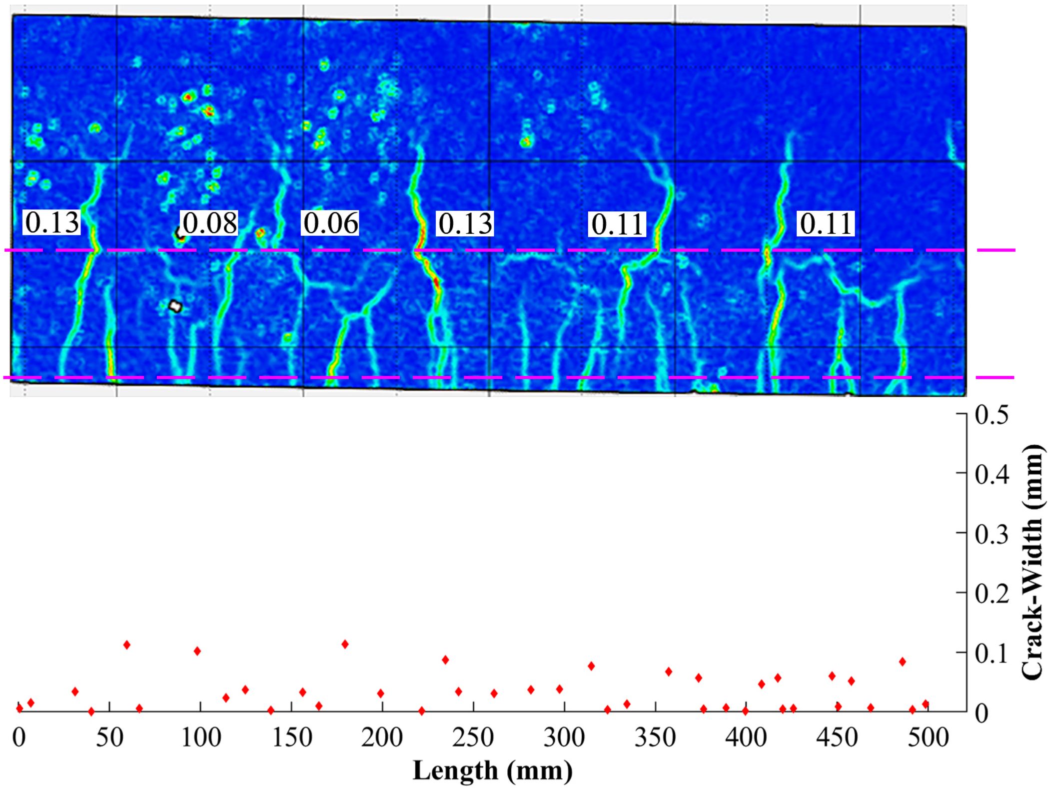

Figure 3.126: Development of cracks at load step 40 KN

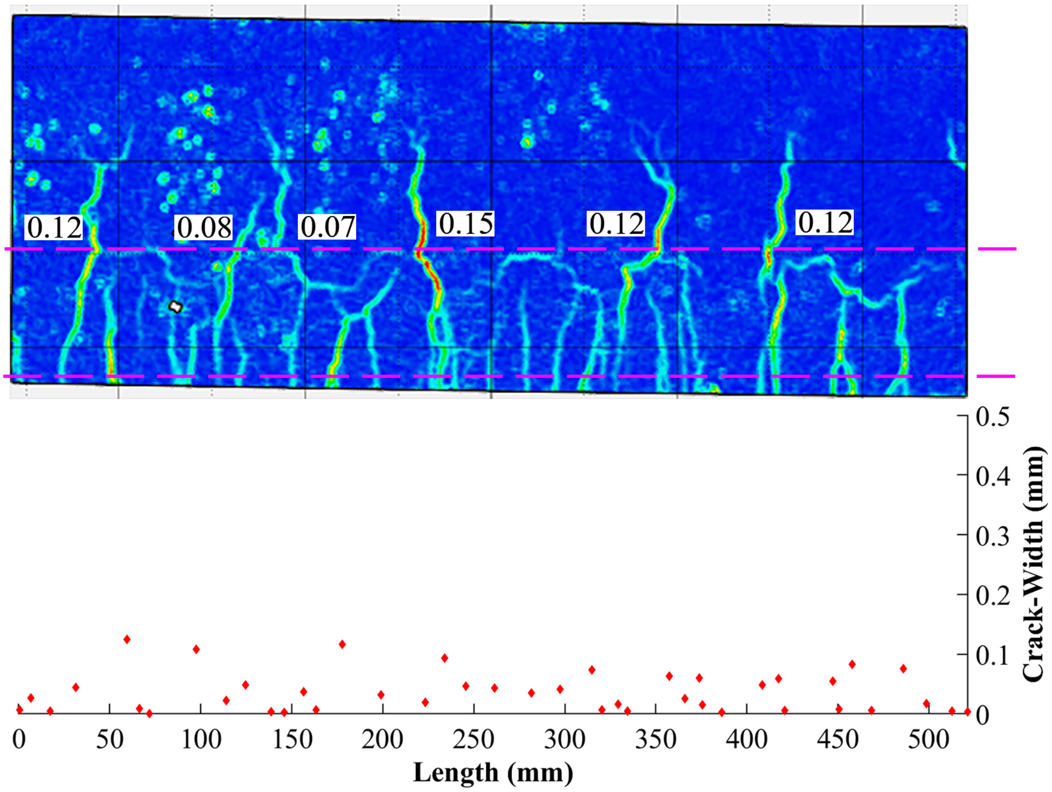

Figure 3.127: Development of cracks at load step 45 KN

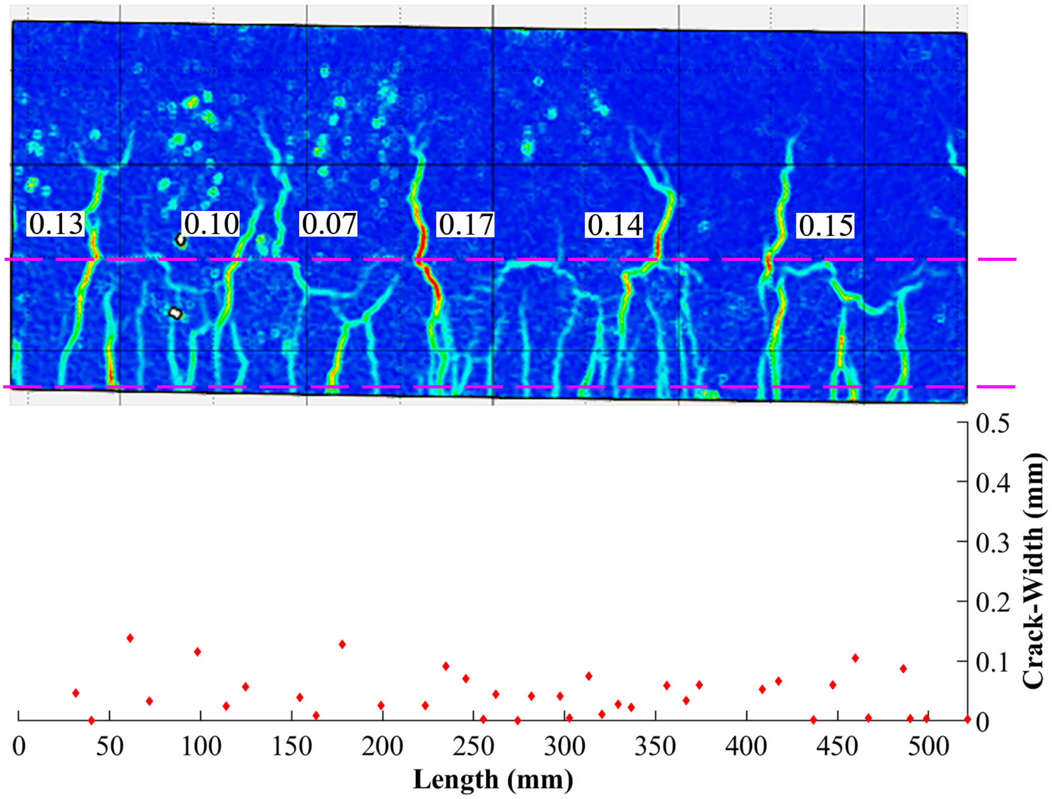

Figure 3.128: Development of cracks at load step 50 KN

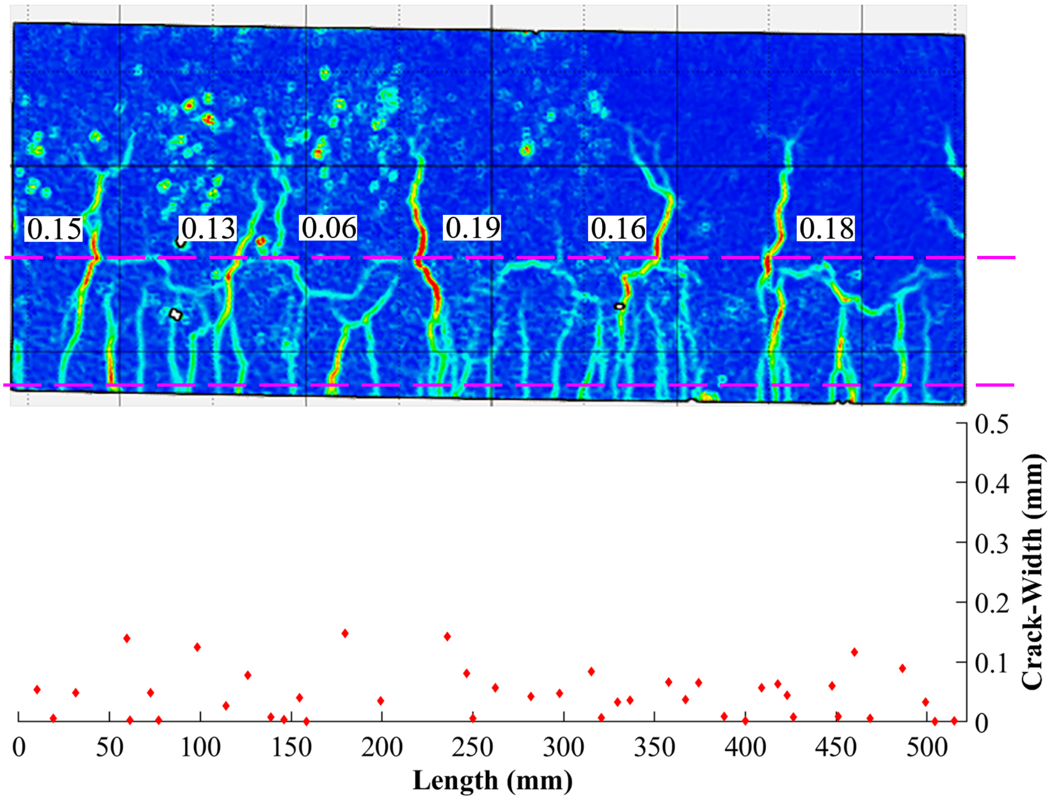

Figure 3.129: Development of cracks at load step 55 KN

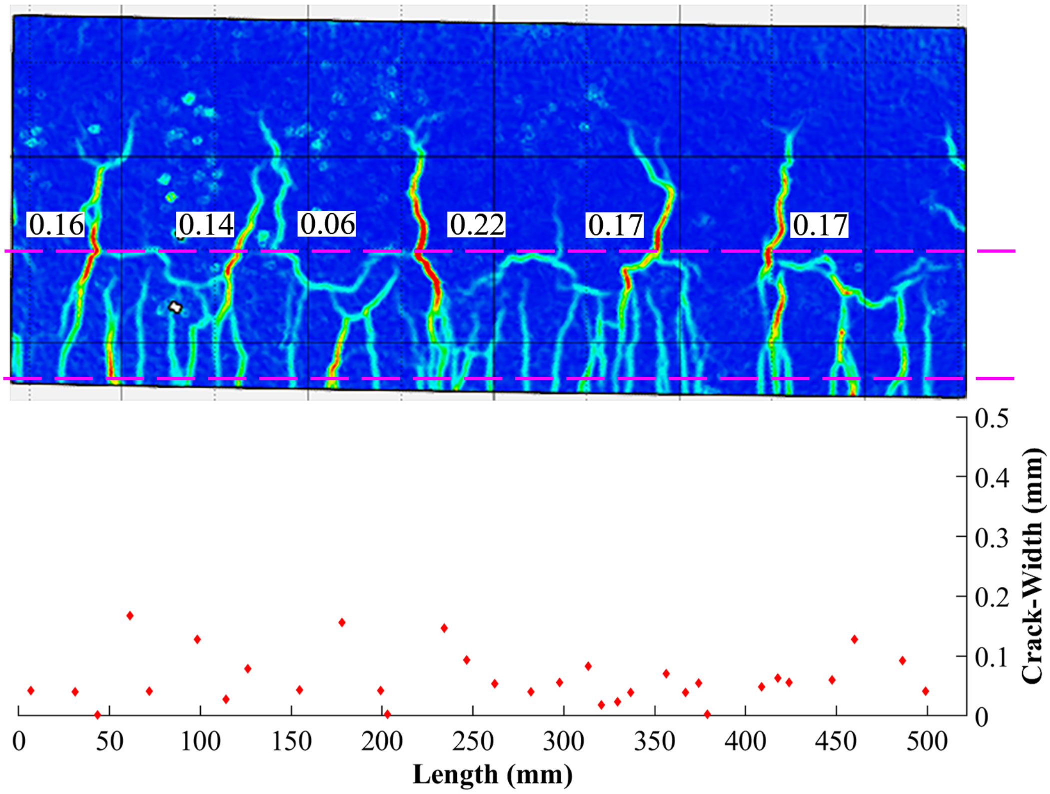

Figure 3.130: Development of cracks at load step 60 KN

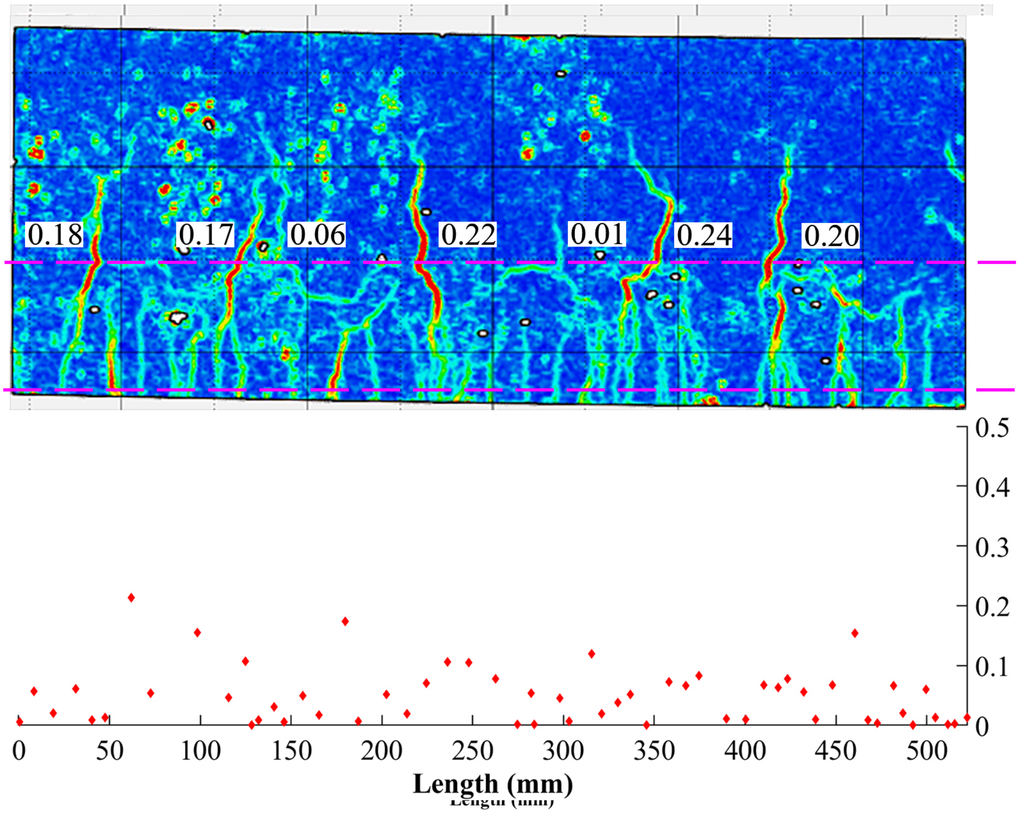

Figure 3.131: Development of cracks at load step 65 KN

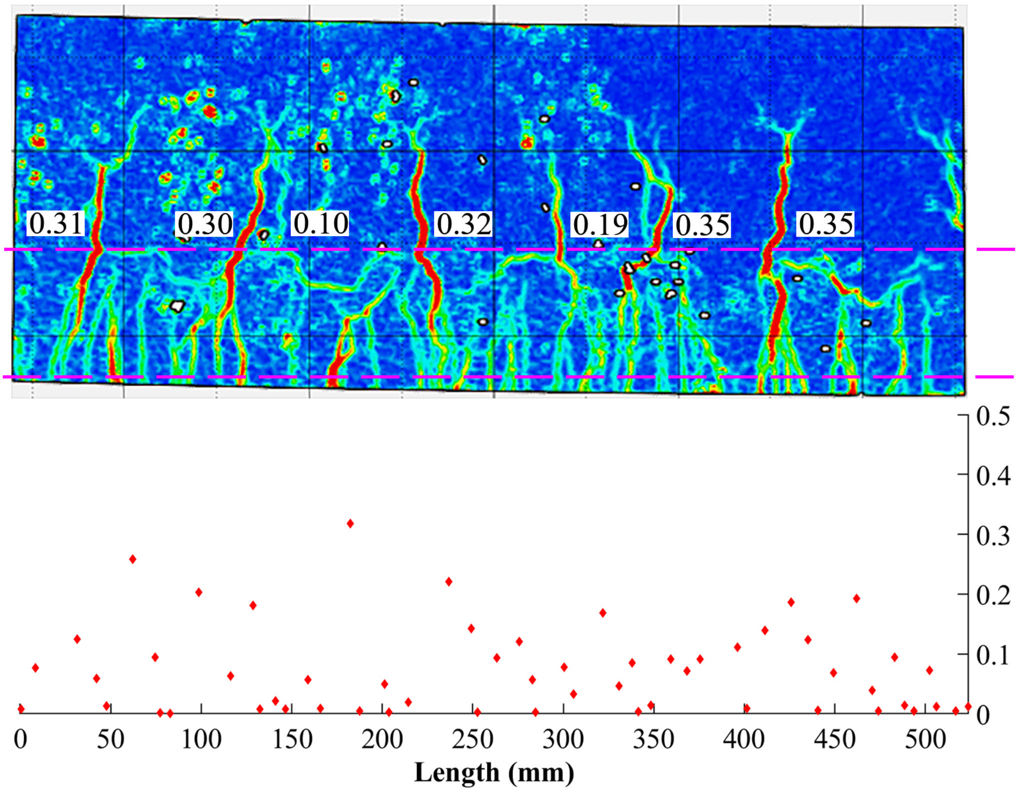

Figure 3.132: Development of cracks at load step 70 KN

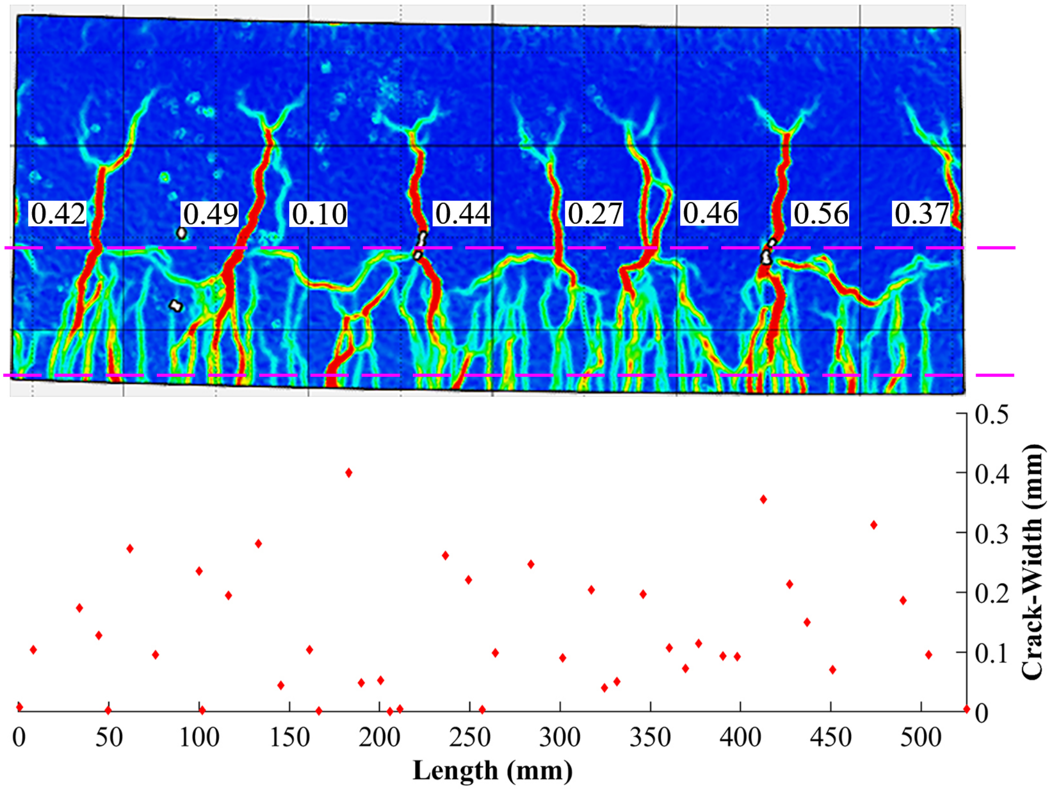

Figure 3.133: Development of cracks at load step 75 KN

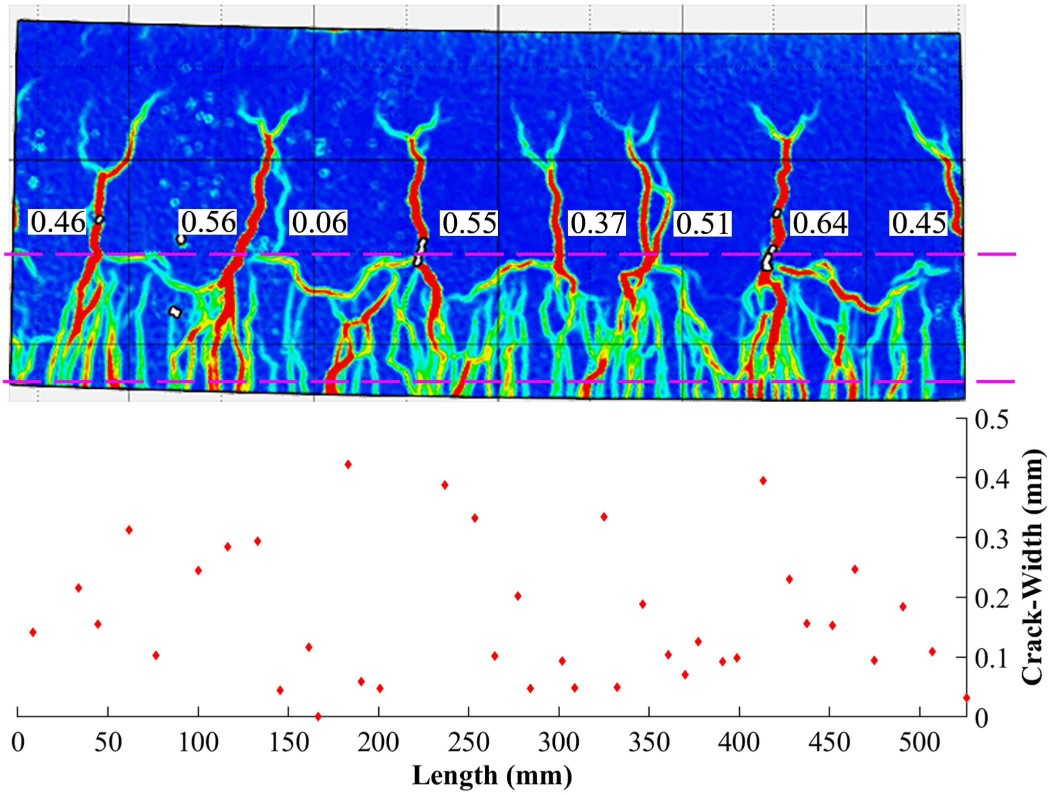

Figure 3.134: Development of cracks at load step 77 KN

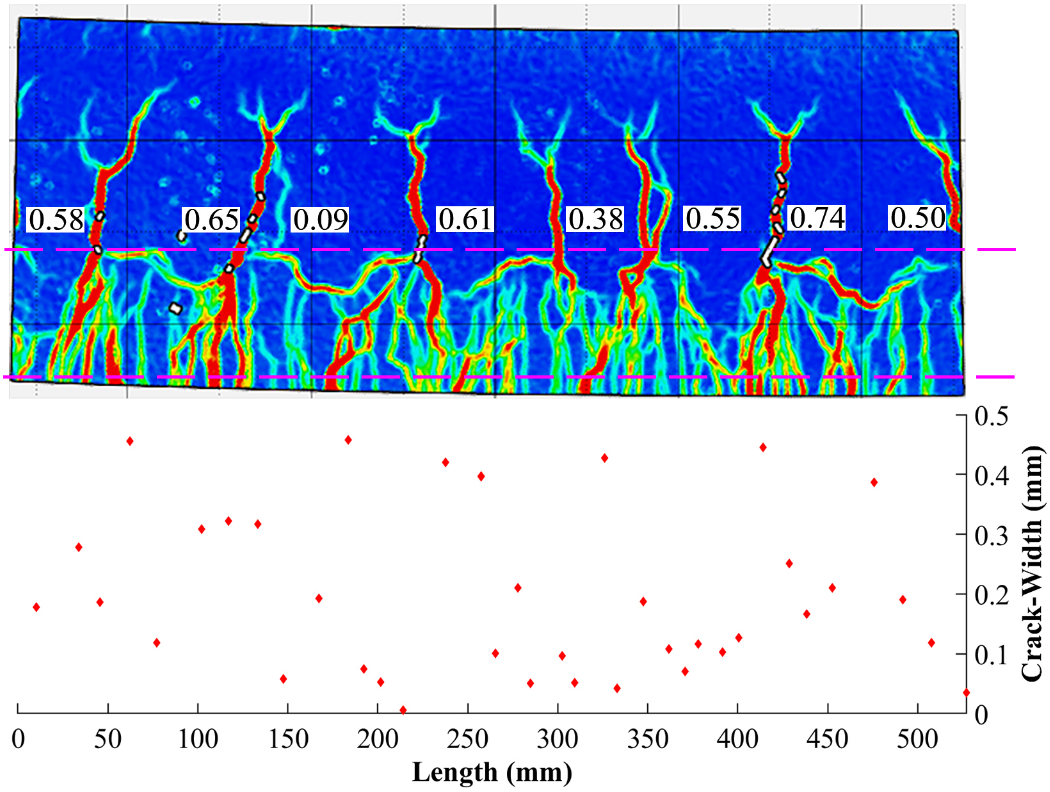

Figure 3.135: Development of cracks at load step 78 KN

Inspection using Image J and visual inspection is conducted to determine the maximum crack-widths and are compared with the results obtained using GOM correlate software as shown in Figure 3.136. The calibration of the values obtained from GOM correlate is performed by comparing the deformations with the values obtained from LVDTs as shown in Figure 3.137.

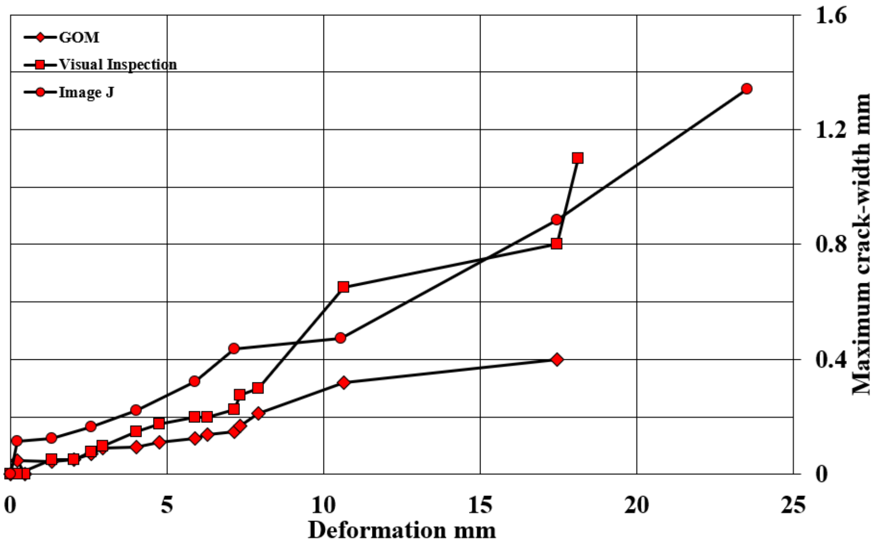

Figure 3.136: Comparison of maximum crack-widths measured using GOM, Image J and Visual Inspection

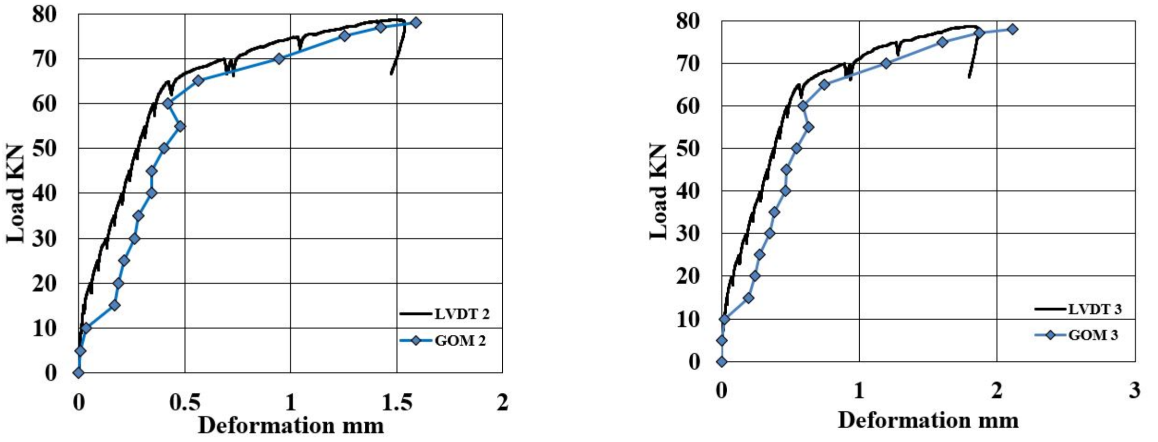

(a) P vs D plots of LVDT 2 vs GOM 2 **(b)** P vs D plots of LVDT 3 vs GOM 3

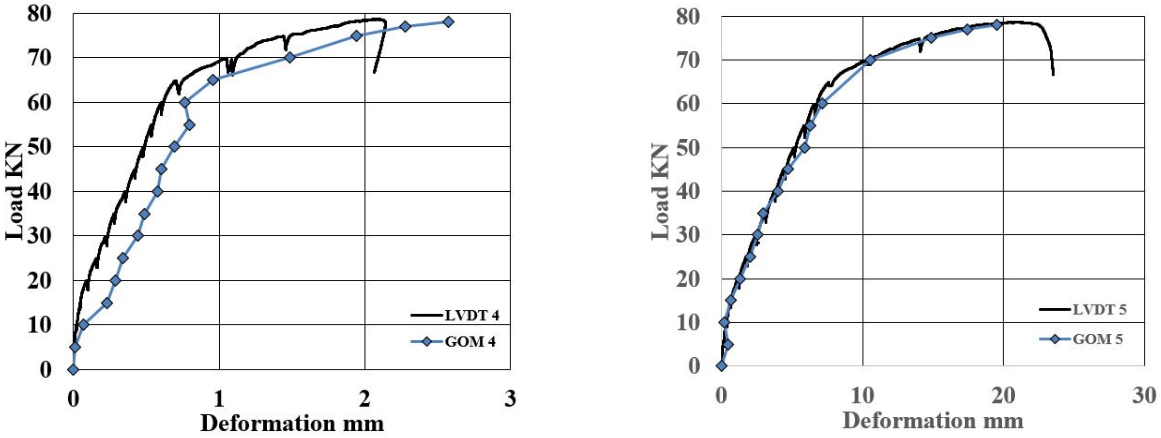

(c) P vs D plots of LVDT 4 vs GOM 4 **(d)** P vs D plots of LVDT 5 vs GOM 5

Figure 3.137: Calibration plots of GOM deformation with LVDT deformation

3.6.7 Hybrid Beam with Smooth Interface and HMPE Fibers (S-HMPE)

The load vs deformation vs maximum crack-width of the beam specimen (S-HMPE) at section 1 mm above the bottom edge of the beam is shown in Figure 3.138. The properties of the beam specimen after the testing are discussed in Table 3.11.

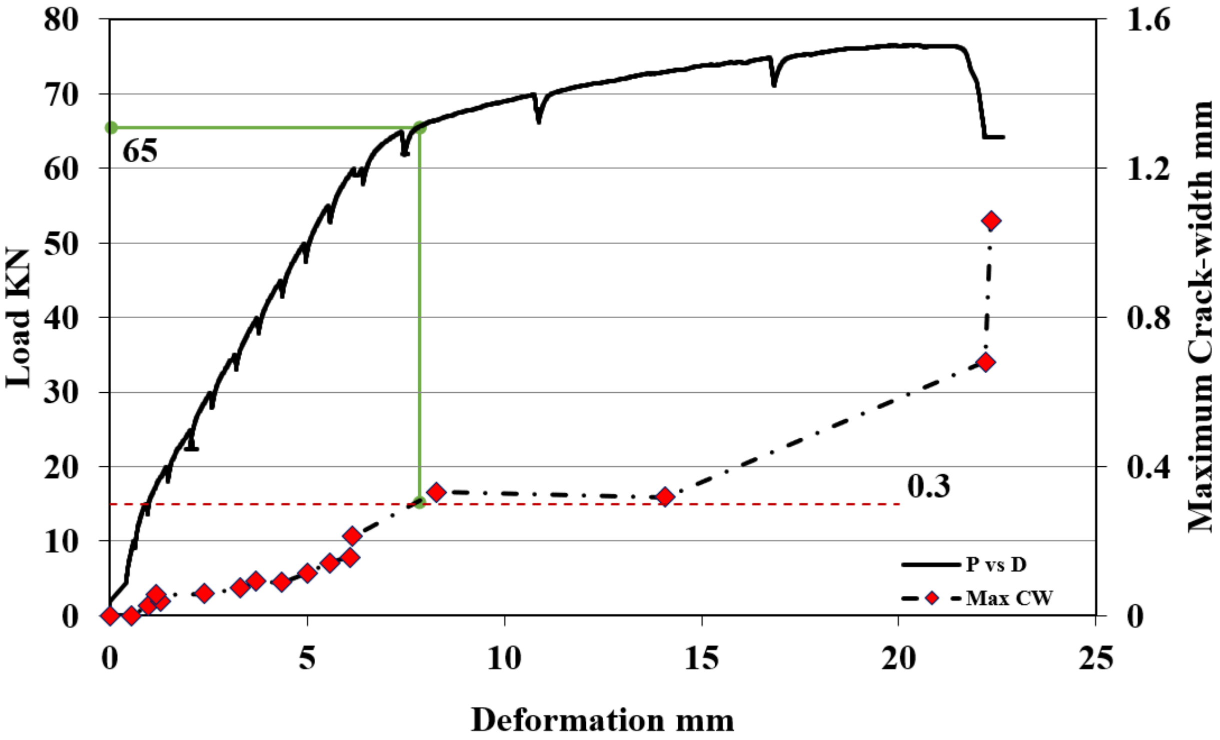

Figure 3.138: Load (P) vs Deformation (D) vs Maximum Crack-Width (Max CW)

Table 3.11: Properties of S-HMPE beam specimen in constant moment region after testing

Property	**Value**
Number of cracks in the concrete layer	9
Average spacing between cracks	60.23 mm
Maximum load	77 KN
Maximum deformation	22.6459 mm
Maximum crack-width	1.059 mm
Load at crack-width of 0.3 mm	65 KN

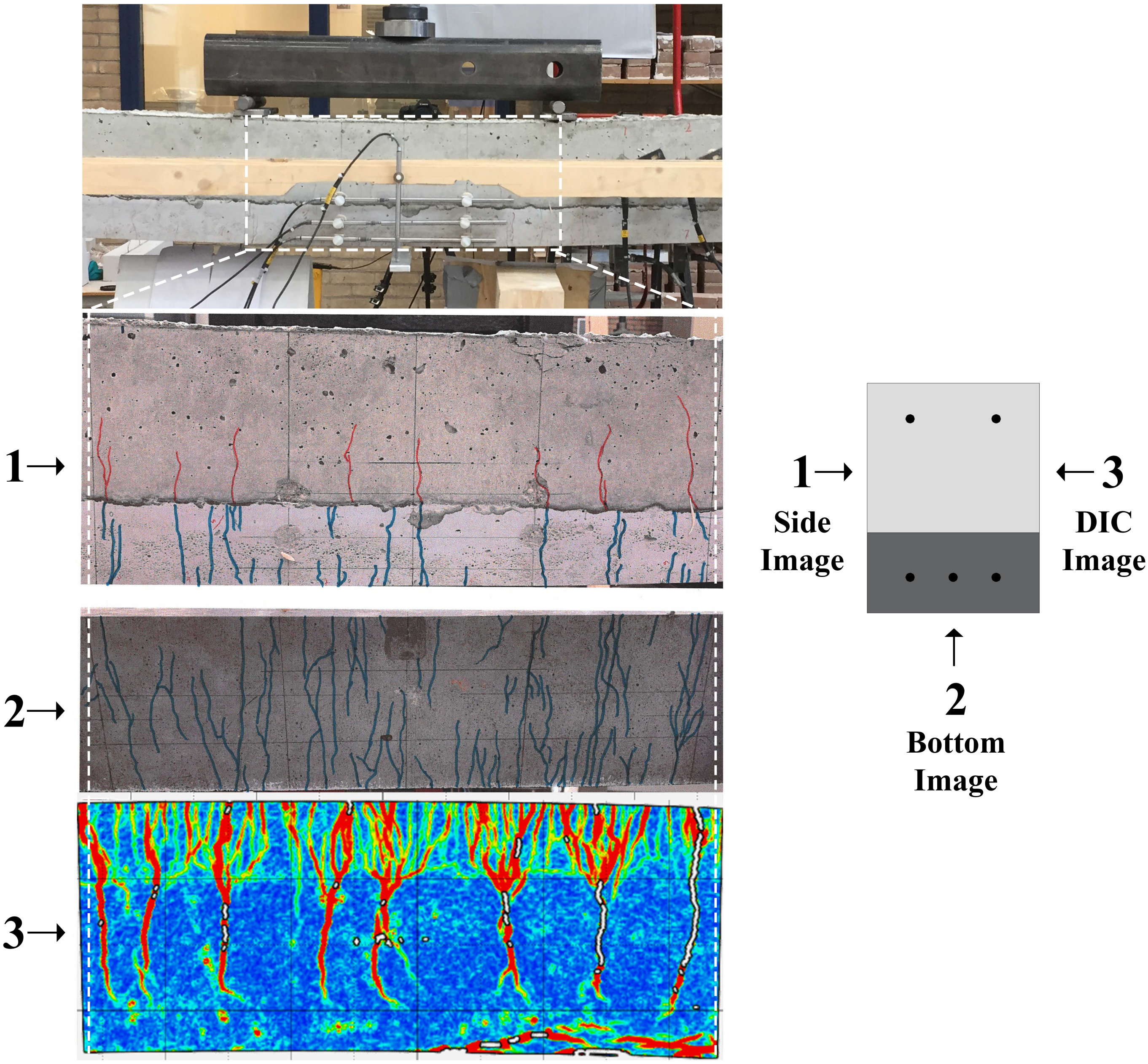

Figure 3.139: 1-LVDT side, 2-Bottom side and 3-DIC side of S-HMPE beam specimen

The crack pattern of the beam S-HMPE is shown in Figure 3.139. The initial cracks appear in the SHCC layer at a load step of 10 KN as shown in Figure 3.140a. This is confirmed by the jumps seen in strain at section 1. The initial cracks appear in the CC layer at the load step of 15 KN as seen in Figure 3.140b also confirmed by the jump in strain at section 3. From Figure 3.140c, it can be observed that a large number of distributed cracks are formed in SHCC layer due to sufficient debond length.

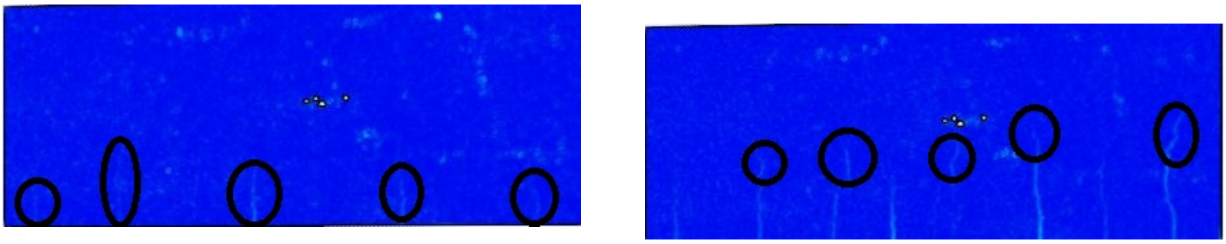

(a) First cracks in SHCC layer and cracking at the interface at load step 10 KN

(b) First cracks in CC layer at load step of 15 KN

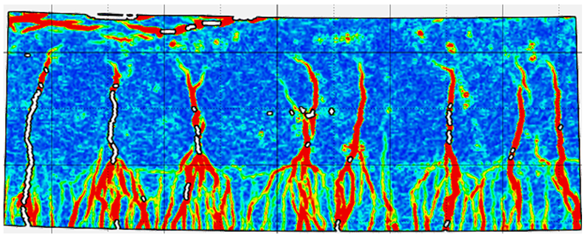

(c) uniformly distributed cracks in SHCC layer

Figure 3.140: Cracking in S-HMPE specimen

A step-by-step propagation of cracks along with an increase in the crack-widths for all the load steps applied to the S-HMPE beam specimen are shown in Figures 3.141 to 3.154. The crack-widths are measured in the SHCC layer and concrete layer at the sections indicated in Figures 3.141 to 3.154. Since the number of cracks in the concrete layer are less, the crack-width at every load step is labelled next to the cracks. However, the number of cracks in the SHCC layer are too many to be individually labelled and so a scatter plot indicating the crack-width of various cracks is shown for every load step. The labelled crack-widths are in millimeters (mm).

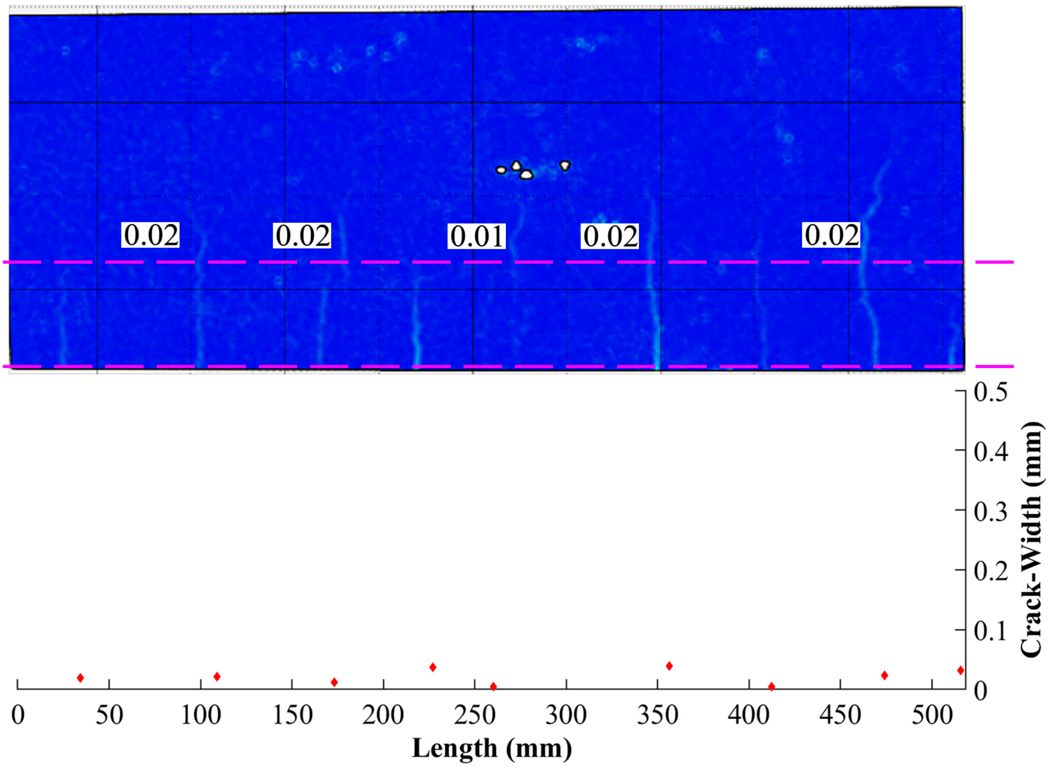

Figure 3.141: Development of cracks at load step 15 KN

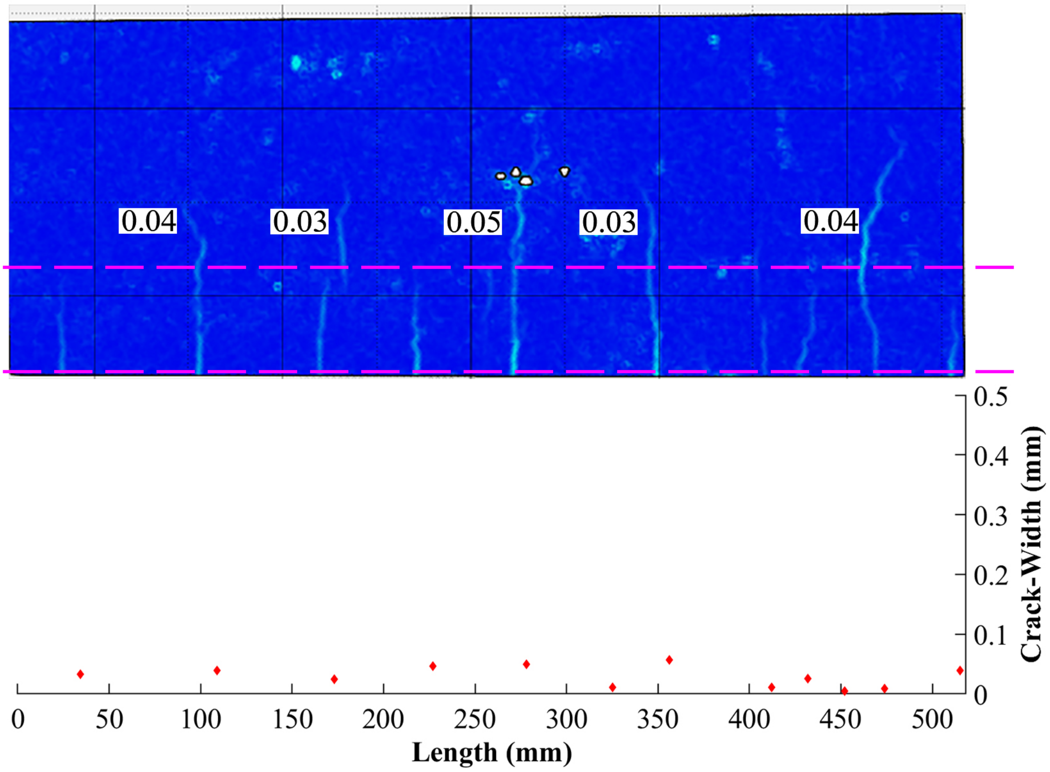

Figure 3.142: Development of cracks at load step 20 KN

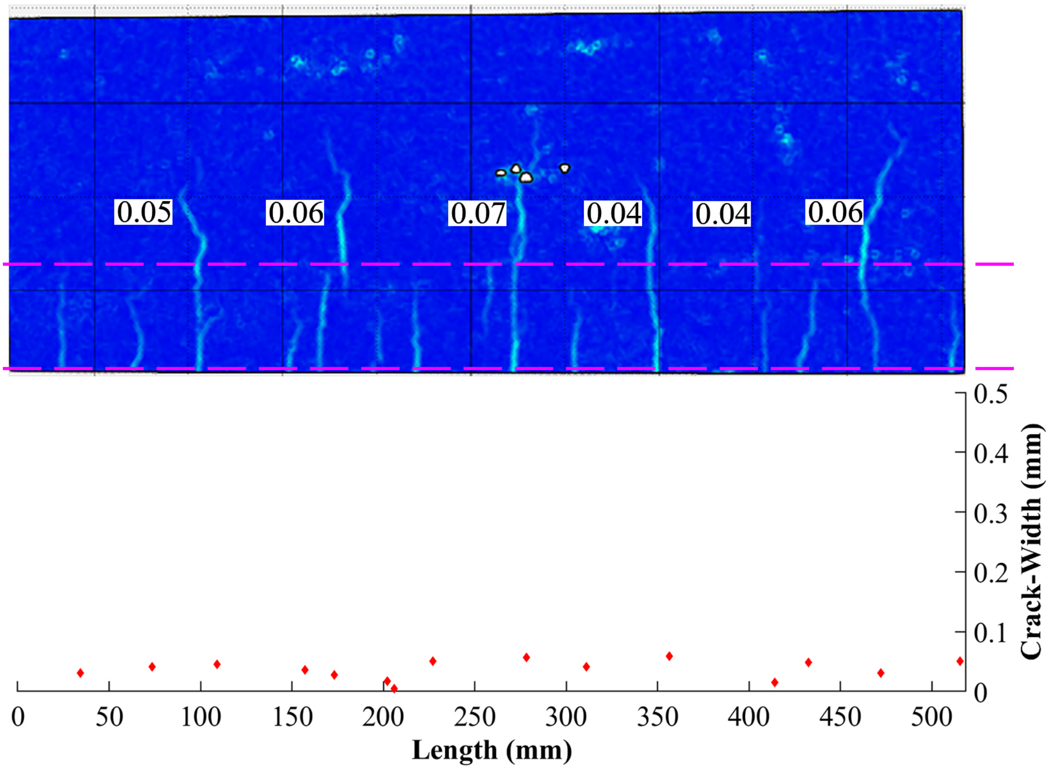

Figure 3.143: Development of cracks at load step 25 KN

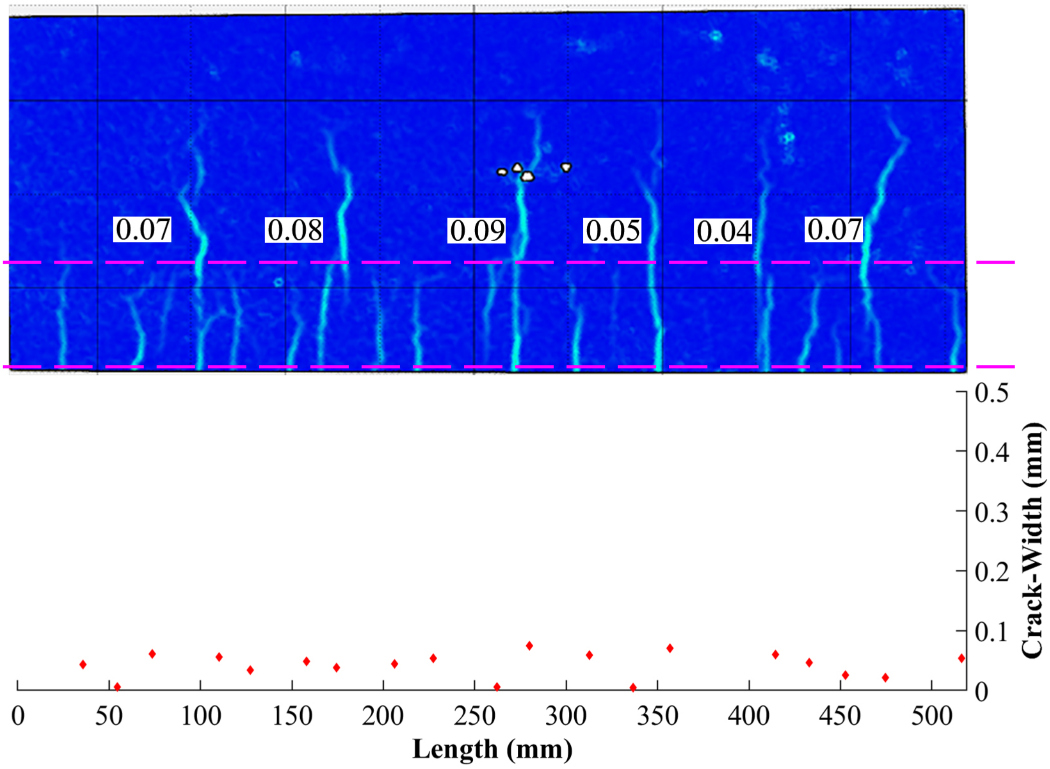

Figure 3.144: Development of cracks at load step 30 KN

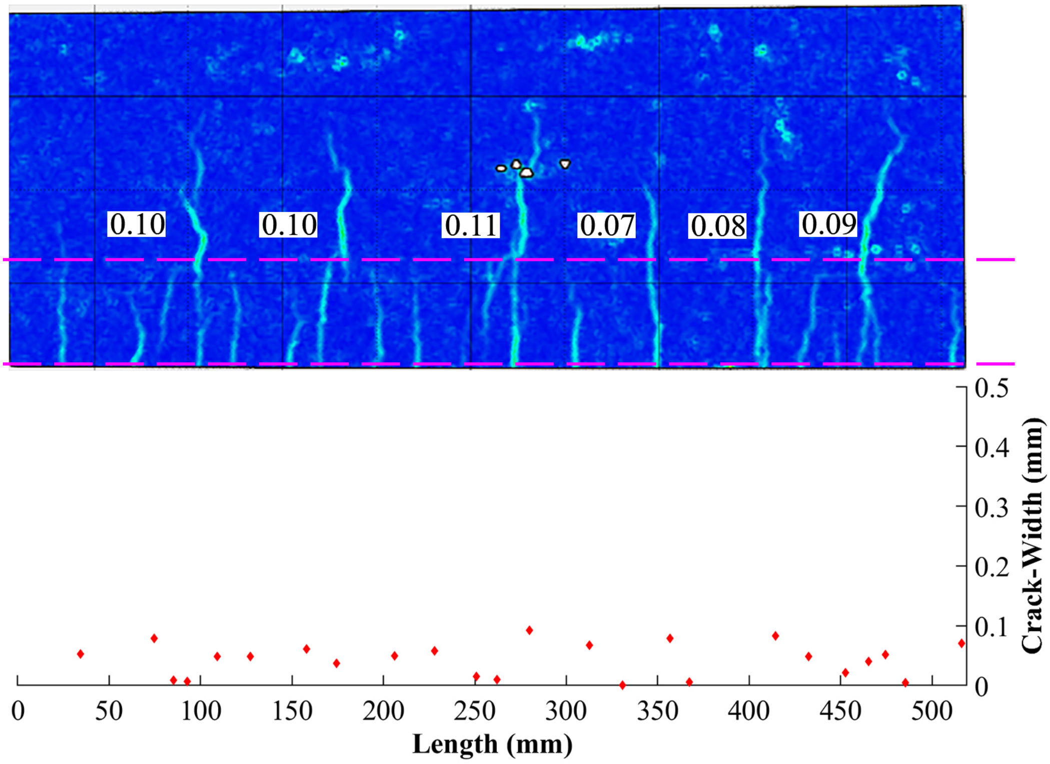

Figure 3.145: Development of cracks at load step 35 KN

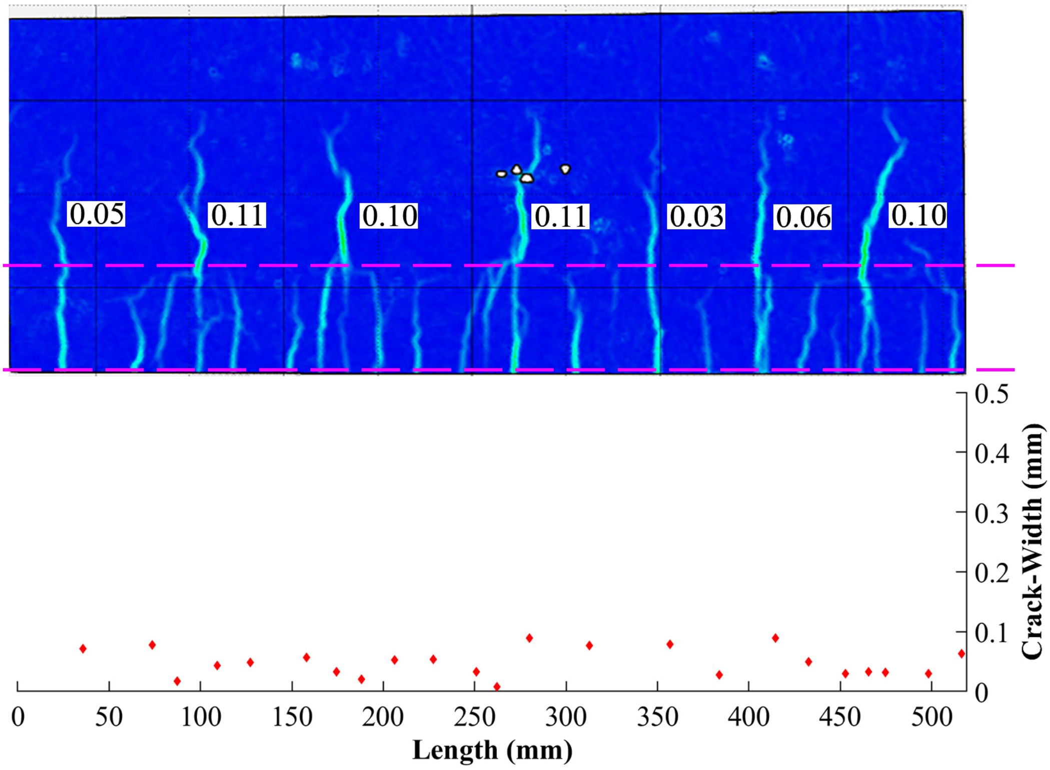

Figure 3.146: Development of cracks at load step 40 KN

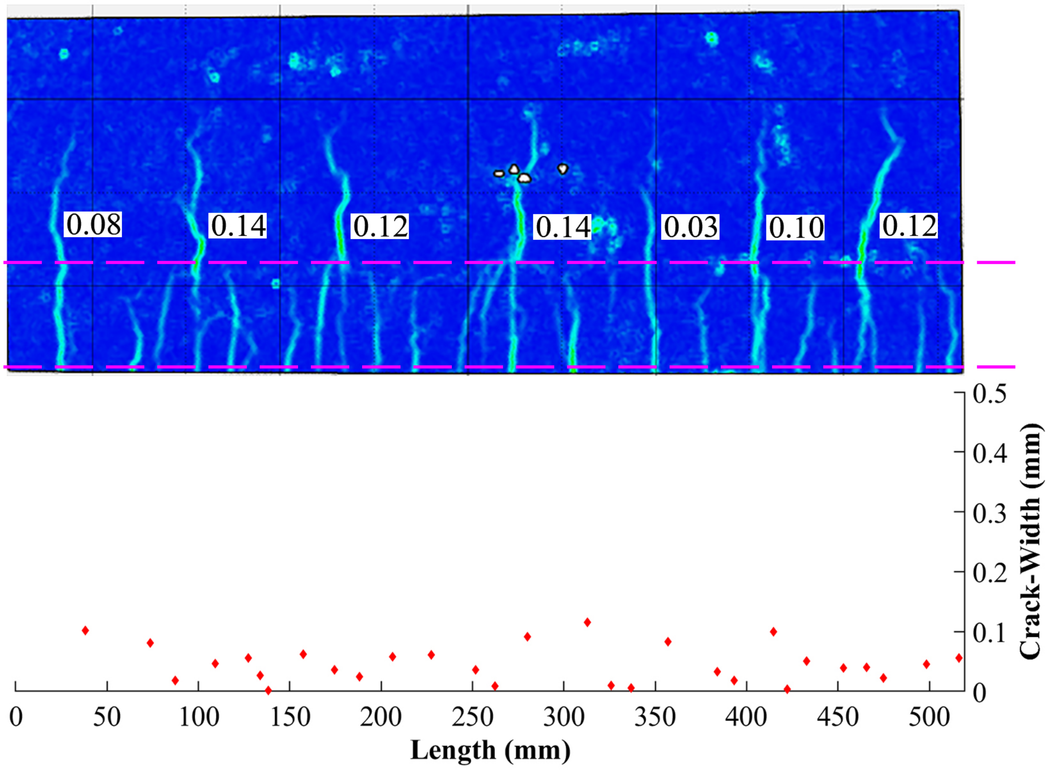

Figure 3.147: Development of cracks at load step 45 KN

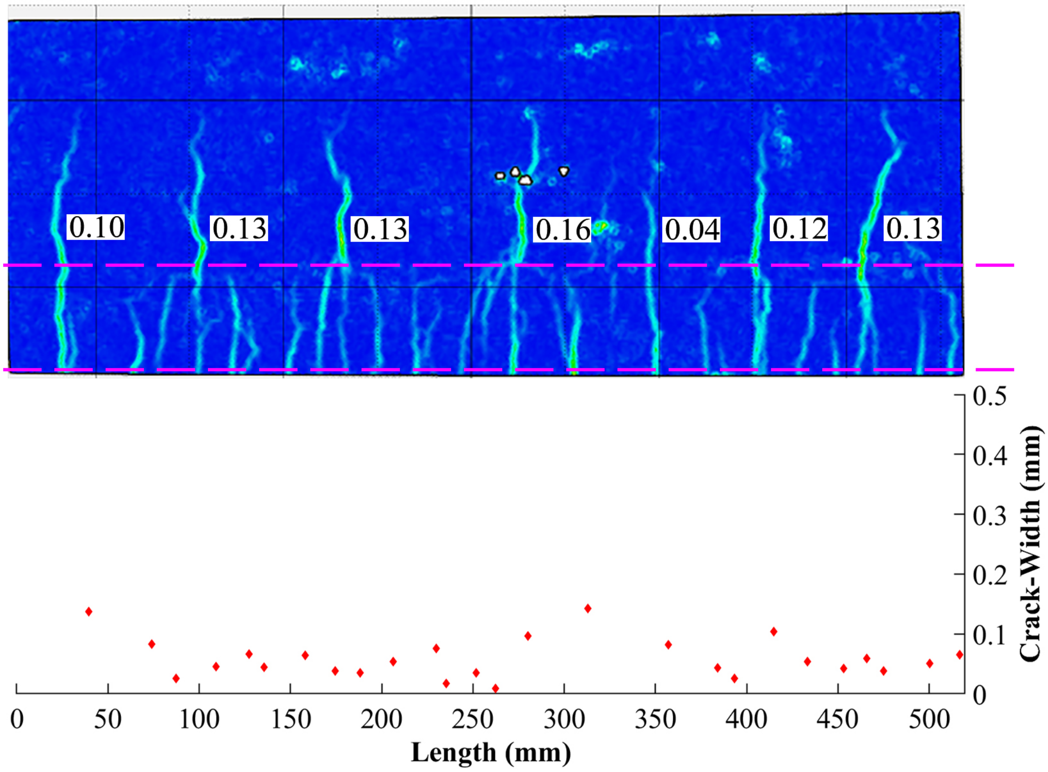

Figure 3.148: Development of cracks at load step 50 KN

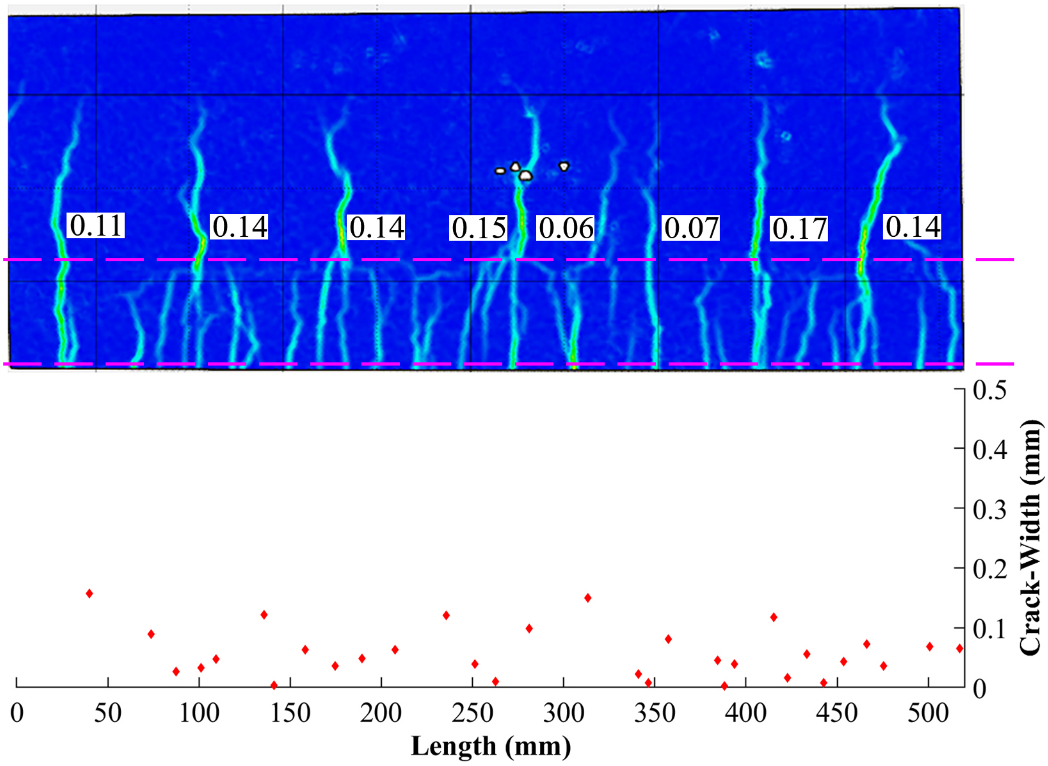

Figure 3.149: Development of cracks at load step 55 KN

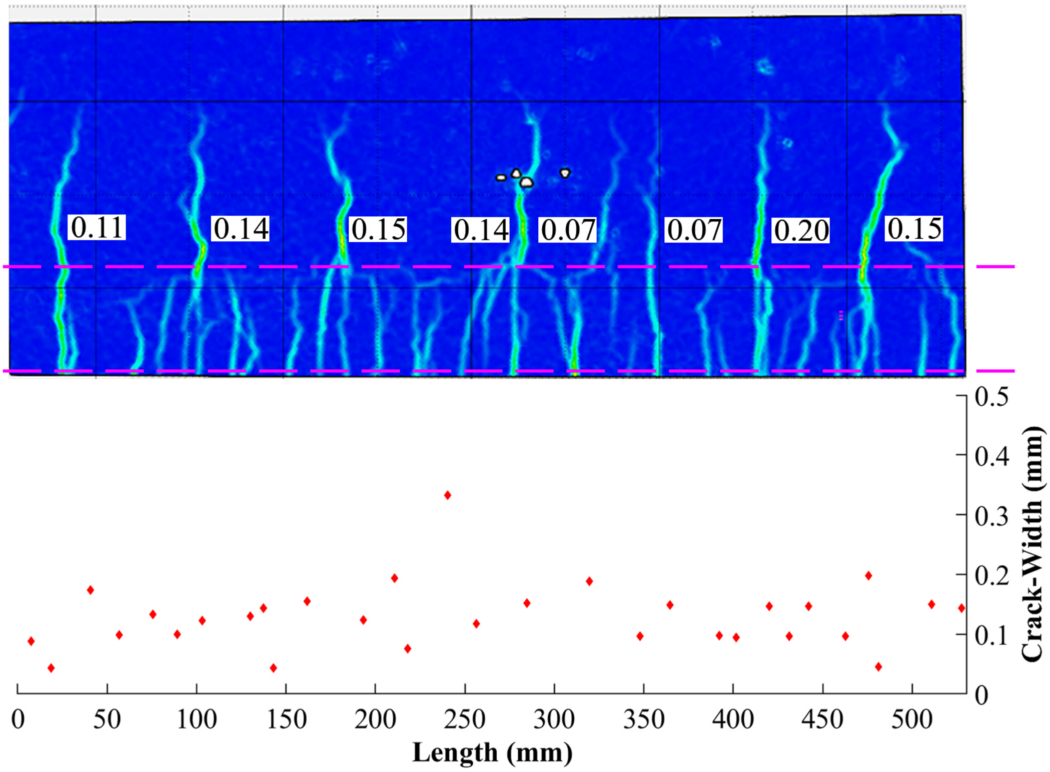

Figure 3.150: Development of cracks at load step 60 KN

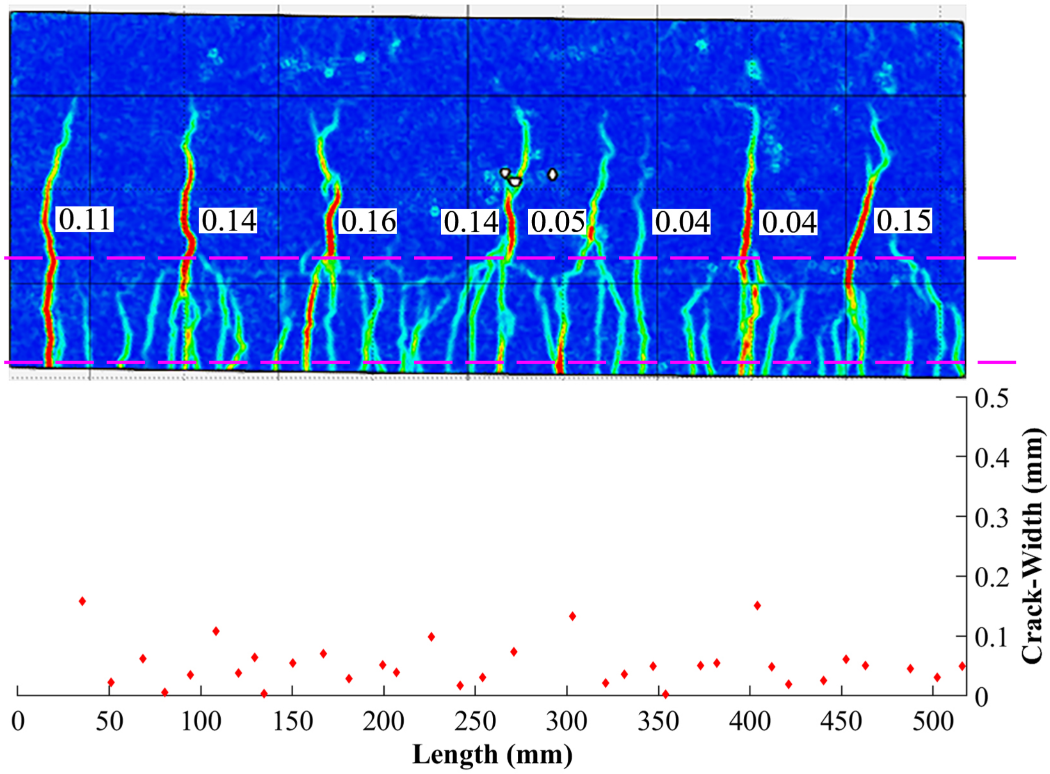

Figure 3.151: Development of cracks at load step 65 KN

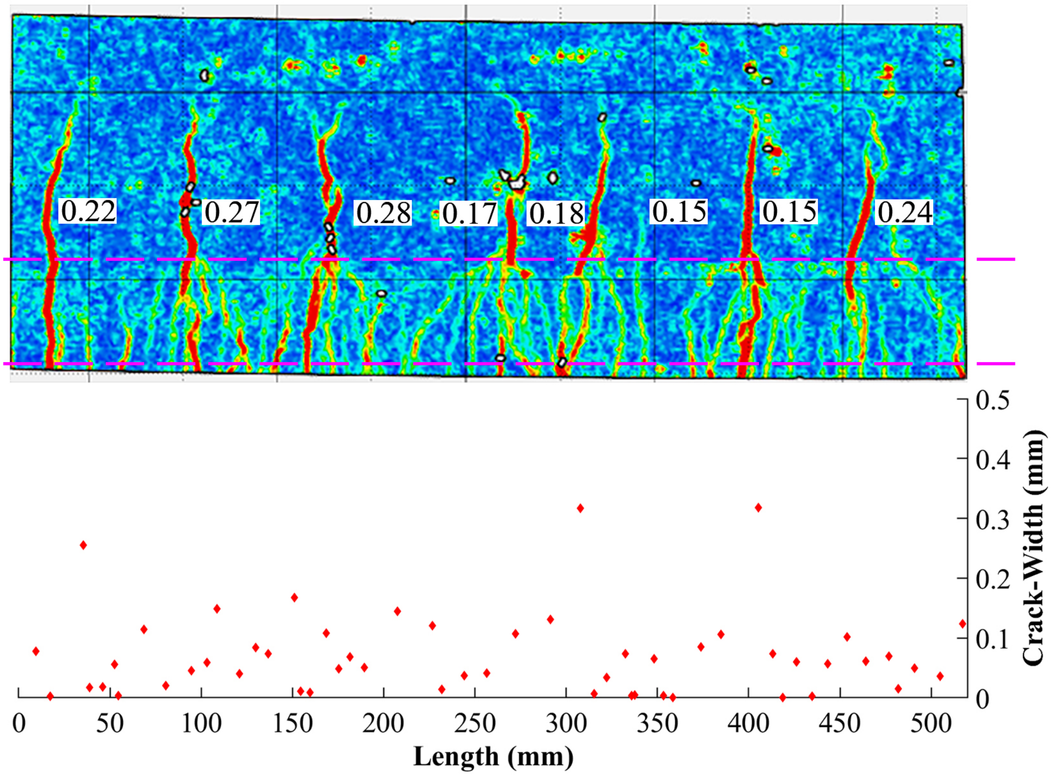

Figure 3.152: Development of cracks at load step 70 KN

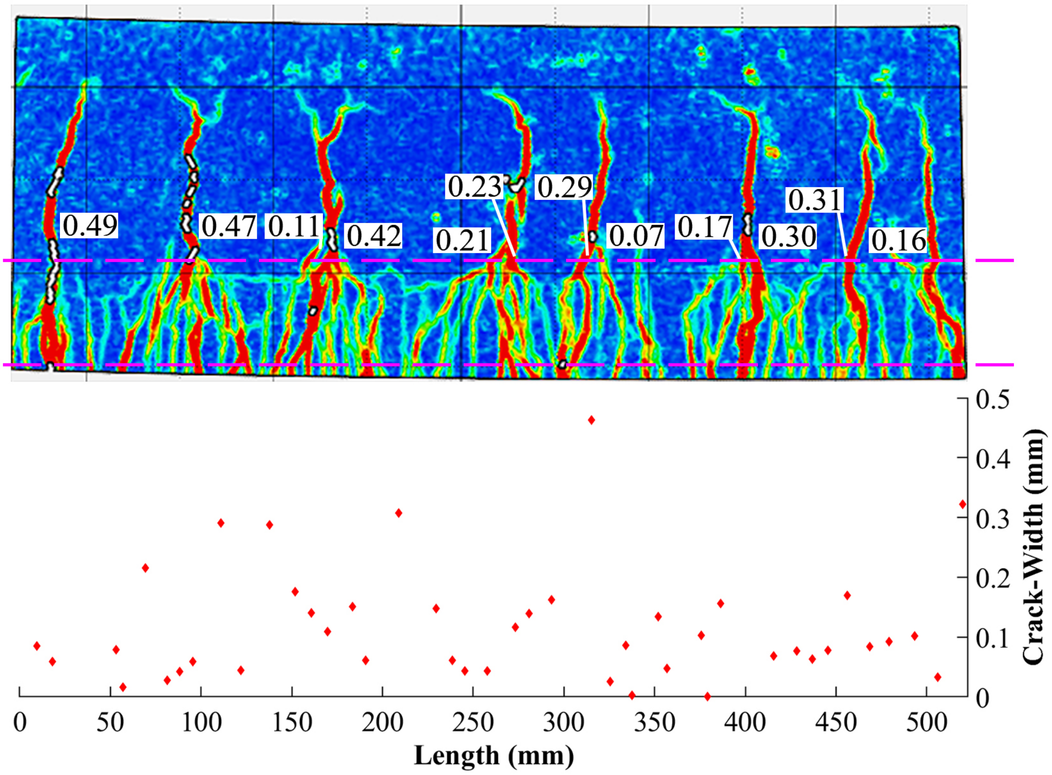

Figure 3.153: Development of cracks at load step 75 KN

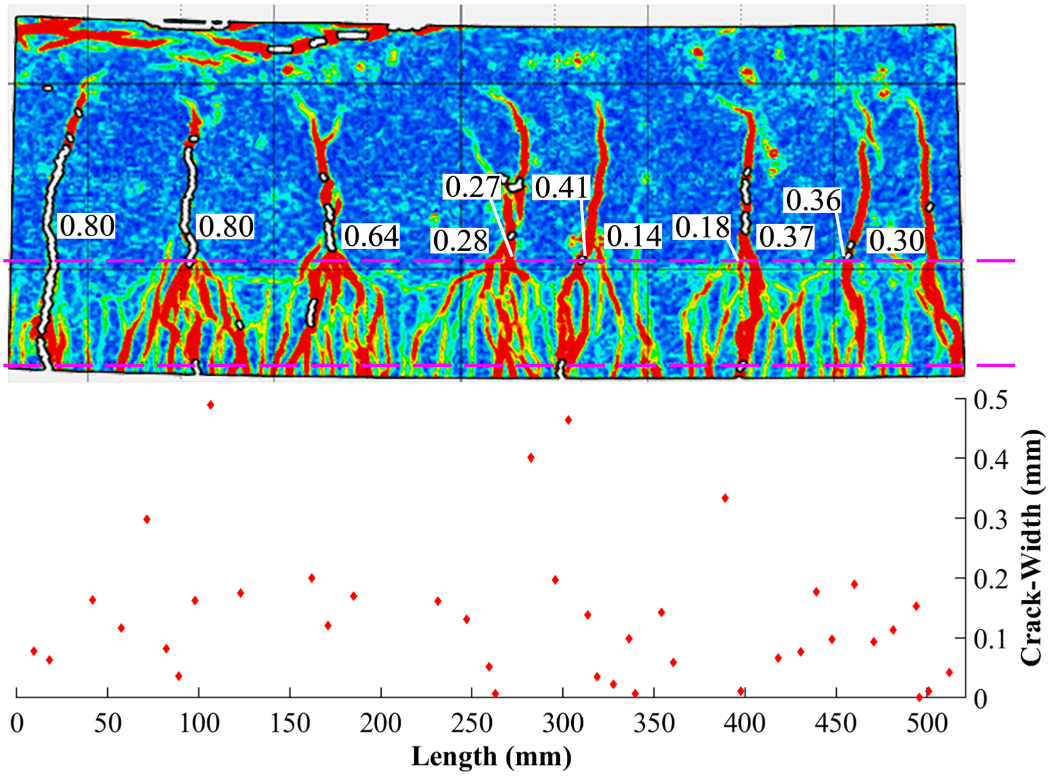

Figure 3.154: Development of cracks at load step 77 KN

At the last two load steps, the measured crack-widths exceed 0.5 mm and are not shown in Figures 3.153 and 3.154 as the limit of the crack-width plots is set to 0.5 mm. Figures 3.155 and 3.156 show the crack-width of all the cracks in the SHCC layer at the last two load steps.

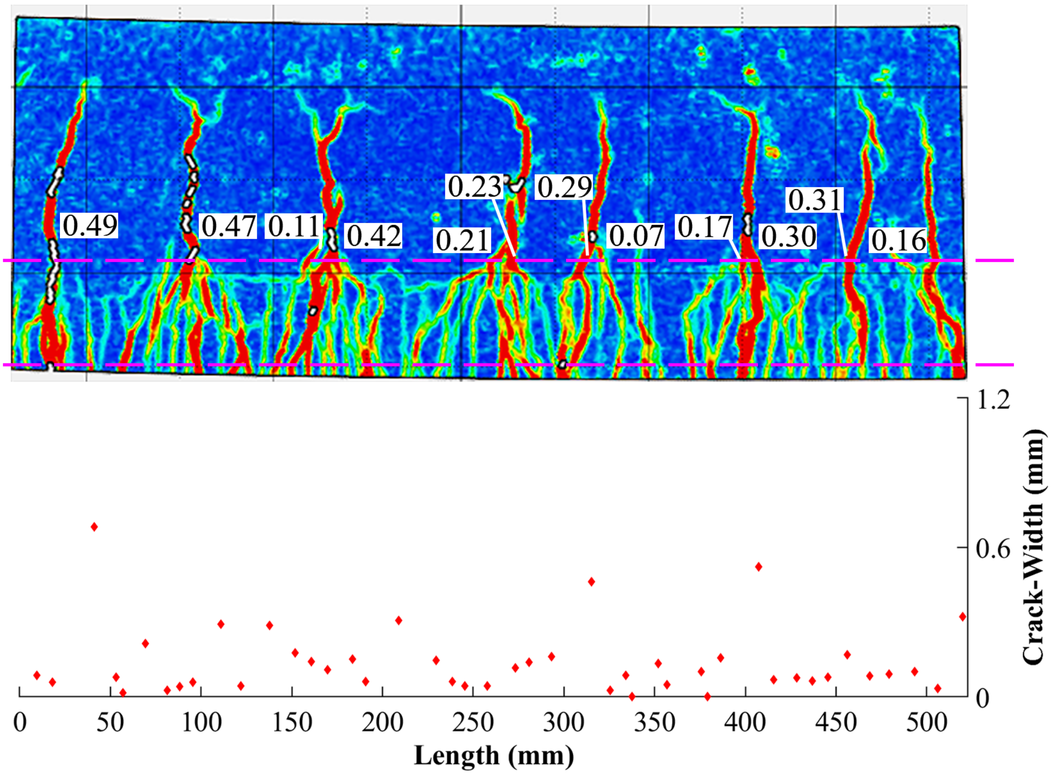

Figure 3.155: Development of large cracks at load step 75 KN

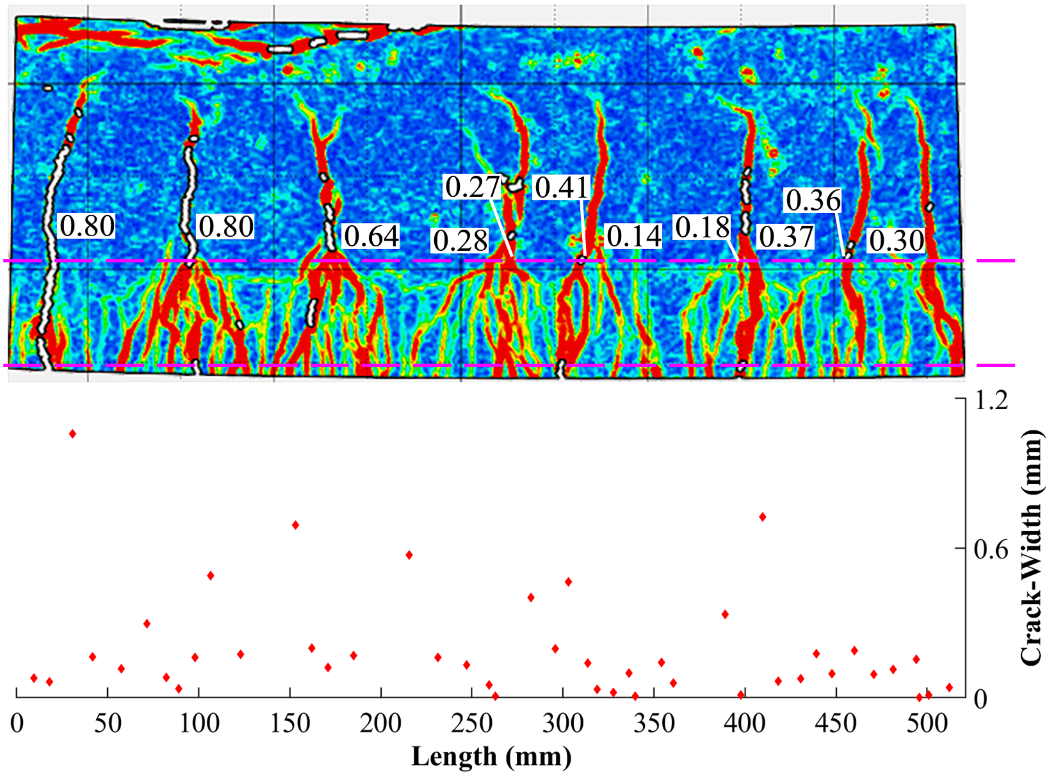

Figure 3.156: Development of large cracks at final load step 77 KN

The maximum crack-width calculated using the GOM correlate software are validated with the values measured by visual inspection and Image J as shown in Figure 3.157. The deformations measured using GOM correlate are compared with the deformations measured using LVDTs and is calibrated as shown in Figure 3.158.

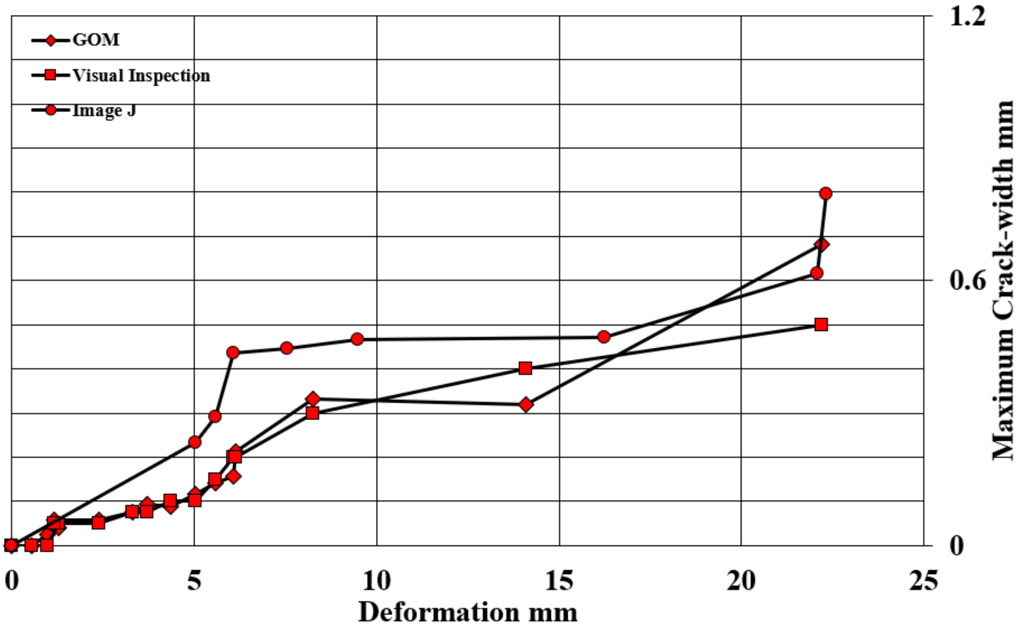

Figure 3.157: Comparison of maximum crack-widths measured using GOM, Image J and Visual Inspection

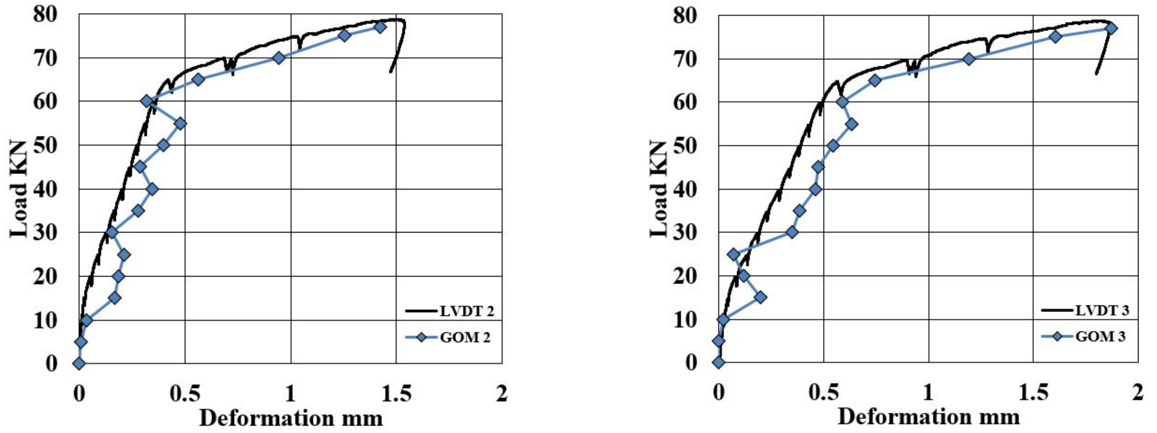

(a) P vs D plots of LVDT 2 vs GOM 2 **(b)** P vs D plots of LVDT 3 vs GOM 3

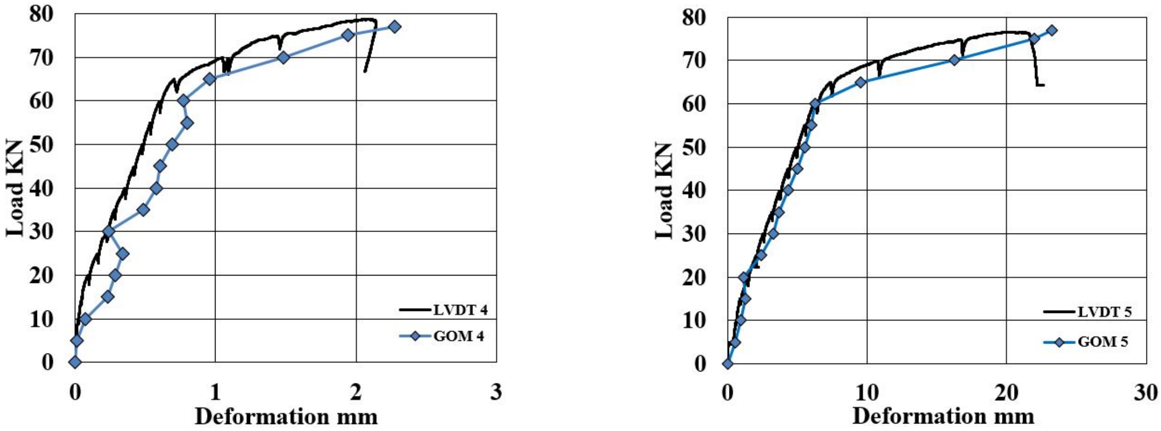

(c) P vs D plots of LVDT 4 vs GOM 4 **(d)** P vs D plots of LVDT 5 vs GOM 5

Figure 3.158: Calibration plots of GOM deformation with LVDT deformation

.

3.6.8 Comparison of Experimental Results

A comparative study is conducted to understand the influence of interface and the fiber type used in SHCC. The reference sample S-PVA is compared to all the other beam specimens tested to determine the influence in terms of bearing capacity and crack-width control.

This master thesis is an extension of the research done by Huang (2017) [1]. For comparison, beam specimen with smooth interface tested during this research is plotted against a similar specimen with smooth interface tested by Huang (2017) [1] and shown in Figure 3.159. The load at which the maximum crack-width in SLS is reached is 71 KN in this master thesis research and 63 KN in the research conducted by Huang (2017) [1].

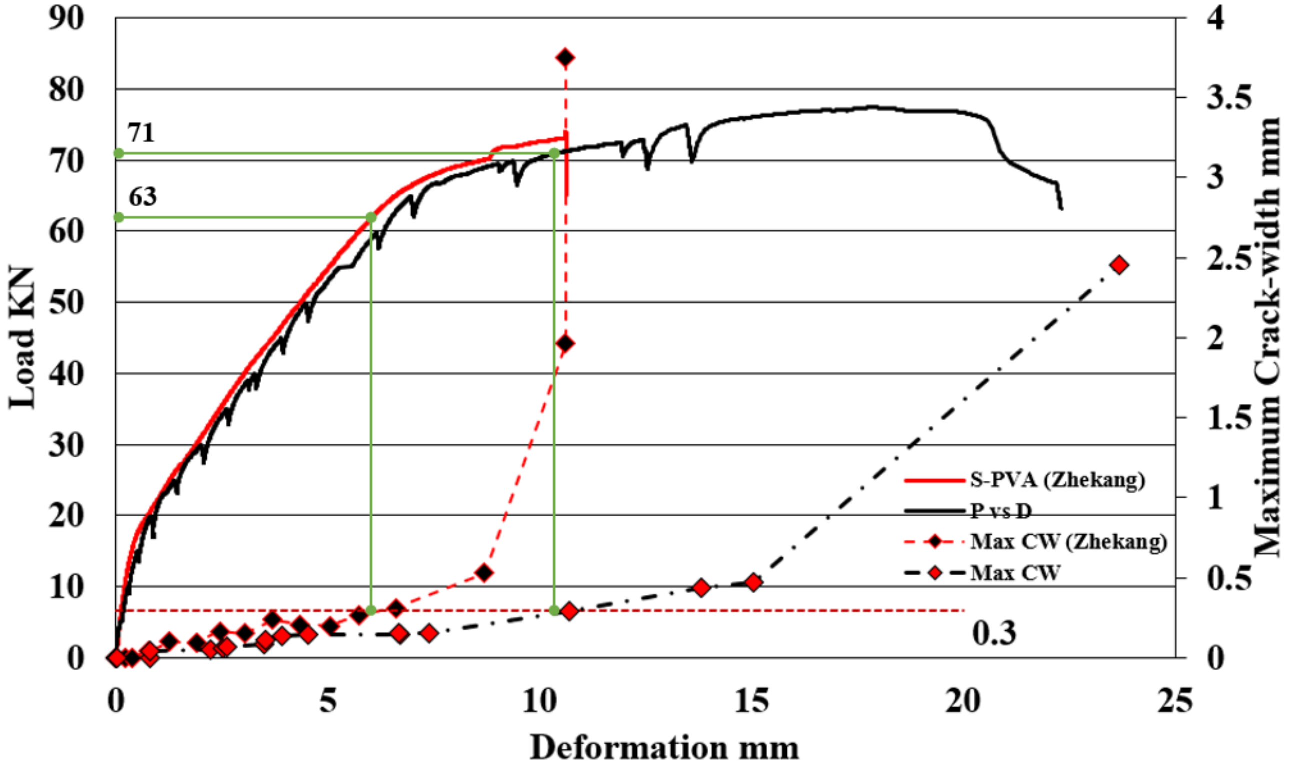

Figure 3.159: Comparison between S-PVA and CC indicating the load at which maximum allowable crack-width at SLS is exceeded

Figure 3.160 shows a comparison plot between CC and S-PVA beam specimens. It can be observed from the plot that when SHCC is applied in the tensile zone of the beam, the bearing capacity and crack-width control is significantly improved. The maximum allowable crack-width at SLS is reached at a lower load step of 39 KN in a CC beam specimen whereas, in S-PVA the same is reached at a very high load step of 71 KN.

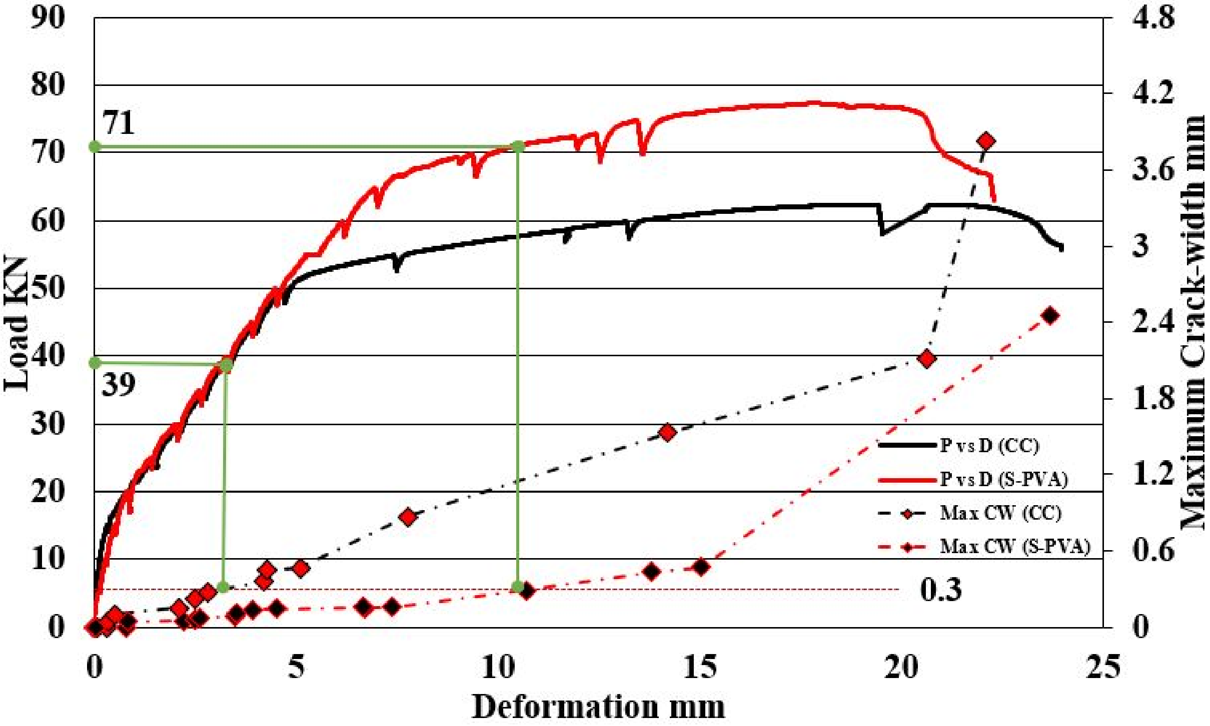

Figure 3.160: Comparison between S-PVA and CC indicating the load at which maximum allowable crack-width at SLS is exceeded

When artificial delamination is introduced in the interface by applying tape strips of 20 mm at 50 mm intervals, it is seen that the bearing capacity is slightly reduced as the maximum possible load that is applied on PD-PVA sample is 73 KN and for S-PVA it is 77 KN. Also, introducing delamination reduces the load at which the maximum allowable crack-width at SLS is reached to 54 KN as seen in Figure 3.161.

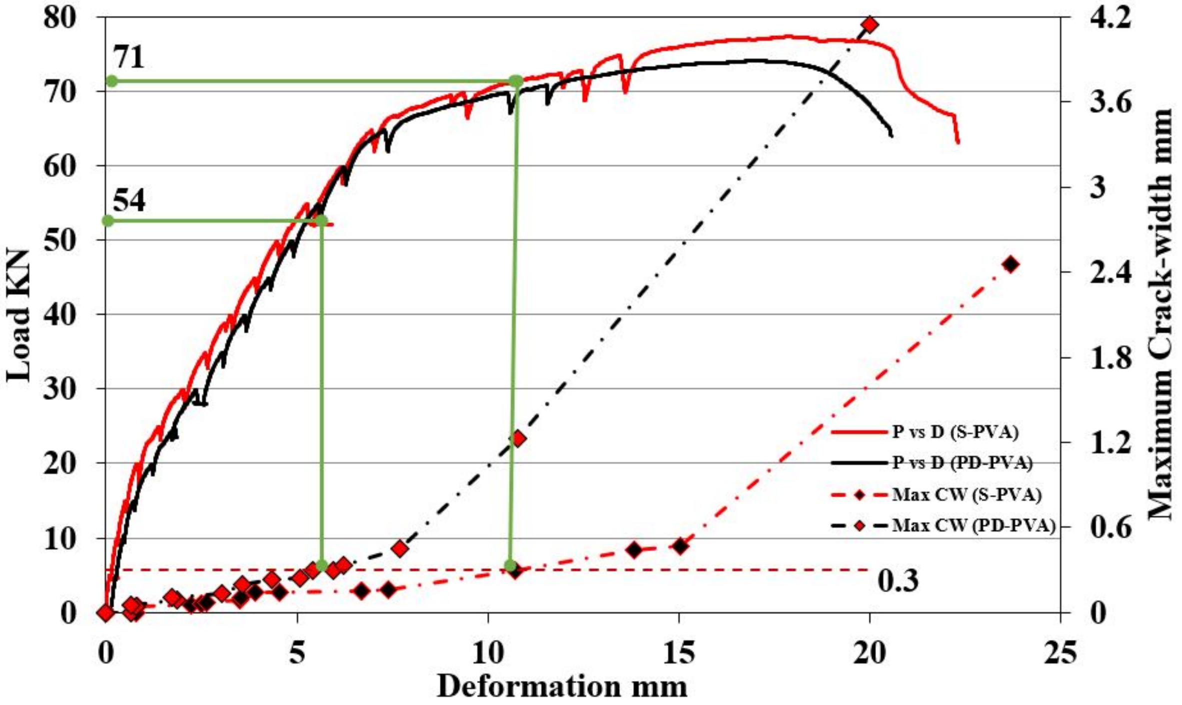

Figure 3.161: Comparison between S-PVA and PD-PVA indicating the load at which maximum allowable crack-width at SLS is exceeded

By introducing complete delamination at the interface in the constant moment region, the bearing capacity of the beam CD-PVA reduces slightly as the maximum possible load that could be applied reduces to 75 KN from 77 KN as in the case of S-PVA beam. A large reduction in the load at which the maximum allowable crack-width at SLS is reached, is observed in CD-PVA beam specimen. The value reduced to 44 KN which is comparable to the value obtained in the case of CC beam specimen as seen in Figure 3.162.

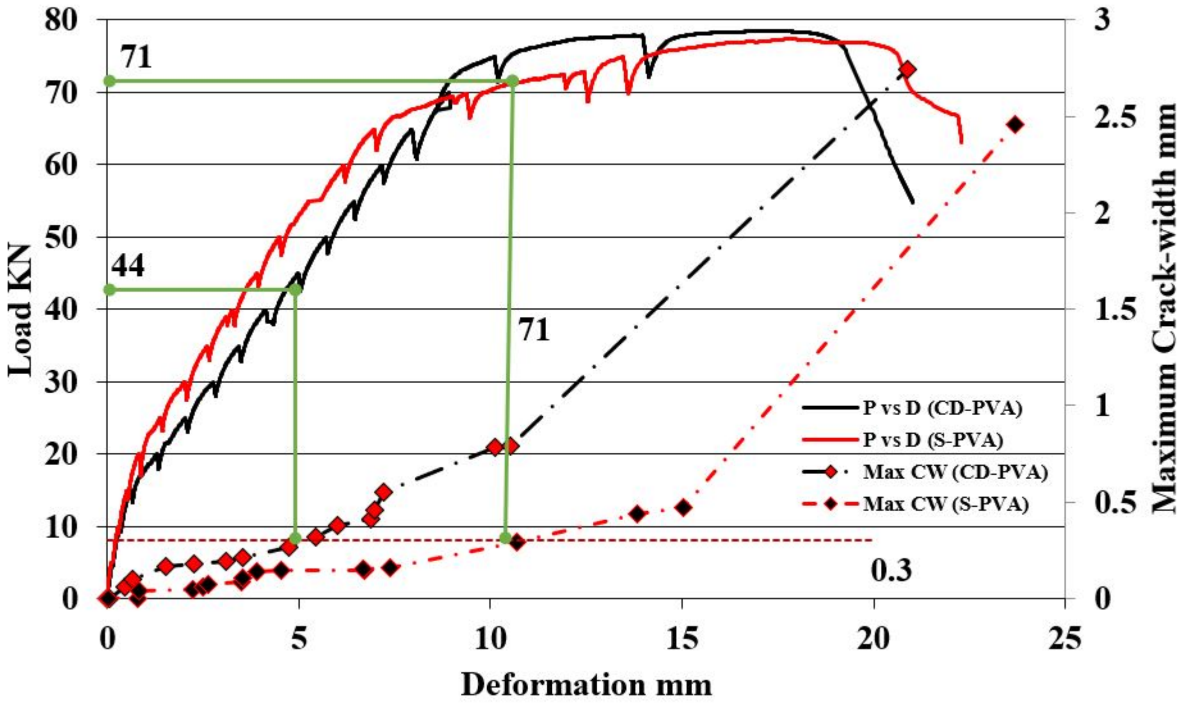

Figure 3.162: Comparison between S-PVA and CD-PVA indicating the load at which maximum allowable crack-width at SLS is exceeded

For beam specimen with a profiled interface (P-PVA), the maximum load that can be applied on the beam specimen is a little higher than that of S-PVA beam specimen. A maximum load of 78 KN can be applied on the beam with profiled interface. From Figure 3.163 it can be observed that the load at which the maximum allowable crack-width at SLS is reached is 69 KN which is close to the value reached by S-PVA specimen.

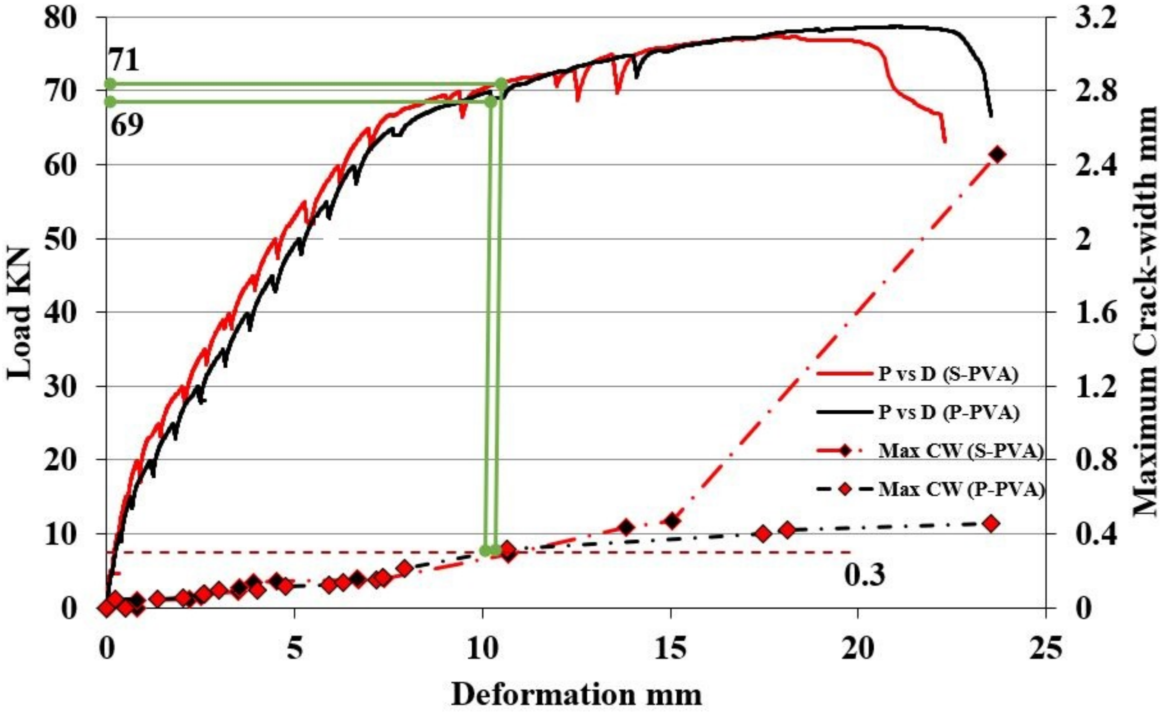

Figure 3.163: Comparison between S-PVA and P-PVA indicating the load at which maximum allowable crack-width at SLS is exceeded

By replacing the fibers in SHCC and maintaining a smooth interface in the constant moment region, a maximum load of 77 KN can be applied on the beam specimen S-HMPE. As seen from Figure 3.164, the load at which the maximum allowable crack-width at SLS is reached is 65 KN. When compared to S-PVA beam specimen, this specimen behaves almost like S-PVA specimen but not better.

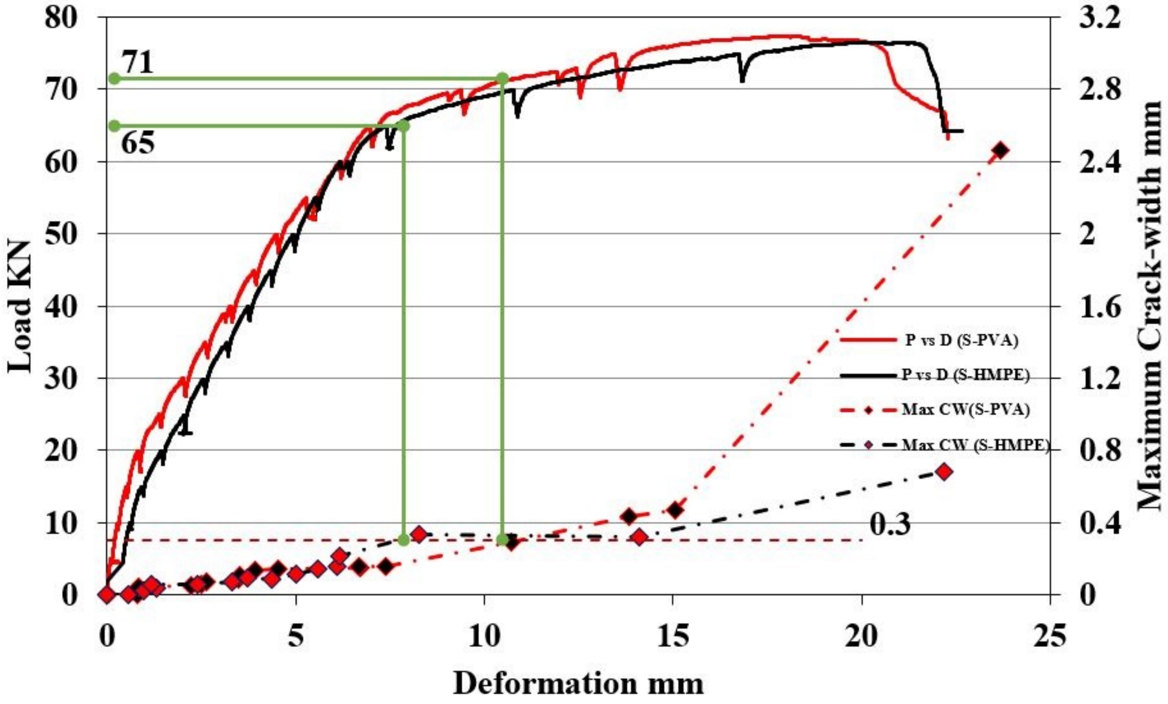

Figure 3.164: Comparison between S-PVA and S-HMPE indicating the load at which maximum allowable crack-width at SLS is exceeded

A bar graph indicating the load at which the maximum crack-width is reached in SLS is shown in Figure 3.165.

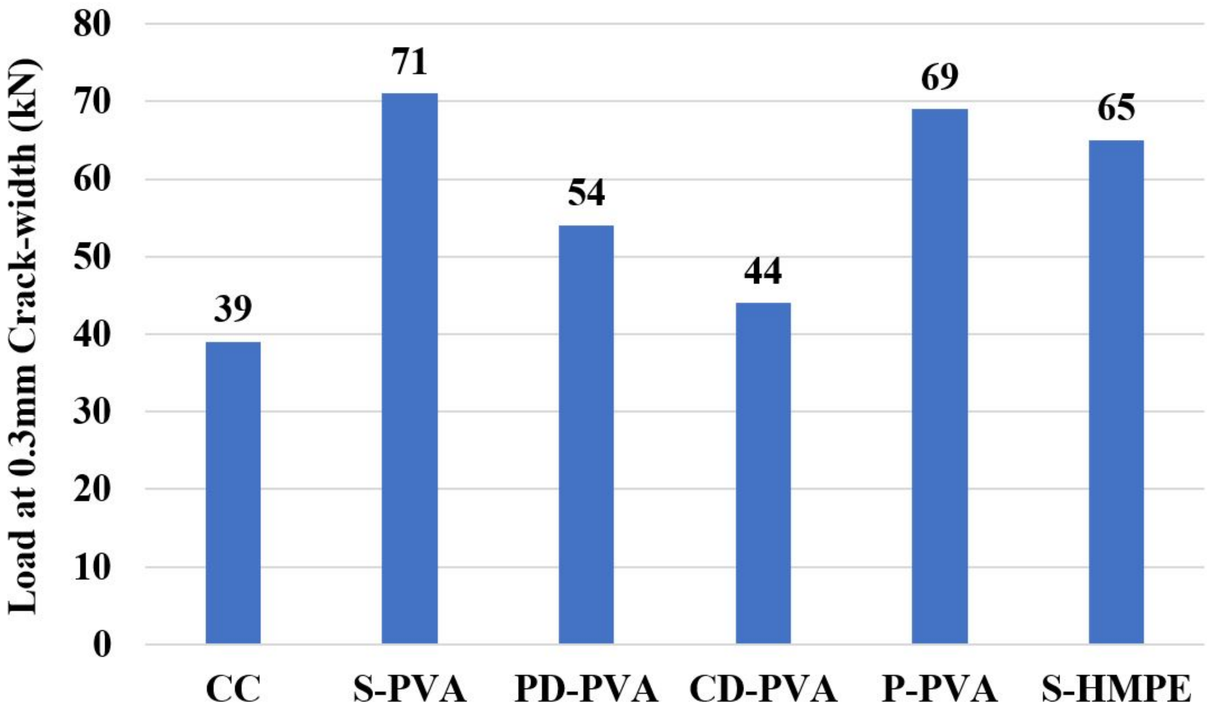

Figure 3.165: Comparison between S-PVA and CC indicating the load at which maximum allowable crack-width at SLS is exceeded

3.6.9 Dicussion

Based on the results obtained, it is noted that in beam specimens with complete debond (CD-PVA) and partial debond (PD-PVA), artificially applied at the interface, the crack in SHCC localised at an early load step of 50 KN and 45 KN respectively as shown in Figure 3.86 and 3.105. To reason this out, the stresses in the concrete and SHCC layer is determined for a completely bonded and unbonded unreinforced composite beam specimen.

The properties of Concrete and SHCC layers are shown in Table 3.12 and 3.13.

Table 3.12: Properties of Concrete layer

Property	**Value**
Width b_{cc}	150 mm
Height h_{cc}	130 mm
Young's Modulus E_{cc}	33144.3 N/mm^2

Table 3.13: Properties of SHCC layer

Property	**Value**
Width b_{shcc}	150 mm
Height h_{shcc}	70 mm
Young's Modulus E_{shcc}	18000 N/mm^2

Bonded composite beam

In linear elastic stage for composite beams with complete bond at the interface, the stresses in concrete and SHCC layer are calculated using equations 3.1 to 3.8 .

The equivalent area ratio (n) is calculated using equation 3.1

$$n = \frac{E_{cc}}{E_{shcc}} \tag{3.1}$$

The location of neutral axis (NA) of the composite beam from the top fibre of the composite beam is determined using the equation 3.2.

$$NA = \frac{(b_{cc}.h_{cc})(h_{cc}/2) + (n.b_{shcc}.h_{shcc})(h_{cc} + h_{shcc}/2)}{(b_{cc}.h_{cc}) + (n.b_{shcc}.h_{shcc})} \tag{3.2}$$

The net moment of Inertia (I_{net}) is calculated using equation 3.3

$$I_{net} = I_{cc} + I_{shcc} \tag{3.3}$$

$$I_{cc} = \frac{(b_{cc}.h_{cc}^3)}{12} + (b_{cc}.h_{cc})(y^2) \tag{3.4}$$

$$I_{shcc} = \frac{(b_{shcc}.h_{shcc}^3)}{12} + (b_{shcc}.h_{shcc})(y^2) \tag{3.5}$$

Here, y is the distance between the centroid and the neutral axis.

The external moment (M) acting can be calculated using the equation 3.6

$$M = P.a \tag{3.6}$$

Here, P is the load applied to the beam in a four-point bending set-up and a is the distance between the support and applied load (500 mm).

The stress in the concrete and SHCC layer is calculated using equations 3.7 and 3.8

$$\sigma_{top} = \frac{M.y_{top}}{I_{net}} \tag{3.7}$$

$$\sigma_{bottom} = \frac{1}{n}.\frac{M.y_{bot}}{I_{net}} \tag{3.8}$$

Unbonded composite beam

In linear elastic stage for composite beams with complete debond at the interface, the stresses in concrete and SHCC layer is calculated using equations 3.9 to 3.16.

The individual moment of Inertia I_{cc} and I_{shcc} is calculated using equations 3.9 and 3.10

$$I_{cc} = \frac{(b_{cc}.h_{cc}^3)}{12} \tag{3.9}$$

$$I_{shcc} = \frac{(b_{shcc}.h_{shcc}^3)}{12} \tag{3.10}$$

The external moment (M) acting is calculated using the equation 3.11

$$M = P.a \tag{3.11}$$

Here, P is the load applied to the beam in a four-point bending set-up and a is the distance between the support and applied load (500 mm).

Since the composite layers are debonded, the external moment is equal to the individual moments M_{cc} and M_{shcc} as indicated in equation 3.12

$$M = M_{cc} + M_{shcc} \tag{3.12}$$

The length of the beam is a long and so the curvature (κ) is assumed to be the same in both layers of the composite beam. Hence, the relation shown in equation 3.13 and 3.14 is obtained.

$$\frac{E_{cc}.I_{cc}}{M_{cc}} = \frac{E_{shcc}.I_{shcc}}{M_{shcc}} \tag{3.13}$$

$$\frac{M_{cc}}{M_{shcc}} = \frac{E_{cc}.I_{cc}}{E_{shcc}.I_{shcc}} \tag{3.14}$$

The stress in the Concrete and SHCC layer is calculated using equations 3.15 and 3.16

$$\sigma_{top} = \frac{M.\frac{y_{cc}}{2}}{I_{cc}} \tag{3.15}$$

$$\sigma_{bot} = \frac{M.\frac{y_{shcc}}{2}}{I_{shcc}} \tag{3.16}$$

Based on the equations from 3.1 to 3.16 the stresses in the concrete and SHCC layer for bonded and unbonded composite beams are shown in Table 3.14 and 3.15.

Table 3.14: Stresses in completely bonded composite beam

Composite Layer	**Stress** N/mm^2
Concrete	5.93×10^{-4} P
SHCC	4.13×10^{-4} P

Table 3.15: Stresses in completely unbonded composite beam

Composite Layer	**Stress** N/mm^2
Concrete	1.09×10^{-3} P
SHCC	3.19×10^{-4} P

From Table 3.15 it is observed that the concrete layer which is unreinforced has a higher moment capacity which is not possible in reality as the concrete layer has highly localised cracks unlike the SHCC layer having a distributed crack pattern. Thus, the Young's Modulus of the cracked concrete, indicated in Table 3.16, is used in linear elastic calculations. However, the Young's Modulus of SHCC is not reduced as it is more ductile than concrete.

Table 3.16: Reduced Young's Modulus of concrete layer

Interface type	**Young's Modulus** N/mm^2
Bonded	9000
Unbonded	9000

The stresses in the top and bottom fibre of the composite beam with a reduced Young's Modulus of concrete are indicated in Tables 3.17 and 3.18 for bonded and unbonded composite beam specimens, respectively.

Table 3.17: Stresses in completely bonded composite beam

Composite layer	**Stress** N/mm^2
Concrete	4.26×10^{-4} P
SHCC	6.06×10^{-4} P

Table 3.18: Stresses in completely unbonded composite beam

Composite layer	**Stress** N/mm^2
Concrete	9.02×10^{-4} P
SHCC	9.71×10^{-4} P

From Tables 3.17 and 3.18, it is observed that the stress generated in the SHCC layer of unbonded composite beam is 1.6 times higher as compared to the stress generated in the SHCC layer of bonded composite beam.

In reference to the beam specimen with completely delmainted interface shown in Figure 3.166 to 3.180, it can be clearly noted that the tensile strain in the y-direction is generated (indicated in red) at the interface at a much earlier load step of 30 KN. Due to this, a situation of debond prevails from a very early load step creating higher stress in the SHCC layer subsequently, leading to early localisation of cracks.

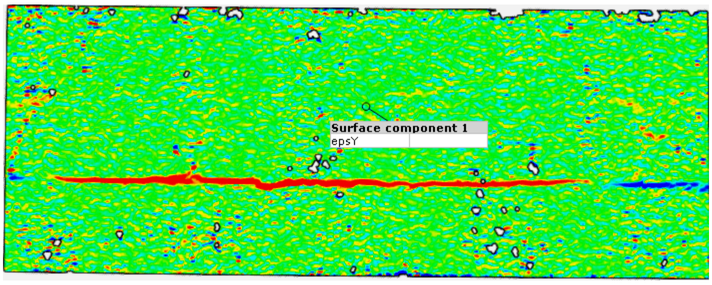

Figure 3.166: Strain in y direction at load step 30 KN

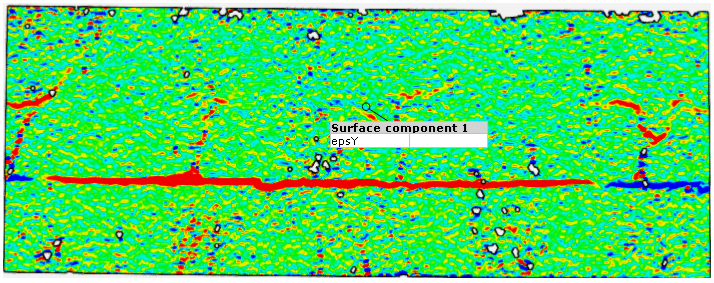

Figure 3.167: Strain in y direction at load step 35 KN

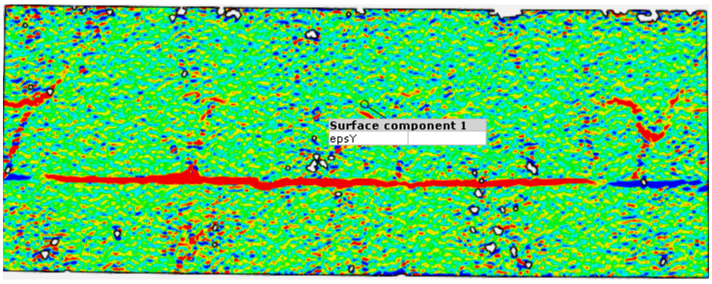

Figure 3.168: Strain in y direction at load step 40 KN

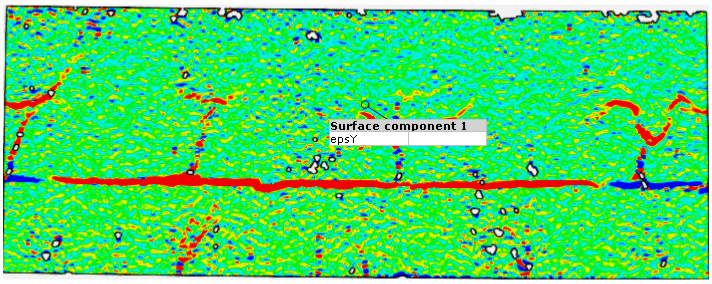

Figure 3.169: Strain in y direction at load step 45 KN

For the PD-PVA beam specimen with partial delamination at the interface, the considered case of bonded and unbonded composite beams act as the upper and lower bound values for stresses in the SHCC layer. From Figure 3.170 to Figure 3.181, a comparison of the strain in y direction is made with beam specimen containing smooth interface (S-PVA) outside the constant moment region as well. It can be clearly seen that a tensile strain is generated (indicated in red) at the interface from load step 30 onwards for the PD-PVA beam specimen. Whereas, no such tensile strain is generated at the same load steps for the S-PVA beam specimen. So, it can also be inferred that the stresses acting in the SHCC layer are higher and hence, the cracks localise at an earlier load step of 50 KN.

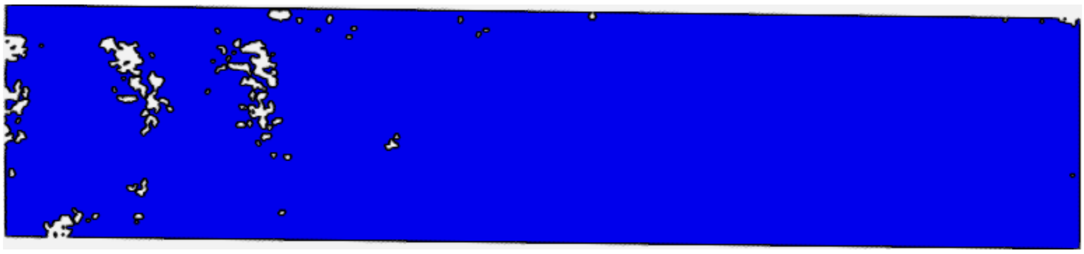

Figure 3.170: Strain in y direction; S-PVA; Load Step 0

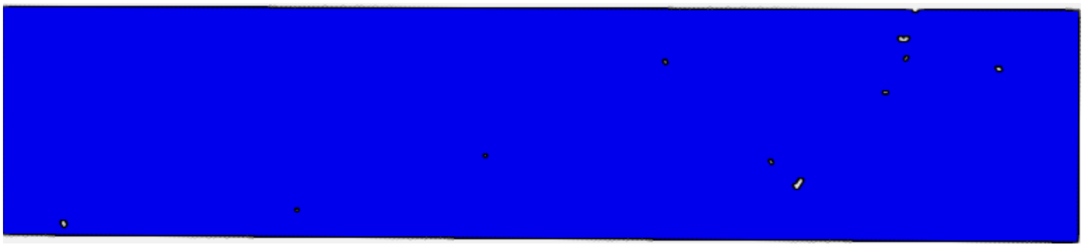

Figure 3.171: Strain in y direction; PD-PVA; Load Step 0

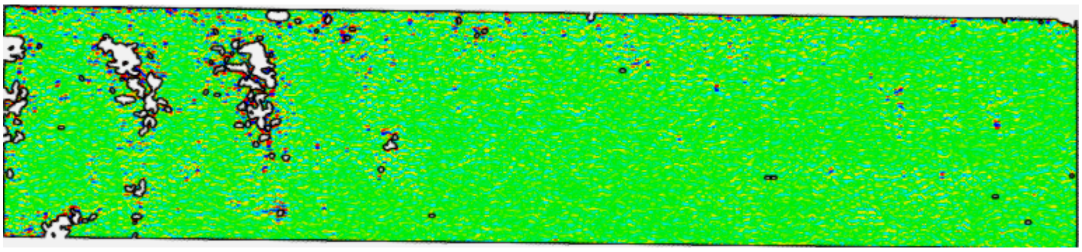

Figure 3.172: Strain in y direction; S-PVA; Load Step 10

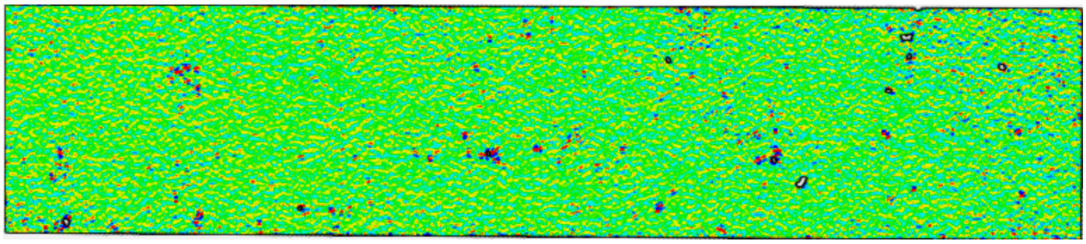

Figure 3.173: Strain in y direction; PD-PVA; Load Step 10

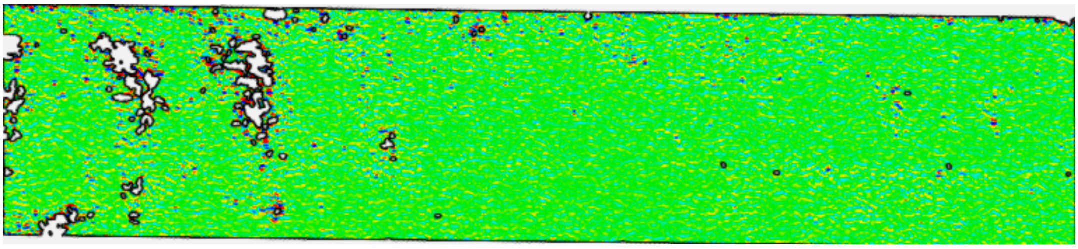

Figure 3.174: Strain in y direction; S-PVA; Load Step 20

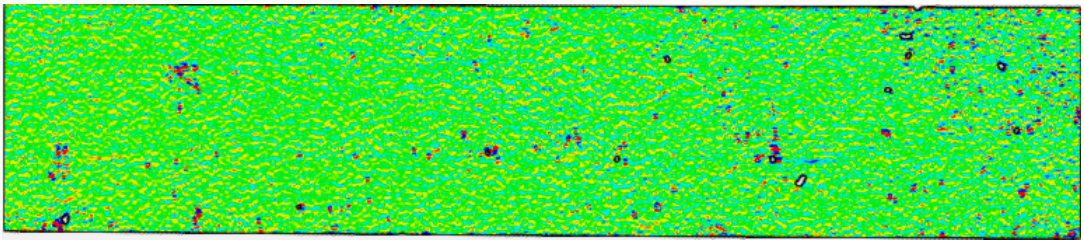

Figure 3.175: Strain in y direction; PD-PVA; Load Step 20

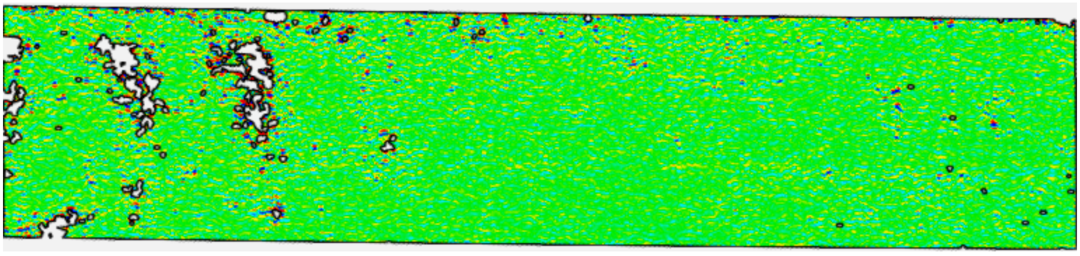

Figure 3.176: Strain in y direction; S-PVA; Load Step 30

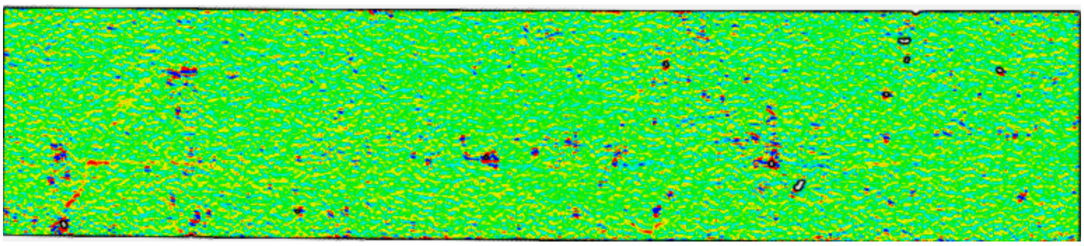

Figure 3.177: Strain in y direction; PD-PVA; Load Step 30

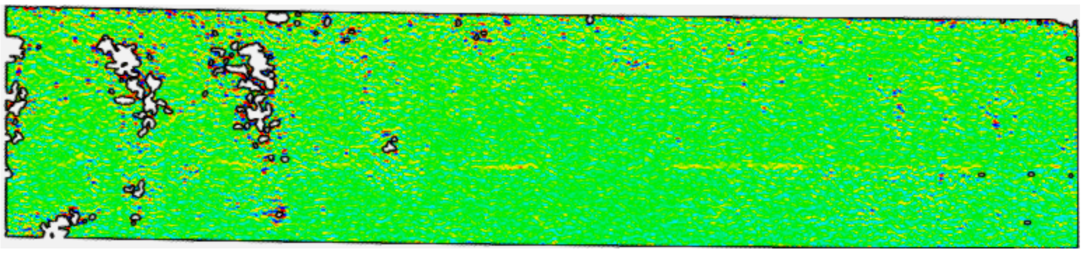

Figure 3.178: Strain in y direction; S-PVA; Load Step 40

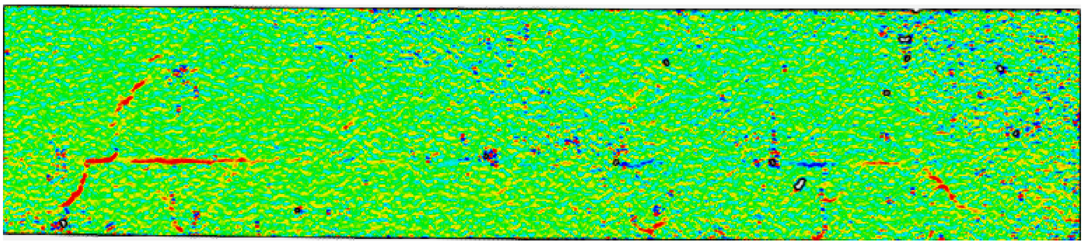

Figure 3.179: Strain in y direction; PD-PVA; Load Step 40

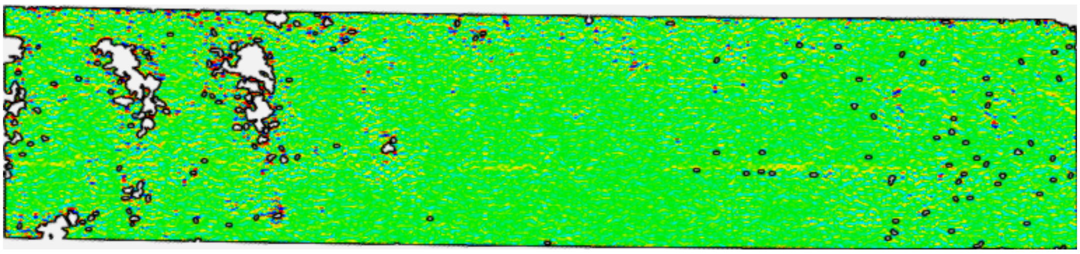

Figure 3.180: Strain in y direction; S-PVA; Load Step 50

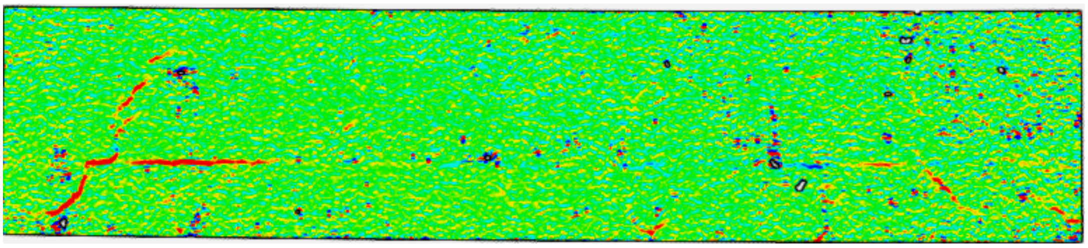

Figure 3.181: Strain in y direction; PD-PVA; Load Step 50

Chapter 4

Numerical Analyses

The pre-work required to test the beam specimens experimentally include the process of laying the reinforcement, casting the concrete in two layers along with tedious preparation of the interface and curing for a prolonged duration. Moreover, the output obtained from the experiments have to be post-processed to determine the behaviour such as cracking pattern, maximum crack-width and bearing capacity.

To reduce the effort and time, attempts to make the numerical models of the beams with varying interface is considered. If numerical models that replicate the experimental beam behaviour are successfully made then modeling study can be conducted simply to determine some of the parameters instead of repeating large experimental series. To make such models, Diana Finite Element Analysis (FEA) {version 10.3} is used. To match the behaviour with the experimental results, the material properties used as inputs are determined either experimentally or taken from published research papers.

4.1 Geometry

All beams are modelled in two-dimensional environment (2D) with regular plane stress elements. The geometry of all the beams is kept the same as the ones experimentally tested for comparison. The length of the beams is 1900 mm and the cross-section is 150 mm x 200 mm with 70 mm layer of SHCC on the tension side of the beam.

Steel plates of size 50 mm x 25 mm are positioned at the locations of support and loads to replicate the similar situation of support and loads as in the experimental set-up.

Figure 4.1 represents the longitudinal reinforcement bars of 8 mm diameter. Three such bars are provided in the tension region of the beam and two bars in the compression region of the beam. Vertical lines represent six two-legged 8mm diameter stirrup bars provided outside the constant moment region as shown in Figure 4.1.

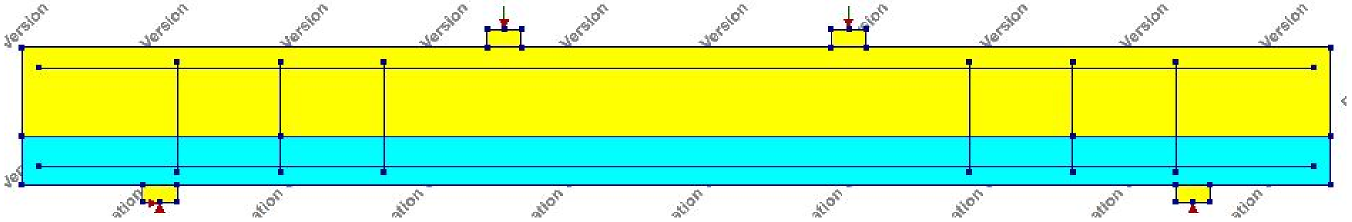

Figure 4.1: Geometry of the beam

Even though all the beams have the same cross-section and height of SHCC, the interface property varies. Smooth, profiled, partial and full debond interfaces created in the experimental beams are replicated in the numerical models. Figure 4.2 to 4.6 show all the beam models with their respective interfaces and type of fiber used.

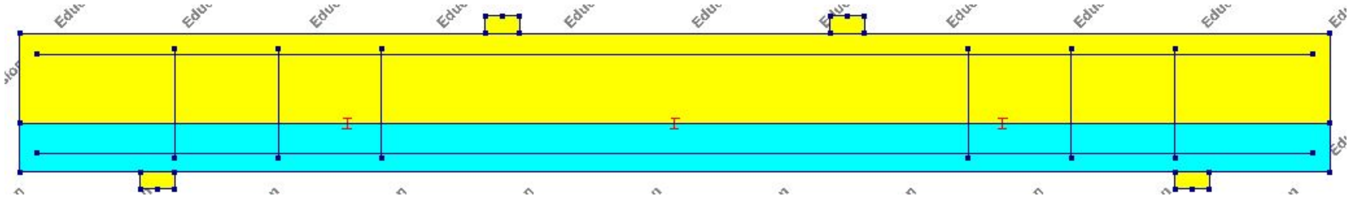

Figure 4.2: Hybrid beam; Smooth Interface; PVA fiber

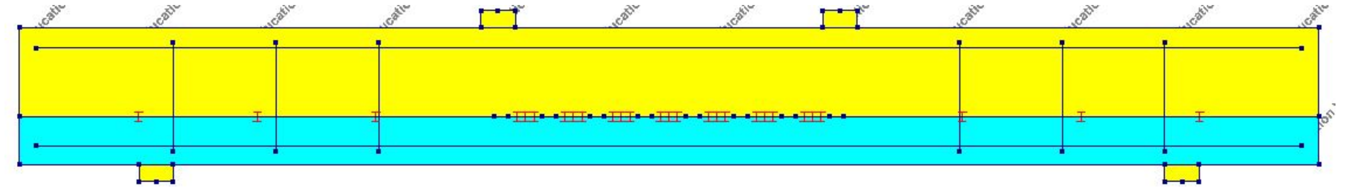

Figure 4.3: Hybrid beam; Partially delaminated interface; PVA fiber

Figure 4.4: Hybrid beam; Completely delaminated Interface; PVA fiber

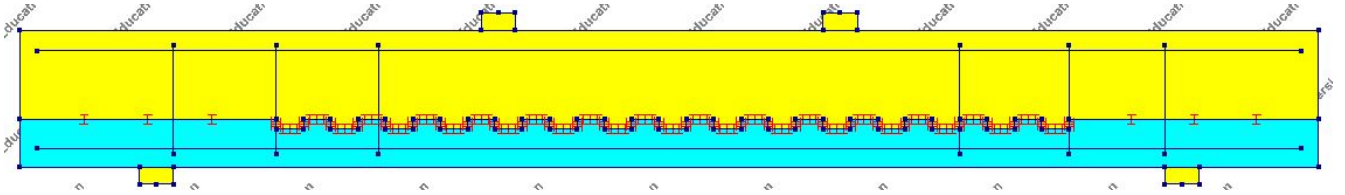

Figure 4.5: Hybrid beam; Profiled Interface; PVA fiber

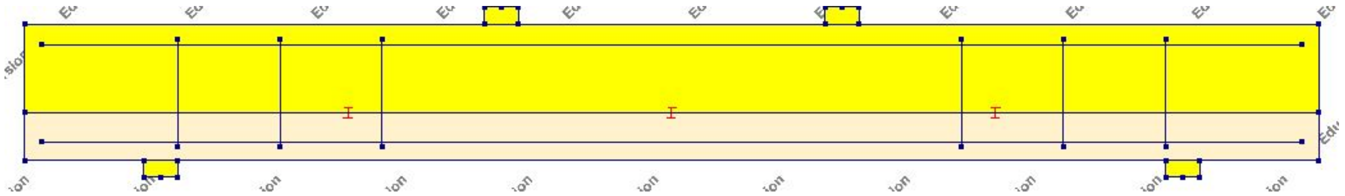

Figure 4.6: Hybrid beam; Smooth Interface; HMPE fibers

4.2 Material Properties

The constitutive material models used in the analyses can majorly govern the possible failure mechanisms in the concrete and SHCC layers of the hybrid beam. Hence, providing the appropriate material models becomes significantly relevant.

4.2.1 Concrete

A total strain-based rotating crack model is used because it follows a smeared approach for the fracture energy distribution and does not suffer from spurious stress-locking [27]. The tensile behaviour of concrete is modelled using a Hordijk tension softening curve as shown in Figure 4.7a as it results in more localised cracks than diffused cracks over large areas [27]. The compressive behaviour is modelled such that the maximum compressive stress is limited and so it is recommended to use the Parabolic stress-strain diagram with softening branch as shown in figure 4.7b. The material parameters of concrete used in the analyses are listed in table 4.1

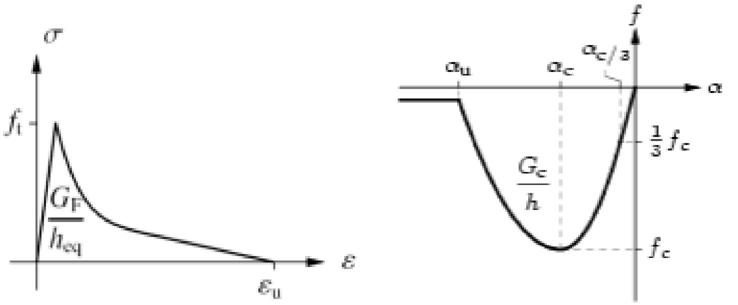

(a) Hordijk Tension Softening Curve **(b)** Parabolic compressive behaviour

Figure 4.7: Material properties of modelled concrete

Table 4.1: Material properties of concrete grade C30/37

Property	**Value**
Material Class	Concrete and masonry
Material Model	Total Strain-based cracking model
Mean Compressive Strength (fcm)	39.2 MPa
Characteristic Compressive Strength (fck)	31.2 MPa
Young's Modulus (E)	33144.3 MPa
Poisson's Ratio	0.2
Crack Orientation	Rotating
Tensile Curve	Hordijk
Tensile Strength (fctm)	2.97 MPa
Mode-I tensile fracture energy (Gf)	0.14129 N/mm
Compressive fracture Energy (Gc)	35.322 N/mm

4.2.2 SHCC

A total strain-based rotating crack model is used to input the compressive and tensile behaviour of SHCC. The tensile behaviour is modelled using *fib* fiber reinforced concrete tensile curve to replicate the hardening behaviour of SHCC as shown in Figure 4.8a and 4.8b. The compressive behaviour is modelled using an ideal compressive curve as shown in Figure 4.9.

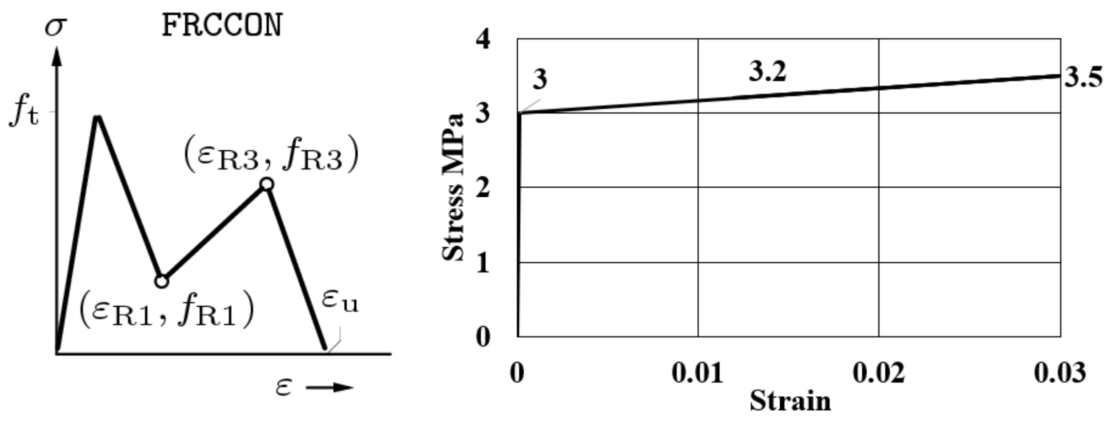

(a) *fib* fiber reinforced concrete tensile curve

(b) Strain hardening behaviour of SHCC

Figure 4.8: Tensile behaviour of SHCC

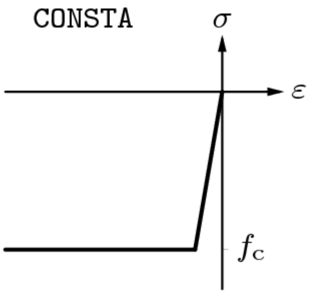

Figure 4.9: Compressive behaviour of SHCC

Table 4.2: Material properties of SHCC

Property	**Value**
Material Class	Concrete and masonry
Material Model	Total Strain-based cracking model
Mean Compressive Strength (fcm)	38.8 MPa
Characteristic Compressive Strength (fck)	30.8 MPa
Young's Modulus (E)	18000 MPa
Poisson's Ratio	0.2
Crack Orientation	Rotating
Tensile Curve	fib fiber reinforced concrete
Compression Curve	Ideal

4.2.3 Reinforcement Steel

The properties of the reinforcing steel used in the beams as shown in Table 4.3. Diana FEA provides the option to include reinforcements as completely embedded in the concrete layer (100% bond) or to provide a bond-slip interface between the concrete and steel reinforcement. CEB-FIB 2010 bond-slip interface model is used for the analyses. The stress-strain plot of reinforcing steel is shown in Figure 4.10c and the traction-slip plot between the concrete and steel is shown in Figure 4.10b. Diana FEA also requires the value of normal and shear stiffness as inputs to model the bond-slip behaviour. These values are taken based on the research of Eriksen et al. [28]. The hybrid beam has two layers of concrete with different Young's Modulus. Table 4.4 and 4.5 shows the value of normal and shear stiffness for bond-slip interface between the reinforcement and the concrete layer (C30/37 or SHCC).

Table 4.3: Material properties of Reinforcing steel

Property	**Value**
Young's Modulus (E)	210000 MPa
Plasticity Model	Von Mises Plasticity
Von Mises Hardening Function	Total Strain- yield Stress
Hardening Hypothesis	Strain Hardening
Hardening Type	Isotropic hardening
Bond-slip interface failure model	CEB-FIB 2010 Bondslip function

$$\text{Normal Stiffness} = \frac{E}{2R}.10^3 (N/mm^3) \tag{4.1}$$

$$\text{Shear Stiffness} = \frac{\tau auf}{0.1} (N/mm^3) \tag{4.2}$$

where, $\tau auf = \sqrt{fck}$

Table 4.4: Normal and Shear stiffness for bond-slip in concrete layer

Property	**Value**
Normal Stiffness	4143037.5 N/mm^3
Shear Stiffness	55 N/mm^3

Table 4.5: Normal and Shear stiffness for bond-slip in SHCC layer

Property	**Value**
Normal Stiffness	2250000 N/mm^3
Shear Stiffness	55 N/mm^3

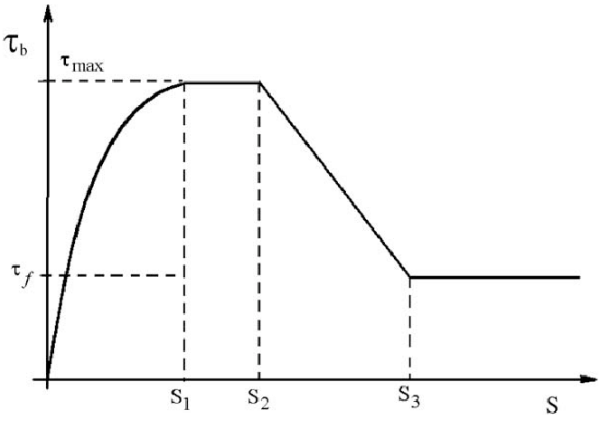

(a) CEB-FIB 2010 bond-slip interface model

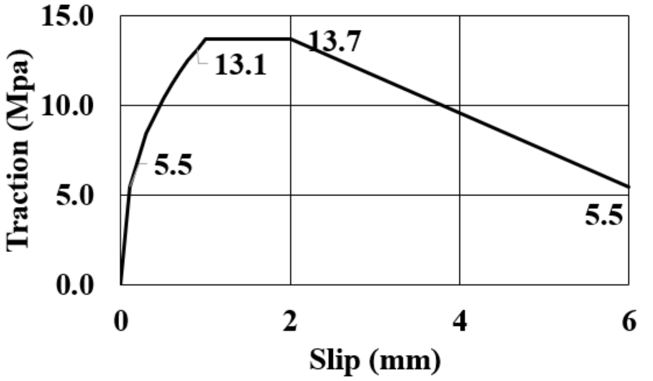

(b) Traction-slip plot of interface between steel and concrete

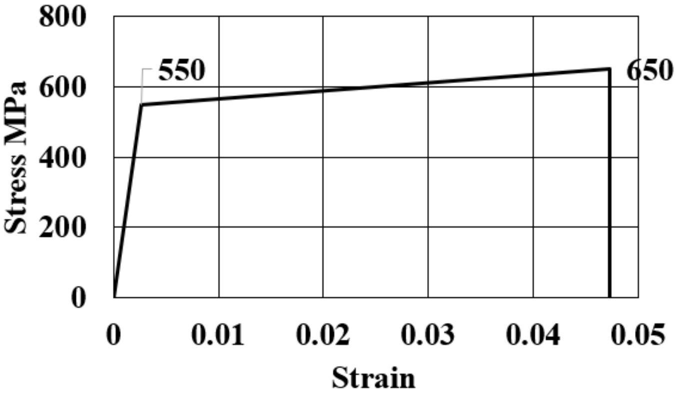

(c) Total stress-yield strain plot in steel

Figure 4.10: Properties of reinforcing steel

4.2.4 Steel plate

The steel plates are provided at the location of the loading points and the support points for all the beams. In the analyses, the steel plates are modelled as a linear elastic material with Young's modulus of 200 GPa and a Poisson's ratio of 0.3. An interface is defined at the region of contact between the steel plates and the concrete beam. The normal and shear stiffness of the interface is calculated from the properties of concrete. The normal stiffness is taken to be the same value as the Young's Modulus of concrete and the shear stiffness is equal to the Young's Modulus of concrete divided by 1000 as shown in table 4.6 [27].

Table 4.6: Properties of interface between steel plate and beam

Property	**Value**
Normal Stiffness	33144.3 N$/mm^3$
Shear Stiffness	33.144 N$/mm^3$

4.3 Interface Properties

The interface between the SHCC and the concrete layer is modelled using interface class elements in Diana FEA. A coulomb friction material model is used at the interface because this region is governed by frictional behaviour [29]. The inputs to model the interface is listed in table 4.7. The friction angle of 0.6 used as an interface property is based on the research of Mohamad et al. (2015) [30]. The normal and shear stiffness at the interface is based on the input suggested in [31] and shown in equations 4.3 and 4.4. Table 4.8 shows the values used as input for normal and shear stiffness at the interface. For the regions of the interface where delamination is introduced, the normal and shear stiffness values are taken as shown in table 4.9.

Table 4.7: Material properties of Interface

Property	**Value**
Class	Interface elements
Material Model	Coulomb friction
Type	2D line interface
Cohesion	2 N$/mm^2$
Friction Angle	0.6 rad
Dilatancy Angle	0 rad

$$\text{Normal Stiffness} = \frac{E}{Elementsize.10^2}(N/mm^3) \tag{4.3}$$

$$\text{Shear Stiffness} = \frac{E}{100}(N/mm^3) \tag{4.4}$$

Table 4.8: Normal and Shear stiffness of the bonded part of the interface

Property	**Value**
Normal Stiffness	132577.2 N$/mm^3$
Shear Stiffness	331.433 N$/mm^3$

Table 4.9: Normal and Shear stiffness of the delaminated part of the interface

Property	**Value**
Normal Stiffness	1 N$/mm^3$
Shear Stiffness	1 N$/mm^3$

4.4 Loading and Support Conditions

In the experimental set up, the point loads are located at the top of the beam at a distance of 700 mm from both ends. The load is transferred to the beam using steel plates of 50 mm x 25 mm. All the beam models to be numerically analysed are also loaded in the same way as in the experiments as seen in Figure 4.1.

At a distance of 200 mm from one edge of the beam, the translation in both horizontal (T1) and vertical directions (T2) is restricted and at a distance of 200 mm from the other edge of the beam, only the translation in the vertical direction (T2) is restricted as shown in Figure 4.1. Directly under the point loads, the translation (T2) is restricted to apply a displacement controlled load as shown in Figure 4.1.

4.5 Meshing

By defining element size of 25 mm as the seeding method, Hexa/quad mesher type and on-shape mid-side node location, all the beams in the analyses are meshed. The elements used in the mesh are CQ16M and CL12I as seen from 4.11 [29].

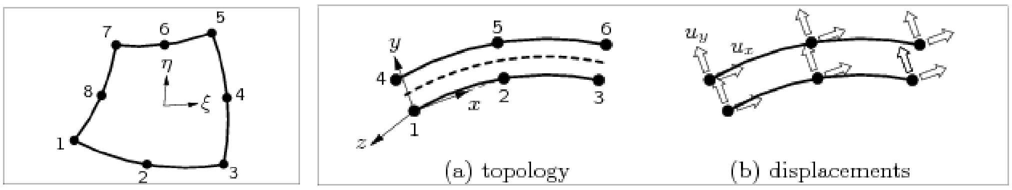

(a) CQ16M element **(b)** CL12I

Figure 4.11: Elements used in the beam models

4.6 Analysis Procedure

A displacement controlled load of step size 0.1 for a maximum deformation of 25 mm is applied at the two loading points on the beam with only physical non-linearity effect turned on. Regular Newton-Raphson method with a maximum of 100 iterations is also applied as the equilibrium iteration for all the analyses. Energy norm with a tolerance of 0.001 is applied to all the analyses to check the convergence criterion. Output such as displacements, reaction forces, total strain and crack-widths is generated for all the analyses.

4.7 Results and Discussion

The results obtained by the numerical analyses of the beam specimens is discussed in this section and compared to the obtained experimental results.

4.7.1 Hybrid Beam with Smooth Interface (S-PVA)

The Figure 4.12 shows the behaviour of S-PVA specimen analysed both numerically and experimentally and plotted in a load vs deformation vs maximum crack-width graph. It can be observed that the plot of load vs deformation obtained by the numerical analysis is much stiffer than the plot obtained from the experimental testing of the same specimen. Also, the numerical model is less ductile in comparison to the results obtained from the experimental testing.

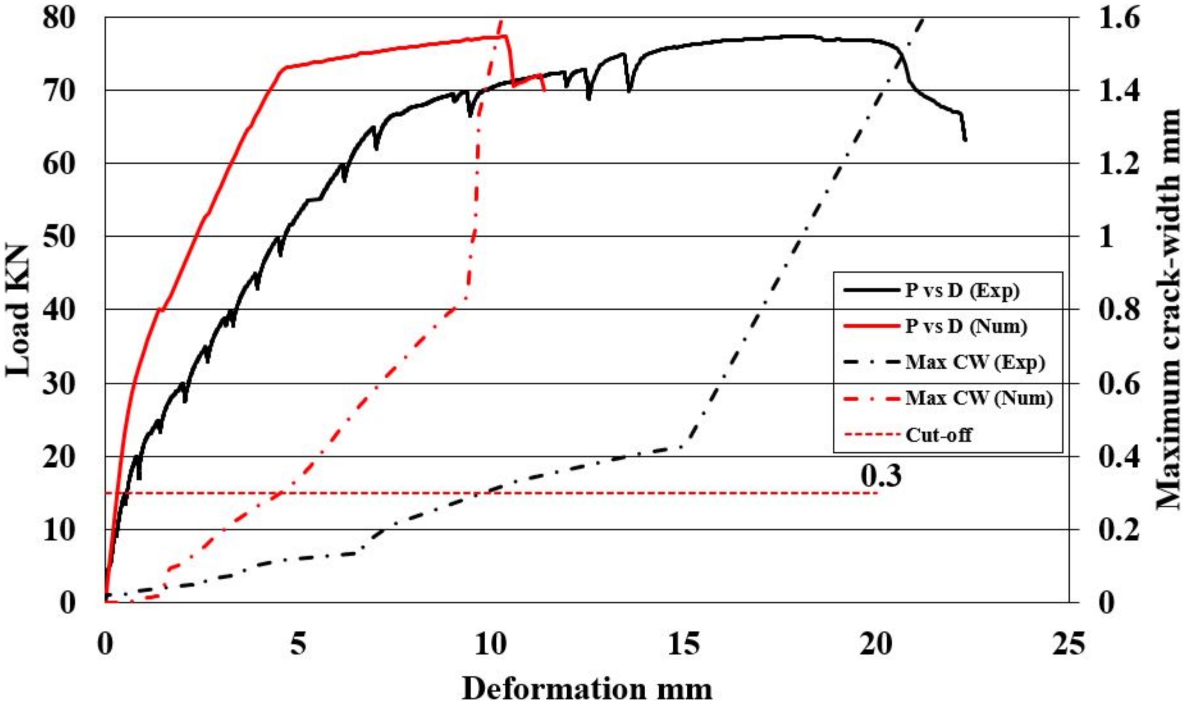

Figure 4.12: Comparison between numerical (Num) and the experimental (Exp) results of S-PVA specimen

To understand this difference in stiffness between the numerical model and the experimental beam specimen, a sensitivity analyses of the possible parameters governing is performed. Parameters such as Young's Modulus of SHCC, CC, normal and shear stiffness applied to the bond-slip reinforcement and the normal and shear stiffness applied at the interface are varied. It is apparent that the only parameter governing significantly is the normal and shear stiffness applied to the interface.

Once the normal stiffness was reduced by a factor of 1000 and shear stiffness is reduced by a factor of 100, as indicated in the Table 4.10, it is observed that the load vs deformation plot of beam specimen obtained by numerical analysis overlaps with the plot obtained by the experimental testing as can be seen in Figure 4.13. However, the ductility aspect could not be improved.

Table 4.10: Normal and Shear stiffness of the bonded part of the interface

Property	Value
Normal Stiffness	132.5772 N/mm^3
Shear Stiffness	3.31433 N/mm^3

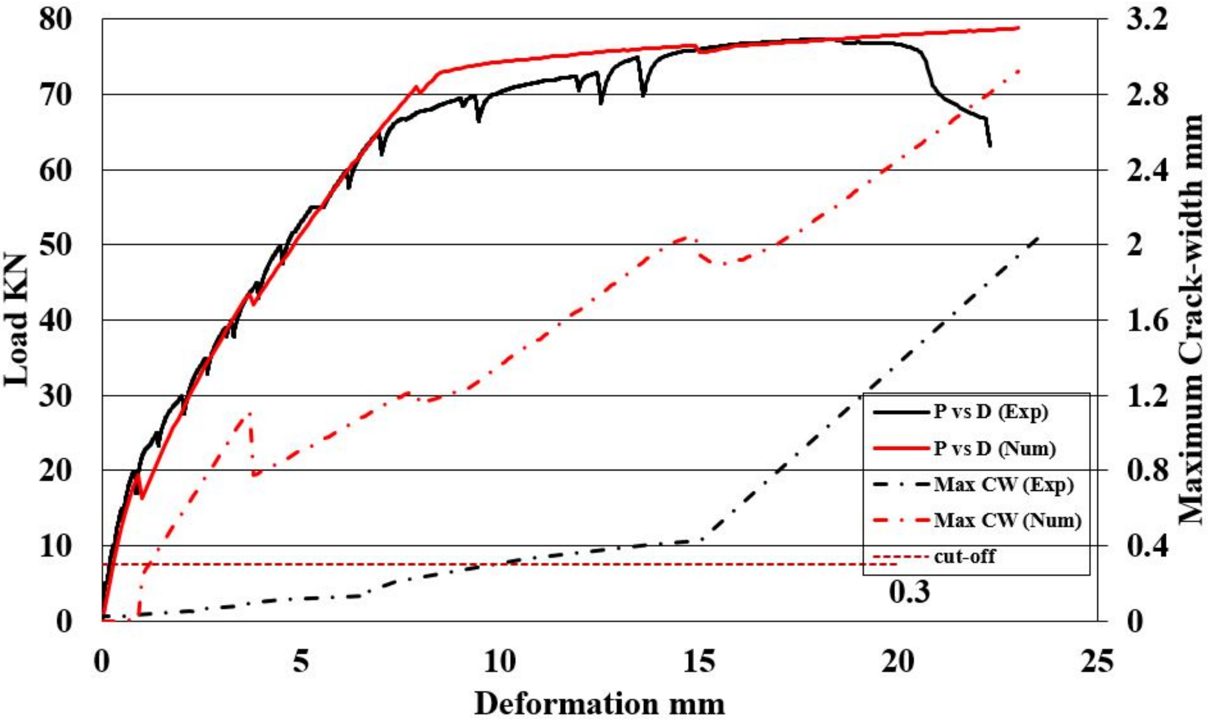

Figure 4.13: Comparison between numerical (Num) and the experimental (Exp) results of S-PVA specimen with reduced stiffness at the interface

Without reducing the stiffness at the interface, the cracking pattern obtained is shown in Figure 4.14. It is observed that six cracks are formed in the CC layer at the end of the numerical analysis as seen in Figure 4.14a whereas, the number of cracks formed in the CC layer after the experimental testing are seven as shown in Figure 4.14c. Despite having almost the same number of cracks, the crack-width at the various loading steps is very different from one another. By reducing the stiffness at the interface, four large cracks are formed in the constant moment region as shown in Figure 4.14b.

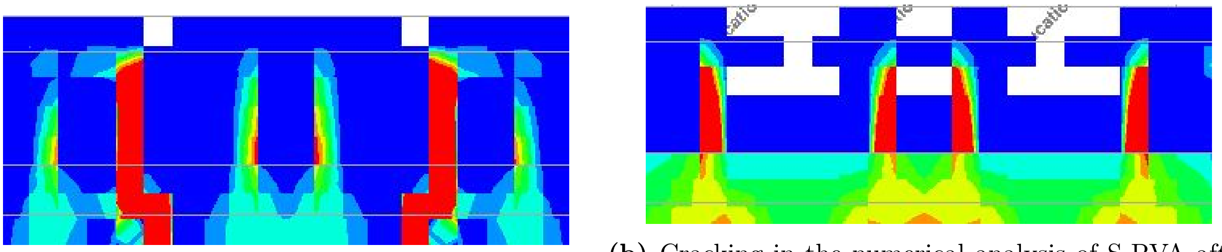

(a) Cracking in the numerical analysis of S-PVA

(b) Cracking in the numerical analysis of S-PVA after reduction in interface stiffness

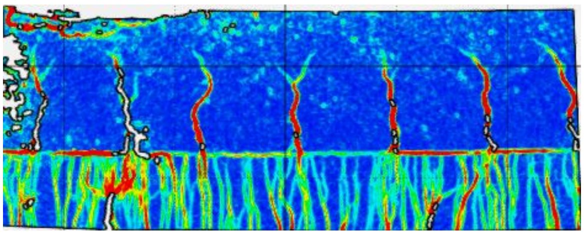

(c) Cracking in the experimental testing of S-PVA

Figure 4.14: Crack comparison in S-PVA specimen

4.7.2 Hybrid Beam with Completely Delaminated Interface (CD-PVA)

The Figure 4.15 shows a comparison between the numerical analysis and the experimental testing of the CD-PVA beam specimen. It is seen from the plot that, the load vs deformation plot obtained from the numerical analysis of the beam is stiffer than the results obtained from the experimental testing. Hence, the stiffness of the interface is reduced as shown in Table 4.10. Figure 4.16 shows the plot of load vs deformation with reduced interface stiffness parameters. It can be seen here that the load vs deformation plots obtained after reducing the stiffness from numerical analysis and the experimental testing are very close to each other with overlaps at a few places.

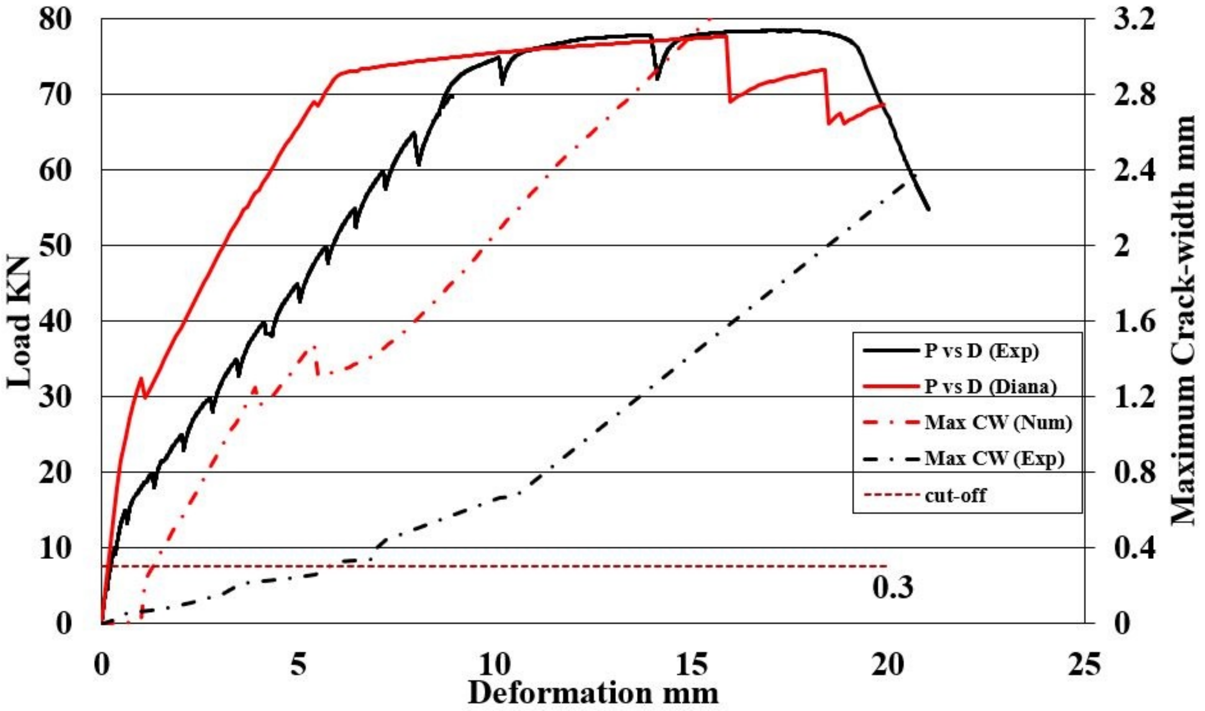

Figure 4.15: Comparison between numerical (Num) and the experimental (Exp) results of CD-PVA specimen

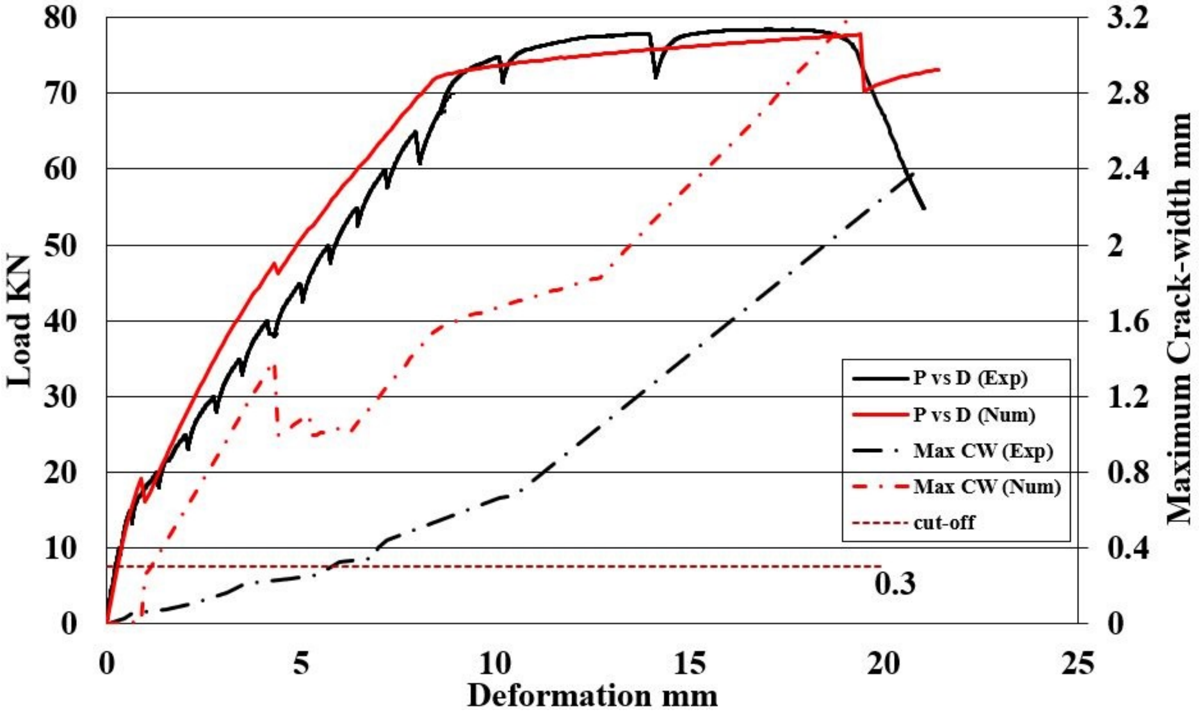

Figure 4.16: Comparison between numerical (Num) and the experimental (Exp) results of CD-PVA specimen with reduced stiffness at the interface

The cracking pattern obtained using the numerical analysis with and without a reduction in the stiffness at the interface is shown in Figures 4.17a and 4.17b respectively. The cracks observed are different in terms of the number of cracks and their respective crack-widths in comparison to the ones obtained by experimental testing as shown in Figure 4.17.

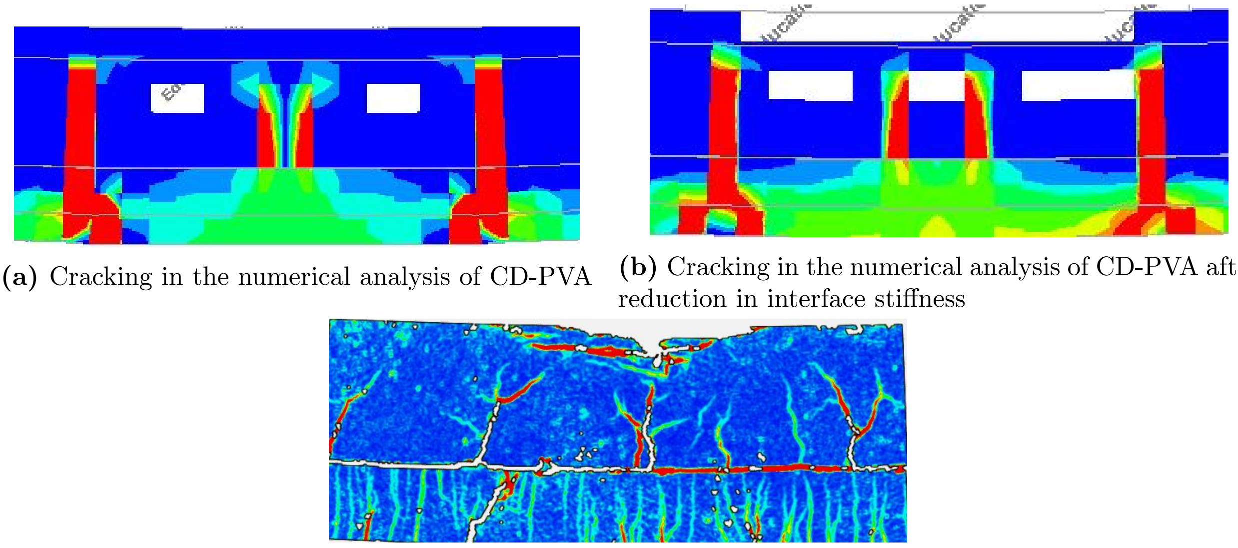

(a) Cracking in the numerical analysis of CD-PVA

(b) Cracking in the numerical analysis of CD-PVA after reduction in interface stiffness

(c) Cracking in the experimental testing of S-PVA

Figure 4.17: Crack comparison in CD-PVA specimen

Since, the numerically analysed beam specimens S-PVA and CD-PVA do not show correlation with the results obtained experimentally, further study with variation of interface properties and type of fiber is discontinued. This is because the material and the interface property options available on Diana are limited in replicating the actual behaviour.

Chapter 5

Conclusions and Recommendations

In the beginning of this master thesis research, a hypothesis is postulated stating that varying the interface property and the fiber type used in SHCC can influence the mirco-cracking behaviour of SHCC. To investigate this hypothesis, a set of research questions are framed and answered by testing the beam specimens both experimentally and numerically. The conclusions deduced are summarised as follows:

1. This research is an extension of the study conducted by Huang (2017) [1] who tested hybrid beam specimens with smooth interface and variable thickness of the SHCC layer. A beam specimen with smooth interface and 70 mm thick layer of SHCC is tested in a four-point bending set-up for this research and compared to the similar beam specimen tested by Huang [1]. A comparable behaviour is observed validating the benefit of using SHCC in the tension zone of SHCC-Concrete Hybrid beams. The load at which the maximum allowable crack-width of 0.3 mm at SLS localised is 71 KN in this research and 63 KN in the research done by Huang (2017) [1].
2. It is observed that for all the beam specimens tested, varying the interface properties did not have a major impact on the bearing capacity. A possible reason could be that the interface property is varied only within the constant moment region and the surface outside this region is bonded.
3. When the interface property is varied among smooth, profiled, partial and full debond in the constant moment region, it is observed that different surface preparations cause differences in the cracking pattern observed. The beam specimens with smooth interface surface (S-PVA) and Profiled interface surface (P-PVA) developed sufficient bond at the interface. Because of this local adhesion between the two layers, the surface roughness played a minor role.
4. S-PVA roughened with wire brush for better bond, exhibits development of sufficient debonding length at the interface. Due to this, the strain generated could be distributed over a longer length allowing the cracks to be distributed throughout the SHCC layer thus, preventing any early localisation or failure. It is also observed that only a few cracks from the SHCC layer propagate directly to the conventional concrete layer because of the surface roughening. While, the majority of the cracks formed remain in the SHCC layer because of debonding of the interface. The load at which maximum allowable crack-width in SLS is reached is 71 KN which is 82 % higher than that of conventional concrete beam specimen (CC).
5. P-PVA with toothed grooves in the constant moment region enabled a better mechanical interlocking at the interface and a very small debond length. As a result, it is observed that the cracks generated in the SHCC layer further concentrate over a very small debond length at the interface. A pronounced monolithic behaviour is observed as the cracks from the SHCC layer directly propagate into the conventional concrete layer. Also, the load at which the maximum allowable crack-width in SLS is reached is 69 KN which is comparable to S-PVA i.e. 3 % smaller and 77 % higher than the CC specimen.

6. Artificial debond at the interface, within the constant moment region, is introduced with the intention to relieve strains in a controlled manner in beam specimens with partial debond (PD-PVA) and complete debond (CD-PVA). It is observed that the beam specimen with partial debond localises at an early load step of 50 KN. The load at which the maximum allowable crack-width is reached is at 54 KN which is 31.5 % smaller than the load in case of S-PVA and 38.5 % higher than the load in case of CC specimen. For beam sample with artificial debond introduced completely in the constant moment region (CD-PVA), a controlled delamination allows the complete usage of the SHCC layer. This is because the cracks developed are both uniformly distributed and evenly spaced. However, the cracks in the SHCC layer localise at an early load step of 45 KN. The load at which the maximum allowable crack-width in SLS is reached is 44 KN which is 61 % smaller than the load in case of S-PVA and only 13 % higher than the load in the case of CC specimen. A possible reason for the early localisation of crack in the SHCC layer, in both PD-PVA and CD-PVA beam specimens, is the higher stresses generated in the SHCC layer due to the severely cracked concrete layer.

7. During pre-study, the beam specimen with HMPE fibers in SHCC (S-HMPE) indicated a better behaviour than beam specimen with PVA fibers in SHCC, in terms of bearing capacity and number of distributed cracks but its performance is similar to the beam specimen with PVA fibers during the experimental testing. The load at which the maximum allowable crack-width is reached is 65 KN which is only 9 % smaller than the load in case of S-PVA and 67 % higher than the load in the case of CC specimen. The reason why HMPE fibers are unable to out perform the PVA fibers despite having better mechanical properties could be due to the additional boundary condition introduced by applying a layer of CC on top of it. This applied additional constraint restricts the free flexural deformation of SHCC layer containing HMPE fibers and is clearly observed in the crushing of the CC layer before the SHCC layer fails. Another possible reason for this result could be the difference in standard deviation noticed while conducting the pre-study for SHCC samples with HMPE fibers. The samples show sufficient difference in the stress vs deformation plot as shown in Figure 3.3b for specimens HMPE1 and HMPE4.

8. The numerical models analysed to replicate the beam behaviour show a higher stiffness and a lower ductility than the obtained experimental results. Based on the sensitivity analysis, the reduction in the normal and shear stiffness factors of the interface reduced this additional stiffness. However, the ductility aspect of the beam specimens could not be improved numerically. Even though Diana FEA is able to predict the number of cracks close to the ones obtained experimentally, the crack-width values are completely out of range to the ones measured experimentally. Thus, it can be concluded that the material models and interface properties are insufficient in completely replicating the strain-hardening behaviour of SHCC along with interface properties of SHCC hybrid beams according to the authors knowledge.

Based on the obtained results and conclusions from this master thesis research, the following recommendations are made:

1. To analyze the influence of interface properties in tension and shear using analytical and numerical techniques.

2. Introduce a new material model for numerical modelling of the fiber volume, orientation and type in order to replicate the ductile behaviour of SHCC.

3. Use a software that enables measurement of the crack-widths throughout the surface under study, as GOM correlate measures the crack-widths only at specific sections.

Appendix

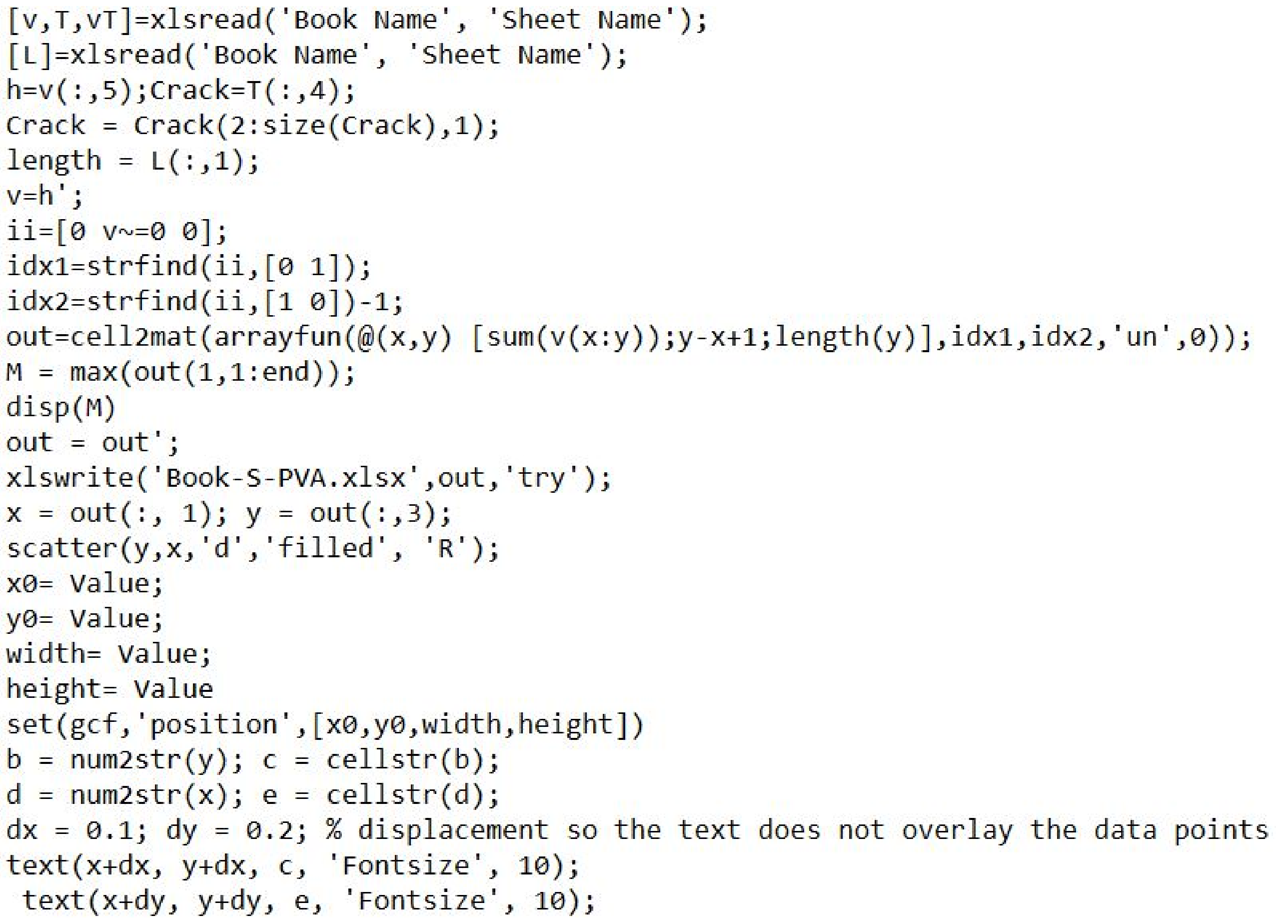

```
[v,T,vT]=xlsread('Book Name', 'Sheet Name');
[L]=xlsread('Book Name', 'Sheet Name');
h=v(:,5);Crack=T(:,4);
Crack = Crack(2:size(Crack),1);
length = L(:,1);
v=h';
ii=[0 v~=0 0];
idx1=strfind(ii,[0 1]);
idx2=strfind(ii,[1 0])-1;
out=cell2mat(arrayfun(@(x,y) [sum(v(x:y));y-x+1;length(y)],idx1,idx2,'un',0));
M = max(out(1,1:end));
disp(M)
out = out';
xlswrite('Book-S-PVA.xlsx',out,'try');
x = out(:, 1); y = out(:,3);
scatter(y,x,'d','filled', 'R');
x0= Value;
y0= Value;
width= Value;
height= Value
set(gcf,'position',[x0,y0,width,height])
b = num2str(y); c = cellstr(b);
d = num2str(x); e = cellstr(d);
dx = 0.1; dy = 0.2; % displacement so the text does not overlay the data points
text(x+dx, y+dx, c, 'Fontsize', 10);
 text(x+dy, y+dy, e, 'Fontsize', 10);
```

Figure 5.1: Code to calculate maximum crack-width on Matlab

Bibliography

[1] Z. Huang, “Flexural behaviour of reinforced concrete beams with a layer of shcc in the tension zone: Experimental study,” 2017.

[2] V. C. Lepech, M.; Li, “Water permeability of cracked cementitious composites,” *Paper 4539 of Compendium of Papers CD ROM, ICF 11, Turin, Italy*, 3 2005.

[3] P. V. C.Li, *Durability of Strain-Hardening Fibre-Reinforced Cement Based Composites (SHCC)*, 01 2011.

[4] B. Bissonnette, L. Courard, D. W. Fowler, and J.-L. Granju, *Bonded Cement-Based Material Overlays for the Repair, the Lining or the Strengthening of Slabs or Pavements: State-of-the-Art Report of the RILEM Technical Committee 193-RLS*, 01 2011.

[5] H. Beushausen, “Long-term performance of bonded concrete overlays subjected to differential shrinkage,” 2005.

[6] Y. He, X. Zhang, D. Hooton, and X. Zhang, “Effects of interface roughness and interface adhesion on new-to-old concrete bonding,” *Construction and Building Materials*, vol. 151, pp. 582–590, 10 2017.

[7] Q. Li and S. Xu, “Experimental investigation and analysis on flexural performance of functionally graded composite beam crack-controlled by ultrahigh toughness cementitious composites,” *Science in China Series E Technological Sciences*, vol. 52, pp. 1648–1664, 06 2009.

[8] M. Mohamad and I. Ibrahim, “Interface shear strength of concrete-to concrete bond with and without projecting steel reinforcement,” *Jurnal Teknologi*, vol. 75, pp. 1–2015, 07 2015.

[9] M. Luković, “Influence of interface and strain hardening cementitious composite (shcc) properties on the performance of concrete repairs,” Ph.D. dissertation, 01 2016.

[10] N. U. H. N. Ahmed Kamal, Minonu Kunieda, “Evaluation of crack opening performance of a repair material with strain hardening behaviour,” *Elsevier*, pp. 1–9, 2008.

[11] . B. J. A. O. Esmaeeli, E., “Flexural strengthening of rc beams using hybrid composite plate (hcp): Experimental and analytical study,” *Composites Part B-Engineering*, vol. 79, pp. 604–620, 2008.

[12] M. Mansourinik and F. Taheri-Behrooz, “The effect of interface debonding on flexural behaviour of composite sandwich beams,” *Journal of Sandwich Structures & Materials*, p. 109963621878198, 06 2018.

[13] I. Curosu, V. Mechtcherine, and O. Millon, “Effect of fiber properties and matrix composition on the tensile behavior of strain-hardening cement-based composites (shccs) subject to impact loading,” *Cement and Concrete Research*, vol. 82, pp. 23 – 35, 2016.

[14] W.-P. S. Ming-Hsiang shih, “Application of digital image correlation method for analysing crack variation of reinforced concrete beams,” *Indian Academy of Sciences*, 10 2012.

[15] "Eurocode 2: Design of concrete structures en1992-1-1."

[16] J. D.-S. S. Wang, k and A. F. Karr, "Permeability study of cracked concrete," *Cement and Concrete Research*, vol. 27, no. 3, pp. 381–393, 1997.

[17] L. M. Sahmaran, M. and V. Li, "Transport properties of engineered cementitious composite under chloride exposure," *ACI Materials Journal*, vol. 104, no. 4, p. 604–611, 2007.

[18] P. Jun and V. Mechtcherine, "Behaviour of strain hardening cement-based composites (shcc) under repeated tensile loading," *Proceedings of Rilem Symposium on High-Performance Fibre Reinforced Cementitious Composites HPFRCC5- H.-W. Reinhardt and A.Naaman (Eds.), Rilem Publications*, p. 97–104, 2007.

[19] T. Morita, A. Nishida, N. Yarnazaki, U. Schneider, and U. Diederichs, "An experimental study on spalling of high strength concrete elements under fire attack," *Fire Safety Science*, vol. 6, pp. 855–866, 2000.

[20] I. Yoshitake, K. Baba, T. Ito, and K. Nakagawa, "Behavior of fiber reinforced concrete under fire temperature."

[21] M. Pigeon and F. Saucier, "Effect of fiber properties and matrix composition on the tensile behavior of strain-hardening cement-based composites (shccs) subject to impact loading," *In Proceedings, International Symposium on Advances in Concrete Technology, Athens*, p. 741–773, 1992.

[22] "Aci committee 546, guide for repair of concrete bridge superstructure (aci 546.1 r-80), american concrete institute, detroit, 20 pp., 1980."

[23] E. K. Schrader, "Mistakes, misconceptions, and controversial issues concerning concrete and concrete repairs," *Concrete International*, vol. 14, 1992.

[24] D. M. R. Taha, *International Congress on Polymers in Concrete (ICPIC)*, 2018.

[25] R. Ramesh, "Digital image correlation," *ASEM*, 2010.

[26] F. B. Paolo Caporossi, Paolo Mazzanti, "Digital image correlation (dic) analysis of the 3 december 2013 montescaglioso landslide (basilicata, southern italy): Results from multi-dataset investigation," *International Journal of Geo-information*, 07 2018.

[27] B. B. M.A.N. Hendriks, A. de Boer, "Guidelines for the nonlinear finite element analysis of concrete structures," *Rijkswaterstaat Technical Document (RTD)*, 6 2017.

[28] M. K. Magus Eriksen, "Investigation of cracking behaviour in reinforced concrete panels with bond-slip reinforcement," *Rijkswaterstaat Technical Document (RTD)*, 6 2016.

[29] "Coulomb friction," *Diana Manual.*

[30] I. S. I. Mazizah Ezdiani Mohammed, "Interface shear strength of concrete-to-concrete bond with and without projecting steel reinforcement," *Rijkswaterstaat Technical Document (RTD)*, 6 2015.

[31] "Interface material model," *Atena Programming Documentation.*